Elastohydrodynamic Model of Hydraulic Rod Seals with Various Rod Surfaces

A Ph.D. Dissertation
Presented to
The Academic Faculty

By

Yuli Huang

In Partial Fulfillment
of the Requirements for the Degree
Doctor of Philosophy in Mechanical Engineering

Georgia Institute of Technology
December 2014

Elastohydrodynamic Model of Hydraulic Rod Seals with Various Rod Surfaces

Approved by:

Dr. Richard F. Salant, Advisor
School of Mechanical Engineering
Georgia Institute of Technology

Dr. Kenneth M. Will
School of Civil and Environmental Engineering
Georgia Institute of Technology

Dr. Jeffrey L. Streator
School of Mechanical Engineering
Georgia Institute of Technology

Dr. Gerhard Poll
Institute of Machine Design and Tribology
Leibniz University of Hannover

Dr. Scott S. Bair
School of Mechanical Engineering
Georgia Institute of Technology

Date Approved: October 30, 2014

ACKNOWLEDGEMENTS

I would like to express my sincere gratitude to my Ph.D. advisor, Professor Richard F. Salant, for his advice, encouragement, support and guidance during my graduate study at Georgia Institute of Technology. His attitude and practice on academic research would be a lighthouse for the rest of my life.

I would also like to thank my thesis committee members: Professor Jeffrey L. Streator, Dr. Scott S. Bair, Professor Kenneth M. Will, and Professor Gerhard Poll for their great help on my thesis work.

I gratefully acknowledge the National Science Foundation, Center for Compact and Efficient Fluid Power, which provided the financial support for this research.

Finally, I wish to thank my parents Changling Huang and Yan Li, and my wife Jiayao Ni. Their understanding, love, and support are the propulsion that advance me all these years.

TABLE OF CONTENTS

LIST OF TABLES

LIST OF FIGURES

NOMENCLATURE

A area of the sealing zone

A_{cav} cavity area

A_{land} land area

d cavity depth or protrusion height

E elastic modulus

F cavitation index, 1 when $\Phi \geq 0$, 0 when $\Phi < 0$

f friction coefficient for asperity contact

H dimensionless average film thickness, h/σ

h fluid film thickness

H_T dimensionless average truncated film thickness, h_T/σ

K load ratio, $L/P_{dc,smooth}$

L load per unit area

L_x length of solution domain in x direction

L_y length of solution domain in y direction

P dimensionless fluid pressure, p / p_a

p_a ambient pressure

P_c contact pressure, or dimensionless contact pressure, p_c / E

p_{cav} cavitation pressure

$P_{dc,smooth}$, P_{sc} static contact pressure with smooth rod

P_f fluid pressure

$\hat{q}$ dimensionless flow rate per unit circumferential length, $12\mu_0 qL / \left(p_a \sigma^3 \right)$

q_x flow rate per unit width in x direction

q_y flow rate per unit width in y direction

R asperity radius

$\hat{t}$ dimensionless time, $t/t_{reference}$

U surface speed of rod

$\hat{x}$ dimensionless axial coordinate in x direction, x/L_x

$\hat{y}$ dimensionless axial coordinate in y direction, y/L_y

$\hat{\alpha}$ dimensionless pressure-viscosity coefficient, αp_a

α dimensionless asperity radius, R/σ

β dimensionless asperity density, $\eta \mathrm{R}^2$

$\tilde{\varepsilon}$ $\mu_0 L^2/(\sigma^2 p_a t_{reference})$

Φ fluid pressure/density function

$\phi_f, \phi_{fss}, \phi_{fpp}$ shear stress factors

$\phi_{s.c.x}$ shear flow factor

ϕ_{xx} pressure flow factor in *x* direction

ϕ_{yy} pressure flow factor in *y* direction

Λ dimensionless ratio, L_x/ L_y

μ_0 viscosity at atmospheric pressure

ρ density

$\hat{\rho}$ dimensionless density, ρ/ρ_f

ρ_f fluid density

$\hat{\sigma}$ dimensionless rms roughness of sealing element surface, $\sigma R^{1/3} \eta^{2/3}$

σ rms roughness of sealing element surface

$\hat{\tau}_f$ average dimensionless viscous shear stress in the *x* direction, τ_f / E

$\hat{\tau}_c$ dimensionless shear stress due to contacting asperities, τ_c / E

ν Poisson's ratio

ξ $R^{1/3}\eta^{2/3}EL / p_a$

ζ dimensionless rod speed, $\mu_0 UL / \left(p_a \sigma^2 \right)$

η asperity density

SUMMARY

The reduction or elimination of leakage of hydraulic fluid from fluid power systems is considered a fundamental prerequisite for the expanded use of fluid power. There is also a need to reduce seal friction to both reduce energy dissipation and eliminate control problems. These seals are developed through empirical means at the present time, since the fundamental physics of seal operation has been unclear.

This research develops numerical models for analyzing reciprocating hydraulic rod seals with various rod surfaces. These models consist of coupled fluid mechanics, contact mechanics and deformation analyses. Both flooded and starved lubrication boundary conditions are applied.

For seals with a smooth rod and a plunge-ground rod, the model combines a 1-D finite volume Reynolds equation solver with a 2-D axisymmetric finite element deformation and static contact mechanics analyses, and a Greenwood-Williamson contact mechanics analysis with rod motion. Leakage and friction, along with sealing zone details with the plunge-ground rod are compared with those with the smooth rod. The influence of rod surface finish on seal performance is investigated and explained, under both flooded and starved conditions

For seals with a micro-patterned rod, the model consists of finite volume Reynolds equation solver, finite element deformation and static contact mechanics analyses and a Greenwood-Williamson dynamic contact mechanics analysis. This

model is able to handle rod surface pattern with 3-dimensional geometrics. Simulations with different micro-pattern geometries are performed to analyze the fundamental mechanism of surface pattern effects on seal operation. Again, both flooded and starved conditions are applied and the results for both cases are compared and analyzed.

CHAPTER 1. INTRODUCTION

1.1 Problem Description

Fluid power, especially hydraulics technology, plays an important role in today's industry since it offers important advantages over other power transmissions technologies, which include: high horsepower-to-weight ratio, high torque at low speed, multi-functional control, elimination of complicated mechanical trains of gears, etc. A significant amount of research has been applied to the hydraulic system. Improving the system and component efficiencies is one of the most important topics of this research, since inefficiencies have been considered a major weakness of current fluid power systems [1].

The reciprocating rod seal is one of the most critical components in hydraulic systems, as it prevents leakage of hydraulic fluid into the environment. Figure 1 shows the hydraulic cylinders on an excavator and the position of the rod seal in the hydraulic cylinder. The friction force between the seal and rod produces an energy loss and increases control difficulties in the system, suggesting that the friction between the rod seal and the rod is an important aspect of seal performance as well as leakage.

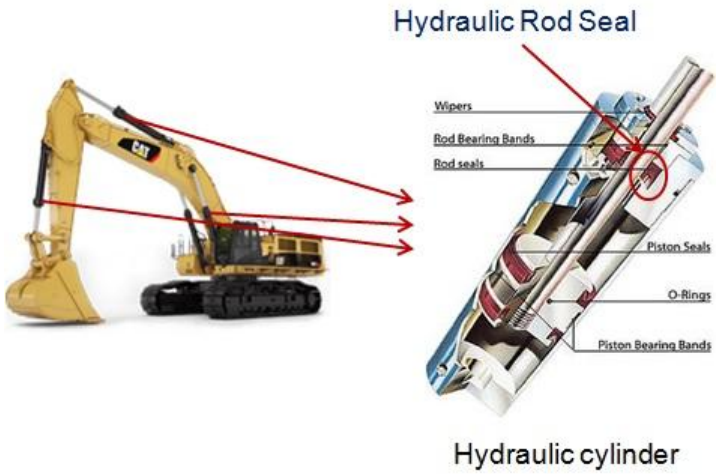

Figure 1.1: Hydraulic cylinder and hydraulic rod seal

At the present time, although a great deal of research has been applied to such seals, both experimental and theoretical, the details of sealing are not clear. While most studies consider flooded lubrication conditions, many seals operate with starved lubrication, which will cause significant changes in the friction compared to flooded lubrication. To date, there have been no numerical investigations applied to rod seals with starved lubrication boundary conditions. While the seal surface roughness has been considered in previous research, the influence of the rod surface on seal behavior, in particular the surface finish or surface pattern, is not clear.

In summary, This research investigates the problems listed below:

1. How does rod seal performance with starved lubrication differ from that with flooded lubrication?

2. How does rod surface finish affect rod seal performances?

3. How do designed surface patterns affect rod seal performance?

1.2 Objective of the Research

The primary goal of this research is to develop numerical models for analyzing reciprocating hydraulic rod seals under flooded and starved boundary conditions with various rod surfaces. These models are used to predict important seal performance characteristics like fluid transport and friction between the seal and rod, as well as the details of the sealing zone, such as the fluid pressure distribution, contact pressure distribution and fluid film thickness distribution.

The numerical models in this research have an important improvement compared to previous ones: they are able to simulate both flooded and starved lubrication instead of only flooded lubrication. For reciprocating rod seals, the starved situation is very common. When the rod moves out of the hydraulic cylinder (normally called the outstroke), there is always sufficient fluid, supplied by the cylinder, to lubricate the sealing interface, and the flooded boundary condition exists. When the rod moves into the cylinder (normally called the instroke), it transports the fluid lying on the rod surface as a result of the preceding outstroke, back into the cylinder. Therefore, the maximum fluid transport into the cylinder is equal to the fluid transport during the preceding outstroke process. If this maximum instroke fluid transport is lower than that necessary for flooded lubrication, starvation will occur. The numerical models in this research that apply starved boundary conditions give a more accurate prediction of seal performance for applications in which starvation occurs. They also help understand flooded and starved lubrication of the rod seal.

While some previous numerical models of the rod seal have taken seal surface roughness into account, the rod has generally been considered as smooth. However, there have been some empirical studies [2-4] that indicate that the rod surface finish does have an effect on seal behavior. The models developed in this research include the rod surface finish, namely the plunge-ground finish, which is very common for the rod seal. Both the U-cup and step seal with a plunge-ground rod are simulated. The analysis of these results provide an understanding of the mechanism of surface finish's influence on seal performance.

A three dimensional rod seal model is developed, for the study of a rod with a designed 3-D surface pattern. Such a surface texture on the shaft of a rotary lip seal has previously been studied [5-7] for the purpose of leakage reduction. In the present study these surface patterns are examined to see if they could reduce the friction between the rod and shaft while keeping essentially zero net leakage of the seal. Various pattern characteristics are be studied to find the important characteristics of the rod surface pattern that affect seal performances.

1.3 Brief Summary of Each Chapter

Chapter 1 gives a brief description of the problems that this research investigates, and expresses the objective of this research.

Chapter 2 provides the research background. The experimental and theoretical studies of rod seals over the past decades are described. The numerical studies of seals and lubrication are also discussed, showing the fundamentals and developments of

seal modeling research. Studies on flooded and starved boundary conditions of lubrication are presented, giving an idea of how these different lubrication conditions are investigated and treated in other applications. There are already some experimental and numerical studies on surface finish or surface patterns effects in various tribological applications. This chapter reviews that research, suggesting the possibilities that finish or patterns on rod surfaces could bring to seal performance.

Chapter 3 describes the Elasto-Hydrodynamic Lubrication (EHL) models that have been developed and applied in this research. Three major components of the EHL models: fluid mechanics, micro-scale contact mechanics; deformation and macro-scale contact mechanics, are introduced separately. This chapter also discusses the computational algorithms for various cases including two dimensional and three dimensional models, along with flooded and starved lubrication boundary conditions.

Chapter 4 discusses the studies on rod seals with a smooth rod. The assumptions and boundary conditions for two different seal types, the U-cup seal and step seal, are introduced. The results that are obtained using the EHL computational models with various conditions (2D and 3D, flooded and starved boundary) are presented and compared. Chapter 4 also demonstrates the effects of choosing different surface characteristics for the numerical simulations.

Chapter 5 focuses on the rod seal with a plunge-ground rod, using the two dimensional model. Both the U-cup seal and step seal have been analyzed and compared. For the U-cup seal, since starvation may occur during the operation, both

flooded and starved boundary conditions have been applied. For a better understanding of how the plunge-ground rod surface finish affects seal performances, hypothetical U-cup seal and step seal models with different surface characteristics have been generated and simulated. The comparison of results from hypothetical and original seals are presented and explained.

Chapter 6 analyses the rod seal with a micro-patterned rod using three dimensional models. There are two categories of seal patterns: cavities and protrusions on the rods. The geometrics and numerical models of these patterns are described, along with the computational algorithm that is applied for simulation with these patterns. Various factors that may affect seal performances are analyzed for the cavities and protrusions cases such as: time steps changing, cavity depth/protrusion height, land area ratio, cavity/protrusion shape, etc. In this chapter, both flooded and starved boundary conditions are applied and compared, giving additional understanding of both starvation and surface pattern effects on seal performance. All the simulation results above present not only the fluid transport and friction variation with rod speed, but details of the sealing zone, such as fluid pressure distribution, contact pressure distribution and fluid film distribution. These details give a deeper understanding of how the rod seal operates and how it is affected by various rod surfaces.

Chapter 7 discusses the main conclusions of this research and forecasts the possible application and future work.

CHAPTER 2. LITERATURE REVIEW

A great deal of research on reciprocating hydraulic rod seals, both experimental and theoretical, has been performed since the mid twentieth century and is described in a recent review [8]. However, the theoretical studies did not have a significant impact on industrial seal design. Only recently, has the numerical modeling technique begun to play an important role in seal research, design and test.

2.1 Experimental and Theoretical Studies of Rod Seals

2.1.1 Experimental Studies

Experimental research on hydraulic seals has made steady progress, which can be attributed to the successful development of experimental techniques, especially optical and micro-scale measurement techniques. The measurements of leakage, friction, contact pressure distributions and fluid film thickness have been the main objectives of the experimental studies of seals. White and Denny's research in 1947 [9] founded the basic understanding of elastomeric reciprocating seal operational behavior. Their studies included the measurements of tensile strain, contact stress and seal friction.

For measuring the leakage, the most common method is collecting the fluid leaked out of a cylinder using a counting cup and weighing the mass of the fluid that is collected during a certain number of strokes [10-16]. This method is also a standard,

used in industry for seal design and test. If the fluid leaked out is so little that it can't be collected, the seal is then considered to be effectively no net leakage. There are other techniques that are more precise and provide real-time results such as measuring the electrical capacitance of leaked oil layers using electrodes [17].

The measurement of the friction force exerted on the rod by the seals is included in most of the experimental studies. Although the friction force itself can be measured using a force transducer [18-20], there are two major problems: First, is the suspension of the rod or housing, which may introduce an additional force to the measured friction; second is the separation of the instroke and outstroke friction. In White and Denny's research [9], they designed a friction measurement system that has two seals at two ends of the housing. Lawrie and O'Donoghue [21] developed a technique with a rod and a closed housing, while Gawrys and Kollek [22] introduced the concept of a divided rod, which consists of two rods connected by a force transducer. Cheyney et al. [23] created a test rig for separating the outstroke and instroke friction forces.

The techniques used for measuring static contact pressure distributions include the strain gauge, piezoelectric force transducer, photo elastic method and inductive transducer. Most of these techniques were developed and applied in the 1970s and 1980s by Field, Molari, Austin, Kawahara and others [11, 13, 14, 24-28].

To measure the fluid film thickness, optical interferometry has been used since the 1960s [29-33]. The main problem that this research had to overcome is the low

reflectivity of rubber surfaces due to the roughness and dark color. Smoothening the seal surface or covering it with an external thin sheet would improve the reflectivity, but would also change the natural surface roughness of the seal, which may change the measured contact film thickness. Rana [34] developed a gold coating method to solve this dilemma: with a 50nm thick layer of gold coating, the influence on seal roughness was minimized while the reflectivity was increased. Besides optical interferometry, the direct observation of the fluid film achieved was with the development of high speed and micro-scale camera filming techniques. Schrader, Kawahara and Rana [26, 35-37] have designed various test methods to record the sealing surface using a high speed camera. Rana's recent experiments were able to observe hydraulic fluid starvation at the edges of the sealing contact. Poll and his research group [38-40] developed methods to measure the fluid film thickness, using a magnetic fluid or fluorescence image processing technique. Poll's recent work [41] applied the fluorescence method to analyze the lubricant film thickness on rod seals.

2.1.2 Theoretical Studies

Rod seals are normally made of compliant materials, either elastomers like rubber compounds or thermoplastics such as polyurethanes and PTFE. When strains exceed a certain limit, such materials exhibit non-linear stress-strain behavior. For rubber-like materials, hyperelastic material models are most commonly used [42-44]. Such models include the Ogden model [45-47], Neo-Hookean model [48] and Mooney-Rivlin model [49, 50]. The thermoelastic and thermoplastic materials

exhibit time dependent behavior, or viscoelasticity. Lakes' book [51] discussed several phenomenological models for capturing the viscoelastic response seen in those materials. His book also presented the constitutive equations describing these models. All these models now have been integrated into commercial finite element analysis (FEA) software such as ABAQUS and ANSYS. A basic understanding of these models is necessary for choosing the appropriate material model in the FEA modeling.

Most of the early theoretical seal modeling studies [8], with some exceptions, have made two assumptions: full film lubrication between the seal lip and the reciprocating rod, and perfectly smooth mating surfaces. In early 1970 it was found that those basic assumptions are questionable. In particular, experimental friction measurements indicate that mixed lubrication occurs over a wide range or operating conditions [13, 26, 33]. Also, the surface roughness, especially seal surface roughness, plays an important role in rod seal operation [52]. Because of the mixed lubrication and surface roughness, the lubricating film (on a scale of micrometers) is accompanied by mechanical contact. The fluid mechanics which is determined by the fluid film thickness distribution, is coupled with both the macro scale elastic deformation mechanics of the seal and the micro-scale contact mechanics of the sealing surfaces. The coupling between these equations and models is handled in two ways: the inverse method or the direct method.

For the inverse method, the hydrodynamic (fluid) pressure P_f is assumed to be known and equal to the static contact pressure $P_{c,static}$, since the static interference of

seal is much larger than the additional deformations caused by fluid pressure. Solving the Reynolds equation gives the fluid film *H*. A great deal of research has used this inverse method. [9, 10, 29, 53, 54]. However, this method relies on the assumption of full film lubrication, which is highly questionable, since experimental work indicates mixed lubrication, as discussed above.

In the direct method, iteration is applied. The film thickness distribution H is guessed initially. Through solving the Reynolds equation, the fluid pressure P_f is obtained. The contact pressure P_c is obtained using a contact model such as the Greenwood-Williamson contact model [55]. The fluid pressure P_f and the contact pressure P_c are then inserted into the elastic equations, which is solved for the deformation, giving a new H value. This new H, serving as the new input to the Reynolds equation and contact model, leads to a new fluid pressure P_f and contact pressure P_c. The iteration is continued until the solution converges. Frequently, instability problems occur with the direct method and there a number of studies on the improvement of the numerical stability have been performed. Field and Nau's research [56] introduced this methodology. Ruskell [57] tried to improve the instability problem by combining the elasticity equation of the seal and the Reynolds equation. Yang and Hughes [58], Prati and Strozzi [59] both used a similar method as Ruskell. Nikas [60-65] then developed a method that separates the effect of the roughness asperities and the bulk contact pressure effect. Still, most of the research above, especially the earlier studies, still assume full-film lubrication and neglect the seal surface roughness.

2.2 Surface Finish and Surface Pattern Influence

A great deal of research on fluid lubrication between rough surfaces has been performed [66-70]. Patir and Cheng developed a flow factor method that considered the roughness effect for lubrication between two sliding surfaces. To take account of possible cavitation, models based on the Jakobsson-Floberg-Olsson (JFO) theory have been developed since early 1980. Elrod [71] introduced an algorithm in which all of the JFO conditions are met within one universal Reynolds equation. Payvar and Salant [72] developed a similar algorithm, which minimizes the numerical instability. Harp and Salant [73, 74] performed research that considered both surface roughness and inter-asperity cavitation. Some later studies of Nikas [60-63, 75] did take into account the surface roughness as well as mixed lubrication, but was limited to rectangular seals. Yang and Salant [76, 77] successfully combined the factors of surface roughness, mixed lubrication and cavitation, and applied them to complex seal geometries. That work was limited to steady-state operation. Recent research by Thatte and Salant [78-81] developed models that include transients and consider the effects of viscoelasticity. Schmidt and Poll [82] also developed transient 2D finite element approach for the simulation of reciprocating rod seals with mixed lubrication.

Although the surface roughness of the rod is relatively small compare to that of the seal, some empirical studies [2-4] indicated that the rod surface finish does have an effect on seal behavior. A recent numerical and experimental study by Jia [83, 84]

revealed that the surface finish of the shaft could control the direction of the lubricant flow with a rotary seal.

Research has found that a micro-patterned surface may have a friction-reduction effect [85-87]. Wakuda, et al. [88] applied micro-texture to a ceramic surface that slides against steel materials with lubrication. Andersson [89] did research on textured steel surfaces under sliding conditions. Scaraggi and his research group performed similar studies [90-92] on lubricated, micro-textured, sliding surfaces. All the above results show a significant reduction of friction because of the surface texture. Etsion's research group also applied surface texture on piston ring [93-95] and mechanical seal [96, 97]. These research also found friction reduction effect. Shinkarenko, et al. [98-101] performed computational studies on the impact of a laser surface-textured elastomer on a rotary seal, while Etsion [102] investigated the manufacturing method and influence of surface-texturing on the shaft. Stephens and his research group [5-7] completed a series of experiments on rotary lip seals with deterministic surface textures on the shaft. They found the surface texture could help reduce the friction between the seal and shaft. Most of the above studies were applied to the rotary seal rather than rod seal. It is important to note that these two types of seals have different mechanisms of preventing leakage. Also, rotary seals generally operate with full film lubrication while rod seals generally operate with mixed lubrication, as discussed earlier.

2.3 Flooded and Starved Boundary Conditions of Lubrication

The effect of starvation can be important in lubrication flows. Figure 2.1 shows a sketch of flooded and starved lubrication during the instroke of a rod seal . With the flooded condition, the lubricant supply at the inlet to the sealing zone is sufficient to lubricate the entire sealing zone, while for the starved case, the lubricant supply at the inlet is not sufficient. The latter commonly occurs with the rod seal. When the rod moves out of the hydraulic cylinder (the outstroke), there is always sufficient fluid, supplied by the cylinder to lubricate the entire sealing interface, and the flooded boundary condition exists. When the rod moves into the cylinder (the instroke), it transports the fluid lying on the rod surface as a result of the preceding outstroke, back into the cylinder. Therefore, the maximum fluid transport into the cylinder is equal to the fluid transport during the preceding outstroke process. If this maximum instroke fluid transport is lower than that necessary for flooded lubrication, starvation will occur. Under such a condition, only a portion of the sealing zone will be lubricated, as shown in Figure 2.1. The inlet of the pressurized lubricated region will be a free boundary. To determine that region boundary is the key to the solution of the starvation problem. Since starvation changes the pressurized lubricated region, the friction force, especially the contact friction, may change compared to that with a flooded boundary. Chiu's research [103] introduced the importance of starvation effects in fluid lubricated contacts when calculating the rolling and sliding resistance and traction encountered in ball and roller bearings. Boness [104] performed both experimental and theoretical investigations of

restricting the lubricant to a roller bearing to reduce the amount of cage and roller slip. Brewe et al [105, 106] developed equations to calculate the change in film thickness with various inlet fluid levels. There are many other studies of the starvation effect in lubrication, but most of them are applied to journal bearings [107-110] or ball bearings [111-113]. Popovici's recent study [114] also focus on hard EHL with starvation. Hamrock did research on soft EHL[115, 116] with fully flooded and starved cases. Most of this research has relatively simple geometrics.

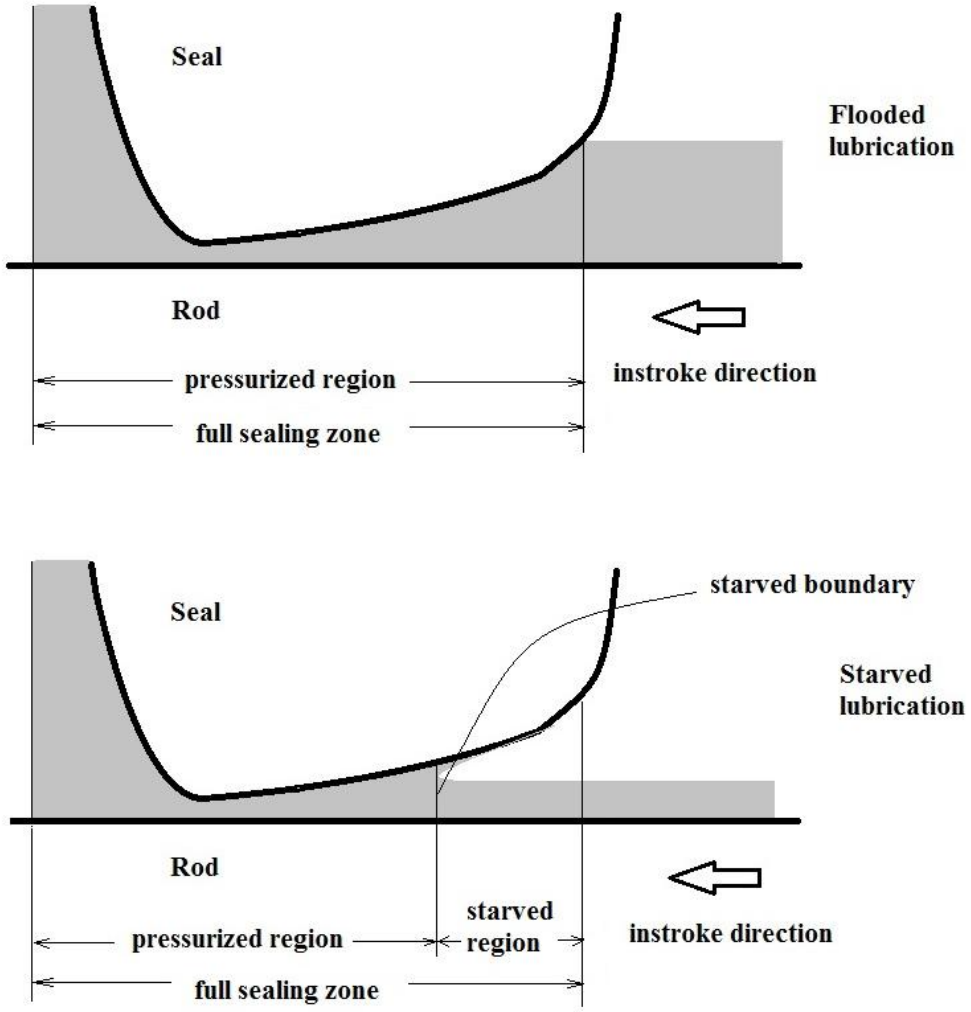

Figure 2.1: Flooded and starved lubrication

For the reciprocating seal, starvation is common because a sufficient lubricant supply only exists during outstroke inlet. During the instroke, lubricant supply at the inlet film relies on the lubricant deposited on the rod during the outlet. In addition, the behavior of the compliant seal material is more complicated than that of the bearing material. There is no published research on starved lubrication of the rod seal at the present time.

CHAPTER 3. EHL COMPUTATIONAL MODELS

3.1 Introduction

This chapter describes the development of the elastohydrodynamic (EHL) computational models for simulating dynamic rod sealing operation with various rod surfaces. Figure 3.1 shows a typical U-cup rod seal, schematically. Of primary interest is the sealing zone, where the seal meets the rod. A close-up of this region is also shown in Figure 3.1 for a perfectly smooth rod. The scales of the asperities on the seal surface are exaggerated, while the spacing between the asperities is much smaller than shown and is on the micron scale. There exists a lubricating film of hydraulic fluid of thickness h (which generally varies in the axial direction) in the sealing zone. The hydraulic fluid pressure distribution, the mechanical contact between the seal asperities and rod surface, and the frictional shear force within the sealing zone, are all key features that impact the seal performances.

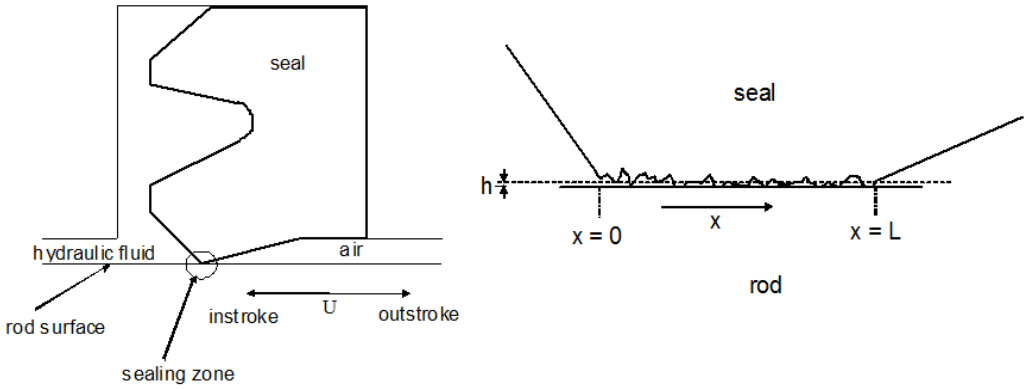

Figure 3.1: Rod seal components and sealing zone

The EHL computational models consist of three components: a fluid mechanics analysis of the lubricating film in the sealing zone; a micro-scale contact mechanics analysis of the seal and rod, contacting; and a deformation/ macro scale contact mechanics analysis of the seal; All three components are coupled together, but in different ways for 2-Dimensional and 3-Dimensional models, as shown in Figure 3.2 and Figure 3.3. Section 3.2 to section 3.4 will discuss each of these components in detail. Section 3.5 will introduce the computational algorithm for the 2-D and 3-D models, along with the computational procedure that considers the starved boundary condition. The reason why there are different schemes for the 2-D and 3-D models is due to the prohibitively large computation times required to directly compute the seal deformations in three dimensions. This will be discussed in Chapter 6.

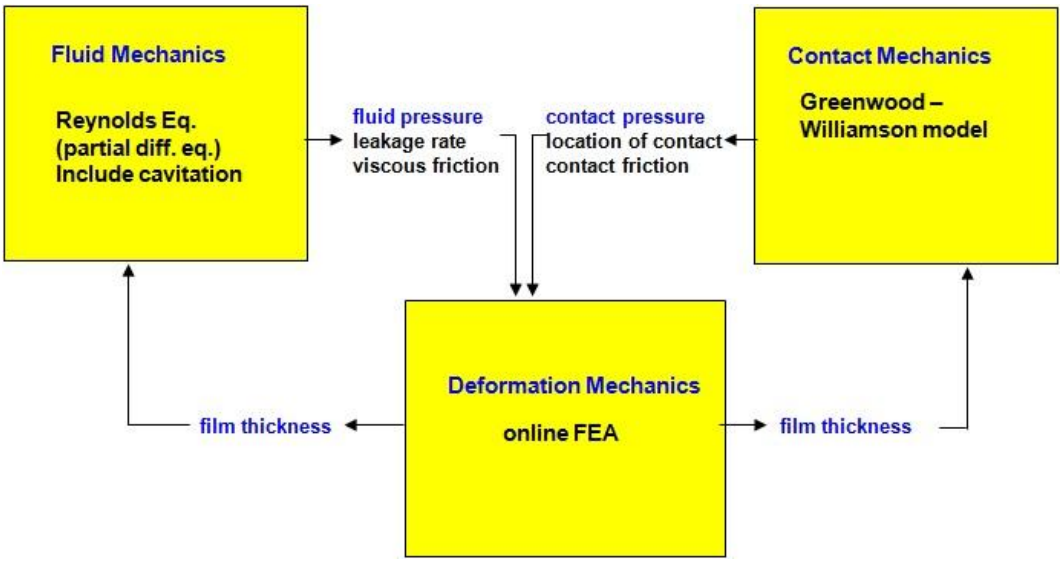

Figure 3.2: Scheme of the 2-D EHL computational model

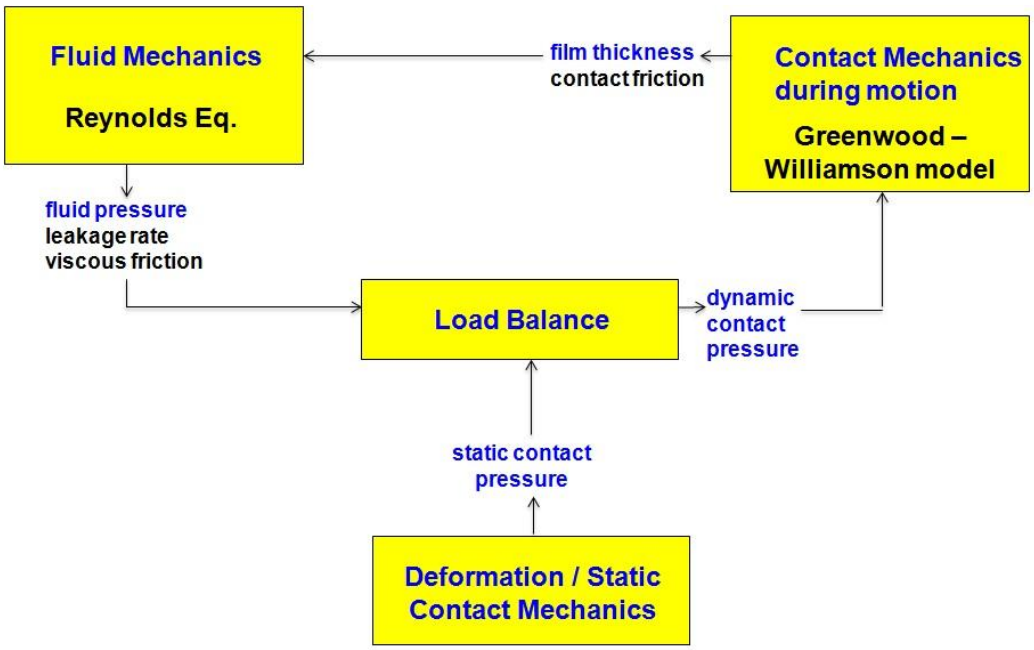

Figure 3.3 Scheme of the 3-D EHL computational model

3.2 Fluid Mechanics Analysis

3.2.1 Reynolds Equation

Reynolds equation is the differential equation governing the pressure distribution in the fluid film, under lubrication conditions. This equation was first derived by Osborne Reynolds in 1886 [117]. The Reynolds equation can be derived from the Navier-Stokes and continuity equations with the following assumptions:

1) The fluid is assumed to be Newtonian, incompressible and laminar.

2) The body forces in the fluid column and fluid inertia are neglected.

3) There is no slip at the boundaries.

4) The curvature of the surfaces is large compared with the film thickness (in case of Cartesian coordinates).

5) The pressure is assumed to be constant throughout the thickness of the fluid film.

The details of the derivation can be found in Hamrock's book[118] in Chapter 7. In two dimensions, the Reynolds equation takes the form:

$$\frac{\partial}{\partial x}\left(\frac{\rho h^3}{\mu}\frac{\partial p}{\partial x}\right)+\frac{\partial}{\partial y}\left(\frac{\rho h^3}{\mu}\frac{\partial p}{\partial y}\right)=6\left(U\frac{\partial \rho h}{\partial x}+2\rho\frac{dh}{dt}\right) \tag{3.1}$$

where h is the film thickness, ρ is the fluid density, μ is the fluid viscosity, and $U=U_1+U_2$. The flow rate can be written as:

$$q_x=\frac{-h^3}{12\mu}\frac{\partial p}{\partial x}+\frac{Uh}{2} \tag{3.2}$$

$$q_y = \frac{-h^3}{12\mu}\frac{\partial p}{\partial y}$$

where q_x and q_y are the flow rates per unit width in the x and y directions.

3.2.2 Taking Cavitation and Surface Roughness into Account

The cavitation phenomenon will occur when the fluid pressure, governed by Eq.(3.1), drops below the cavitation pressure, p_{cav}; in that region both liquid and vapor are present and the uniform pressure is p_{cav} . This phenomenon can be modeled based on the Jakobsson-Floberg-Olsson (JFO) theory. The algorithms of these models have been developed by Elrod [71] and Payvar and Salant [72]. Payvar and Salant introduced a variable Φ that has different definitions in liquid and cavitation regions, and a cavitation index, *F*:

$$\begin{gathered} \frac{p - p_{cav}}{p_{ref} - p_{cav}} = F\Phi \\ \hat{\rho} = \frac{\rho_e}{\rho_f} = 1 + (1 - F)\Phi \end{gathered} \tag{3.3}$$

In the full film region where fluid pressure is higher than p_{cav} , the cavitation index *F*=1, from Eq.(3.3) that gives:

$$\begin{gathered} \hat{p} = \frac{p - p_{cav}}{p_{ref} - p_{cav}} = \Phi \\ \hat{\rho} = \frac{\rho_e}{\rho_f} = 1 \end{gathered} \tag{3.4}$$

and in the cavitation region, the cavitation index F=0:

$$\begin{gathered} \hat{p} = \frac{p - p_{cav}}{p_{ref} - p_{cav}} = 0 \\ \hat{\rho} = \frac{\rho_e}{\rho_f} = 1 + \Phi \end{gathered} \tag{3.5}$$

From the above, in the liquid region Φ represents the dimensionless pressure, while in the cavitation region, Φ is related to the dimensionless equivalent density.

For taking the surface roughness into account, the "flow factor" method developed by Patir and Cheng is applied to obtain the "average" Reynolds equation, as part of a comprehensive micro-scale fluid flow model. More detail about this "flow factor" method can be found in Patir and Cheng [67, 68].

The Reynolds equation with flow factors becomes:

$$\begin{aligned} &\frac{\partial}{\partial x}\left(\phi_{xx}\frac{h^3}{\mu}\frac{\partial \bar{p}}{\partial x}\right)+\frac{\partial}{\partial y}\left(\phi_{yy}\frac{h^3}{\mu}\frac{\partial \bar{p}}{\partial y}\right) \\ &=6(U_1+U_2)\frac{\partial h_T}{\partial x}+6\sigma(U_1-U_2)\frac{\partial \phi_{s.c.x}}{\partial x}+12\frac{dh_T}{dt} \end{aligned} \tag{3.6}$$

where $\bar{p}$ is the mean (expected) pressure, ϕ_{xx} and ϕ_{yy} are the pressure flow factors. $\phi_{s.c.x}$ is the flow factor that accounts for the additional fluid transport due to the micro-scale pressure gradient caused by the sliding between rough surfaces. h_T is the average truncated film thickness, which is defined as:

$$h_T = \int_{-h}^{\infty}(h+\delta)\,f(\delta)d\delta \tag{3.7}$$

where $f(\delta)$ is the probability density function of δ. The flow rates can be written as:

$$\begin{aligned} \overline{q_x} &= -\phi_{xx}\left(\frac{h^3}{12\mu}\frac{\partial \bar{p}}{\partial x}\right)+\frac{(U_1+U_2)}{2}h_T+\frac{(U_1-U_2)}{2}\sigma\phi_{s.c.x} \\ \overline{q_y} &= -\phi_{yy}\left(\frac{h^3}{12\mu}\frac{\partial \bar{p}}{\partial y}\right) \end{aligned} \tag{3.8}$$

If both the cavitation and surface roughness effects are considered, combining Eq.(3.4), Eq.(3.5) and Eq.(3.7), and introducing the non-dimensionalized variables:

$\hat{x} = x/L_x$, $\hat{y} = y/L_y$, $\Lambda = (L_x/L_y)^2$, $P = p/p_a = F\Phi$, $\hat{\rho} = \rho_e/\rho_f = 1 + (1 - F)\Phi$, $H = h/\sigma$, $\hat{t} = t/t_{ref}$,

yields:

$$\begin{aligned}\frac{\partial}{\partial \hat{x}}\left(\phi_{xx}H^3 e^{-\hat{\alpha}F\Phi}\frac{\partial}{\partial \hat{x}}(F\Phi)\right) + \Lambda\frac{\partial}{\partial \hat{y}}\left(\phi_{yy}H^3 e^{-\hat{\alpha}F\Phi}\frac{\partial}{\partial \hat{y}}(F\Phi)\right) \\ = 6\zeta\frac{\partial}{\partial \hat{x}}(\{1 + (1 - F)\Phi\}\{H_T + \phi_{s.c.x}\}) \\ + 12\varepsilon\frac{\partial}{\partial \hat{t}}(\{1 + (1 - F)\Phi\}H_T)\end{aligned} \tag{3.9}$$

where $\hat{\alpha} = \alpha p_a$ is the dimensionless, $\zeta = \mu_0 UL/p_a\,\sigma^2$ is the dimensionless rod velocity, $\varepsilon = \mu_0 L^2/(\sigma^2 p_a t_{ref})$ is the dimensionless squeeze term coefficient, σ is the RMS roughness of the seal surface.

In the liquid region

$$\Phi \geq 0, F = 1 \; and \; P = \Phi$$

and in the cavitation region

$$\Phi < 0, F = 0 \; and \; P = 0, \hat{\rho} = 1 + \Phi$$

The truncated film thickness term is given by

$$H_T = \frac{H}{2} + \frac{H}{2}erf\left(\frac{H}{\sqrt{2}}\right) + \frac{1}{\sqrt{2\pi}}e^{-H^2/2} \tag{3.10}$$

assuming a Gaussian distribution of asperity heights on the contact surfaces.

If the lubricating film is only one-dimensional in a Cartesian coordinate system, Eq.(3.9) becomes

$$\frac{\partial}{\partial \hat{x}}\left(\phi_{xx}H^3 e^{-\hat{\alpha}F\Phi}\frac{\partial}{\partial \hat{x}}(F\Phi)\right) = 6\zeta\frac{\partial}{\partial \hat{x}}(\{1+(1-F)\Phi\}\{H_T+\phi_{s.c.x}\}) + 12\varepsilon\frac{\partial}{\partial \hat{t}}(\{1+(1-F)\Phi\}H_T) \tag{3.11}$$

Once Eq. (3.9) or (3.11) is solved, the flow rate can be obtained from:

$$\hat{q} = -\phi_{xx}H^3 e^{-\hat{\alpha}F\Phi}\frac{\partial(F\Phi)}{\partial \hat{x}} + 6\zeta(\{1+(1-F)\Phi\}\{H_T+\phi_{s.c.x}\}) \tag{3.12}$$

for both 1-D and 2-D cases, since the periodic boundary condition is applied for the 2-D study and there is no net flow (leakage) in the circumferential direction (y direction in Reynolds equation). The fluid transport can be calculated by integrating $\hat{q}$ over the outstroke/instroke time.

The average fluid shear stress on the seal surface is given by

$$\hat{\tau}_f = \frac{-\hat{\sigma}}{\xi}e^{-\hat{\alpha}F\Phi}\frac{\zeta}{H}(\phi_f-\phi_{fss}) - \phi_{fpp}\frac{\hat{\sigma}}{\xi}\frac{H}{2}\frac{\partial(F\Phi)}{\partial \hat{x}} \tag{3.13}$$

where all the flow factors, ϕ_{xx}, ϕ_{yy}, $\phi_{s.c.x}$, ϕ_f, ϕ_{fss} and ϕ_{fpp} are obtained by the method and results presented in Patir and Cheng [68].

The fluid pressure, which is obtained from the solution of Reynolds equation, together with the fluid shear stress, the contact pressure and asperity contact friction, which are obtained from the contact mechanics analysis, is used to compute the micro-scale deformation and film thickness, which is an input to the Reynolds equation, as described in the following sections.

3.2.3 Reynolds Equation Solution Algorithm

There is no closed form solution for the Reynolds equation, in general. A numerical solution method is needed. In this research, a finite volume method is applied to discretize Eq.(3.9) or Eq.(3.11). In addition, the tri-diagonal matrix algorithm (TDMA) method is implemented to solve the finite volume discrete equations. This finite volume discretization and TDMA algorithm is introduced in detail by Patankar [119]. Yang [120] and Thatte [121] also used the finite volume-TDMA algorithm in their fluid mechanics analyses of rod seals. An Alternating Direction Implicit (ADI) method [122] is used for the 2-Dimensional cases. The details of the algorithm development can be seen in Appendix A.

3.2.4 Flooded and Starved Boundary Conditions for Reynolds Equation

As shown in Figure 2.1, for the seals that are studied in this research, with both flooded and starved lubrication, one side (left in Figure 2.1) of the seal is always fully flooded, the sealing side. In the Reynolds equation solving process, that end of the computational mesh is given a constant fluid pressure, with the cavitation index F=1, indicating the fully flooded boundary condition.

The other side (right in Figure 2.1) of the sealing zone is the air side, where the seal is exposed to the atmosphere. With flooded lubrication, the entire sealing area (full sealing zone in Figure 2.1) is a pressurized region without starvation. So in the Reynolds equation solver, a constant atmospheric pressure with F=1 is applied to this end (air side) of the computational mesh as the boundary condition.

With starved lubrication, only part of the sealing zone is pressurized, while the rest is starved. The Reynolds equation solving process is only applied to the pressurized region. With the computational procedure that will be introduced in section 3.5.3 (will be 3.6.3 after another section is inserted), the position of the starved boundary (shown in Figure 2.1) is determined. A constant atmospheric pressure with F=1 is applied on that boundary instead of on the right end of the full sealing zone. All the nodes to the right of that starved boundary are not involved in the Reynolds equation solution process.

3.3 Micro-Scale Contact Mechanics

3.3.1 Greenwood and Williamson Surface Contact Model

The contact mechanics analysis in this research is based on the Greenwood and Williamson surface contact model [55, 123]. The key assumptions of this surface contact analysis model include:

1) All asperity contacts act independently: the load at a given asperity-asperity contact does not cause deformation in the vicinity of any other asperity-asperity contact.

2) Each asperity has a spherical shape near its summit.

3) All asperities of a given surface are assumed to have a radius of curvature equal to the average radius of curvature as determined from measuring the surface profile.

4) The contact between the rough surfaces can be modeled as an equivalent rough surface in contact with a rigid flat.

5) Asperities deform according to Hertzian contact theory.

With the Greenwood-Williamson model, the contact pressure is calculated using the following equation:

$$P_c = \frac{4}{3}\frac{1}{(1-\nu^2)}\hat{\sigma}^{2/3}\frac{1}{\sqrt{2\pi}}\int_H^\infty (z-H)^{3/2}e^{-z^2/2}dz \tag{3.14}$$

A Gaussian distribution of asperity heights is assumed. $\hat{\sigma} = \sigma R^{1/3}\eta^{2/3}$ is the dimensionless RMS roughness of the sealing surface with an RMS roughness of σ, asperity radius of R and asperity density of η. The measurements and calculation method of these surface characteristics will be introduced in the next section. This contact pressure, along with an empirical friction coefficient, *f*, is used to compute the asperity contact friction:

$$\hat{\tau}_c = \frac{\tau_c}{E} = -fP_c\left(\frac{\zeta}{|\zeta|}\right) \tag{3.15}$$

For computing the film thickness distribution that is related to a given asperity contact pressure, a regression method is used to invert Eq.(3.14) [79]:

$$H = a + b\cdot log_{10}(g) + c\cdot(log_{10}(g))^2 + d\cdot(log_{10}(g))^3 + e\cdot(log_{10}(g))^4 + f\cdot(log_{10}(g))^5 \tag{3.16}$$

where $g = -log_{10}|I|$, $I = \frac{P_c}{(4/3(1/(1-\nu^2))\hat{\sigma}^{2/3})}$, and *a*=0.86197, *b*=1.16979, *c*=0.34673, *d*=3.57134, *e*=1.07985, *f*=1.68629. If the contact pressure at the static condition is $P_c = P_{dc}$, then *H* from Eq.(3.15) is the static film thickness distribution, H_{dc}.

In the 2-Dimensional model, the static film thickness distribution, H_{dc}, along with the micro-deformation, H_{def} acquired from either the influence coefficient method or

the online-FEA method, gives the dynamic film thickness: $H = H_{dc} + H_{def}$. In the 3-Dimensional model, since the dynamic contact pressure P_c is acquired through the load balance computation, the dynamic film thickness H is directly calculated through Eq.(3.16).

3.3.2 Surface Characteristics, Measurements and Parameters

There are three surface characteristics in the Greenwood and Williamson surface contact model: the root mean square roughness (RMS) σ, the asperity radius R and the asperity density η. Since the parameters R and η are highly scale dependent, R is identified as the autocorrelation length, taking the surface roughness to be isotropic. According to Streator's work [123], the dimensionless parameters α and β are defined such that:

$$R = \alpha\sigma \text{ and } \eta = \beta/R^2 \tag{3.17}$$

For most surfaces, one expects α to be of order 1-10 and β to be of order 1. That means the nominal distance between asperities, which is approximated by R, should be a bit larger (by a factor of α) than a typical asperity height that σ represents; In addition, with asperities spaced at a nominal distance of R, there are about 1 (β) asperities per R^2.

The seals that are modeled in this research have been measured in previous studies by the same research group [77]. For the U-cup seal made of polyurethane, the measured seal surface RMS roughness is 0.8μm; for the step seal, with a seal element

material of PTFE, the RMS roughness is 4.0μm. Further discussion about the dimensionless parameters α and β will be introduced in the following chapters.

3.4 Deformation and Macro-Scale Contact Mechanics

3.4.1Geometries and Material Properties of Seals

Two different types of seals are considered in this research, the U-cup and the step seal. Figures 3.4a and 3.4b show the undeformed geometries of both types. For rod seals, there is a sealing side that is flooded with lubricant, and during the instroke process when rod move towards this side, there is a sealed pressure (in this study, the sealed pressure is always 1000psi, or 6.89MPa) applied on the seal. During the outstroke process when the rod moves away from the sealing side, the sealed pressure is equal to atmospheric pressure (in this study). There is also an air side where a flooded or starved boundary condition may be applied, and the pressure on this side is always at the ambient value. In this study the rod speed is held constant, at the same value during both instroke and outstroke. A range of speeds is considered. Transient effects due to acceleration/deceleration at the beginning and ends of the stroke are omitted, while those caused by the translating rod surface pattern are taken into account by inclusion of the squeeze film term in the Reynolds equation.

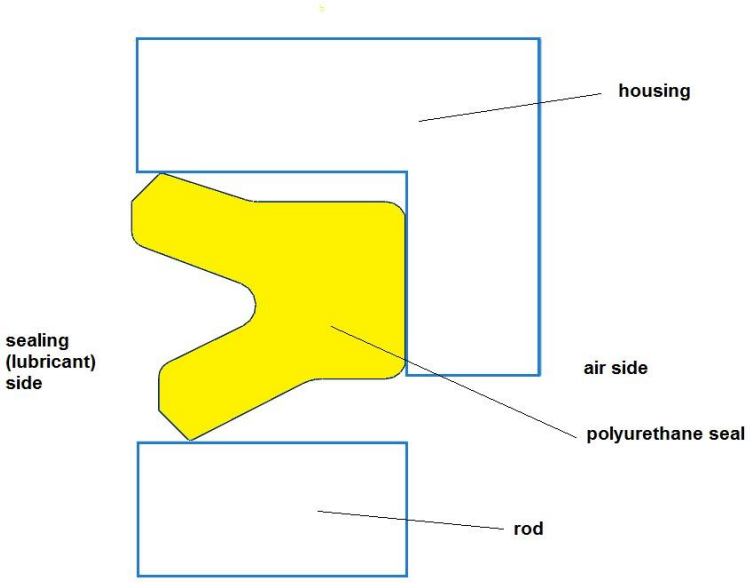

Figure 3.4a: Undeformed geometry of U-cup seal

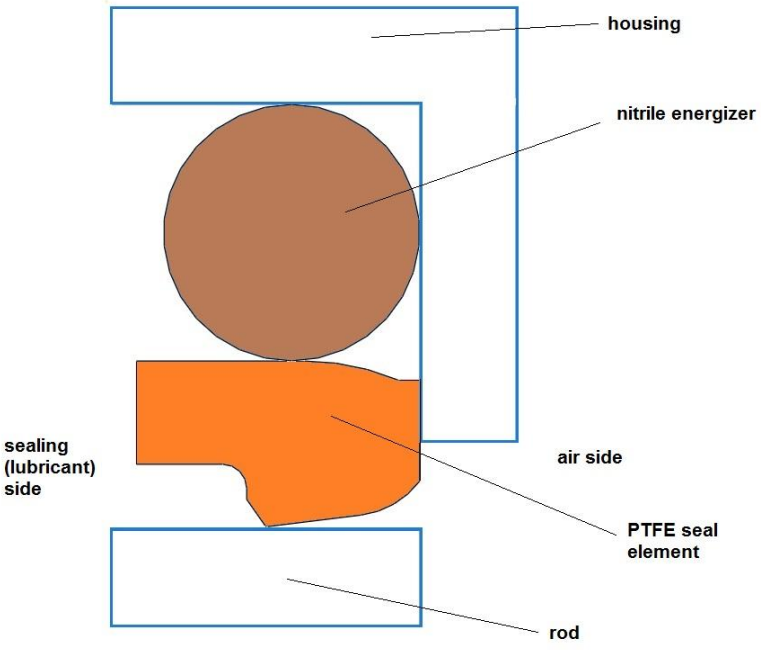

Figure 3.4b: Undeformed geometry of step seal

The vertical space between the rod and the housing is smaller than the size of the seals, so after mounting and pressurization (during the instroke), the seals are deformed. Figures 3.5a and 3.5b show the mounted and deformed geometries of the U-cup and step seals with the von Mises stress distribution inside the seals.

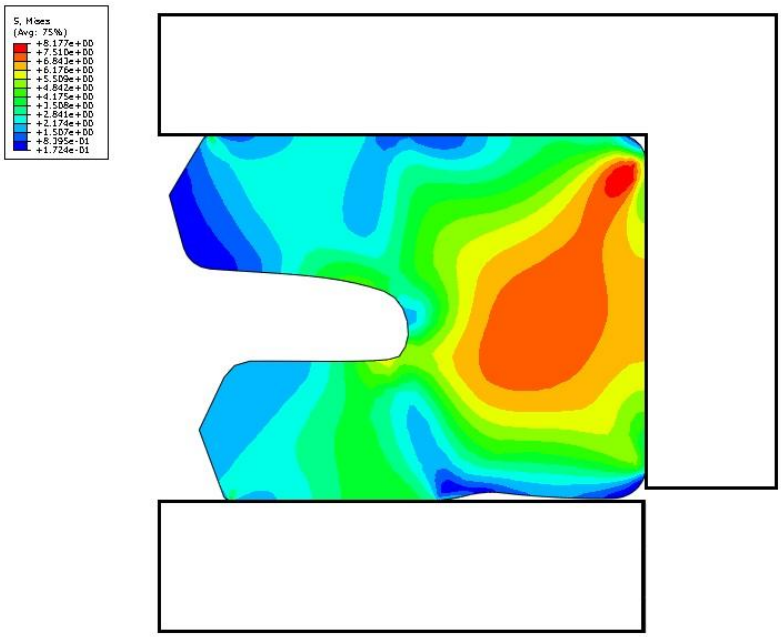

Figure 3.5a: Deformed (mounted & pressurized) geometry of U-cup seal

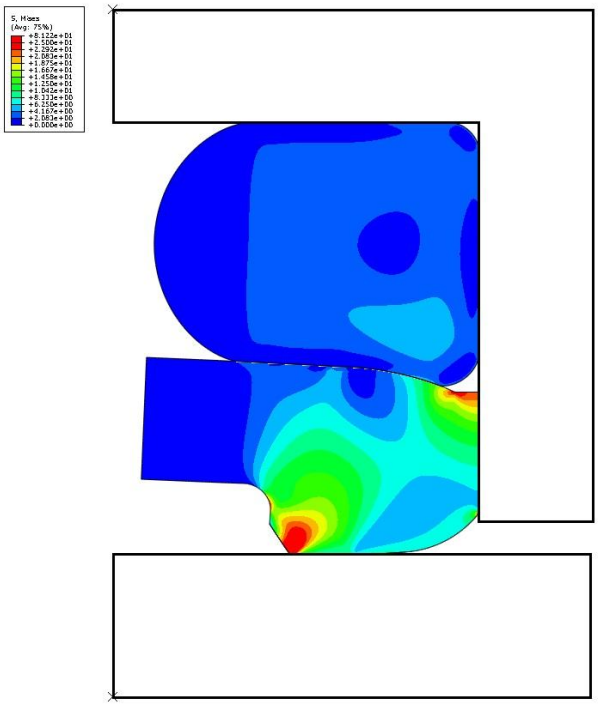

Figure 3.5b: Deformed (mounted & pressurized) geometry of step seal

The U-cup seal under study is made of polyurethane. Since the material of the housing and rod are both steel, which is much more rigid than polyurethane, the model considers the housing and rod as rigid bodies. Only polyurethane's material properties need to be considered. A Mooney-Rivlin hyperelastic model is used with an initial Young's Modulus of 43 MPa, a Poisson's ratio of 0.499, and the coefficients for a two parameter Mooney Rivlin model: C_{10}=0.2MPa, C_{01}=6MPa, and d=0.000279.

The step seal in this research is made of PTFE with a nitrile energizer. Like the U-cup seal model, the steel housing and rod are considered rigid. For PTFE, a hyperelastic model based on uniaxial test data is applied, with a compression

Young's Modulus of 550 MPa, a compression yield stress of 22MPa and a Poisson's ratio of 0.4. The stress-strain test data of PTFE is shown in Figure 3.6. For the nitrile energizer, a Mooney-Rivlin hyperelastic model is used with a Poisson's ratio of 0.499 and the coefficients for a two parameter Mooney Rivlin model: C_{10}=0.32746MPa, C_{01}=1.47067MPa, and d=0.001113.

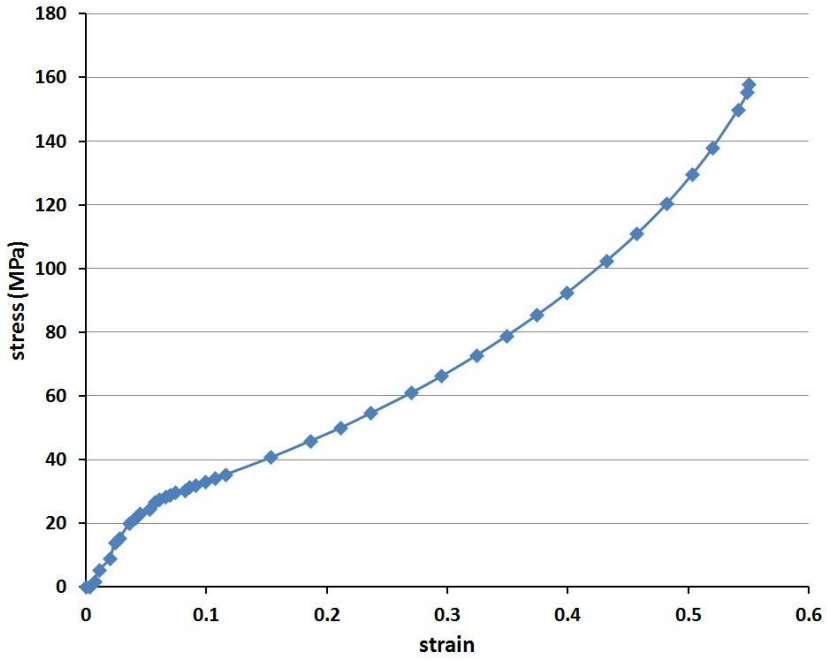

Figure 3.6: Measured PTFE stress-strain curve during compression

3.4.2 Finite Element Solution using ABAQUS

The deformation of the sealing element is computed by the finite element method, using the commercial software ABAQUS. The geometric profile of the seals are pre-built through the commercial CAD software AutoCAD, since the seals

have complex shapes that are difficult to be generated through the ABAQUS CAE module.

The material properties of the U-cup and step seal are generated in ABAQUS based on the description in the previous section.

For the U-cup seal, CAX8R, an 8-node biquadratic axisymmetric quadrilateral, reduced integration element is selected for the seal body, while RAX2, a 2-node linear axisymmetric rigid link (for use in axisymmetric planar geometries) element is chosen for the rod and housing parts. For the step seal, CAX8R element is applied on the seal element and energizer, while RAX2 element is used for the rod and housing parts. The interaction property for calculating the contact between the seal and rod, and the seal and housing is selected as "hard" contact for pressure-over closure option, and the default constraint enforcement method is used.

The meshed U-cup and step seals are shown in Figures 3.7a and 3.7b. Note that the mesh is refined in high pressure gradient areas such as the contact edge and lip tip of the seal. For reducing the computational time, a moderate mesh is sufficient for other area.

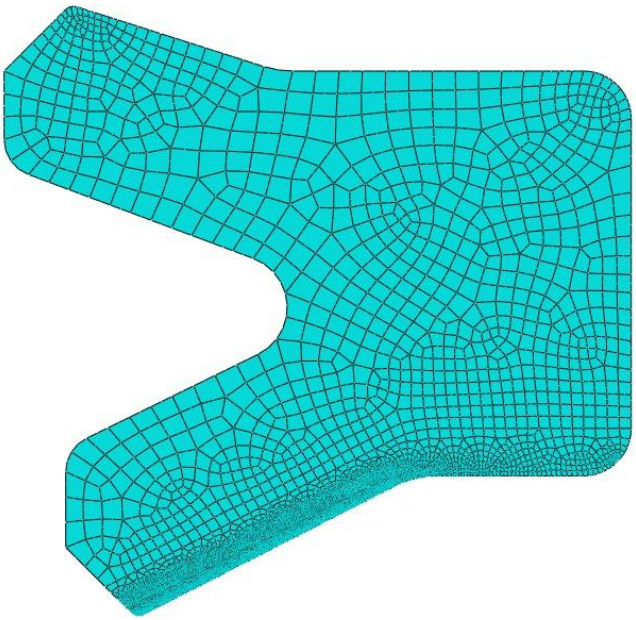

Figure 3.7a: U-cup seal meshing

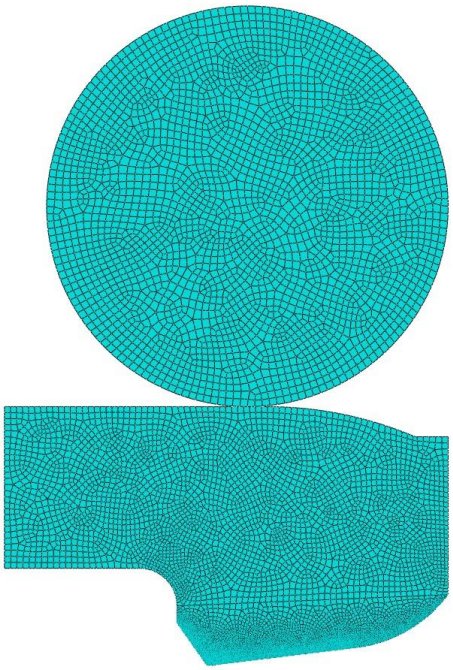

Figure 3.7b: Step seal meshing

Figures 3.8a and 3.8b show the load and boundary conditions for the two types of seals. The housing and rod are both fixed in the axial (Y) direction. The rod is moved up (positive direction) and the housing is moved down (negative direction) in the radial (X) direction for simulating the mounting process until they reach the designed position. The red outline with the red arrows shows where the sealed pressure is applied as a load on the sealing side.

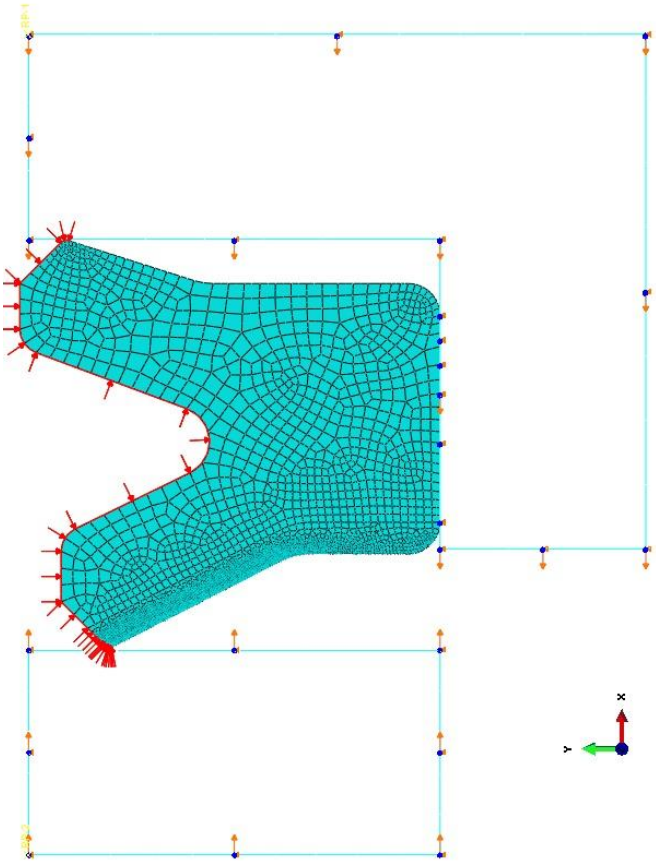

Figure 3.8a: Boundary conditions of U-cup seal

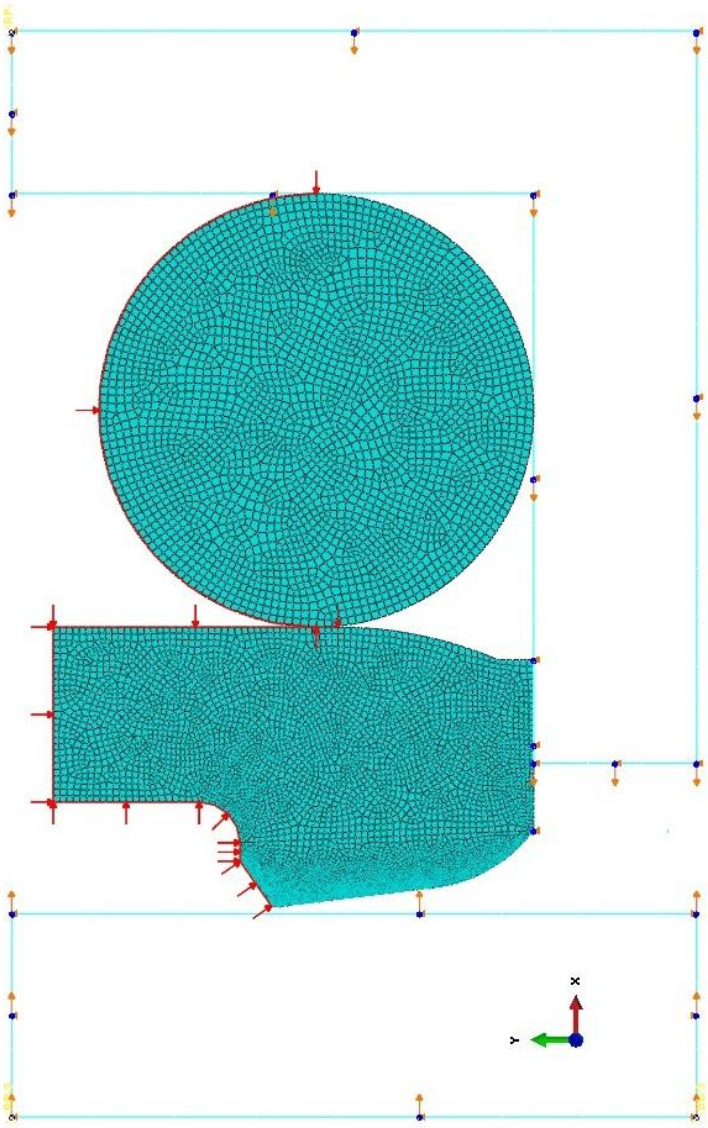

Figure 3.8b: Boundary conditions of step seal

A trial and error iteration process is used to determine the node that separates the sealed pressure area and contact area. More detail can be found in Yang's PhD thesis, Chapter 3. [120].

3.5 Load Balance

In the scheme of the 3-D EHL computational model shown in Figure 3.3, a load balance computation module connects the deformation and macro-scale contact mechanics analysis with the other two components, the fluid mechanics and contact mechanics during motion analyses. This load balance module calculates the total load applied on the sealing zone. Since any deformation during motion is small compared to the interference between the seal and the rod/housing, the total load on the sealing zone during motion should be the same as it is in the static condition.

The force applied on sealing zone during motion includes the fluid pressure and contact pressure. So the load balance calculation in this module can be written as:

$$\oint P_f dA + \oint P_c dA = \oint P_{sc} dA \tag{3.18}$$

It should be noted that a similar load balance (but without the dynamic contact pressure force) is implied in all the previous studies using the inverse Reynolds equation method, discussed in Chapter 2. More details and justification for this load balance calculation, especially for models that consider rod pattern, will be introduced and discussed in chapter 6.

3.6 Computational Procedure

This section discusses the computational procedure for the 2-D and 3-D models. The computational procedure that considers a starved boundary is also introduced.

3.6.1 Two-Dimensional Model

The computational procedure for the 2-Dimensional model is shown schematically in Figure 3.9. With input of the seal and fluid properties, and the operating conditions, the macro-scale contact mechanics and deformation are solved using ABAQUS, in order to obtain the dry contact pressure distribution at each time step for all of the planned instants of time. The dry film thickness is also computed for each time step by equating the latter computed contact pressure with the contact pressure computed with the Greenwood and Williamson model. At each time step, the initial guesses of film thickness and contact pressure distribution are based on the computed dry film thickness and dry contact pressure distributions.

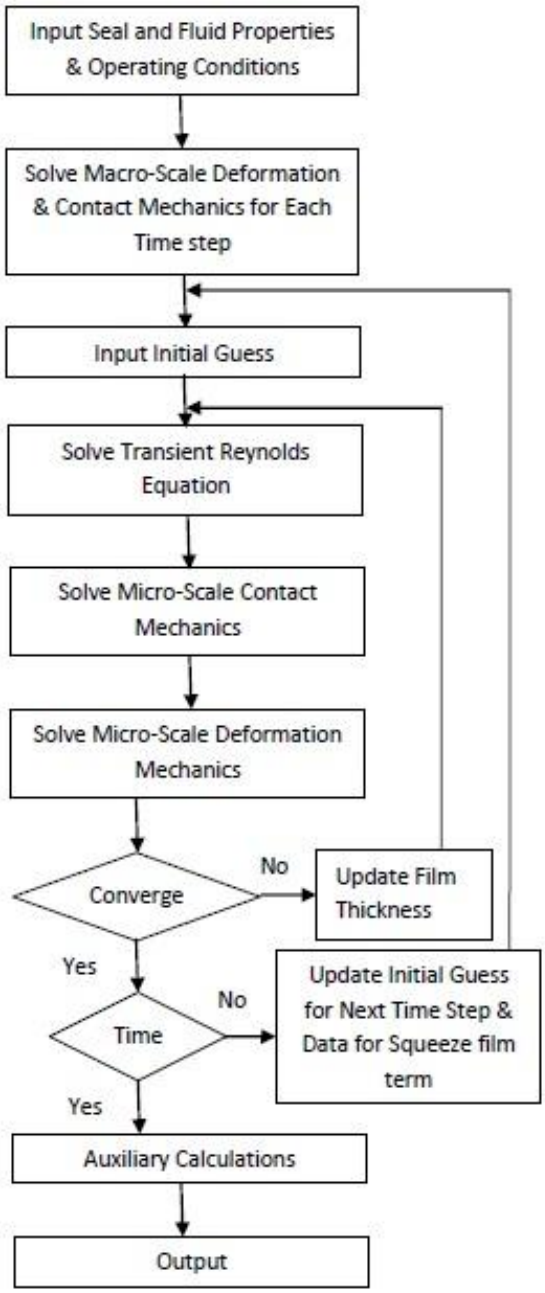

Figure 3.9: Computational procedure for 2-D model

Next, the fluid pressure distribution is obtained by solving the 1-D transient Reynolds equation, Eq. (3.11). The micro-scale contact mechanics is solved from Eqs. (3.14) and (3.15) and the micro-scale deformation of the seal is computed either with ABAQUS directly (the "online" method) or with the influence coefficient method. The computed radial deformation at the interface is added to the dry film thickness to yield the film thickness. Computation continues around the iteration loop shown in the figure until the solution for the film thickness converges, and then advances to the next time step if the rod is not smooth. After all the time steps are completed, auxiliary calculations for the flow rate, fluid transport and friction force are performed.

3.6.2 Three-Dimensional Model

The computational procedure of the 3-D model is shown schematically in Figure 3.10. With input of the seal and fluid properties, and the operating conditions, the macro-scale contact mechanics and deformation in the static state with the smooth rod are solved using ABAQUS, and the static contact pressure distribution is obtained. The static film thickness is also computed by the method introduced in section 3.3 with the Greenwood and Williamson model. The initial guesses of film thickness are based on the computed static film thickness.

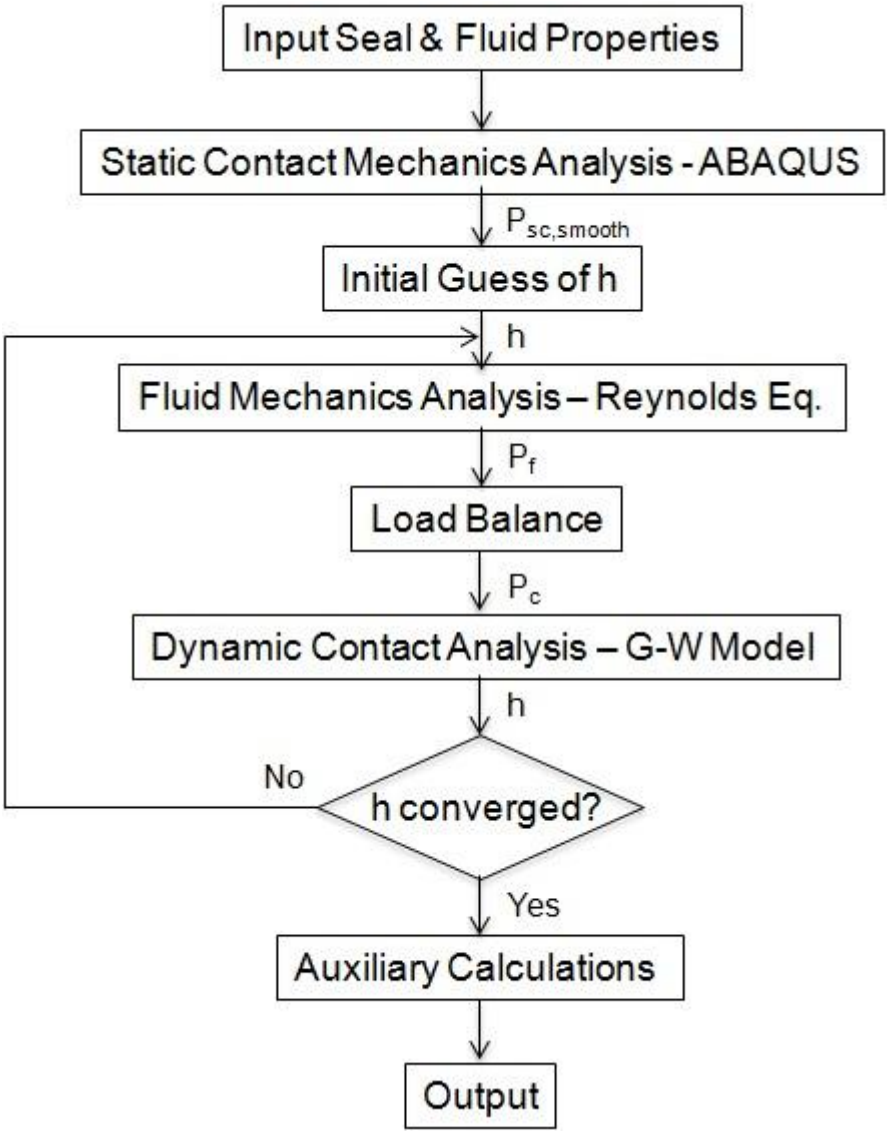

Figure 3.10: Computational procedure for 3-D model

The fluid pressure distribution is obtained by solving the 2-D Reynolds equation, Eq.(3.9), with the algorithm described in section 3.2. A load balance calculation, which will be discussed in detail in Chapter 6, is performed with input of the fluid pressure distribution and the total load on the sealing zone expressed by the static contact pressure. The fluid pressure P_f and a new dynamic contact pressure, P_c, added together, should equal the total load as expressed by the static contact pressure $P_{sc,smooth}$. Therefore P_c can now be computed. Through the dynamic contact analysis using the Greenwood and Williamson model, a new film thickness distribution is obtained. Computation continues around the iteration loop shown in the figure until the solution for film thickness converges. In 3-D cases, only one time step is calculated for the patterned rod. The justification of this single time step calculation will be shown in Chapter 6. After the film thickness is converged, auxiliary calculations for the flow rate, fluid transport and friction force are performed.

3.6.3 Models that Consider a Starved Boundary

Figure 2.1 shows the sketch of starvation during the instroke. Starvation may happen only during the instroke. The simulation results that support this statement will be shown in the following chapters. When starvation happens, the full sealing zone is divided into two zones as shown in the figure, the pressurized zone and the starvation zone The pressurized zone is fully flooded with lubricant, and the fluid mechanics and contact mechanics can be treated as described in previous sections. The starvation zone remains at atmospheric pressure and there is no need to apply a

fluid mechanics analysis in this zone. The contact pressure in the starvation zone is the same as that in the static case, and so is the contact friction.

The computational procedure for models that consider starvation is shown schematically in Figure 3.11. If the fluid transport during the instroke predicted by the flooded model is greater than that of the outstroke, starvation occurs because there is not enough available fluid to adequately lubricate the entire sealing zone during the instroke. The maximum value of the instroke fluid transport is equal to the outstroke fluid transport. To apply the starved boundary condition, an initial guess of the pressurized zone length, which is shorter than the full sealing zone length, is input into the 2-D or 3-D models. A complete computation is executed like described in section 3.5.1 or 3.5.2, but only on the guessed pressurized zone. A fluid transport result, Q, is obtained and compared with the known outstroke fluid transport Q_{out}. If $Q > Q_{out}$, the guessed pressurized zone it is shortened, while if $Q < Q_{out}$, the pressurized zone is lengthend. If $Q = Q_{out}$, the computation is complete and the results are outputted.

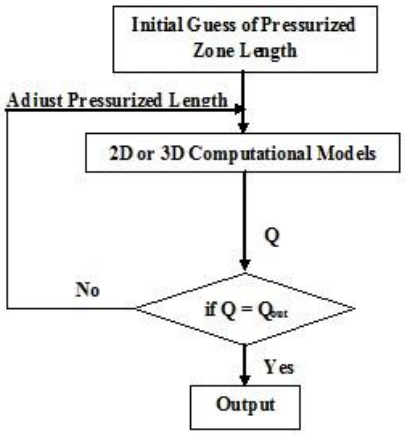

Figure 3.11: Computational procedure that considers starvation

CHAPTER 4. ROD SEAL WITH SMOOTH ROD USING 2D AND 3D MODELS

4.1 Introduction

In this chapter, the studies on rod seals with a smooth rod are discussed. Two types of seal are investigated: the U-cup seal and the step seal. For the U-cup seal, both 2-D and 3-D models are applied. The flooded and starved boundaries and their effect on the U-cup seal are also discussed. In addition, a surface characteristics study is performed on the U-cup seal, with the 3-D model and flooded boundary, to show how the surface characteristic parameters affect seal performance and sealing details. For the step seal, the simulation uses the 2-D model with only the flooded boundary condition, since there will not be starvation over the range of operating conditions studied. All these smooth rod cases studies' results will be used as comparison to the results of the rod with a surface finish or surface texture, in chapter 5 and 6, to demonstrate the influence of the various rod surfaces.

4.2 Assumptions and Boundary Conditions

Figure 4.1 shows a reciprocating rod seal in a hydraulic cylinder, and its operating conditions. During the instroke, the piston is moving into the cylinder, the sealing side of the rod seal is facing a high sealed pressure; during the outstroke, the piston is moving out of the cylinder and the sealing side of the rod seal is facing a low

sealed pressure. In this research, the high sealed pressure is always 1000 psi or 6.89 MPa, and the low pressure is always the ambient value. Note for some applications during the outstroke, the sealed pressure can also be high (e.g. injection molding actuators).

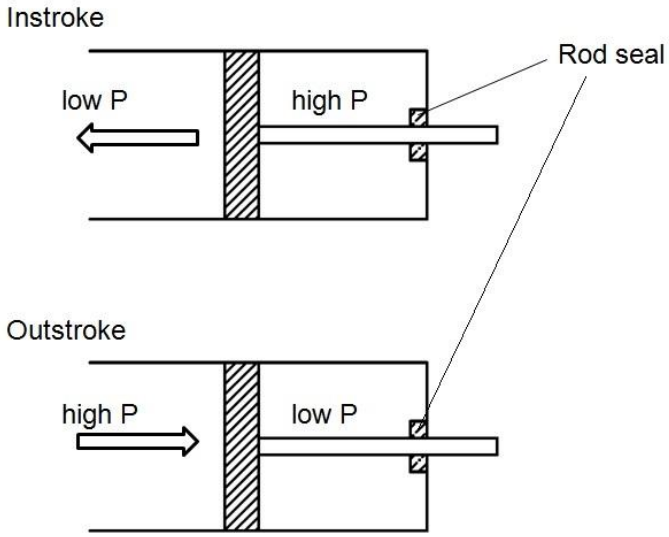

Figure 4.1: Rod seal instroke and outstroke

The difference in the fluid transport components between outstroke and instroke, under the above conditions, is shown in Figure 4.2. During the outstroke, since the pressure at both sides of the seal is the same (atmospheric pressure), there is only Couette flow, which drags the fluid out of the cylinder. During the instroke, besides the Couette flow, which drags the fluid into the cylinder, there is a Poiseuille flow generated by the high sealed pressure at the sealing side, which pushes the fluid out of

the cylinder. So the net fluid transport for the instroke is the Couette flow minus the Poiseuille flow.

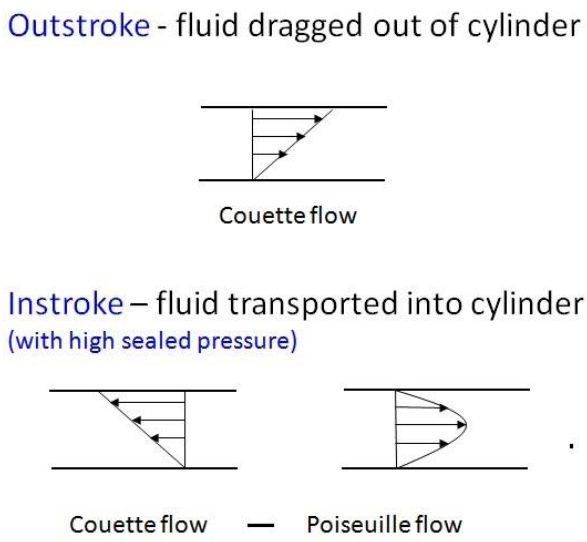

Figure 4.2: Fluid transport components

The basic assumptions for the simulation of the rod seal with a smooth rod are listed below. Most of the assumptions have been mentioned and explained in chapter 3, where the development of the models is discussed.

1) treats rod as smooth; 2) uses flooded or starved boundary conditions; 3) considers elastic deformations; 4) isothermal; 5) axisymmetric for both 2-D and 3-D models; 6) ignores possible adhesion of elastomer to rod; 7) ignores transients at beginning and end of stroke; 8) computes the friction force due to contacting asperities with empirical friction coefficient; 9) calculates surface characteristics with measured data and correlations.

The values of the parameters used in the computations for the U-cup and step seals are given in Table 1.

Table 4.1 Base parameters for smooth rod studies

Seal type	Step seal	U-cup seal(2-D)	U-cup seal(3-D)
Seal material	PTFE	Polyurethane	
Elastic modulus	550×10^{6} Pa	43×10^{6} Pa	
Poisson's ratio	0.40	0.49	
Sealed pressure	6.89 MPa (1000 psi) during instroke; 0.10 MPa (atmospheric) during outstroke; cavitation pressure: 0		
Rod diameter	50mm	44.45mm	
Dry friction coefficient	0.1	0.25	
Reference viscosity	0.043 Pa s		
Pressure-viscosity coefficient	20×10^{-9} Pa^{-1}		
Seal roughness	4.0 μm	0.8 μm	
α	1.75		1.25 and various
β	1.0		1.0 and various
Stroke length	228.6 mm		
Rod speed	0.01-0.3 m/s		

For the Reynolds equation solution, the number of nodes in the computational spatial mesh ranges from 1580 to 8930 for the 2-D models, depending on the type of seal and stroke, selected on the basis of a mesh refinement study. For example, going from 1580 to 3160 nodes (step seal) and going from 8930 to 17860 (U-cup seal) results in deviations of less than 0.5% in fluid transport and friction force. The time step is chosen to be equivalent to 0.1 wavelength of motion of the rod. For a rod speed

of 0.3 m/s this is equivalent to 1.33×10^{-5} s. Increasing the time step to 2.67 × 10-5 s results in a deviation of 0.3% in the fluid transport and 0.14% in the friction force. A similar mesh refinement study is performed for the 3-D model of the U-cup seal with an 812 × 40 = 32480 spatial mesh. Going from 32480 to 64960 results in deviations of less than 0.5% in fluid transport and friction force.

For the finite element analysis via ABAQUS, The mesh contains 36869 elements for the U-cup seal and 42418 elements for the step seal, based on a mesh refinement study. Going from 10906 to 3689 elements (U-cup seal) and from 38048 to 42418 elements (step seal) result in a deviation in contact pressure of less than 0.5%.

4.3 U-cup Seal using 2-Dimensional Model

4.3.1 Leakage and Friction with Flooded and Starved Boundary Conditions

The fluid transport for the outstroke and the instroke of the U-cup seal with flooded and starved boundary conditions, as a function of rod speed, is shown in Figure 4.3 for a perfectly smooth rod, with the fixed, specified stroke length. The fluid transport is defined as the quantity of fluid carried out of or into the cylinder during a single outstroke or instroke, respectively. (Note that a negative value during the instroke indicates fluid is carried out of the cylinder.) As can be seen, the outstroke transport is relatively independent of rod speed, while the instroke fluid transport increases with rod speed. Below a certain critical speed (approximately 0.08 m/s for this case) the outstroke fluid transport exceeds the instroke transport, and the seal will

leak. Above that critical speed, the computed potential instroke fluid transport exceeds the outstroke transport, and in reality fluid starvation will occur, violating the flooded boundary conditions. The instroke fluid transport should be equal to that of outstroke at the same speed, as the starved boundary results show. However, the computed results with the flooded boundary still have an important physical meaning since the larger the potential instroke transport relative to the outstroke transport, the less prone is the seal to leaking due to imperfections in the lip, non-axisymmetry, and other effects not accounted for in the model. In addition, some other applications where the sealed pressure during the outstroke is high (e.g. injection molding actuators), the instroke may not be starved and the flooded results relevant.

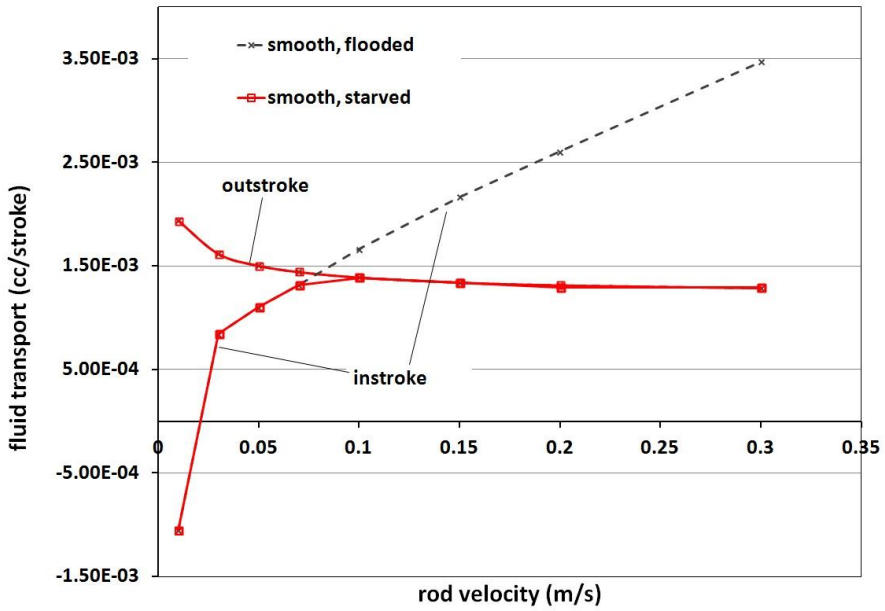

Figure 4.3: Fluid transport, U-cup seal with 2-D model

The friction force on the rod, as a function of rod speed, is shown in Figure 4.4. During the outstroke, when the sealed pressure is ambient, it is relatively low and independent of rod speed. This is because the friction force is primarily produced by contacting asperities rather than by fluid friction. Almost the entire lubricating film is cavitated and hydrodynamic effects are minimal, as will be seen, below. During the instroke, with a high sealed pressure, the friction force is relatively high. For the flooded boundary, except at the lowest rod speeds, the friction force decreases with increasing rod speed. For the starved boundary, the friction force increases with increasing rod speed at the lowest rod speeds, then slightly decreases when the rod speed increases close to the critical speed. After the rod speed is higher than the critical speed, the friction force increases relatively slowly with increasing rod speed.

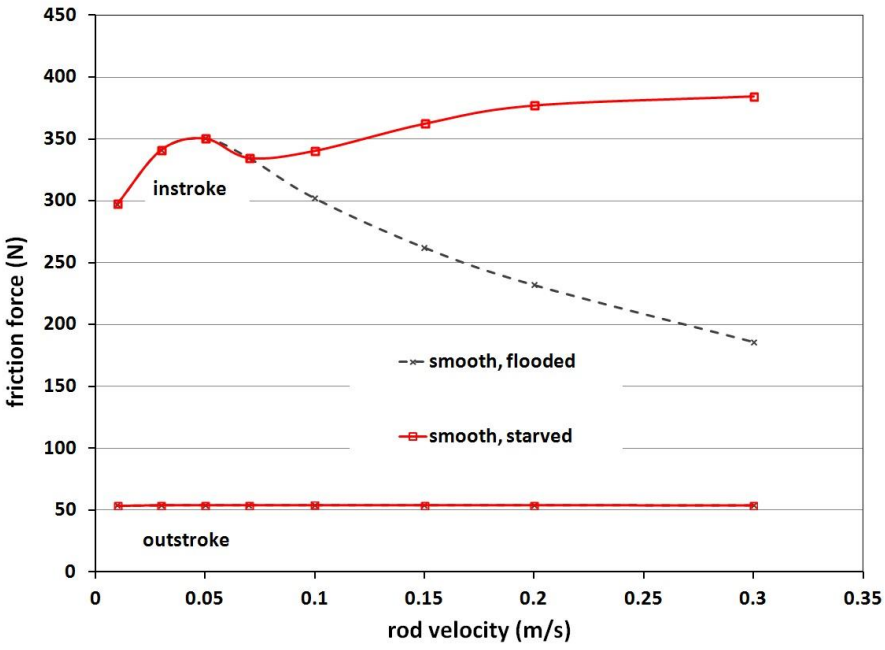

Figure 4.4: Friction force, U-cup seal with 2-D model

From Figure 4.4 it is seen that during the outstroke there is no starvation, and the friction force for both boundary conditions are exactly the same. However, during the instroke the friction force with the starved boundary condition is significantly higher compared to that of the flooded boundary after the rod speed exceeds the critical speed, especially at the higher rod speeds.

The seal characteristics, reported above, describe the gross behavior of the seal. A physical understanding of those characteristics can be obtained by examining the details of the sealing zone, namely the lubricating film thickness distribution and the fluid and contact pressure distributions.

4.3.2 Details of Sealing

Figures 4.5a and 4.5b show the film thickness distributions during the outstroke at rod speeds of 0.05 m/s and 0.3 m/s, respectively. These distributions are almost identical, indicating the film thickness is relatively independent of rod speed during the outstroke. This is because the sealed fluid pressure is not elevated above ambient during the outstroke, so almost the entire lubricating film is cavitated and hydrodynamic effects are minimal, as will be seen in the fluid pressure distribution, below. Notice that for outstroke, there is no starvation occurring.

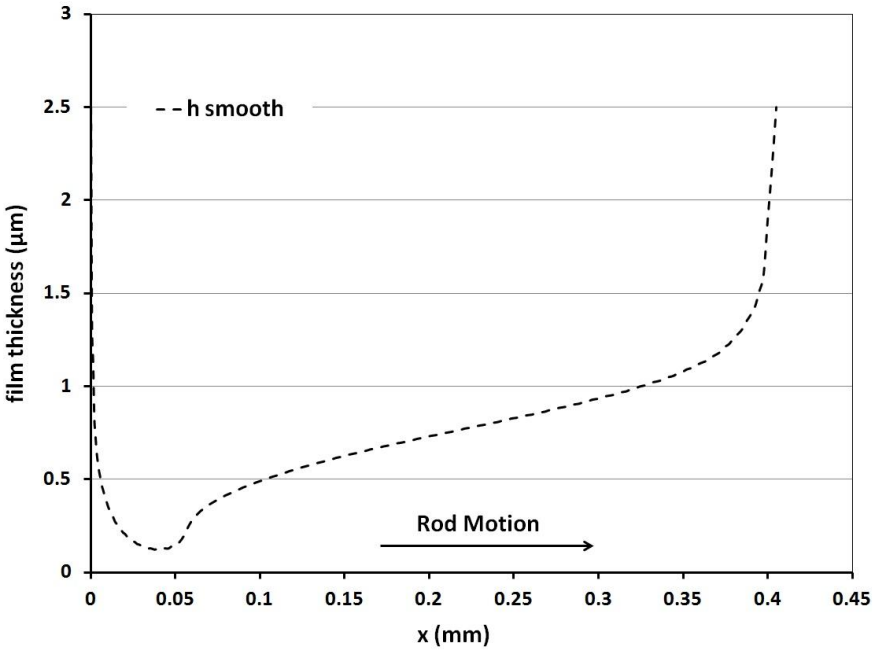

Figure 4.5a: Film thickness of outstroke, 0.05 m/s, U-cup seal

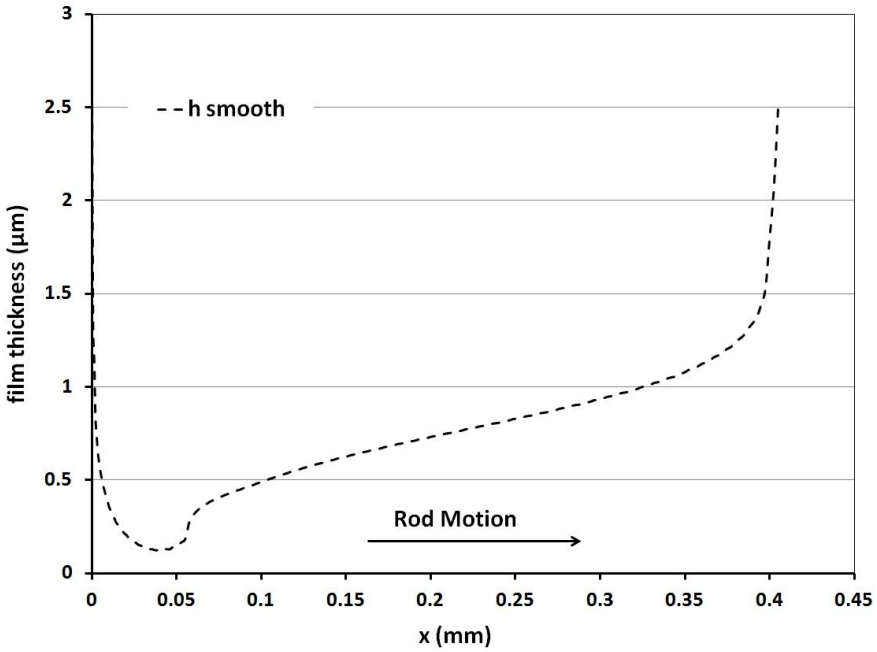

Figure 4.5b: Film thickness of outstroke, 0.30 m/s, U-cup seal

The film thickness distributions during the instroke at rod speeds of 0.05 m/s, 0.15m/s and 0.3 m/s, are shown in Figure 4.6a, 4.6b and 4.6c, respectively. At the rod speed of 0.05 m/s, there is no starvation. One notes that the length of the sealing zone is much larger than that during the outstroke. This is because of the much higher sealed pressure during the instroke, which produces greater deformation and a larger contact area. From these distributions it is clear that the higher rod speeds produce thicker fluid films during the instroke under the flooded boundary condition. But with the starved boundary condition, the shape of fluid film profile changes with rod speed, but the thickness does not change significantly. Also, with the rod speed increasing, the pressurized region (to the left of the starved boundary) decreases. At the same speed, the fluid film with the flooded boundary is thicker than that with the starved boundary.

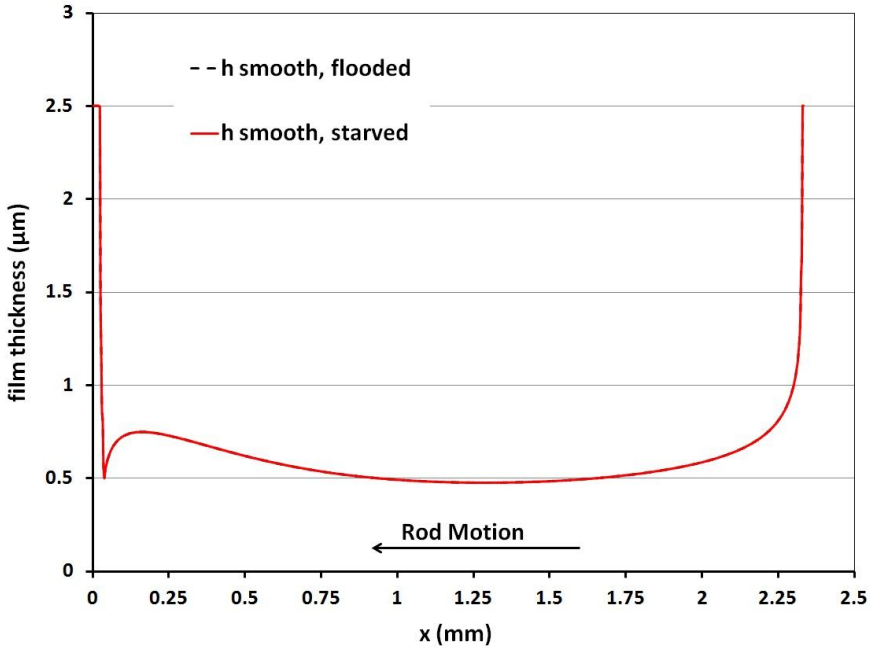

Figure 4.6a: Film thickness of instroke, 0.05 m/s, U-cup seal

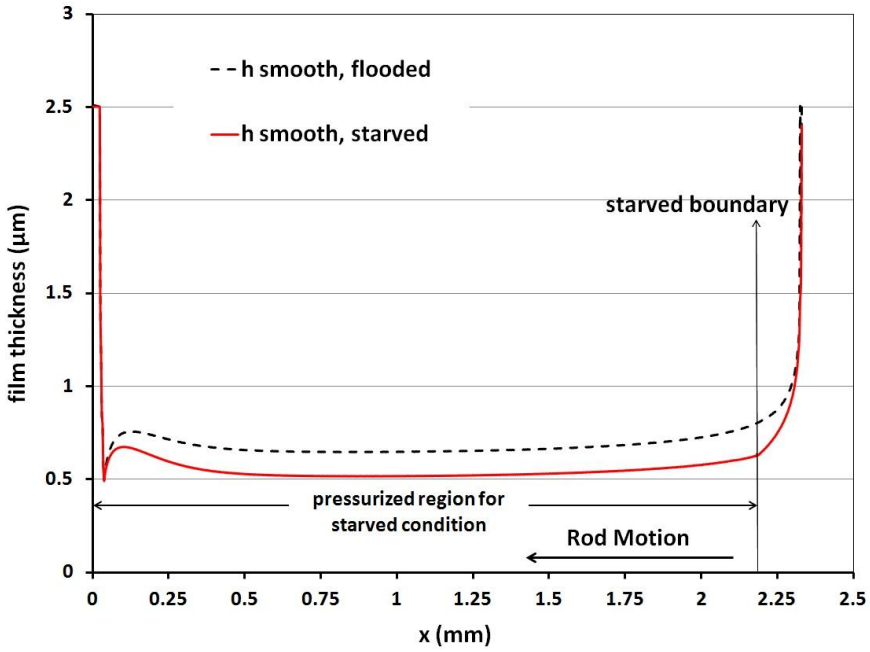

Figure 4.6b: Film thickness of instroke, 0.15 m/s, U-cup seal

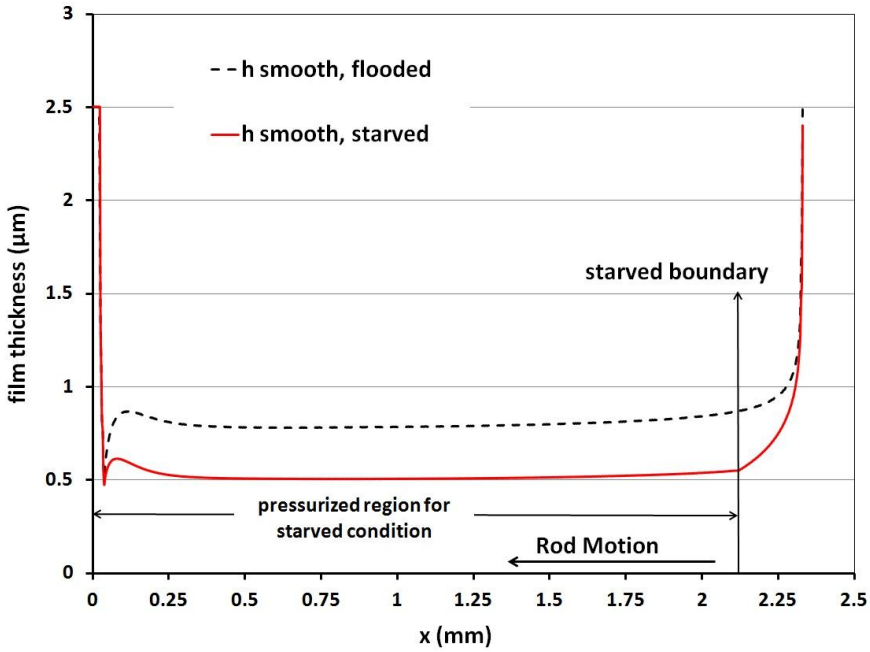

Figure 4.6c: Film thickness of instroke, 0.30 m/s, U-cup seal

Figures 4.7a and 4.7b show the contact pressure and fluid pressure distributions during the outstroke at rod speeds of 0.05 m/s and 0.3 m/s. Comparison of the two figures shows that the contact pressure distributions are virtually independent of rod speed. During the outstroke the sealed pressure is not elevated above ambient, and most of the lubricating film is cavitated. The fluid pressure distributions indicate minimal hydrodynamic action, with the film almost completely supported by the asperities on the seal surface. These results are consistent with the film thickness distributions during the outstroke, discussed above.

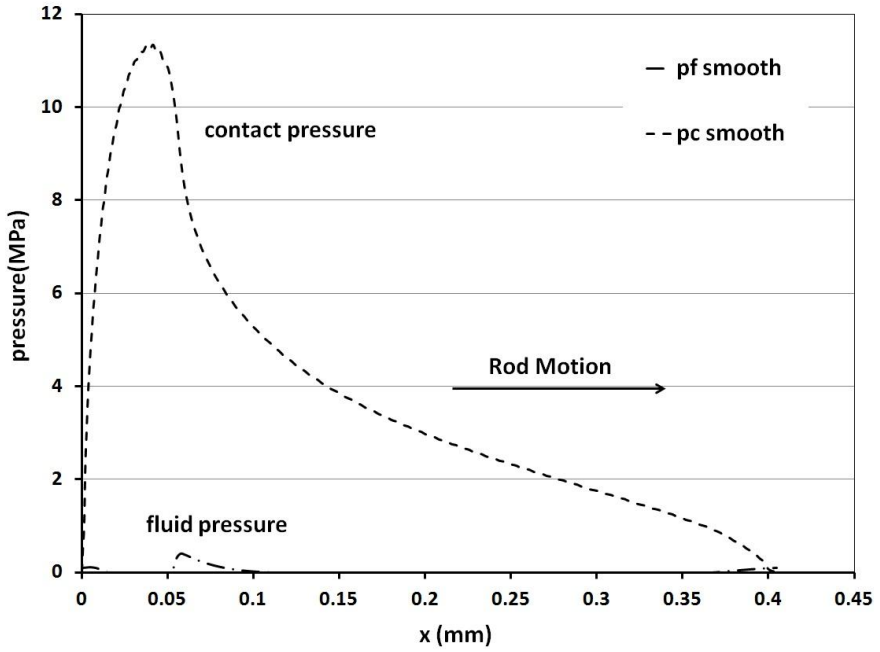

Figure 4.7a: Contact and fluid pressures of outstroke, 0.05m/s, U-cup seal

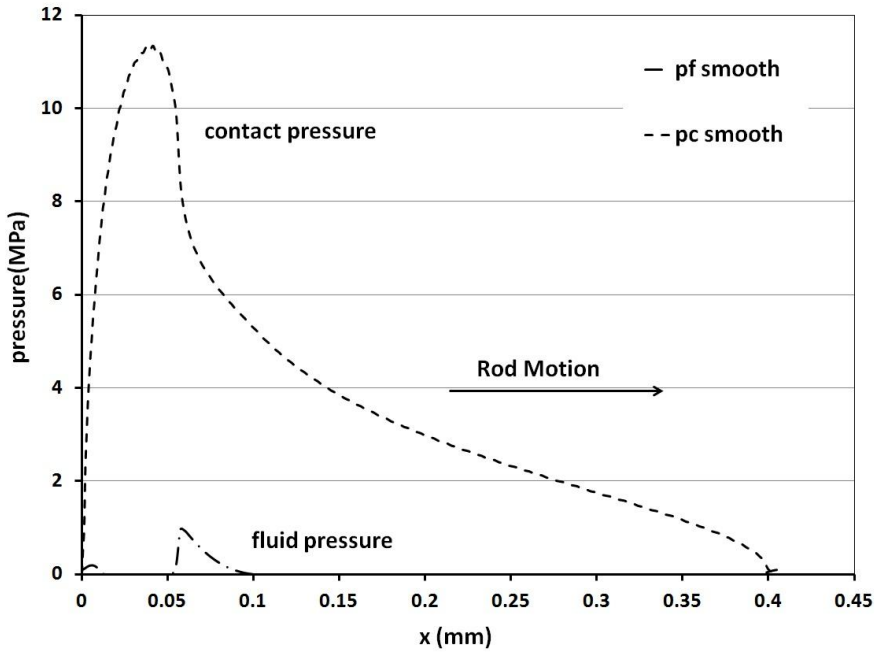

Figure 4.7b: Contact and fluid pressures of outstroke, 0.30m/s, U-cup seal

The contact pressure and fluid pressure distributions during the instroke are shown in Figures 4.8a1, 4.8a2, 4.8b1, 4.8b2, 4.8c1 and 4.8c2 at rod speeds of 0.05 m/s, 0.15m/s and 0.3 m/s. For results under the flooded boundary condition, the contact pressures decrease while the fluid pressures increase with the increasing rod speed.

At the 0.05 m/s speed, there is no starvation. So in Figures 4.8a1 and 4.8a2, the two sets of results (flooded and starved) are exactly the same. For the results under the starved boundary condition, the contact pressures at the 0.15 m/s speed are slightly lower than at the 0.3 m/s speed, while the fluid pressures at the 0.15 m/s speed are slightly higher than at the 0.3 m/s speed.

At the 0.15 m/s speed, the starved contact pressures are higher than that of the flooded; and the starved fluid pressures are lower than that of the flooded; the pressurized region with the starved boundary is shorter than that with the flooded boundary. At the 0.30 m/s speed, the starved results show the similar higher contact pressure, lower fluid pressure, and shorter pressurized region. The differences in contact pressure, fluid pressure and the length of pressurized region between starved and flooded cases are larger than those at the 0.15 m/s rod speed. These contact pressure and fluid pressure results are consistent with each other, and are consistent with the film thickness distributions during instroke. The increased speed would require increased lubricant flow under flooded conditions, and therefore there is more starvation, which causes the pressurized region to be shorter, which also results in a higher contact pressure, lower fluid pressure and increased friction.

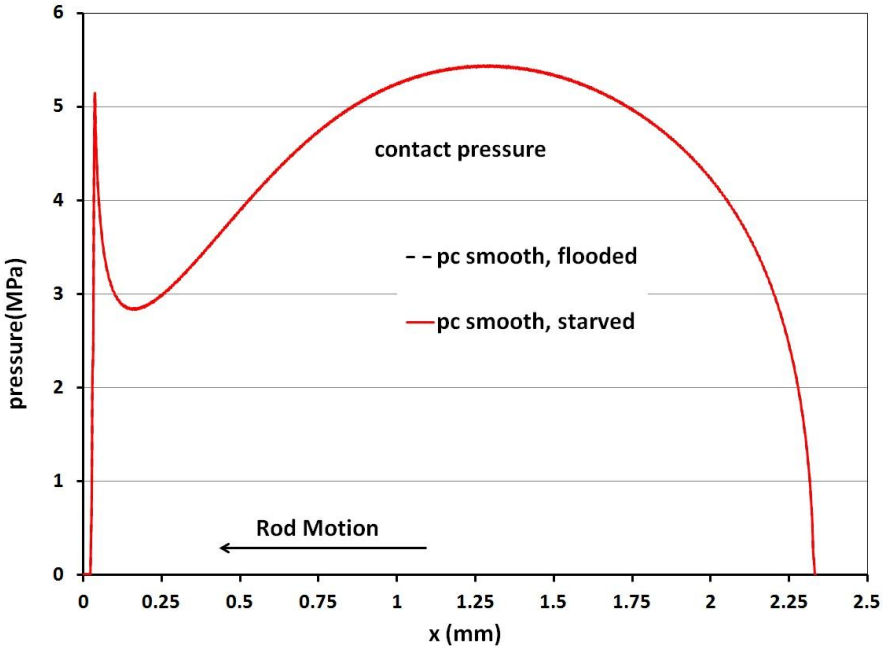

Figure 4.8a1: Contact pressures of instroke, 0.05m/s, U-cup seal

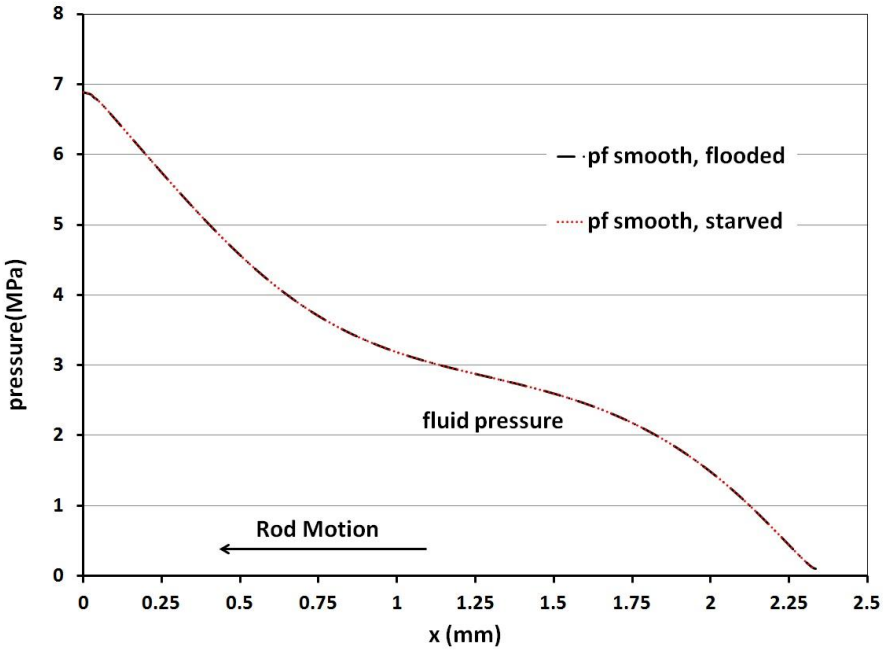

Figure 4.8a2: Fluid pressures of instroke, 0.05m/s, U-cup seal

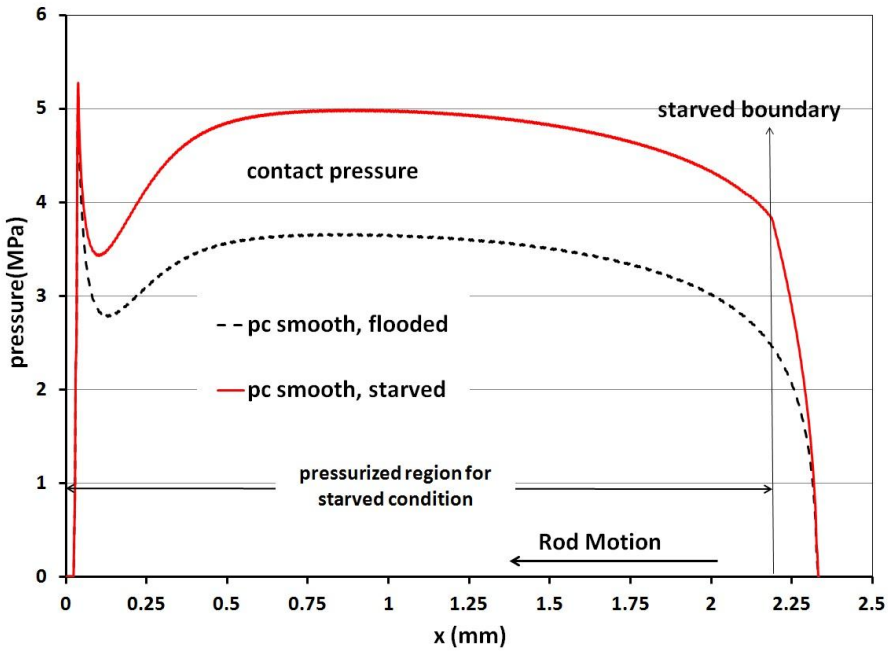

Figure 4.8b1: Contact pressures of instroke, 0.15m/s, U-cup seal

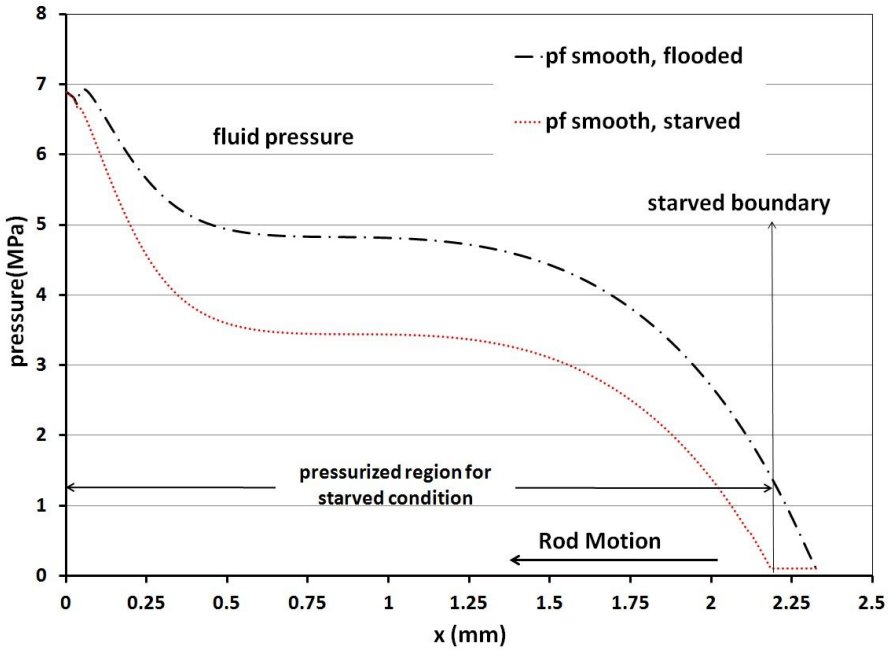

Figure 4.8b2: Fluid pressures of instroke, 0.15m/s, U-cup seal

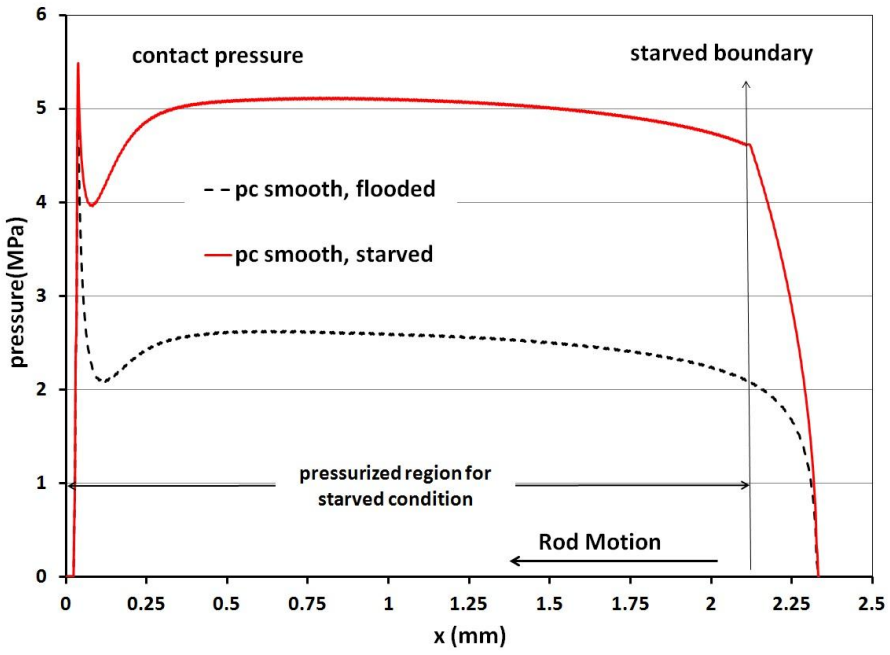

Figure 4.8c1: Contact pressures of instroke, 0.30m/s, U-cup seal

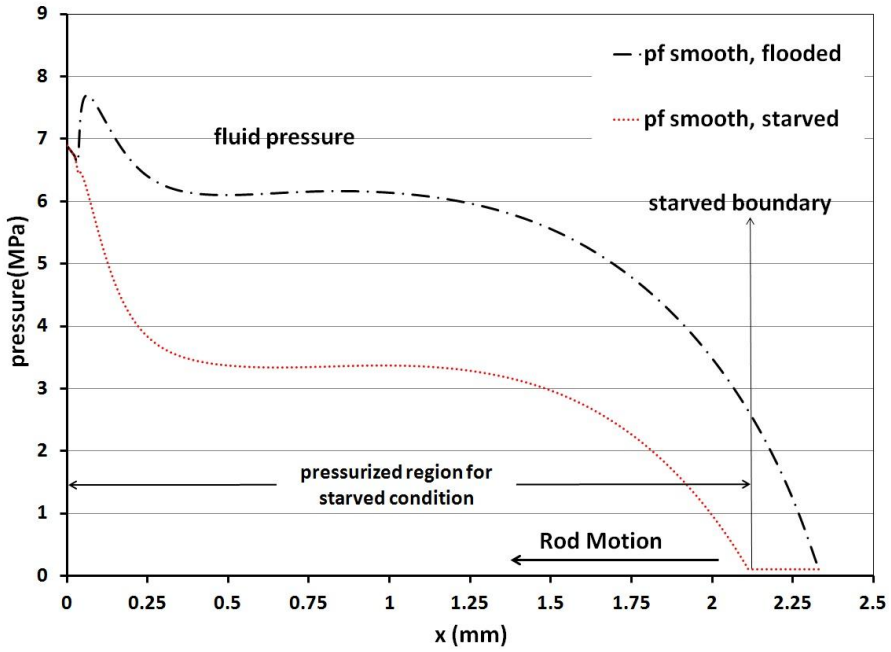

Figure 4.8c2: Fluid pressures of instroke, 0.30m/s, U-cup seal

It is now possible to explain the fluid transport behavior of the seal. During the outstroke the sealed pressure is ambient, so the fluid transport is solely produced by Couette flow. For such flow, the fluid transport depends only on the stroke length (which is fixed) and the film thickness. As described above, the film thickness is relatively independent of rod speed. Therefore the fluid transport during outstroke will be relatively independent of rod speed.

During the instroke, for the flooded boundary, the film thickness increases with speed because the length of the pressurized region remains the same and the fluid pressure increases due to hydrodynamic effects related to the rod speed. This causes the fluid transport to increase with speed. For the starved boundary, the film thickness

does not change significantly because the length of the pressurized region decreases with increasing speed and the fluid pressure does not increase, keeping the fluid transport the same as that of the outstroke.

The friction force results can be explained by considering the contact force and the film thickness. During the outstroke, the friction force is relatively independent of rod speed and surface finish because both the contact force and film thickness are relatively independent of rod speed and surface finish since the film is largely cavitated. During the instroke, for the flooded boundary, except at the lowest speeds the friction force decreases with speed because the contact force decreases with speed, a result of increasing fluid pressure support that due to the hydrodynamic effect. For the starved boundary, the friction force increases with speed because the contact force increases with speed. The friction force with the starved boundary is larger than that with the flooded boundary because the contact force with starved boundary is larger than that with flooded boundary, a result of the shortened pressurized region and smaller fluid pressure compared to the flooded cases.

4.4 Step Seal using 2-Dimensional Model

4.4.1 Leakage and Friction with Flooded Boundary Conditions

The step seal differs from the U-cup seal in three respects: seal geometry, seal material (PTFE sealing element vs. polyurethane) and the surface roughness amplitude (4 μm vs. 0.8 μm).

Figure 4.9 shows the fluid transport as a function of rod speed for the step seal with a smooth rod. Compared to the U-cup seal, the transports are much larger.

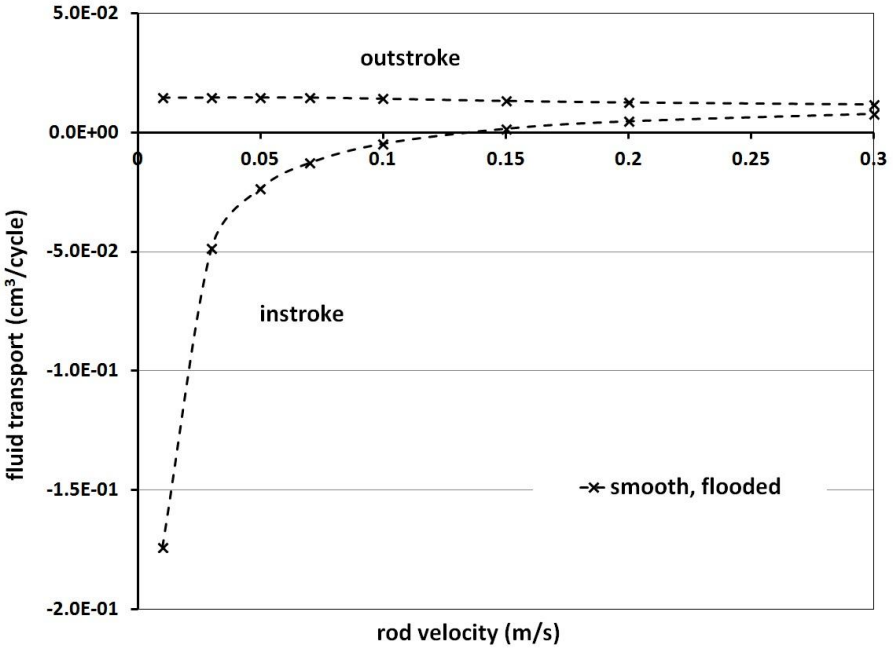

Figure 4.9: Fluid transport, step seal with 2-D model

The transport behavior during the outstroke is similar to that with the U-cup seal in that it is substantially independent of rod speed. During the instroke, at lower speeds the transport is similar to that with the U-cup in that it increases with speed. However at the higher speeds, the slope decreases and the transport levels off. The critical speed, where the outstroke and instroke transports are equal, occurs beyond the range covered in this research. Thus, for the step seal, starvation does not occur in the speed range investigated.

The friction force on the rod, as a function of rod speed, is shown in Figure 4.10. During the outstroke, when the sealed pressure is ambient, it is relatively low and independent of rod speed, as is the case with the U-cup seal and for the same reason. During the instroke, with a high sealed pressure, the friction force is relatively high and, in contrast to the U-cup seal, is independent of rod speed. This lack of a hydrodynamic effect can be understood by considering the film thickness and pressure distributions, below.

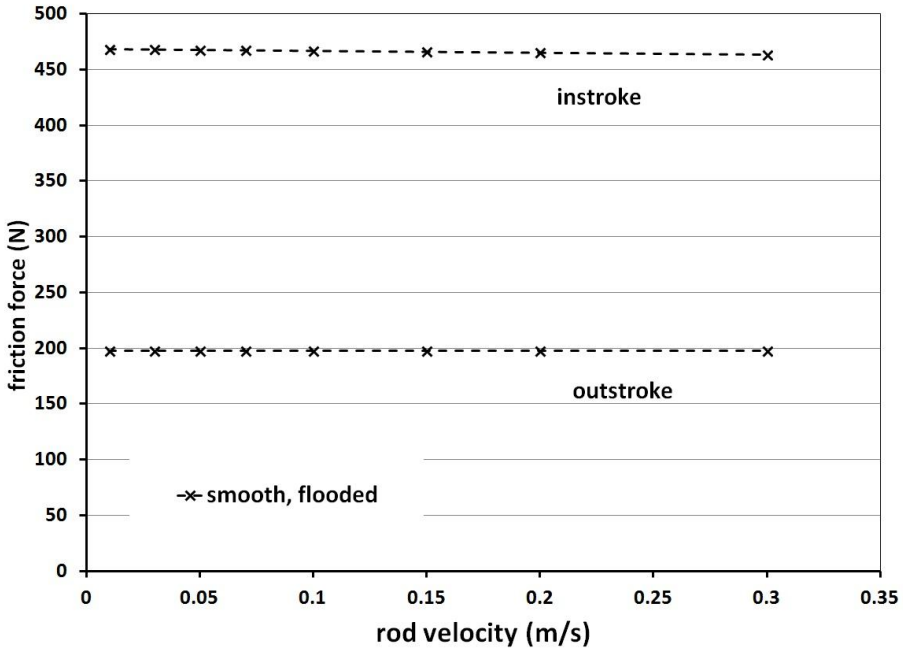

Figure 4.10: Friction force, step seal with 2-D model

As in the case of the U-cup seal some insight into the behavior described above can be obtained by examining the details of the sealing zone.

4.4.2 Details of Sealing

Figures 4.11a and 4.11b show the film thickness distributions during the outstroke at rod speeds of 0.05 m/s and 0.3 m/s. They are almost identical, indicating the film thickness is relatively independent of rod speed during the outstroke, as is the case with the U-cup seal and for the same reason. It is important to note the much larger film thickness with the step seal, due to the larger asperities, in which case the film is almost completely supported by the asperities on the seal surface, as is evidenced by the contact and fluid pressure distributions, below.

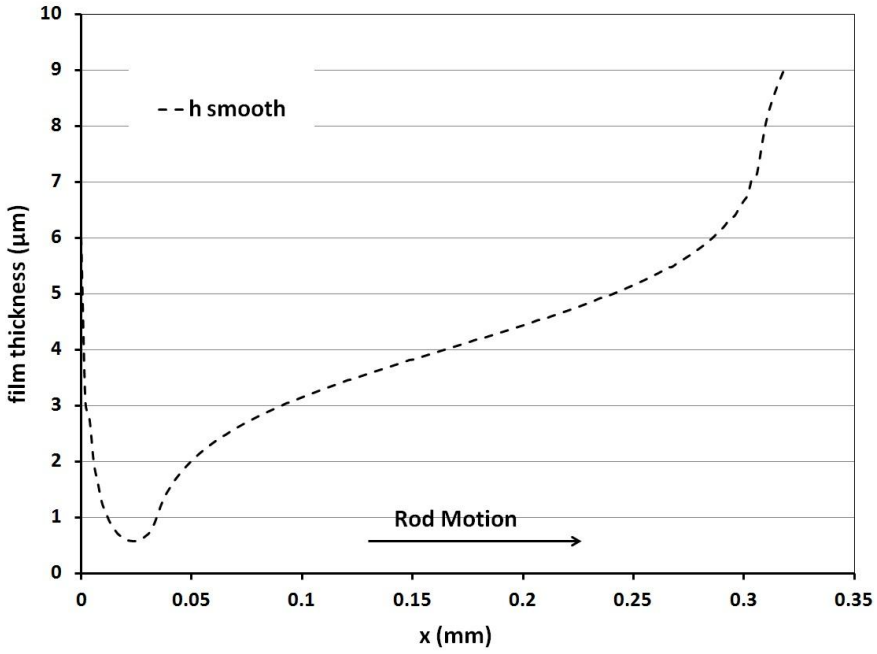

Figure 4.11a: Film thickness of outstroke, 0.05 m/s, step seal

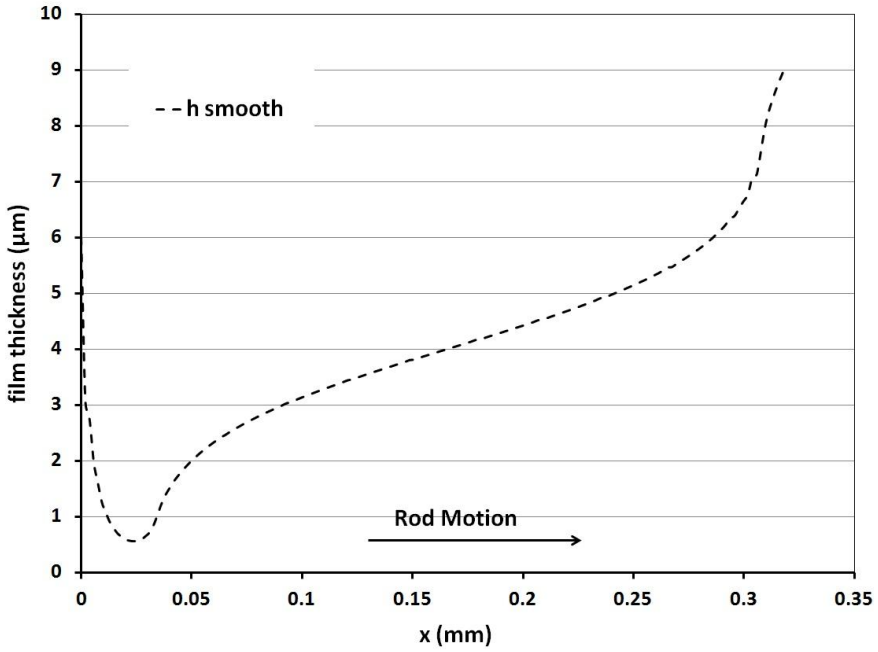

Figure 4.11b: Film thickness of outstroke, 0.30 m/s, step seal

The film thickness distributions during the instroke at a rod speed of 0.05 m/s and 0.3 m/s are shown in Figure 4.12a and 4.12b. The two distributions are almost identical, indicating the film thickness is also relatively independent of rod speed during the instroke. This lack of hydrodynamic effect differs from the U-cup case, and results from the much higher contact pressures (discussed below), which support the film. As in the outstroke, the film thickness is much larger than for the U-cup seal due to the larger asperities.

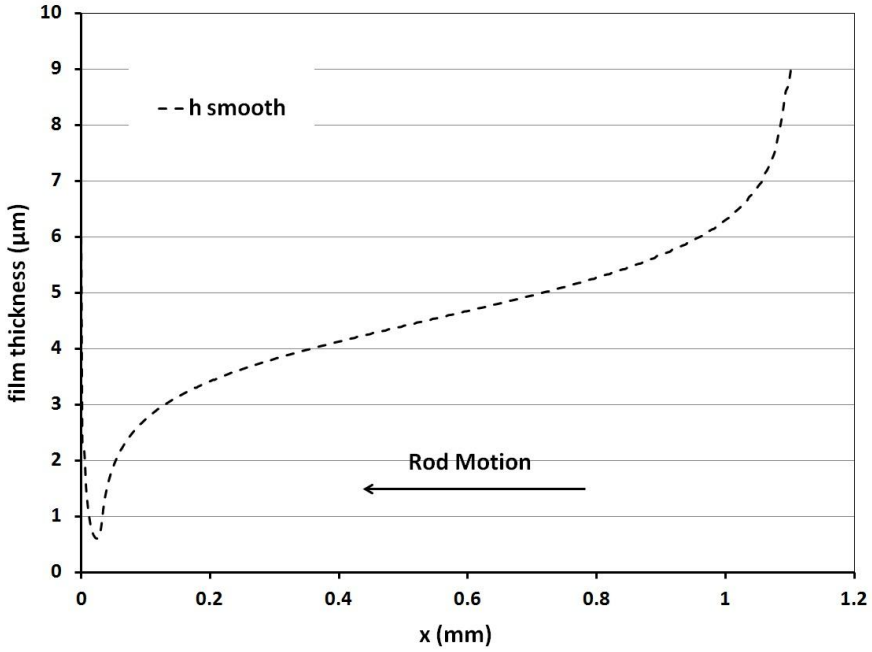

Figure 4.12a: Film thickness of instroke, 0.05 m/s, step seal

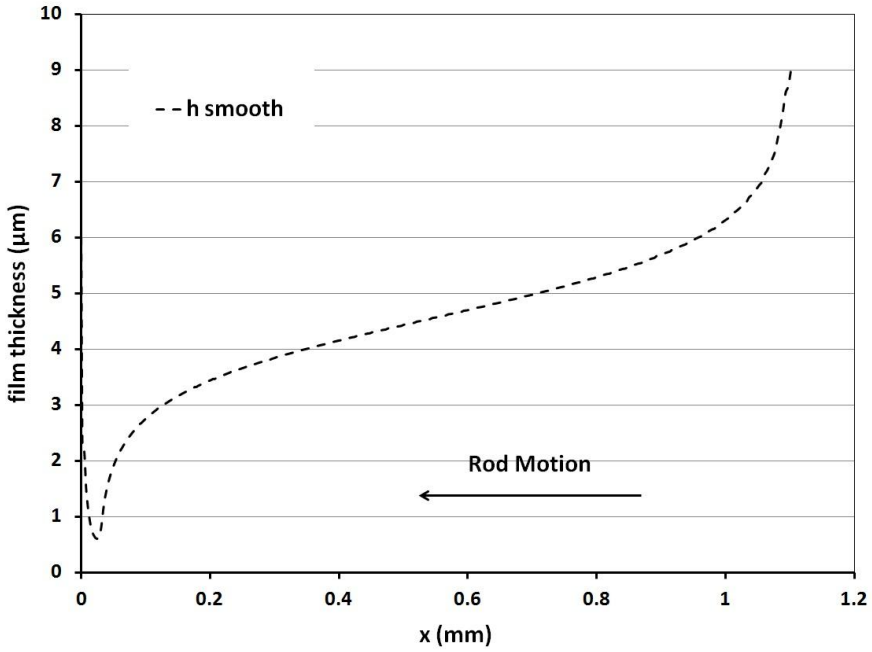

Figure 4.12b Film thickness of instroke, 0.30 m/s, step seal

Figure 4.13a and 4.13b show the contact pressure and fluid pressure distributions during the outstroke at rod speeds of 0.05 m/s and 0.30 m/s. The two distributions are almost identical, as in the case with the U-cup seal and for the same reason. The very high contact pressures, compared to the U-cup, are due to the much higher value of the elastic modulus of PTFE compared to polyurethane. The fluid pressure distribution indicates minimal hydrodynamic action. These results are consistent with the film thickness distributions during outstroke, discussed above, and similar to the results with the U-cup seal except for the high contact pressures.

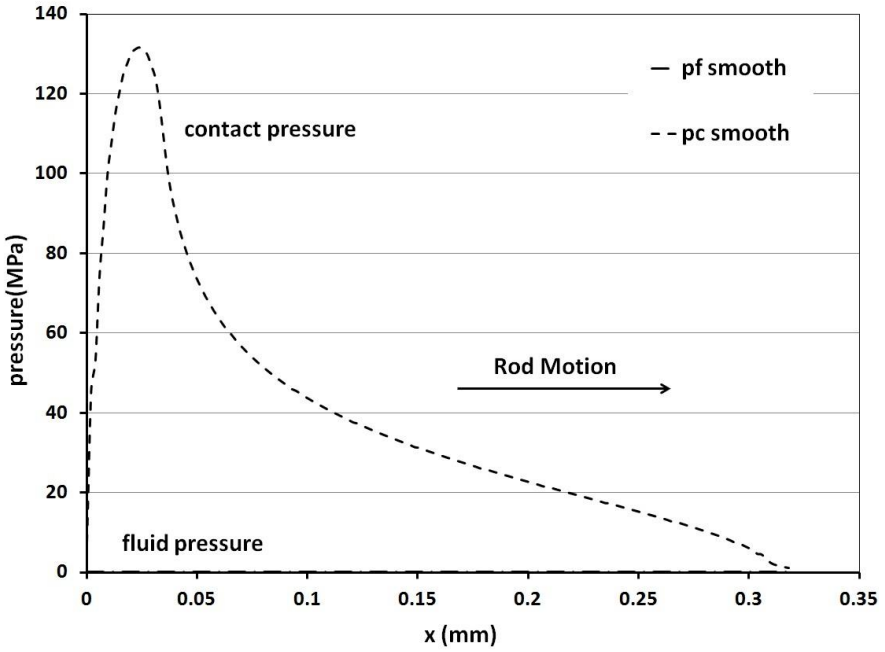

Figure 4.13a: Contact and fluid pressures of outstroke, 0.05m/s, step seal

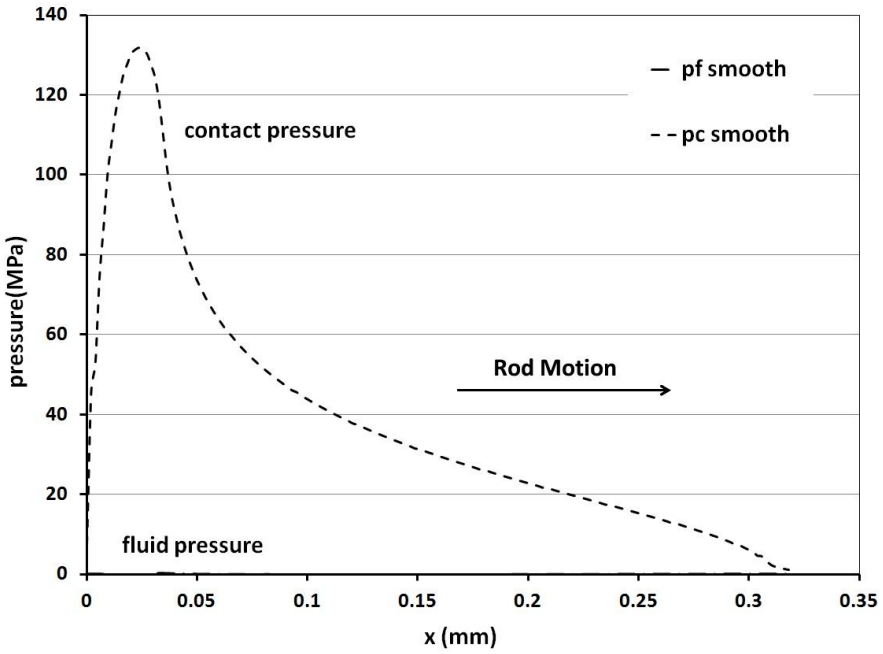

Figure 4.13b: Contact and fluid pressures of outstroke, 0.30m/s, step seal

The contact pressure and fluid pressure distributions during the instroke are shown in Figure 4.14a and 4.14b at rod speeds of 0.05 m/s and 0.30 m/s. The two distributions are almost identical, indicating the contact and fluid pressure distributions are relatively independent of rod speed during the instroke, unlike the U-cup seal case with the flooded boundary condition. The very high contact pressures compared to the fluid pressures show that there is no significant hydrodynamic effect, with the film almost completely supported by the seal surface asperities. As with the U-cup seal, these contact pressure and fluid pressure results are consistent with each other, and are consistent with the film thickness distributions during the instroke, discussed above.

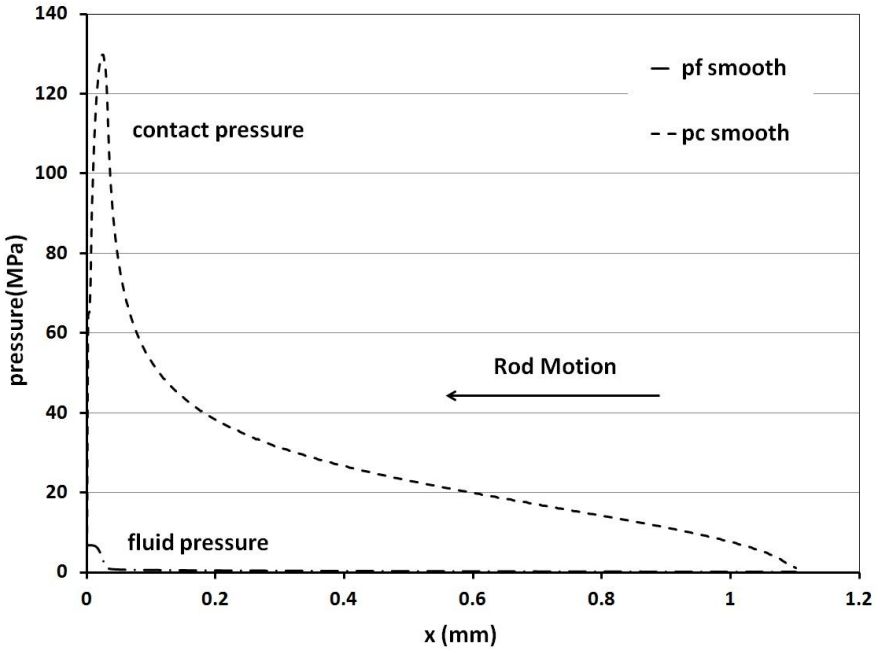

Figure 4.14a: Contact and fluid pressures of instroke, 0.05m/s, step seal

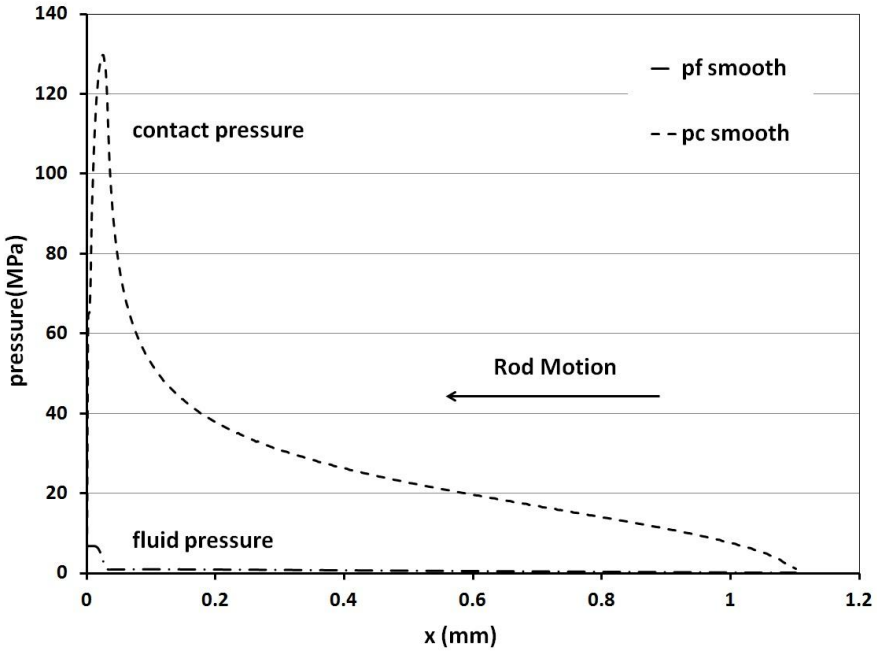

Figure 4.14b: Contact and fluid pressures of instroke, 0.30m/s, step seal

The differences in the gross characteristics of the step seal compared to the U-cup seal can now be explained. First, the much larger roughness results in much thicker fluid films, which result in larger fluid transports, during both outstroke and instroke. The friction force with the step seal is larger than that with the U-cup seal due to the higher contact pressures, because of the lack of hydrodynamic effect due to thicker film.

4.5 U-cup Seal using 3-Dimensional Models

The 3-D models are developed for the analysis of the surface patterned rods. For comparison purposes it is necessary to simulate the smooth rod first. The computational schemes are different for the 2-D and 3-D models, as discussed in Chapter 3. In the 2-D model, the on-line FEA method is applied it accounts for both normal and transverse deformations, via ABAQUS. In the 3-D model, the FEA analysis using ABAQUS computes the static deformation, while the dynamic deformation in the normal direction is calculated indirectly, as described in section 3.5.2. In addition, the surface characteristic parameter, α, of the 3-D model (1.25) is slightly different from that of the 2-D model (1.75), for computational reasons. Thus, one would expect some quantitative differences in the results generated by the two models.

4.5.1 Leakage and Friction with Flooded and Starved Boundary Conditions

The fluid transport for the outstroke and the instroke of the U-cup seal in the 3-D model, with flooded and starved boundary conditions, as a function of rod speed

is shown in Figure 4.15 for a perfectly smooth rod, for the fixed specified stroke length. It is similar to the U-cup seal in the 2-D model. The outstroke transport is relatively independent of rod speed, while the instroke fluid transport increases with rod speed, under flooded conditions, or equals the outstroke transport of the same speed after the rod speed exceeds the critical speed, under starved conditions. The critical speed for the 3-D model is approximately 0.04m/s, which is somewhat lower than that of the 2-D case.

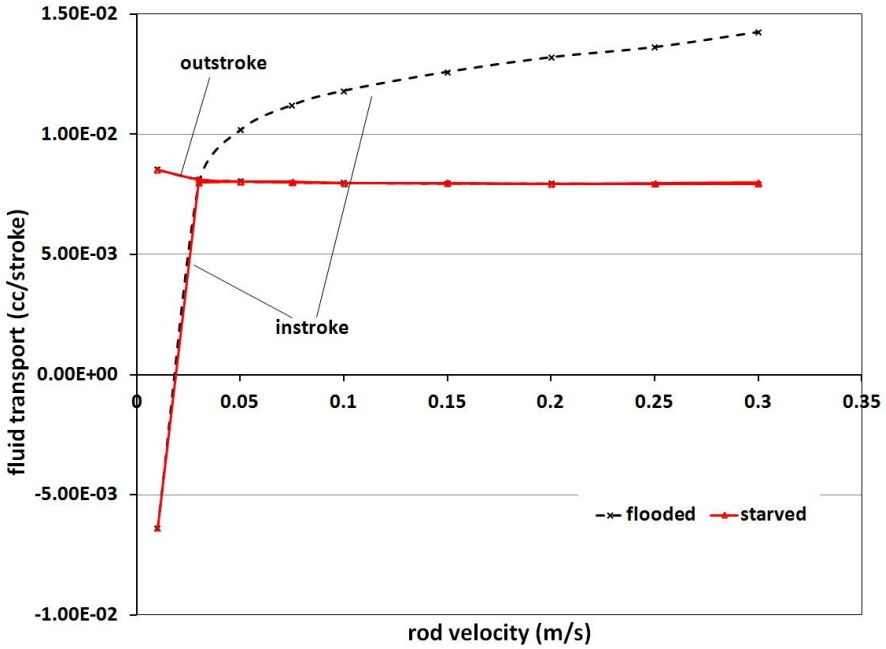

Figure 4.15: Fluid transport, U-cup seal with 3-D model

The friction force on the rod, as a function of rod speed, is shown in Figure 4.16. During the outstroke, when the sealed pressure is ambient, it is relatively low

and independent of rod speed, as is the case with the 2-D model and for the same reason. During the instroke, with a high sealed pressure, the friction force is relatively high. For the flooded boundary, the friction force increases with increasing rod speed at lower speeds, then the friction force decreases with increasing rod speed at higher speeds, which is similar to that of the 2-D model except the friction decrease is less for the 3-D model case. For the starved boundary, the friction force slightly increases with increasing rod speed at the lowest rod speeds, and then increases significantly after the critical speed. Just like with the 2-D model, the friction force with starved boundary conditions is significant higher during the instroke after the rod speed exceeds the critical speed, compared to that with the flooded boundary.

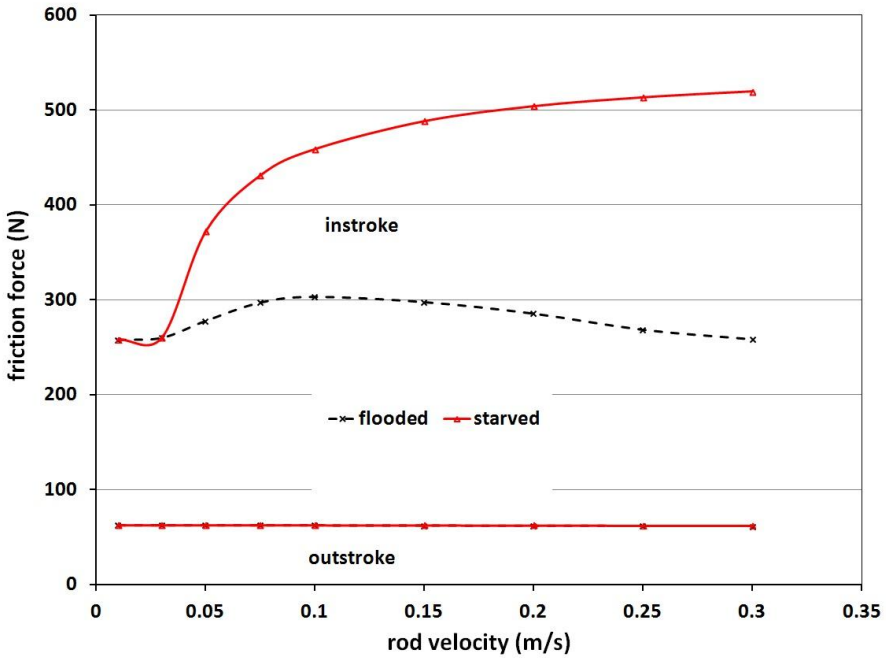

Figure 4.16: Friction force, U-cup seal with 3-D model

By examining the details of the sealing zone ., these seal characteristics can be understood.

4.5.2 Details of Sealing

Figure 4.17a and 4.17b show the film thickness distributions during the outstroke at rod speeds of 0.03 m/s and 0.3 m/s, respectively. These film thickness results, and the pressure. distributions that will be presented below, are 2-Dimensional sections of 3-Dimensional profiles, since for these smooth rod cases, the 3-D results are still axisymmetric. These distributions are almost identical, indicating the film thickness is relatively independent of rod speed during the outstroke, just like the 2-D model results, with the same reason. Note that for outstroke, there is no starvation occurring.

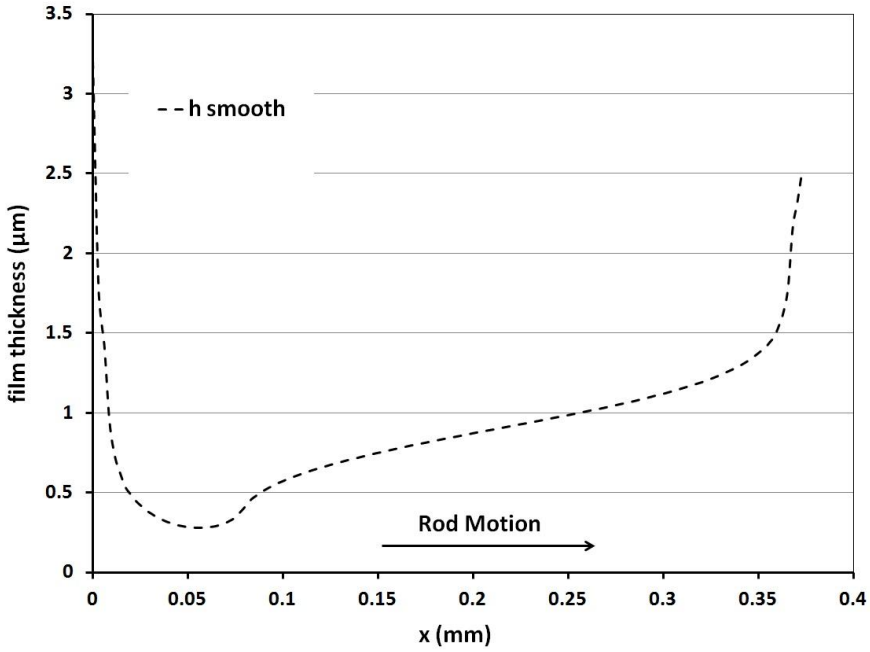

Figure 4.17a: Film thickness of outstroke, 0.03 m/s, U-cup seal, 3-D

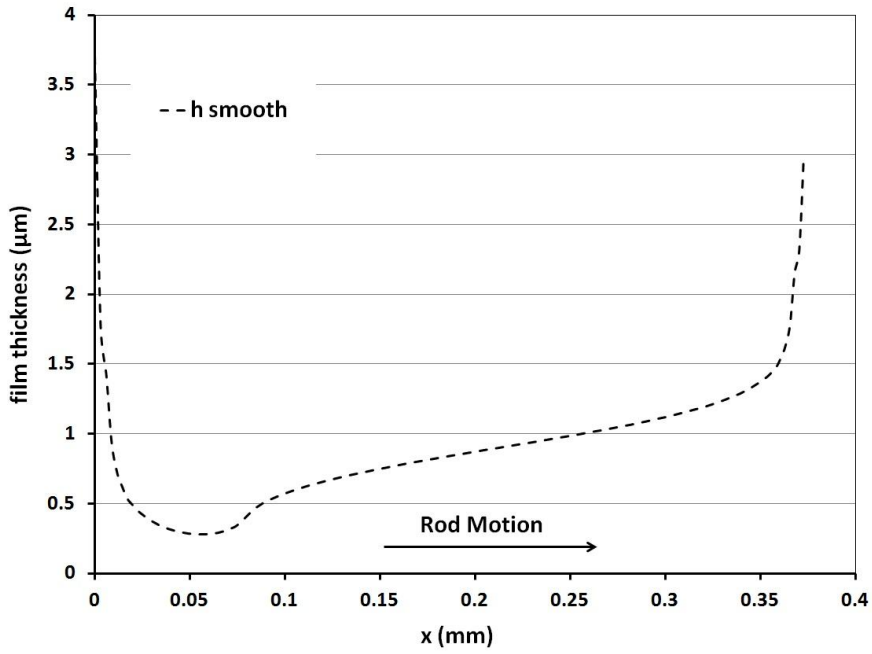

Figure 4.17b: Film thickness of outstroke, 0.30m/s, U-cup seal, 3-D

The film thickness distributions during the instroke at rod speeds of 0.03 m/s, 0.10 m/s and 0.30 m/s, are shown in Figure 4.18a, 4.18b and 4.18c, respectively. At the rod speed of 0.03 m/s, there is no starvation. The length of the sealing zone is much larger than that during the outstroke, which is similar to the 2-D cases for the same reason. For the flooded boundary, the shape of the distributions are changing as the rod speed increases, but the thickness is not increasing significantly. This is unlike the 2-D results, in which the thickness does increase with speed. For the starved boundary, the pressurized region decreases significantly with increasing rod speed. At the high speed, the pressurized region is about 1/9 of the entire sealing area. This is also unlike the 2-D cases, which has a pressurized region that is always slightly shorter than the whole sealing region. At the same speed, the fluid film with the

flooded boundary is thicker than that with the starved boundary, similar to the 2-D cases.

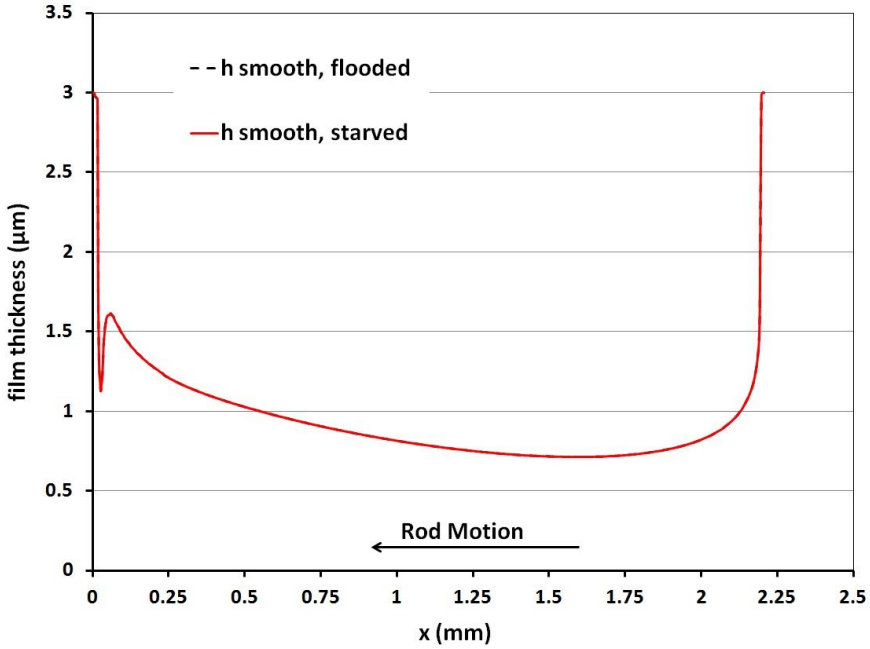

Figure 4.18a: Film thickness of instroke, 0.03 m/s, U-cup, 3-D

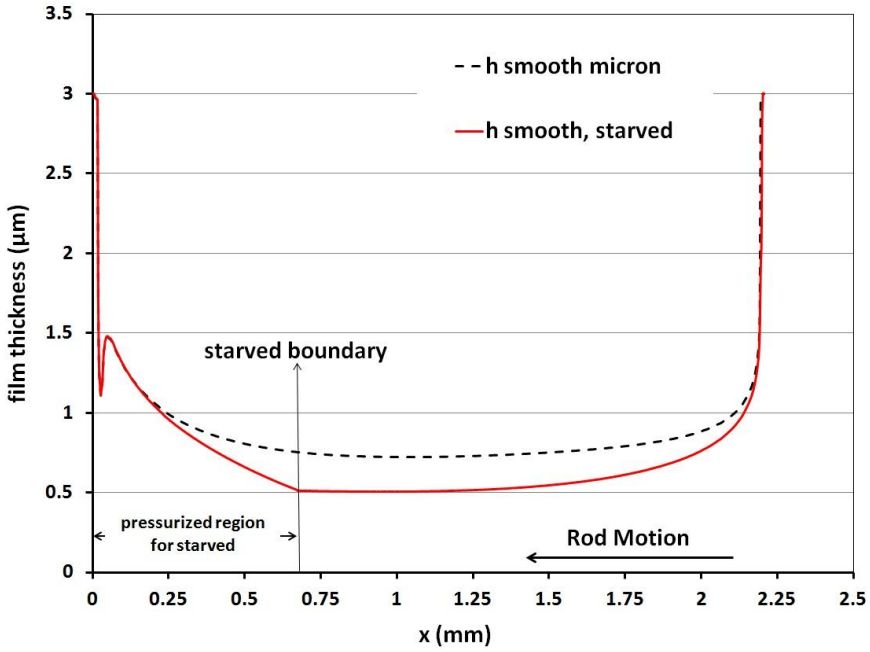

Figure 4.18b: Film thickness of instroke, 0.10 m/s, U-cup seal, 3-D

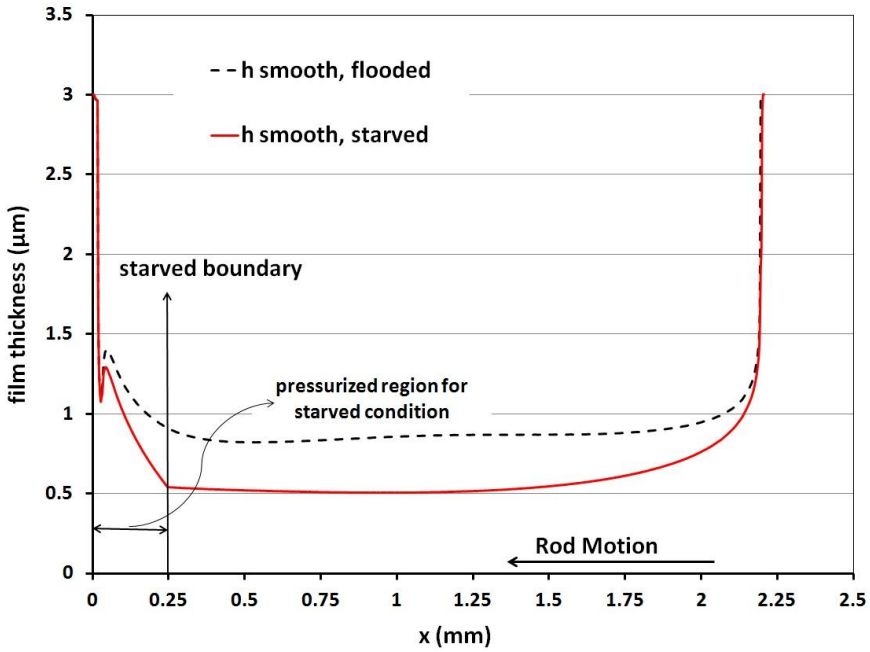

Figure 4.18c: Film thickness of instroke, 0.30 m/s, U-cup seal, 3-D

Figure 4.19a and 4.19b show the contact pressure and fluid pressure distributions during the outstroke at rod speeds of 0.03 m/s and 0.3 m/s. The two figures show that the contact pressure distributions are virtually independent of rod speed. During the outstroke the sealed pressure is not elevated above ambient, and most of the lubricating film is cavitated. These results are consistent with the film thickness distributions during the outstroke, and are similar to the 2-D results with the same explanations.

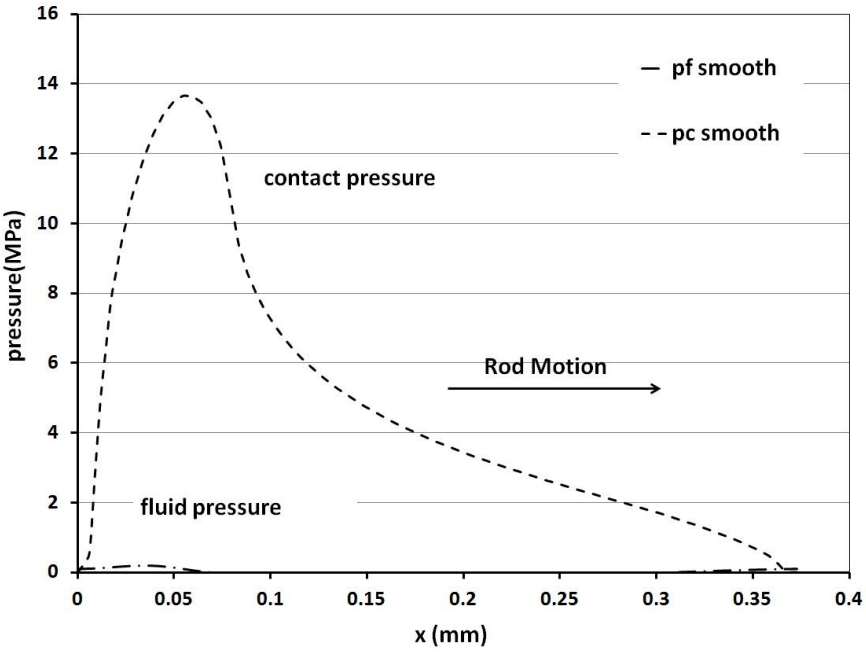

Figure 4.19a: Contact and fluid pressures of outstroke, 0.03m/s, U-cup seal, 3-D

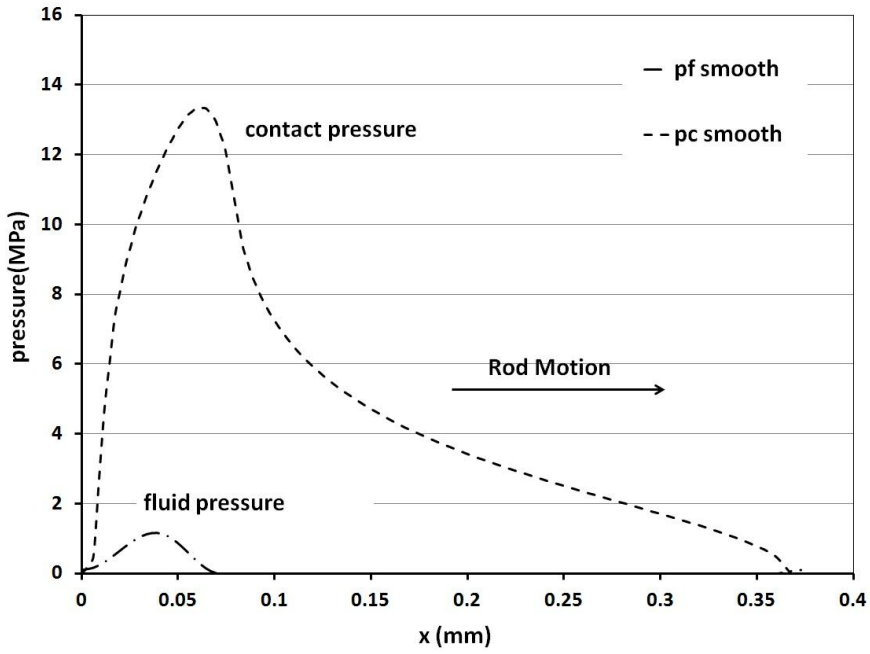

Figure 4.19b: Contact and fluid pressures of outstroke, 0.30m/s, U-cup seal, 3-D

The contact pressure and fluid pressure distributions during the instroke are shown in Figures 4.20a1, 4.20a2, 4.20b1, 4.20b2, 4.20c1 and 4.20c2 at rod speeds of 0.03 m/s, 0.10m/s and 0.3 m/s. For the results under flooded boundary conditions, the contact pressures increase while the fluid pressures decrease with the increasing rod speed when the rod speed is relatively low (especially in the half of the sealing zone that is closest to the sealed side). The contact pressures decrease while the fluid pressures increase with the increasing rod speed, at high speed range (higher than 0.10 m/s).

At the 0.03 m/s speed, there is no starvation; in Figures 4.20a1 and 4.20a2, the two sets of results (flooded and starved) are exactly the same. As it can be seen in Figure 4.15, the critical speed is approximately 0.04 m/s and starvation occurs when

the rod speed exceeds that critical speed. For the starved cases, since the pressurized region decreases significantly with increasing rod speed, the contact pressures increase while the fluid pressures decrease with increasing rod speed. The differences between the contact pressure, fluid pressure and the length of the pressurized region of the flooded cases and starved cases increase with the increasing rod speed, which is similar to that of the 2-D model results. These contact pressure and fluid pressure results are consistent with each other, and are consistent with the film thickness distributions during instroke, discussed above.

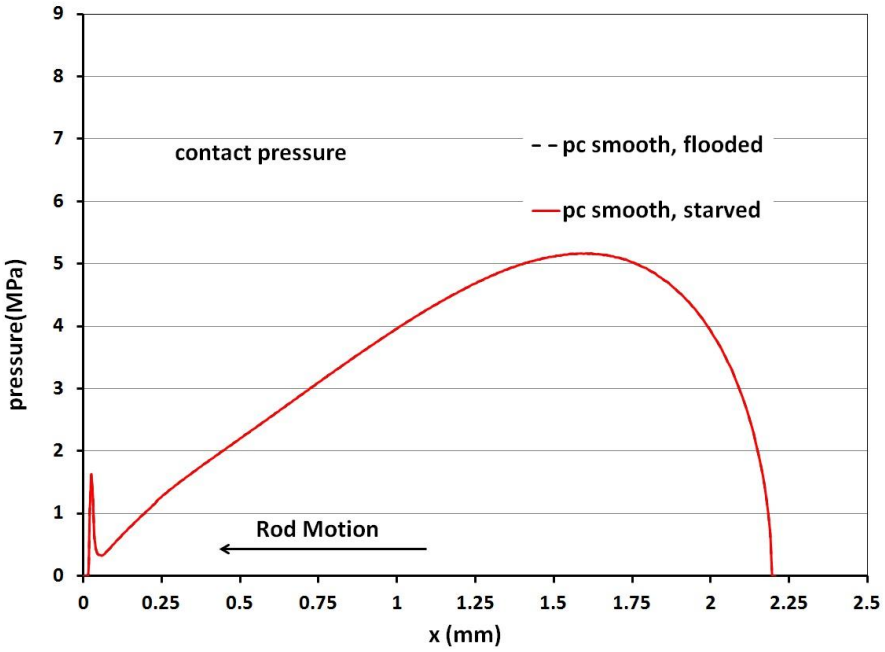

Figure 4.20a1: Contact pressures of instroke, 0.03m/s, U-cup seal, 3-D

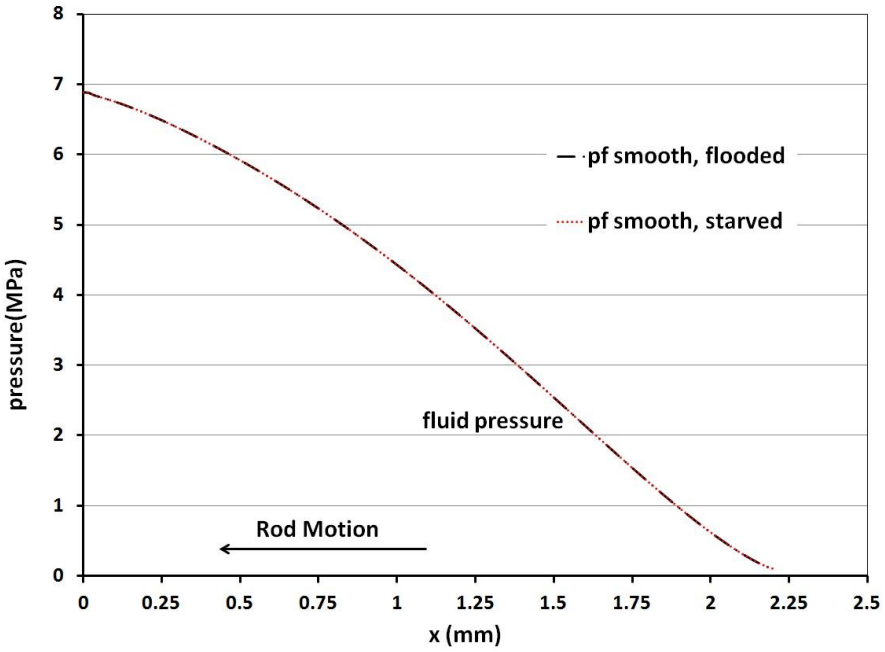

Figure 4.20a2: Fluid pressures of instroke, 0.03m/s, U-cup seal, 3-D

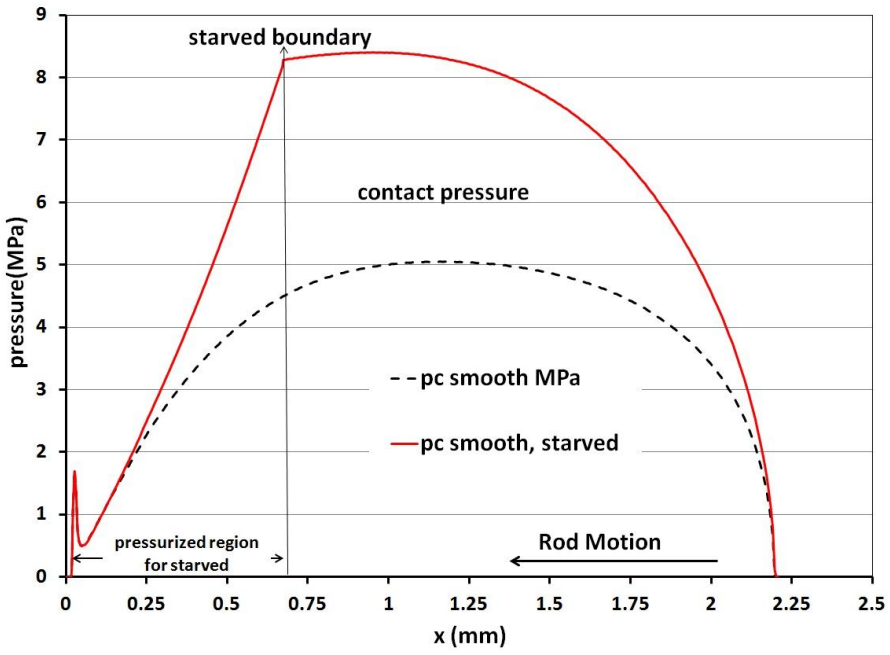

Figure 4.20b1: Contact pressures of instroke, 0.10m/s, U-cup seal, 3-D

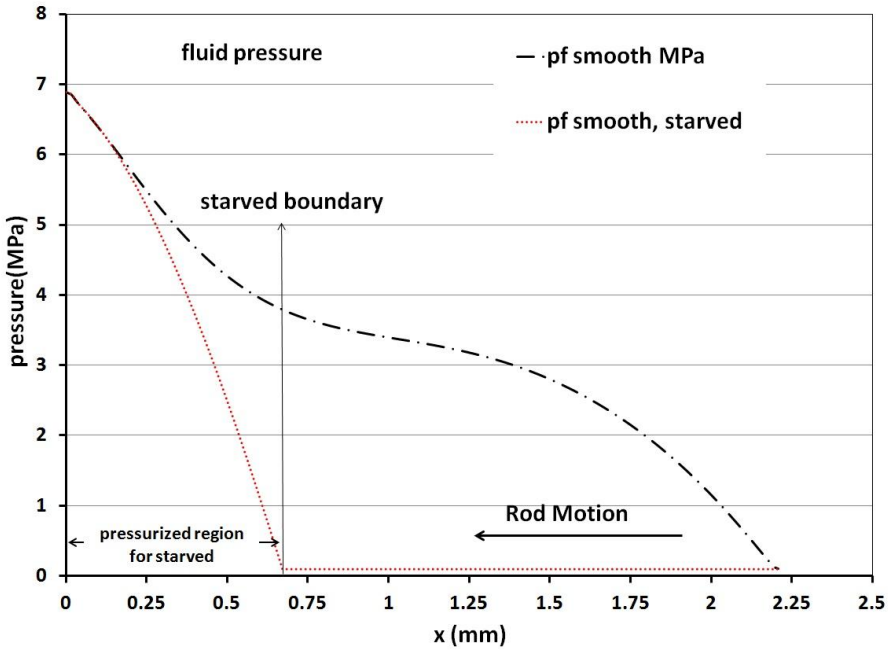

Figure 4.20b2: Fluid pressures of instroke, 0.10m/s, U-cup seal, 3-D

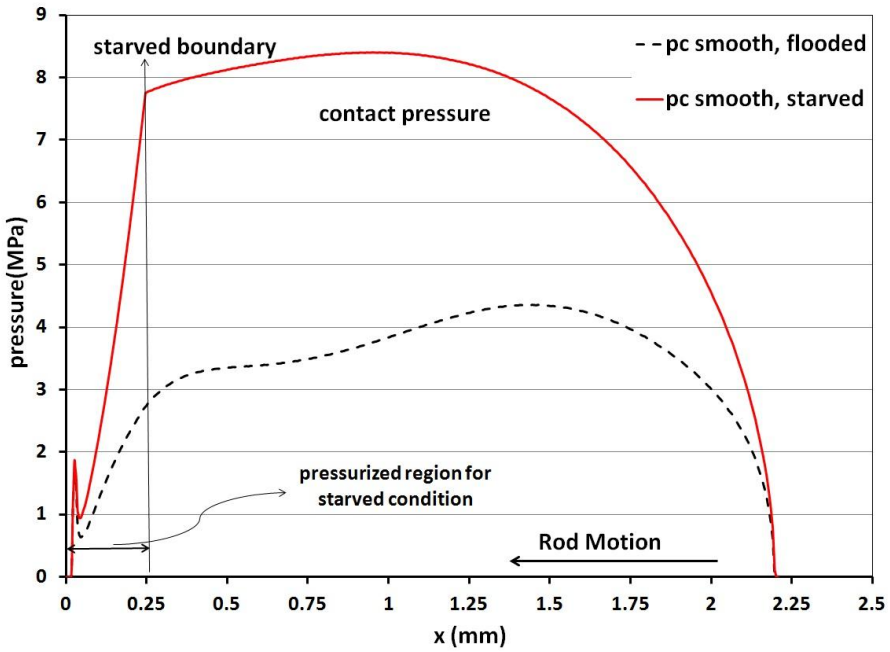

Figure 4.20c1: Contact pressures of instroke, 0.30m/s, U-cup seal, 3-D

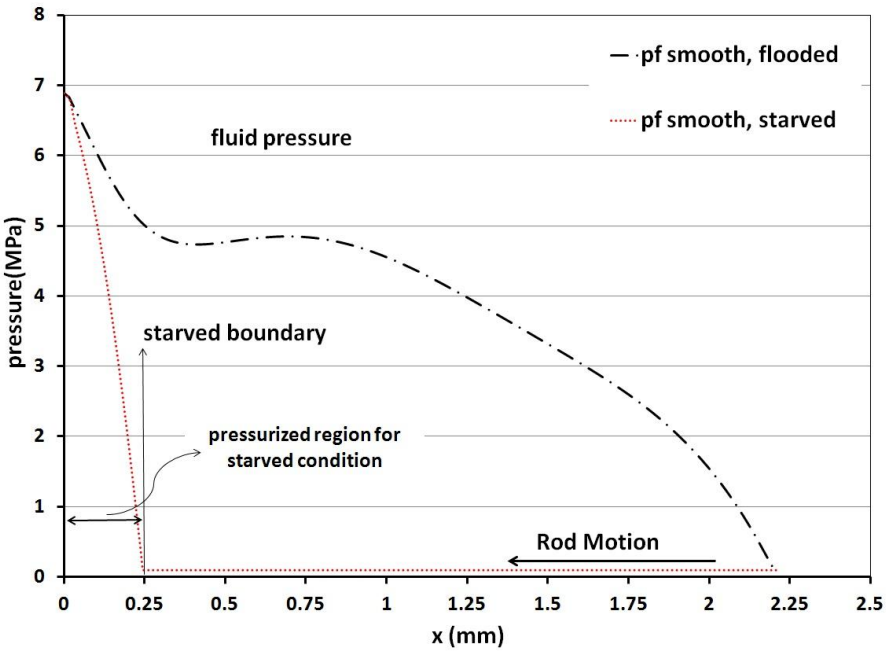

Figure 4.20c2: Fluid pressures of instroke, 0.30m/s, U-cup seal, 3-D

The fluid transport behavior of the seal with the 3-D model can now be explained. During the outstroke, the sealed pressure is ambient. The fluid transport results are very similar to those of the 2-D cases, with the same reason as that discussed in section 4.3.

During the instroke, for the flooded boundary, the shape of the film thickness and the fluid pressure distribution both change with increasing rod speed. Overall, the film grows thicker, causing a larger Couette flow, while the pressure gradient in most of the sealing area becomes less steep, causing a smaller Poiseuille flow. The total fluid transport, which equals the Couette flow minus the Poiseuille flow, therefore increases with the increasing rod speed. For the starved boundary, the combination of

the fluid film thickness and fluid pressure changes keep the fluid transport the same as that of the outstroke.

The friction force results for the outstroke are also similar to that of the 2-D results with the same explanation. During the instroke, for the flooded boundary, at low speed the friction force increases with increasing speed because the contact force increases while the fluid pressure decreases. At high speed (higher than 0.10m/s in this research) the friction force decreases with increasingspeed because the contact force starts to decrease while the fluid pressure increases.

For the starved boundary, the friction behavior during the instroke from the 3-D model is similar to that of the 2-D model, except the increase of the friction force is more pronounced when starvation occurs because of the greater decrease in the length of the pressurized region.

4.6 Effect of Seal Surface Characteristics

In chapter 3, two dimensionless parameters α and β are introduced. α is the measure of seal surface asperity radius ($R = \alpha\sigma$) while β is the measure of seal surface asperity density ($\eta = \beta/R^2$). With the measured RMS seal surface roughness σ, these three parameters determine the seal surface characteristics in the numerical models in this research. While σ can be measured experimentally, the values of α and β are difficult to determine precisely. This section shows how changes in α and β affect the seal performance, based on the 3-D model with both flooded and starved boundary condition.

4.6.1 Effect of Parameter α (the measure of seal surface asperity radius)

Table 4.1 shows the α and β values for the 3-D U-cup seal models. By keeping β=1.0, while changing the α value, the effect of parameter α is investigated. Note that α=1.25 is the default value for 3-D model in this research.

The fluid transports for the outstroke and the instroke of the U-cup seal as a function of rod speed under flooded and starved boundary conditions are shown in Figures 4.21a and 4.21b for various α values with the smooth rod. The fluid transport behavior for the different α values are all similar to the 3-D model results with default value α=1.25. The differences between various α values are: 1) The critical speed increases with the decrease in α; 2) The fluid transport at a given speed, both instroke and outstroke, increases with the decrease in α.

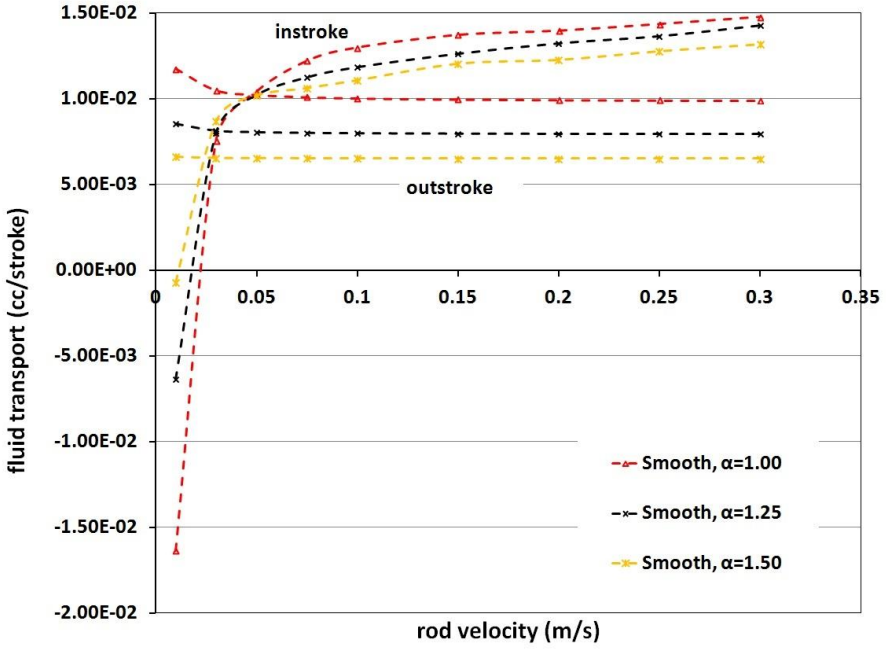

Figure 4.21a: Fluid transport, U-cup seal with various α, 3-D, flooded

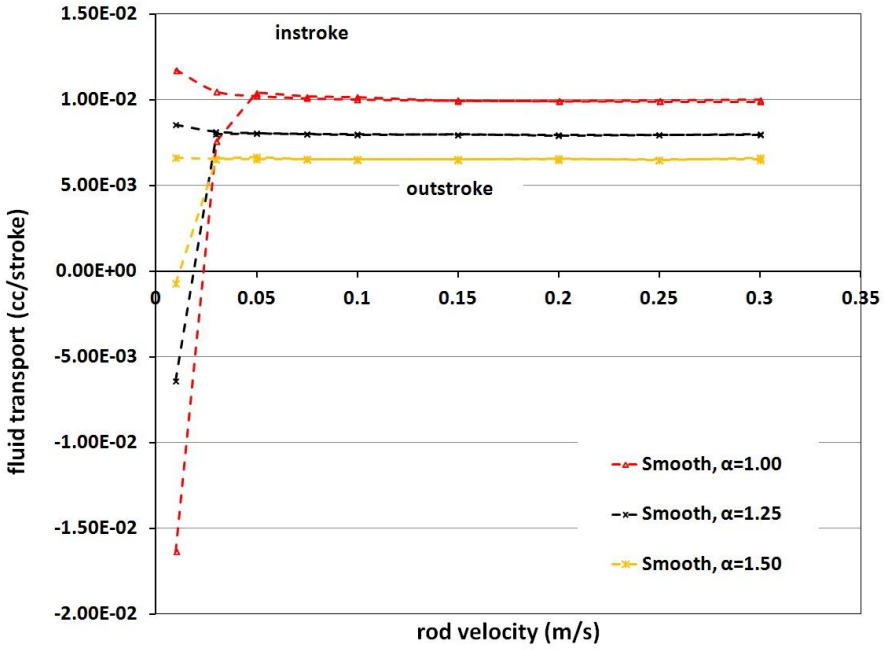

Figure 4.21b: Fluid transport, U-cup seal with various α, 3-D, starved

The friction forces on the rod, as a function of rod speed under flooded and starved boundary conditions, are shown in Figures 4.22a and 4.22b. During the outstroke, all the results are identical to each other. During the instroke, the friction force behavior with different α values are similar, for both flooded and starved cases.

For the flooded cases, the friction increases to a peak and then decreases, with increasing rod speed. For a higher α value (α=1.50), that friction force peak occurs at a lower speed (around 0.075 m/s, compared to 0.10 m/s for α=1.25), and the friction force is lower at high speed. For a lower α value (α=1.00), the friction force peak occurs at a higher speed (between 0.15 and 0.20 m/s), and the friction force is higher at high speed. The values of the peak friction force for various α values are very close, around 300 N, and only slightly increase with decreasing α value.

For the starved cases, the friction increases with the increasing rod speed, for various α values. The friction force at a given rod speed increases with increasing α value. In addition, the friction force with the starved boundary is much larger than that with the flooded boundary, for the same rod speed and same α value.

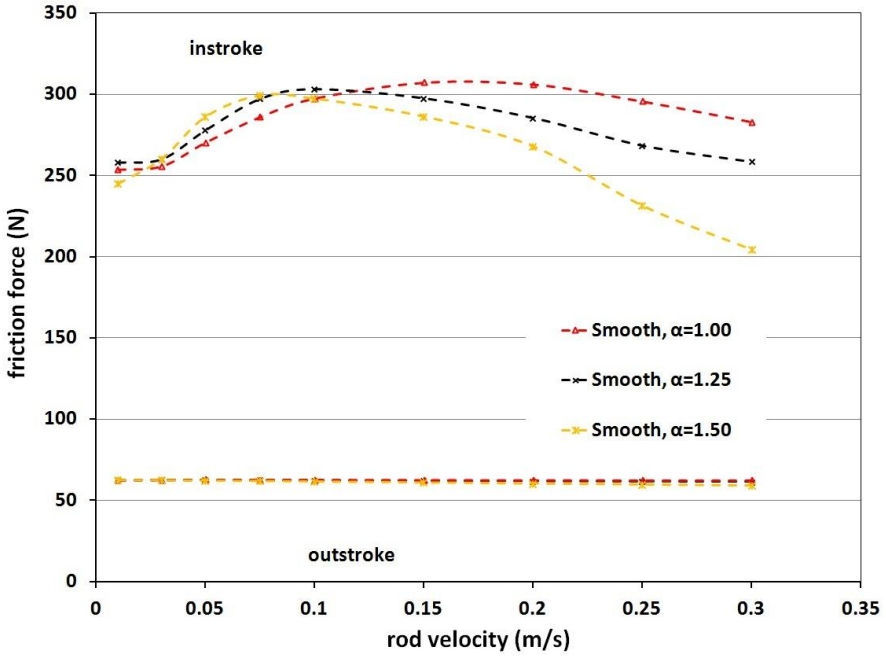

Figure 4.22a: Friction force, U-cup seal with various α, 3-D, flooded

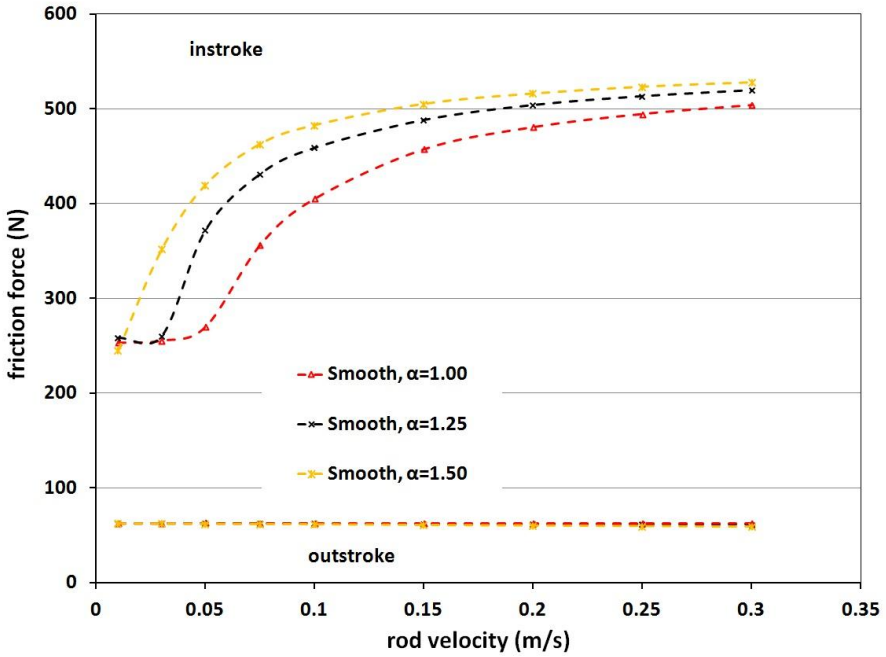

Figure 4.22b: Friction force, U-cup seal with various α, 3-D, starved

To explain the effect of α, an examination of the sealing details is needed. Figure 4.23a and 4.23b show the film thickness distributions during the outstroke at rod speeds of 0.03 and 0.30 m/s, for various α values. For the same α value, the distributions at different speeds are identical, indicating that the film thickness is relatively independent of rod speed during outstroke, for various α values. At a given rod speed, the fluid film thickness decreases as the α value increases. This is consistent with the fluid transport results shown in Figure 4.21 because a thinner film with larger α value creates less fluid transport due to solely Couette flow.

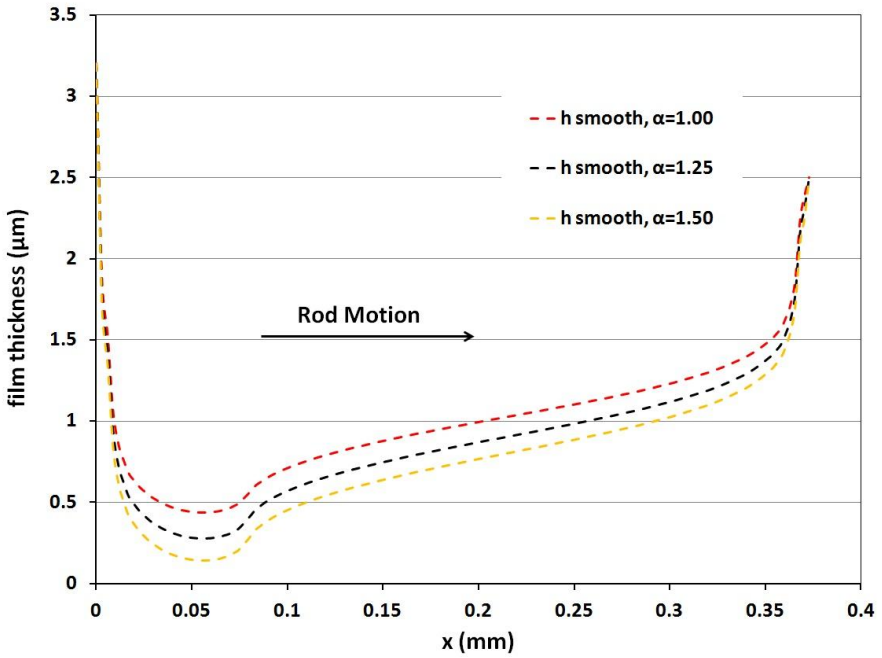

Figure 4.23a: Film thickness of outstroke, 0.03 m/s, U-cup seal, 3-D, various α

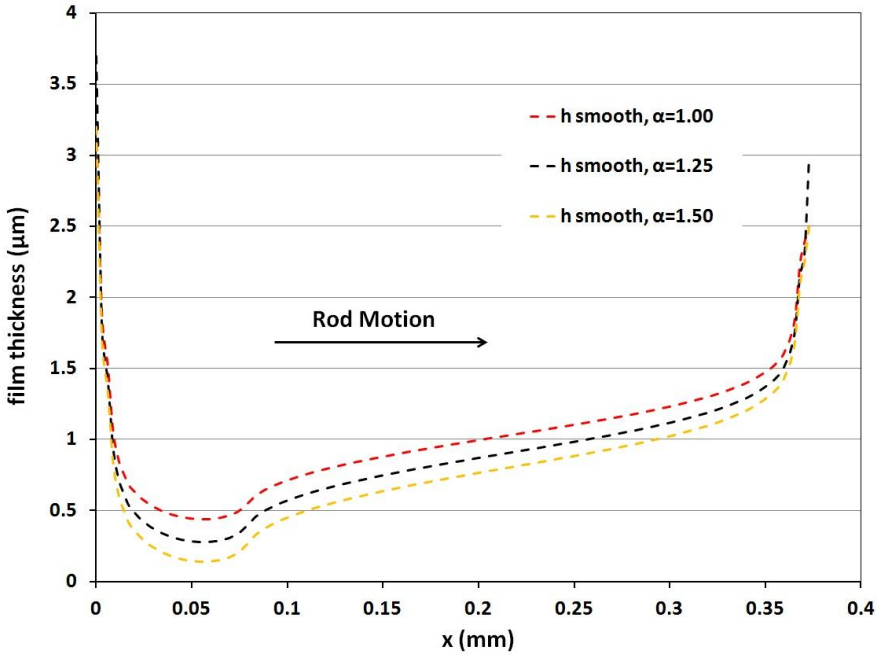

Figure 4.23b: Film thickness of outstroke, 0.30 m/s, U-cup seal, 3-D, various α

The film thickness distributions during the instroke at rod speeds of 0.03, 0.10 and 0.30 m/s under flooded and starved boundary conditions are shown in Figures 4.24a1, 4.24a2, 4.24b1, 4.24b2, 4.24c1 and 4.24c2, respectively. Similar to the outstroke, the film thickness decreases with increasing α at the same rod speed. For the flooded boundary, the shapes of the fluid film profiles are similar to each other at the same rod speed for various α values. That is the reason why the fluid transport behaviors for various α values are similar, which is shown in Figure 4.21. The differences between the various α values' results become smaller at high speed (0.30 m/s). For the starved boundary, the length of the pressurized region (to the left of the starved boundary) decreases with the increasing rod speed, for various α. At the same speed, a larger α value case has a shorter pressurized region.

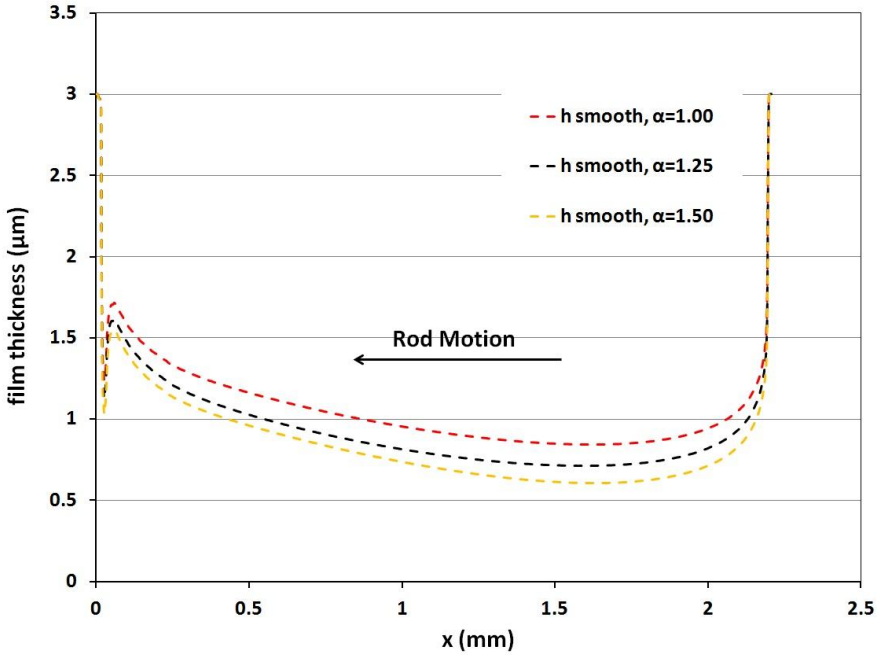

Figure 4.24a1: Film thickness of instroke, 0.03 m/s, U-cup seal, 3-D, various α, flooded

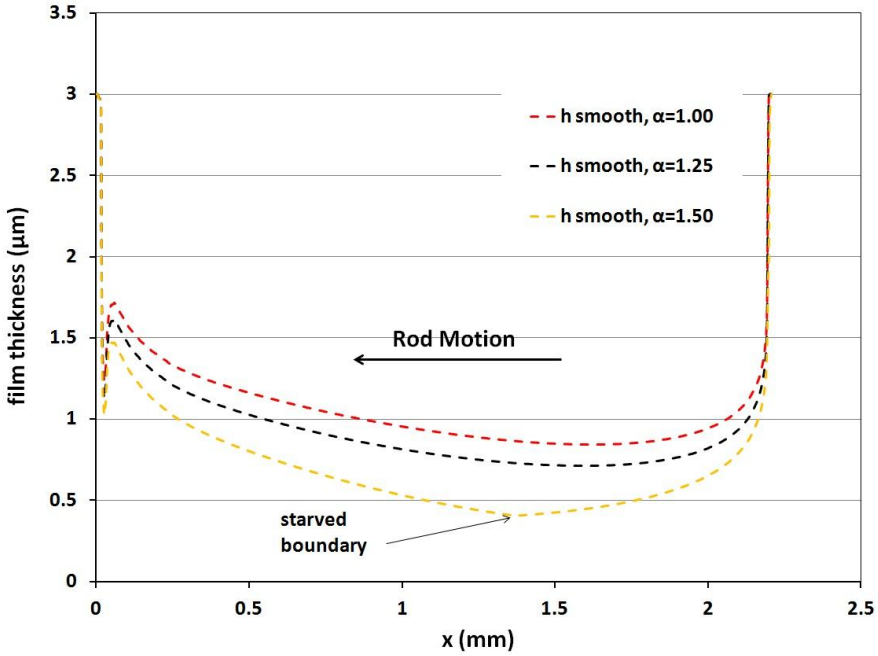

Figure 4.24a2: Film thickness of instroke, 0.03 m/s, U-cup seal, 3-D, various α, starved

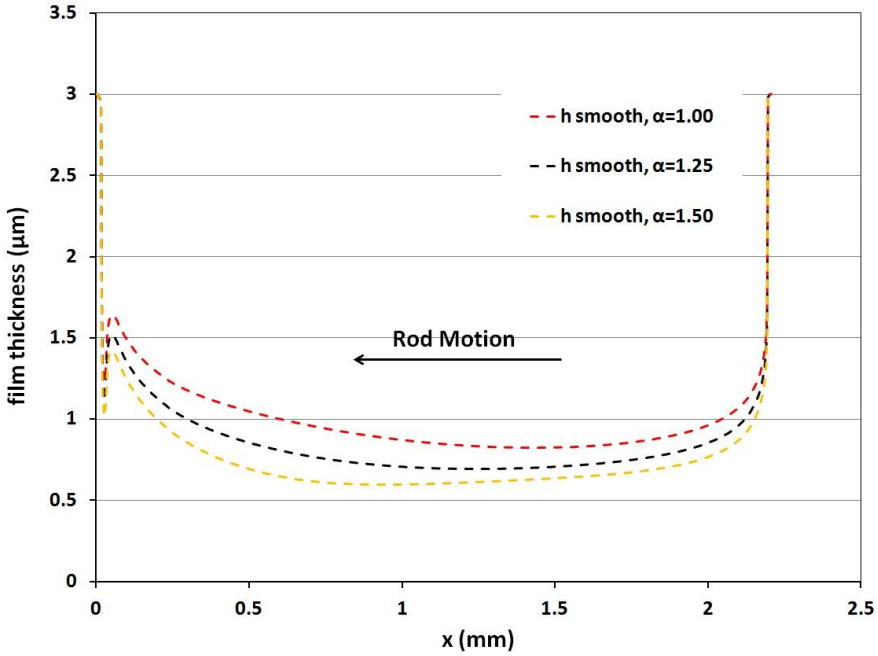

Figure 4.24b1: Film thickness of instroke, 0.10 m/s, U-cup seal, 3-D, various α, flooded

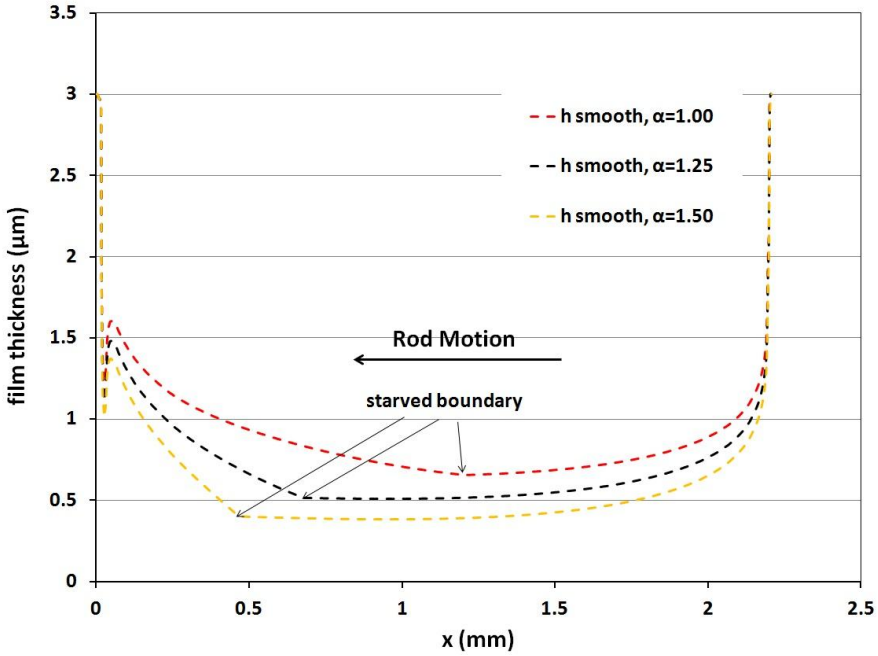

Figure 4.24b2: Film thickness of instroke, 0.10 m/s, U-cup seal, 3-D, various α, starved

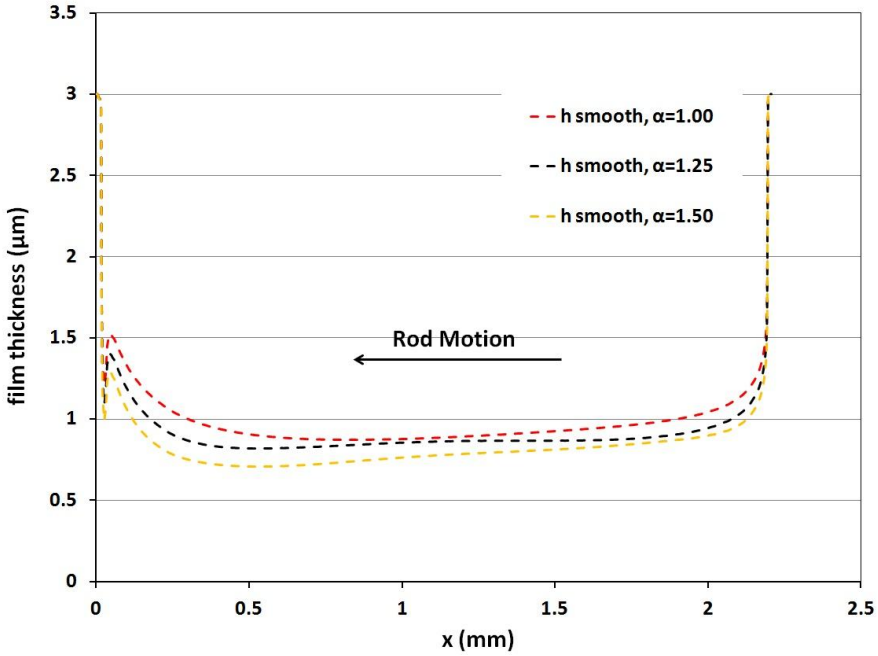

Figure 4.24c1: Film thickness of instroke, 0.30 m/s, U-cup seal, 3-D, various α, flooded

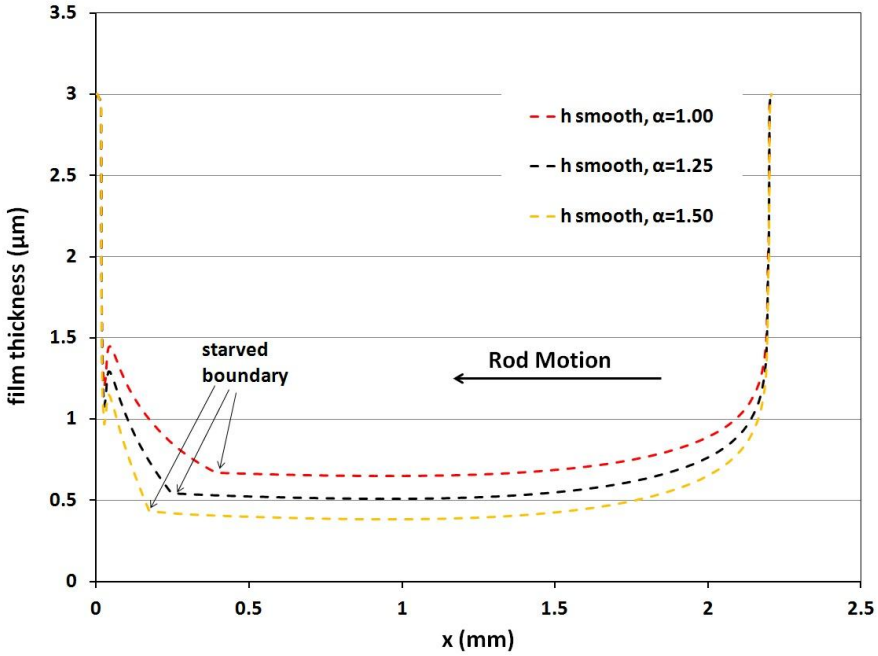

Figure 4.24c2: Film thickness of instroke, 0.30 m/s, U-cup seal, 3-D, various α, starved

Figures 4.25a and 4.25b show the contact pressure and fluid pressure distributions during the instroke at rod speeds of 0.03 m/s and 0.30 m/s for various α values. Comparison of the two figures shows that the contact pressure distributions are virtually independent of rod speed, except very close to the sealing side (left side). Also, most of the sealing area is cavitated, for the various α values and different speeds. For α=1.00 and 1.25, the fluid pressure distributions indicate minimal hydrodynamic action, with the film almost completely supported by the asperities on the seal surface. For α=1.50, at high speed, the fluid pressure is higher than the other two cases near the sealing side, and the contact pressure deceases because the fluid pressure partially supports the seal. These results are consistent with the film thickness distributions during the outstroke.

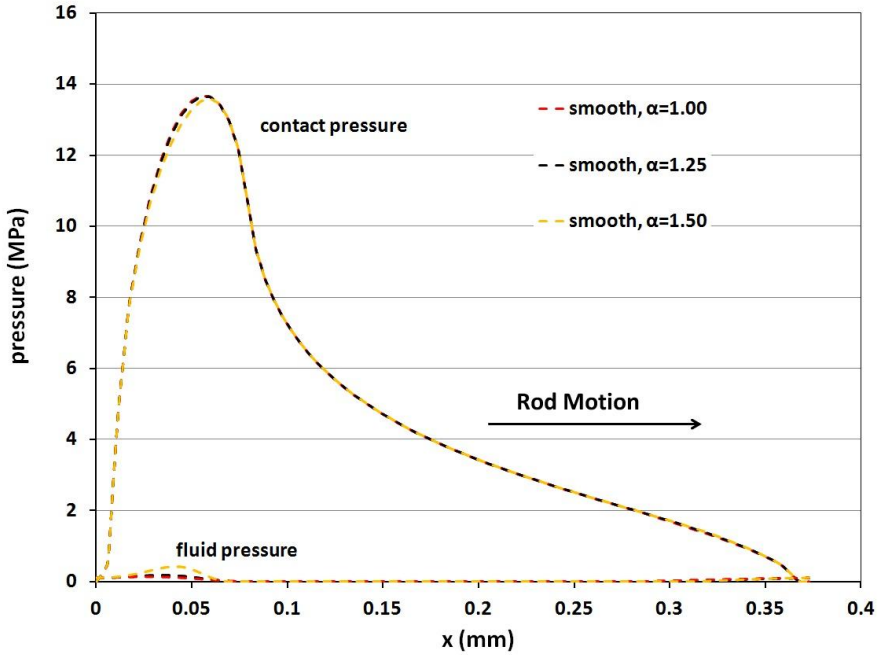

Figure 4.25a: Contact and fluid pressures of outstroke, 0.03m/s, U-cup seal, 3-D, various α

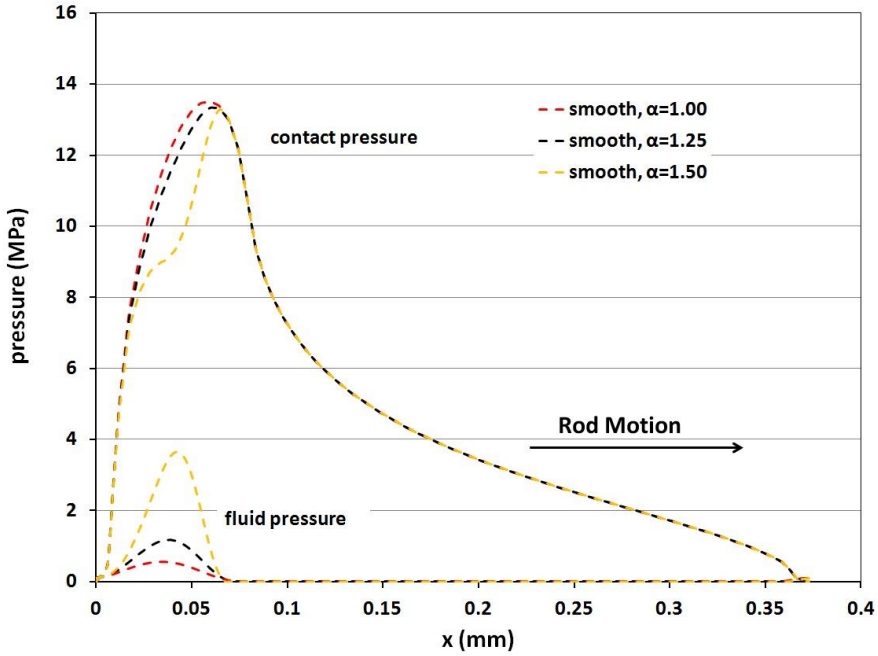

Figure 4.25b: Contact and fluid pressures of outstroke, 0.30m/s, U-cup seal, 3-D, various α

Figures 4.26a1, 4.26a2, 4.26b1, 4.26b2, 4.26c1 and 4.26c2 show the contact pressure and fluid pressure distributions during the instroke at rod speeds of 0.03, 0.10 and 0.30 m/s, under flooded boundary conditions. At the lowest speed (0.03 m/s) the contact pressure and fluid pressure distributions are almost identical to each other for various α values. At the medium speed (0.10 m/s) the contact pressures for α=1.00 and 1.25 are very close, while the contact pressure for α=1.50 is lower than the other two, and the fluid pressure for α=1.50 is slightly higher than the other two. In addition, the overall contact pressure for the medium speed is higher than that of the lowest speed, for the same α. At the highest speed (0.30 m/s), the contact pressure decreases with increasing α, while the fluid pressure increases with increasing α. These results are also consistent with the film thickness distributions during the instroke with the flooded boundary.

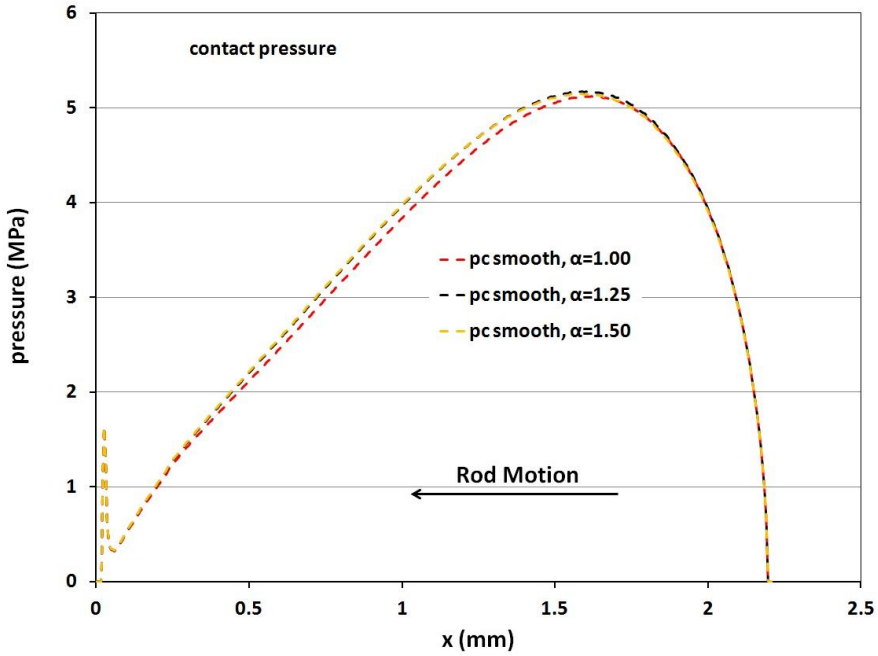

Figure 4.26a1: Contact pressures of instroke, 0.03m/s, U-cup seal, 3-D, various α, flooded

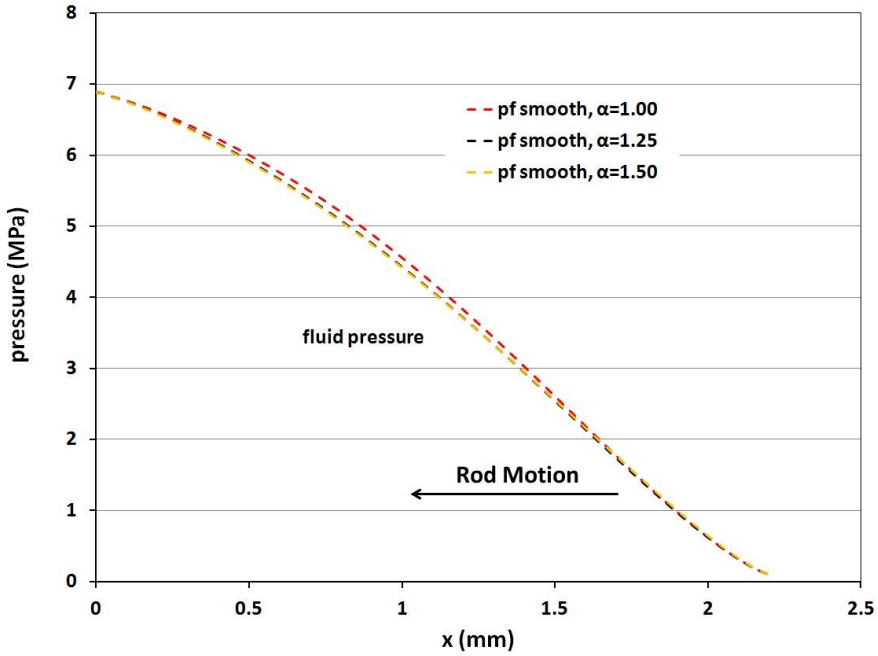

Figure 4.26a2: Fluid pressures of instroke, 0.03m/s, U-cup seal, 3-D, various α, flooded

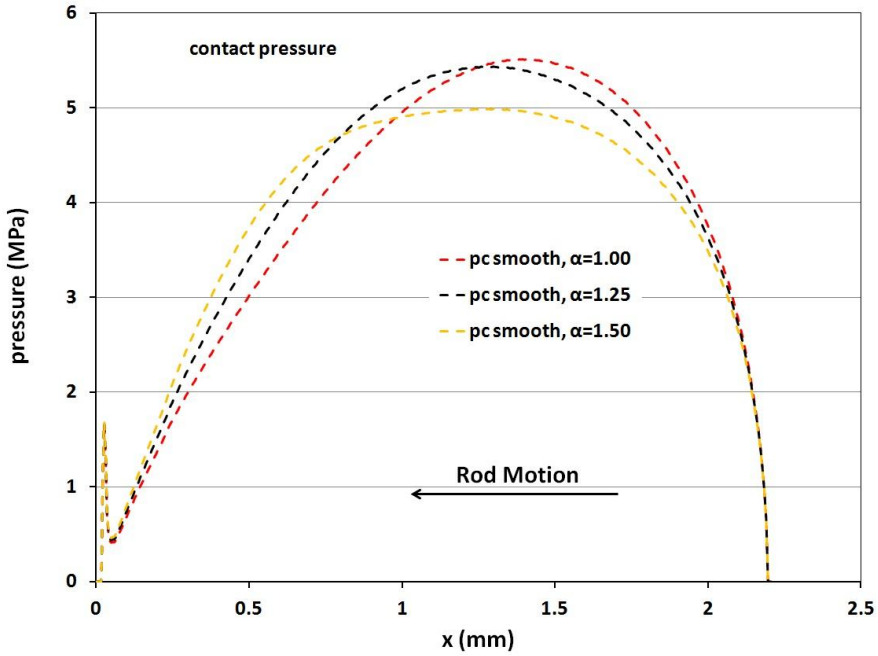

Figure 4.26b1: Contact pressures of instroke, 0.10m/s, U-cup seal, 3-D, various α, flooded

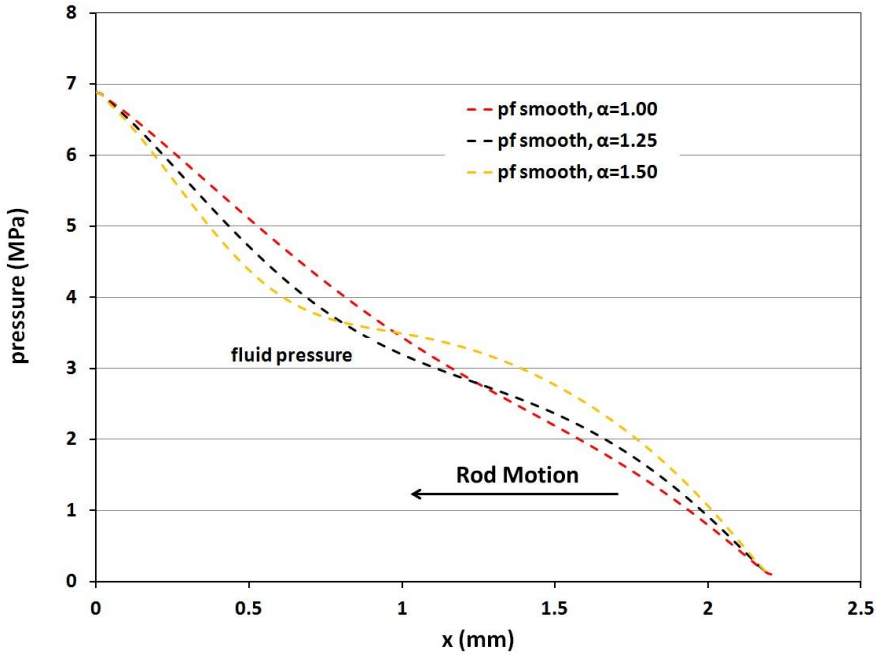

Figure 4.26b2: Fluid pressures of instroke, 0.10m/s, U-cup seal, 3-D, various α, flooded

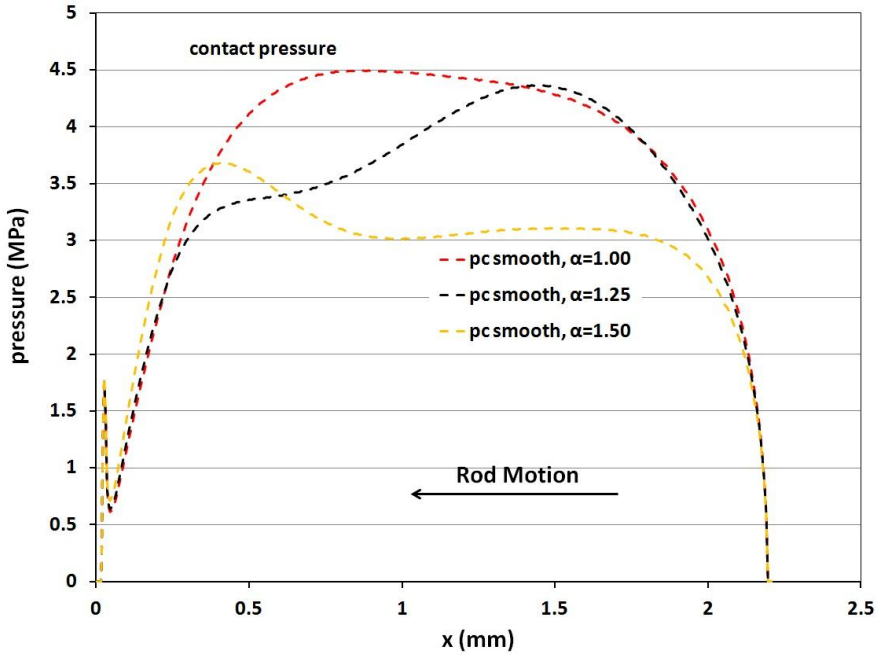

Figure 4.26c1: Contact pressures of instroke, 0.30m/s, U-cup seal, 3-D, various α, flooded

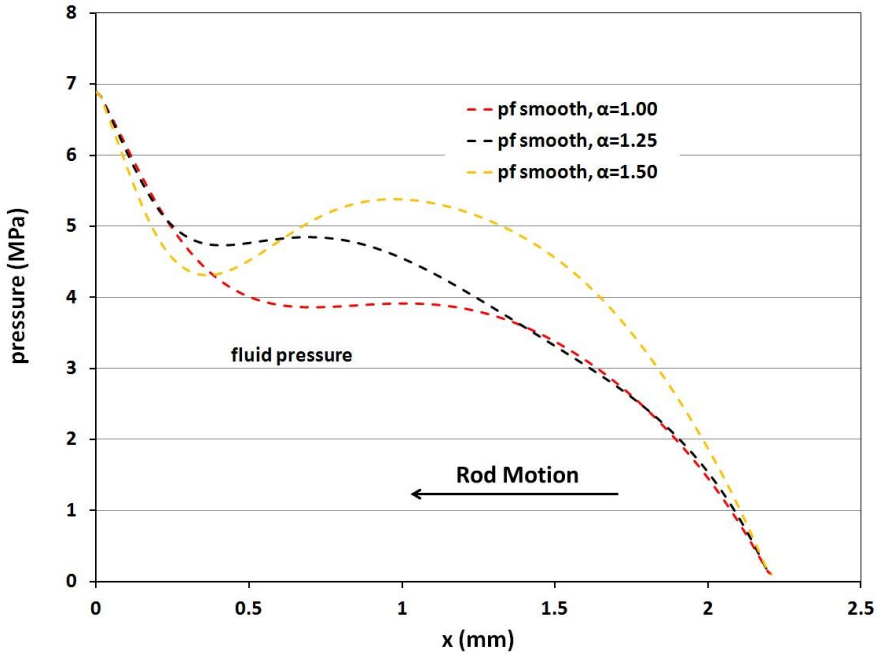

Figure 4.26c2: Fluid pressures of instroke, 0.30m/s, U-cup seal, 3-D, various α, flooded

Figures 4.27a1, 4.27a2, 4.27b1, 4.27b2, 4.27c1 and 4.27c2 show the contact pressure and fluid pressure distributions during the instroke at rod speeds of 0.03, 0.10 and 0.30 m/s, under starved boundary conditions. The overall contact pressure increases while the fluid pressure decreases with increasing α value, at the same rod speed. In addition, with the same α value, the overall contact pressure increases while the fluid pressure decreases with increasing rod speeds. The locations of the starvation boundary can be seen on both the contact pressure and fluid pressure plots. These results are also consistent with the film thickness distributions during the instroke with starved boundary.

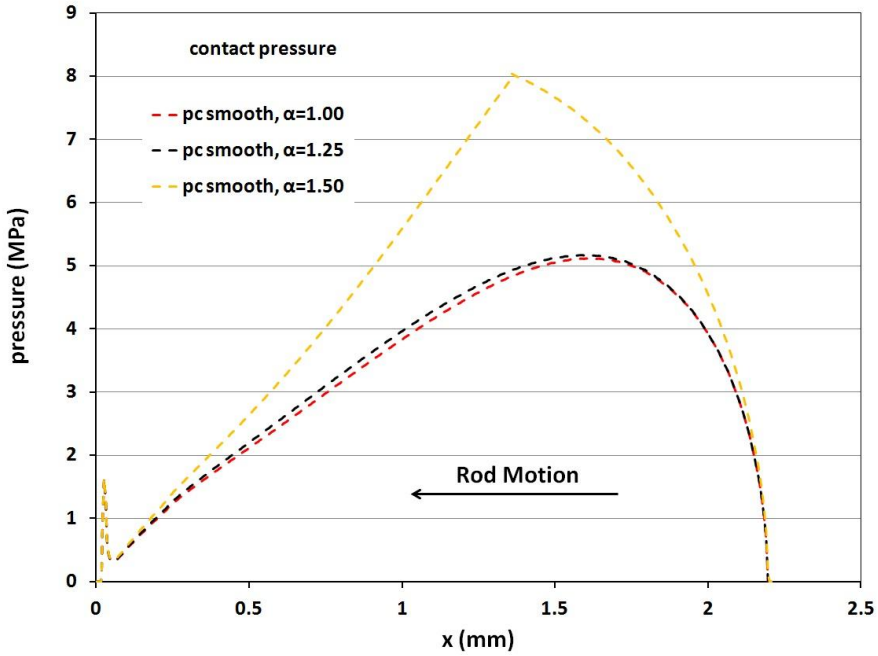

Figure 4.27a1: Contact pressures of instroke, 0.03m/s, U-cup seal, 3-D, various α, starved

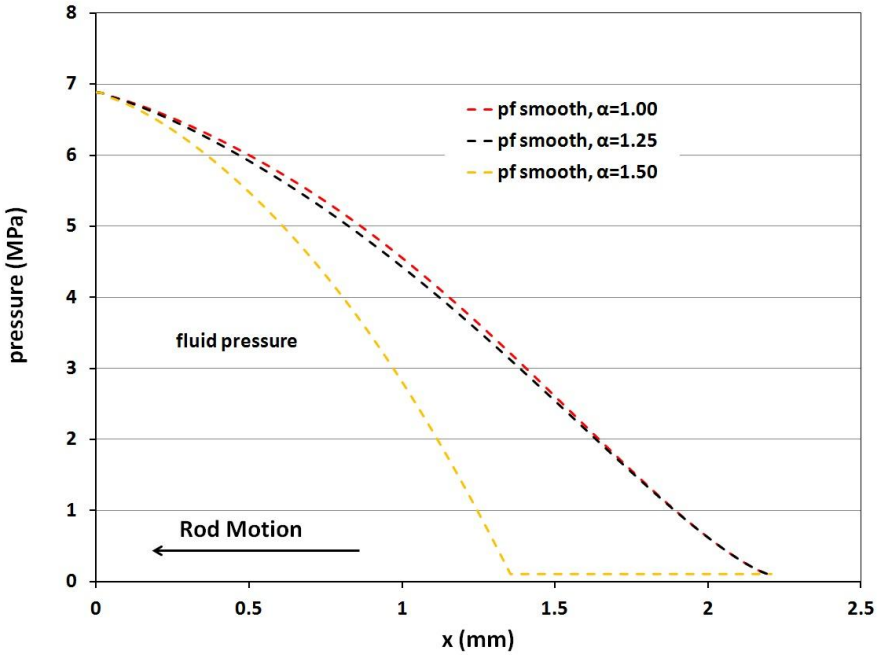

Figure 4.27a2: Fluid pressures of instroke, 0.03m/s, U-cup seal, 3-D, various α, starved

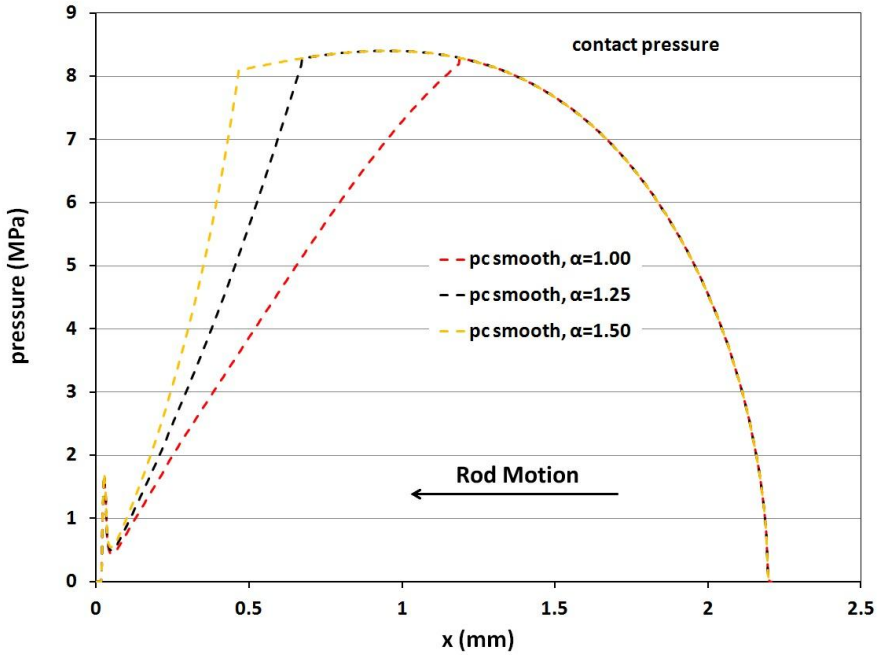

Figure 4.27b1: Contact pressures of instroke, 0.10m/s, U-cup seal, 3-D, various α, starved

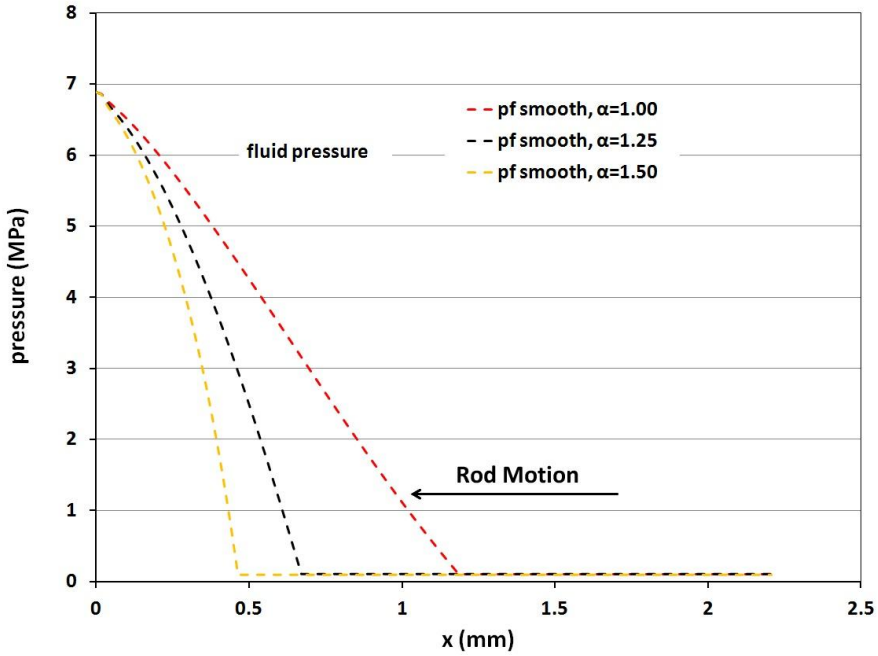

Figure 4.27b2: Fluid pressures of instroke, 0.10m/s, U-cup seal, 3-D, various α, starved

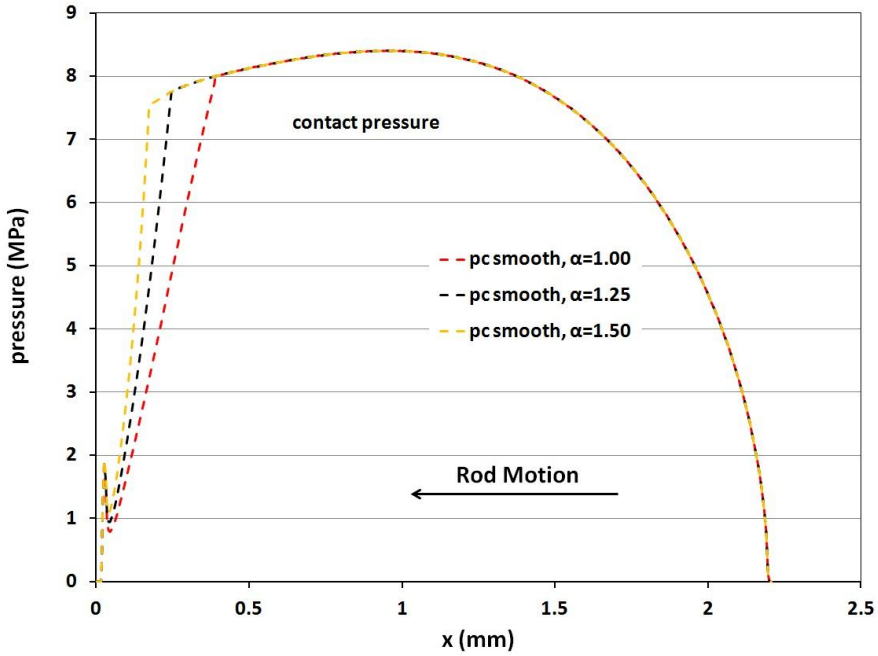

Figure 4.27c1: Contact pressures of instroke, 0.30m/s, U-cup seal, 3-D, various α, starved

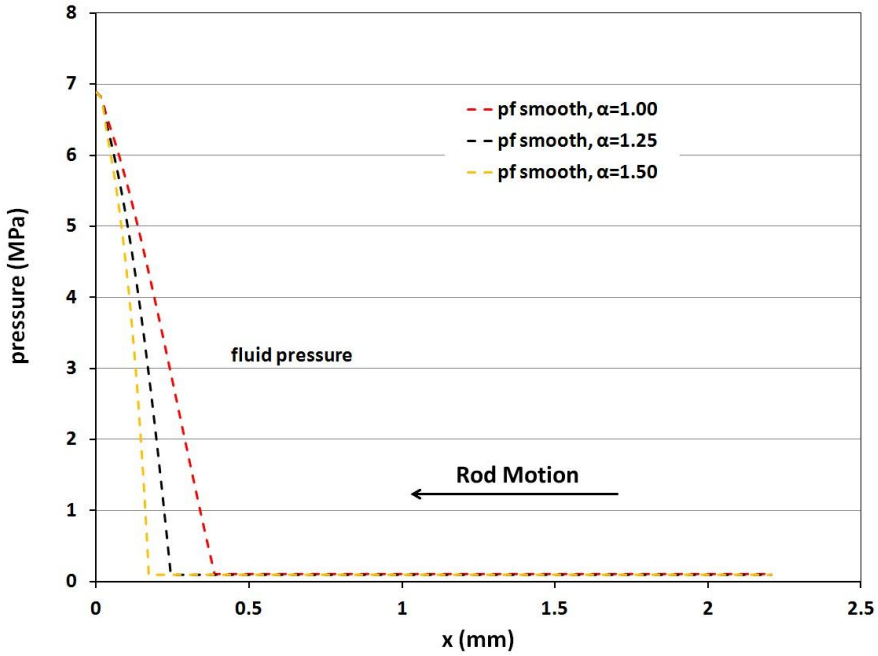

Figure 4.27c2: Fluid pressures of instroke, 0.30m/s, U-cup seal, 3-D, various α, starved

Summarizing, increasing the α value causes a decrease in film thickness. During the outstroke, the thinner film produces less fluid transport, while it has little effect on the contact pressure distribution except at the highest speed. During the instroke, for the flooded boundary, the thinner film also decreases fluid transport, while it generates a higher fluid pressure, especially at higher speeds. The higher fluid pressure offers more support to the seal, decreases the contact pressure, and hence decreases the friction force. For the starved boundary, the thinner film causes more starvation during the instroke, which generates less fluid pressure to support the seal, thereby increasing the contact pressure, and hence increases the friction force.

4.6.2 Effect of Parameter β (the measure of seal surface asperity density)

By keeping α=1.25, while changing the β value, the effect of parameter β is investigated. Note that β=1.00 is the default value for the 3-D model in this research.

The fluid transports for the outstroke and the instroke of the U-cup seal as a function of rod speed under flooded and starved boundary conditions are shown in Figures 4.28a and 4.28b for various β values with the smooth rod. The fluid transport behavior for different β values are all similar to the 3-D model results with the default value β=1.00. The difference between various β values are: 1) the critical speed increases with increasing β value; 2) the fluid transport at a given speed, both instroke and outstroke, increases with increasing β value. These results are very similar to the results in Figure 4.21a and 4.21b (effect of α).

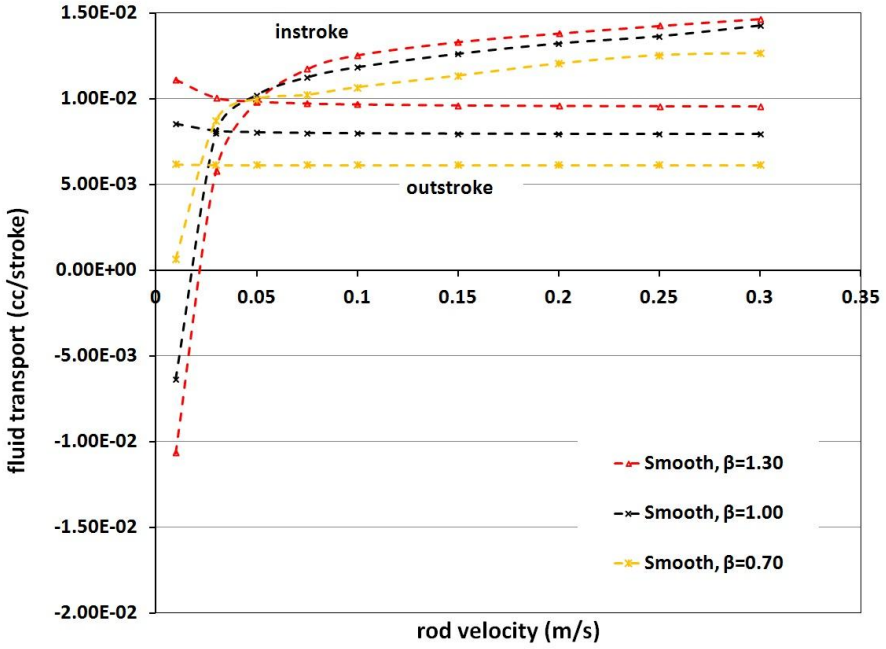

Figure 4.28a: Fluid transport, U-cup seal with various β, 3-D, flooded

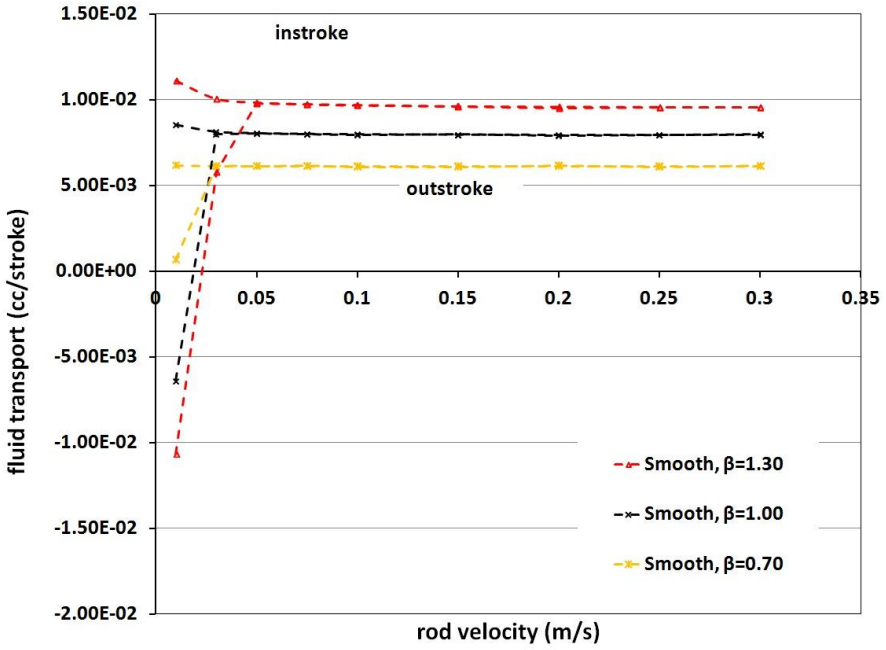

Figure 4.28b: Fluid transport, U-cup seal with various β, 3-D, starved

The friction force on the rod, as a function of rod speed, is shown in Figure 4.29a and 4.29b. During the outstroke, all the results are identical to each other. During the instroke, for the flooded boundary, the friction force behaviors with different β values are similar. The friction increases to a peak then decreases, with increasing rod speed. For a lower β value (β=0.70), that friction force peak occurs at a lower speed, and the friction force is lower at high speed. For a higher β value (β =1.30), the friction force peak appears at a higher speed, and the friction force is higher at high speed. The values of the friction force peak for various β values are very close and only slightly increase with the β value decreasing. For the starved boundary, the friction increases with the increasing rod speed, for various β values. The friction force increases with the decreasing β value at a same rod speed. In addition, the friction force with the starved boundary is much larger than that with the flooded boundary, for the same rod speed and β value.

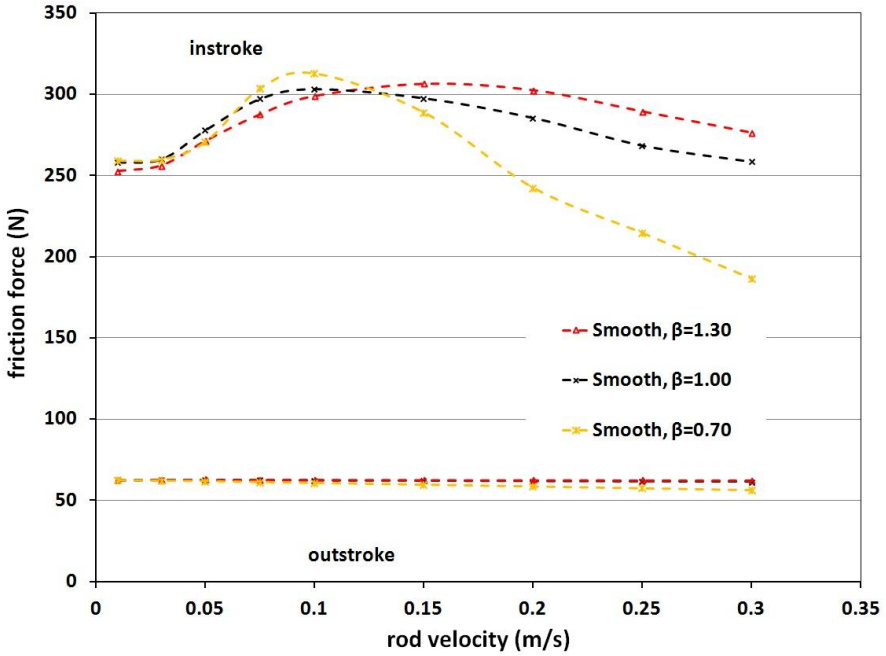

Figure 4.29a: Friction force, U-cup seal with various β, 3-D, flooded

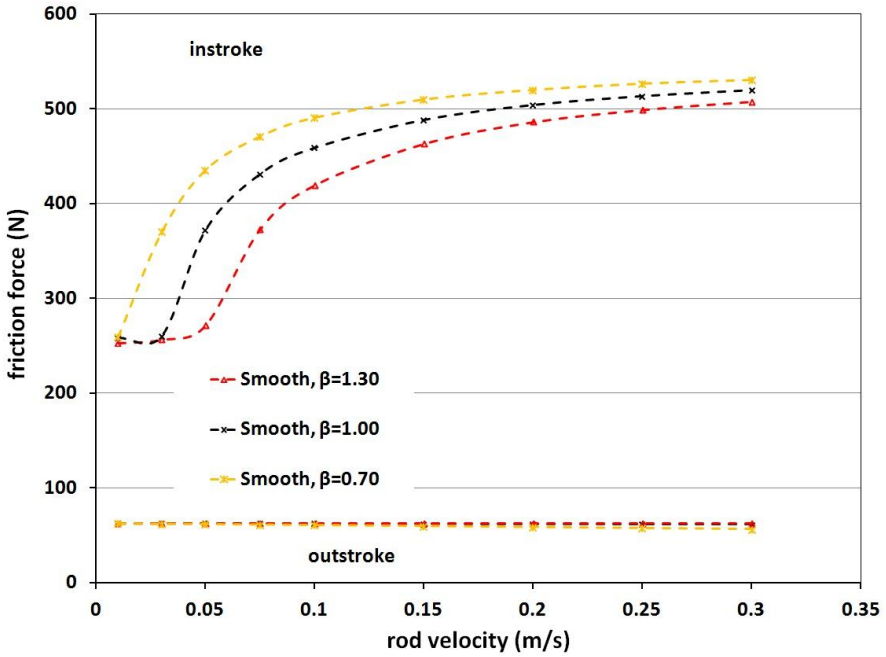

Figure 4.29b: Friction force, U-cup seal with various β, 3-D, starved

The effect of parameter β is very similar to that of parameter α. Figures 4.30a and 4.30b1 and 4.30b2 show the film thickness distributions during outstroke and instroke (flooded and starved), at 0.03 m/s, for various β values. These figures are very similar to the results with various α values. The film thickness decreases with decreasing β value, for both outstroke and instroke, just like the effect of increasing the α value. Since parameters α and β only affect the film thickness directly, while the contact pressure and fluid pressure results depend on the film thickness distributions, the contact pressure and fluid pressure results for various β values should be similar to that of the α value results shown in the previous section. Therefore it is not necessary to present the plots of contact pressure and fluid pressure for various β values.

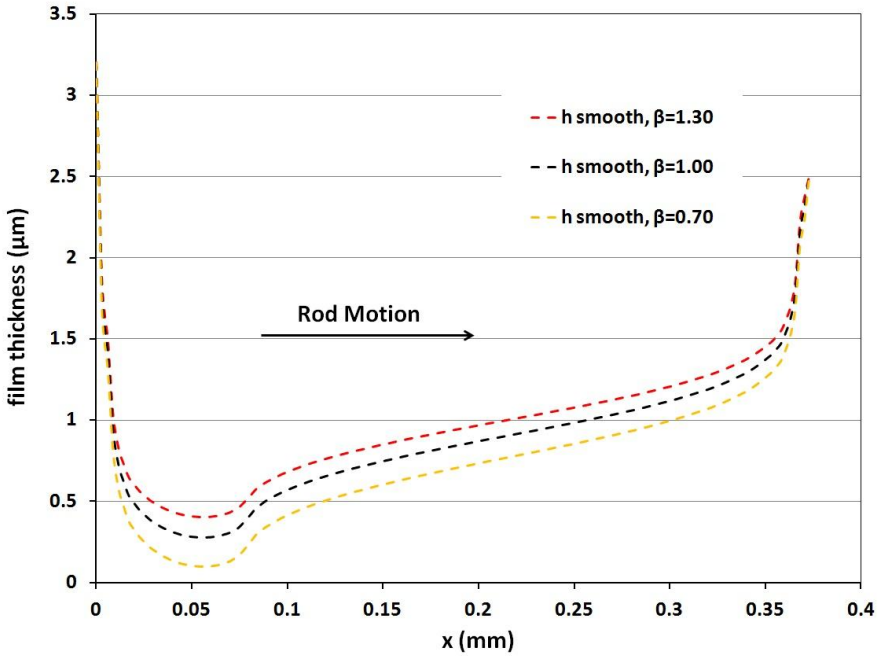

Figure 4.30a: Film thickness of outstroke, 0.03 m/s, U-cup seal, 3-D, various β

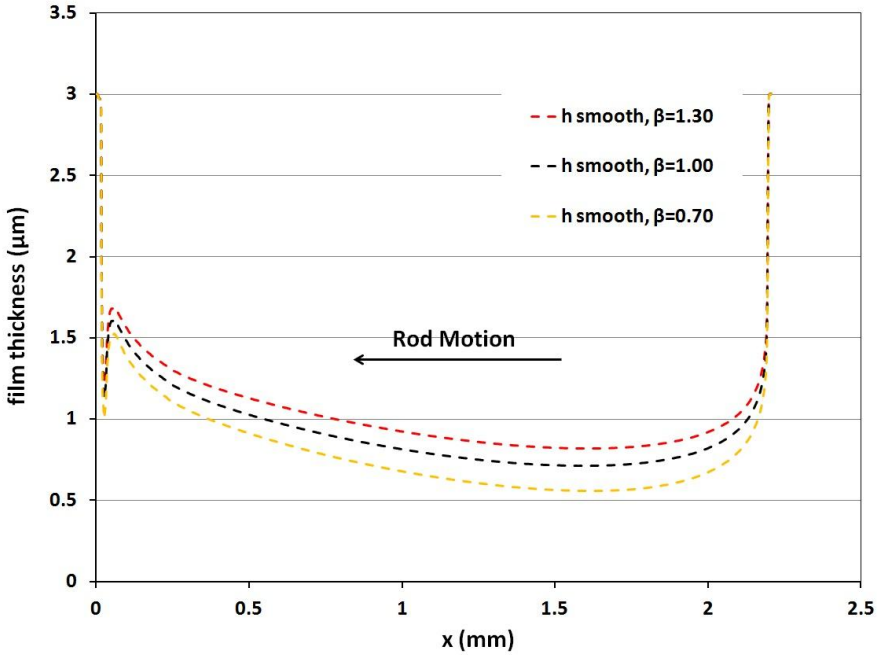

Figure 4.30b1: Film thickness of instroke, 0.03 m/s, U-cup seal, 3-D, various β, flooded

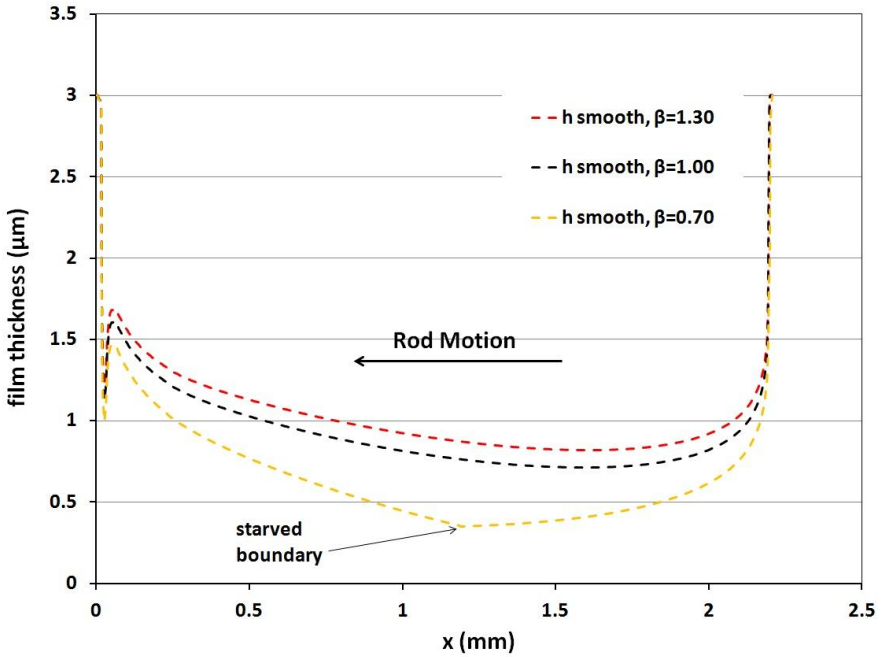

Figure 4.30b2: Film thickness of instroke, 0.03 m/s, U-cup seal, 3-D, various β, starved

Summarizing, the explanation of the β value effects on the seal modeling results is similar to that of the α value. The decrease in β causes a decrease in film thickness. During the outstroke, the thinner film causes less fluid transport, while it has very little effect on the contact pressure distribution except at the highest speed. During the instroke, with the flooded boundary, a thinner film decreases fluid transport, while it also generates higher fluid pressure, especially at higher speed. A higher fluid pressure offers more support to the seal, decreases the contact pressure, and hence decreases the friction force. With the starved boundary, the thinner film causes more starvation during the instroke, which generates less fluid pressure that supports the seal, increases the contact pressure and hence increases the friction force.

4.7 Conclusions

1. For both the U-cup and step seals, the fluid transport during outstroke is relatively independent of rod speed because almost the entire lubricating film is cavitated and hydrodynamic effects are minimal. The film thickness distributions are almost identical at all speeds.

2. For both the U-cup and step seals, the fluid transport during the instroke increases with an increasing rod speed. There is a critical speed where the instroke fluid transport exceeds that of the outstroke. Below this critical speed the seal leaks: above this critical speed, fluid starvation will occur. For the U-cup seal, this critical speed is

between 0.03-0.075; for the step seal, the critical speed is beyond the speed range studied.

3. The friction force during the outstroke is almost independent of rod speed for both U-cup and step seals. The reason is similar to that for the fluid transport phenomenon.

4. The friction force behavior during the instroke is not the same for the U-cup seal and step seal. For the U-cup seal with flooded boundary, the friction force increases to a peak value at low speed and then decreases with increasing rod speed. That is because the fluid pressure decreases at low speed and then increases at high speed while the contact pressure does the opposite. For the U-cup seal with starved boundary, the friction force increases with increasing rod speed because the starvation zone grows longer with increasing speed, the pressurized region decreases and so does the fluid pressure while the contact pressure increases. The contact pressure of the starved case is much larger than that of the flooded case, at the same rod speed, resulting in a much larger friction force. For the step seal with flooded boundary (starvation does not occur for the step seal in this research), the friction force is almost independent of rod speed, since the hydrodynamic effect on the fluid pressure is insignificant compared to the contact pressures.

5. With an increase in the surface characteristic parameter α, the film thickness of the U-cup seal decreases, causing a smaller fluid transport during both instroke and outstroke. The critical speed decreases with the increasing α value. The profiles of friction versus rod speed curves have similar shapes for various α values, but

quantitatively different. The friction force with a starved boundary is much larger than that of the flooded case, for the same rod speed.

6. With an increase in the surface characteristic parameter β, the film thickness of the U-cup seal increases, causing a larger fluid transport during both instroke and outstroke. The critical speed increases with the increasing β value. The profiles of friction versus rod speed curves have similar shape for various β values, but quantitatively different. The friction force with a starved boundary is much larger than that of the flooded case, for the same rod speed.

CHAPTER 5. ROD SEAL WITH PLUNGE-GROUND ROD USING 2D MODELS

5.1 Introduction

In this chapter, the studies on rod seals with a plunge ground rod are discussed. Two types of seal are under investigated: the U-cup seal and the step seal, with 2-D models, because the seal and the plunge-ground rod surface finish are both axisymmetric. For the U-cup seal, both flooded and starved boundaries are discussed. Although starvation is expected in the case of zero sealed pressure during the outstroke (the case mainly considered in this study), there are other applications with a high sealed pressure during the outstroke in which flooded lubrication is expected. For the step seal, only the flooded case is presented, since starvation does not occur in the speed range studied, as shown in the previous chapter. In addition, hypothetical U-cup and step seals are simulated, to help understand the reasons for the differences in the behaviors of these two types of seals. The base parameters for the models in this chapter can be found in Table 4.1. The dimensions of the plunge-ground rod surface are introduced in the next section.

5.2 Plunge-Ground Rod Surface

In this part of the study, the surface finish of a chrome-plated, plunge-ground rod is considered. The surface of such a rod consists of circumferential ridges generated

by the grinding process. The plating process reduces the amplitude of these ridges but they still exist [4, 83]. Figure 5.1 shows a 3D micrograph of a plunge-ground rod surface [83], which contains those ridges running along the axial direction. This surface is modeled in the present study with a sinusoid of 40 μm wavelength and 0.5 μm peak-to-valley amplitude. These dimensions are based on the measurements in Papatheodorou's and Jia's research. A portion of the sealing zone with such a rod surface is illustrated in Fig. 5.1. In this drawing, the seal asperities are omitted and the seal deformation along the ridges is shown.

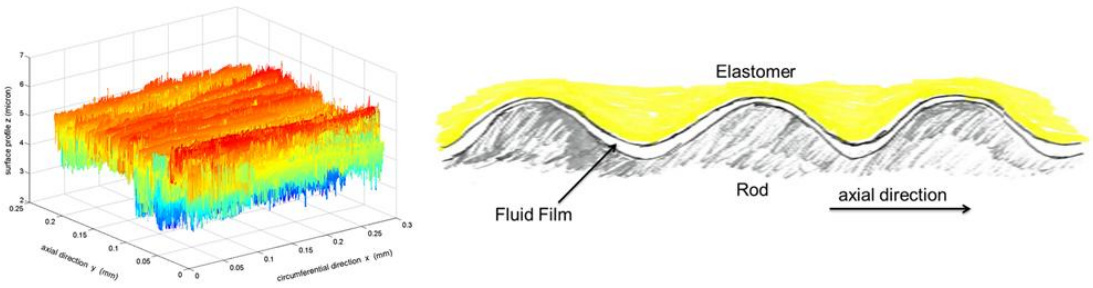

Figure 5.1: 3D micrograph of plunge-ground rod surface and its model

5.3 U-cup Seal

The values of the basic parameters used in the calculations for this chapter are given in Table 4.1. As discussed in the previous chapter, starvation may occur during the instroke process for the U-cup seal, so both flooded and starved boundary conditions are applied. The results for the different boundary conditions are shown separately.

5.3.1 Leakage and Friction with Flooded Boundary Conditions

The fluid transport for the outstroke and the instroke of the U-cup seal as a function of rod speed is shown in Figure 5.2 for both the plunge-ground surface finish and for the smooth rod. The results for the smooth cases have been discussed in the previous chapter. As can be seen, the outstroke transport for the plunge-ground rod cases is relatively independent of rod speed, while the instroke fluid transport increases with rod speed, just like the smooth rod cases. During the outstroke the plunge-ground finish has no significant effect, compared to the smooth rod. However during the instroke under the flooded boundary conditions, the plunge-ground rod produces a lower fluid transport than the smooth rod. The critical speed of the plunge-ground rod is very close to that of the smooth rod, but slightly higher.

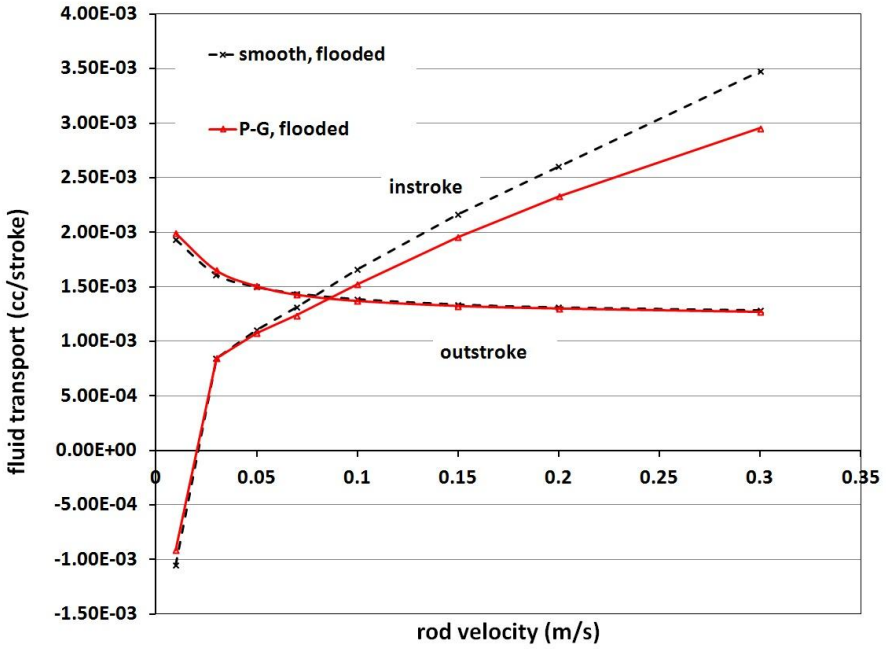

Figure 5.2: Fluid transport, U-cup seal, flooded, σ=0.8μm

The friction force on the rod, as a function of rod speed, is shown in Figure 5.3. During the outstroke, when the sealed pressure is ambient, the friction force is relatively low and independent of rod speed, like the smooth rod for the same reason as that discussed in chapter 4. During the instroke, with a high sealed pressure, the friction force behavior of the plunge-ground rod is also similar to that of the smooth rod. It is seen that the plunge-ground finish has no effect on the friction force, compared to the smooth rod, during the outstroke. However, it does increase the friction force during the instroke under the flooded boundary conditions, especially at the higher rod speeds.

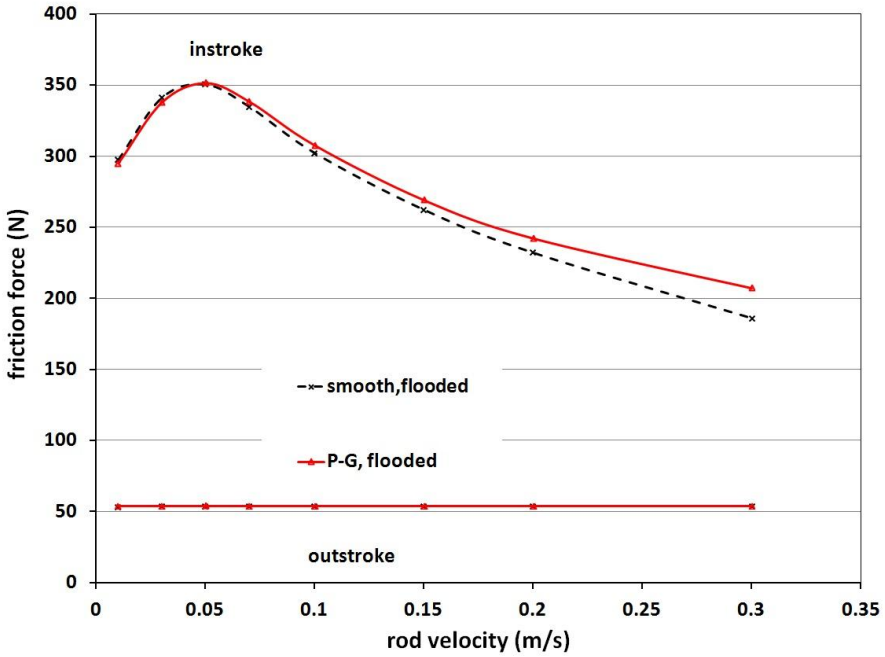

Figure 5.3: Friction force, U-cup seal, flooded, σ=0.8μm

A physical understanding of these characteristics can be obtained by examining the details of the sealing zone, namely the lubricating film thickness distribution and the fluid and contact pressure distributions, as was done in the previous chapter.

5.3.2 Details of Sealing for Flooded Boundary

Figures 5.4a and 5.4b show the film thickness distributions during the outstroke at rod speeds of 0.05 m/s and 0.3 m/s, respectively. These distributions are almost identical, indicating the film thickness is relatively independent of rod speed during the outstroke, for both smooth and plunge-ground rods. The reason for that has been discussed in chapter 4, and will be seen in the fluid pressure distribution, below. Furthermore, the average of the oscillating film thickness with the plunge-ground rod

is almost identical to the film thickness with the smooth rod. It should be noted that the curves for the plunge-ground rod in these figures, and in all subsequent distribution plots, are for one instant of time. As time progresses, the oscillations in the curve move in the direction of the rod motion, with some small variations and with the pattern repeating every rod surface fluctuation period.

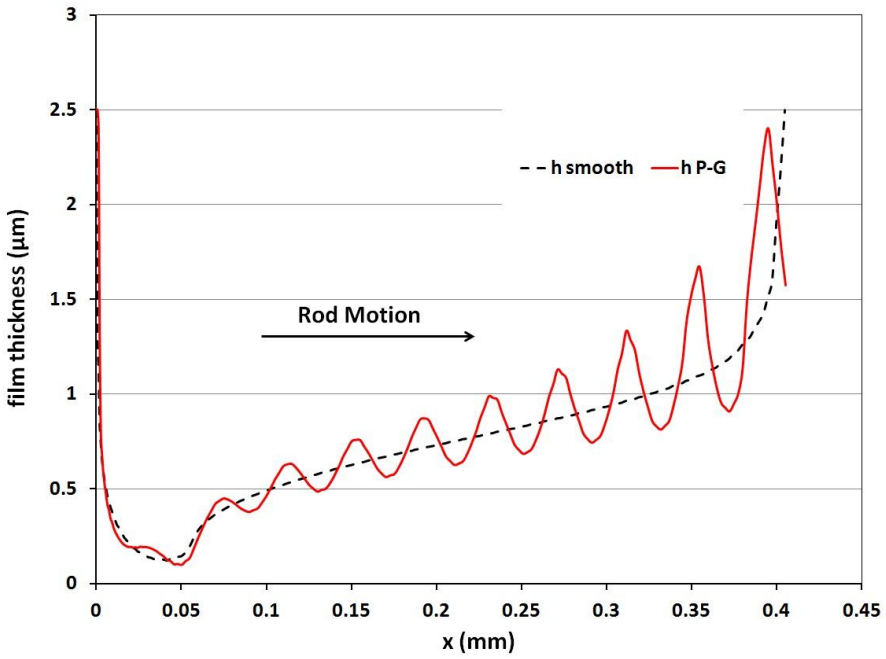

Figure 5.4a: Film thickness of outstroke, 0.05 m/s, U-cup seal, σ=0.8µm, flooded

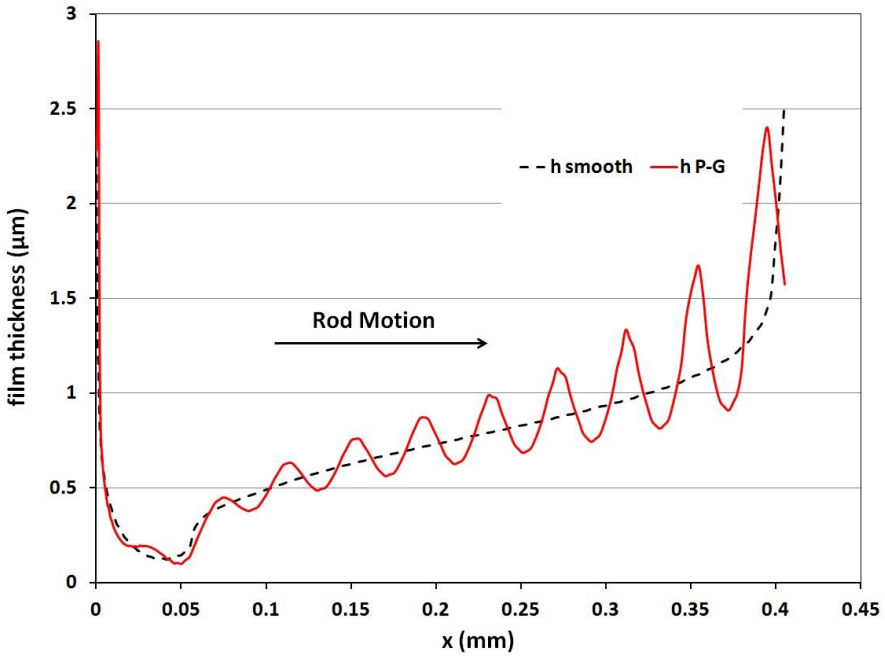

Figure 5.4b: Film thickness of outstroke, 0.30 m/s, U-cup seal, σ=0.8µm, flooded

The film thickness distributions during the instroke at rod speeds of 0.05 m/s, 0.15 m/s, and 0.3 m/s are shown in Figures 5.5a, 5.5b and 5.5c, respectively. The length of the sealing zone is much larger than that during the outstroke, for the plunge-ground rod, similar to the smooth rod cases, because of the much higher sealed pressure during the instroke. From these distributions it is clear that the higher rod speeds produce thicker fluid films during the instroke, under flooded boundary conditions. It is also seen that the average of the oscillating film thickness with the plunge-ground rod is almost identical to the film thickness with the smooth rod.

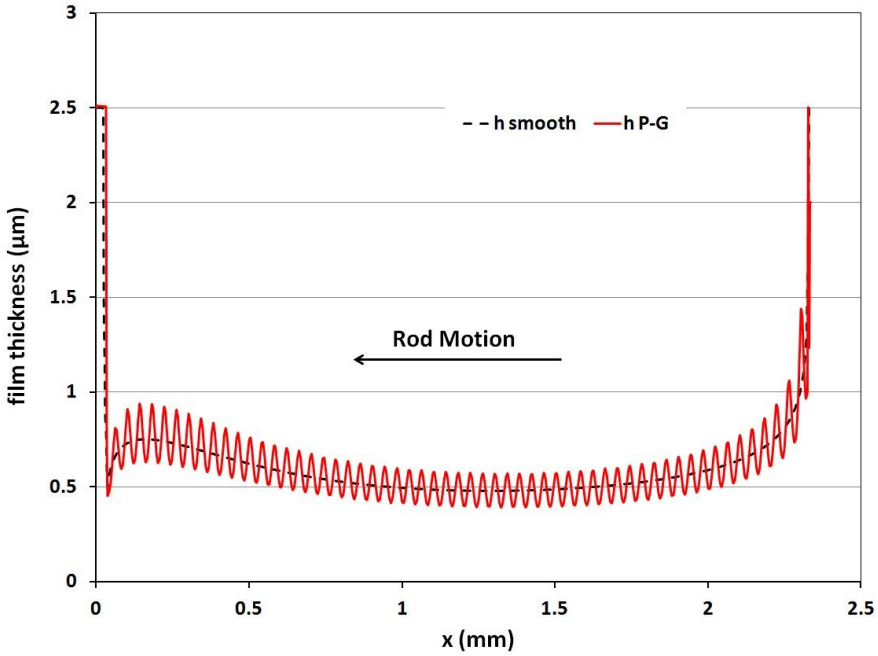

Figure 5.5a: Film thickness of instroke, 0.05 m/s, U-cup seal, σ=0.8µm, flooded

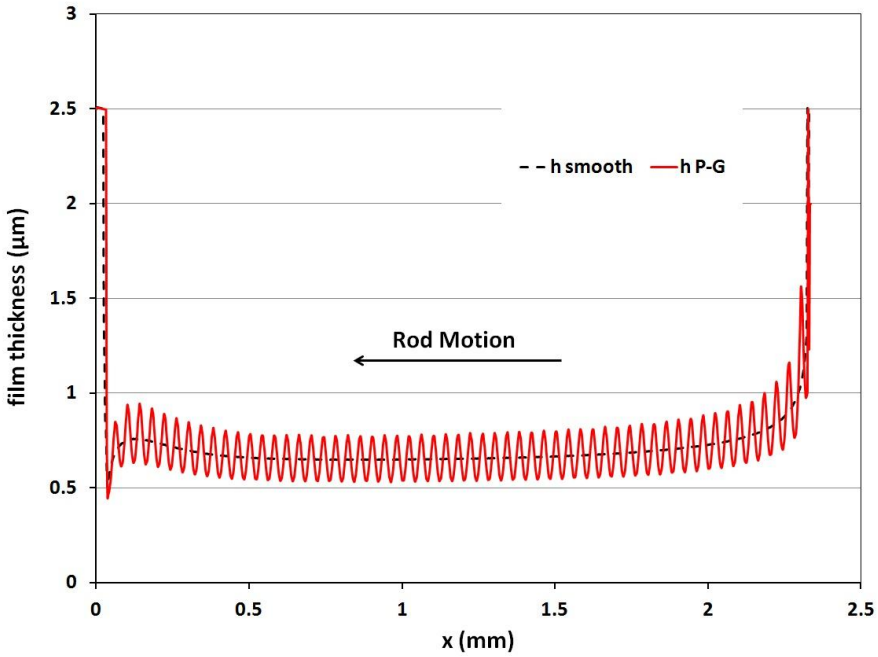

Figure 5.5b: Film thickness of instroke, 0.15 m/s, U-cup seal, σ=0.8µm, flooded

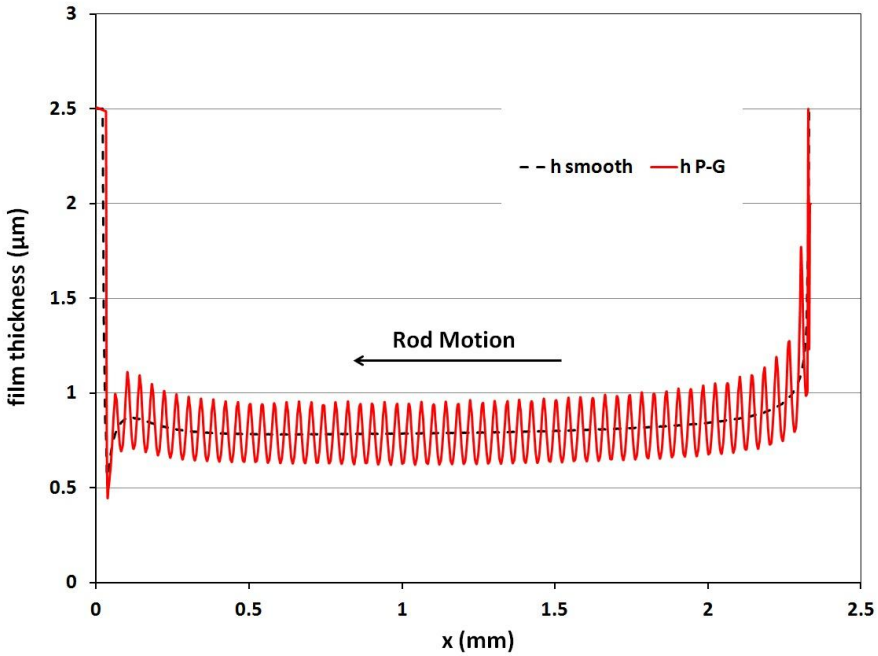

Figure 5.5c: Film thickness of instroke, 0.30 m/s, U-cup seal, σ=0.8µm, flooded

Figures 5.6a and 5.6b show the contact pressure and fluid pressure distributions during the outstroke at rod speeds of 0.05 m/s and 0.3 m/s. Comparison of the two figures shows that the contact pressure distributions are virtually independent of rod speed, for the plunge-ground rod and the smooth rod. It is important to note the large oscillations in the contact pressure that are produced by the ridges on the plunge-ground shaft and that have the same wavelength as those ridges. During the outstroke the sealed pressure is not elevated above ambient, and most of the lubricating film is cavitated, as was discussed in thr previous chapter. For the plunge-ground rod, the fluid pressure distributions indicate minimal hydrodynamic action, with the film almost completely supported by the asperities on the seal surface,

just like the smooth rod cases. These results are consistent with the film thickness distributions during the outstroke, discussed above.

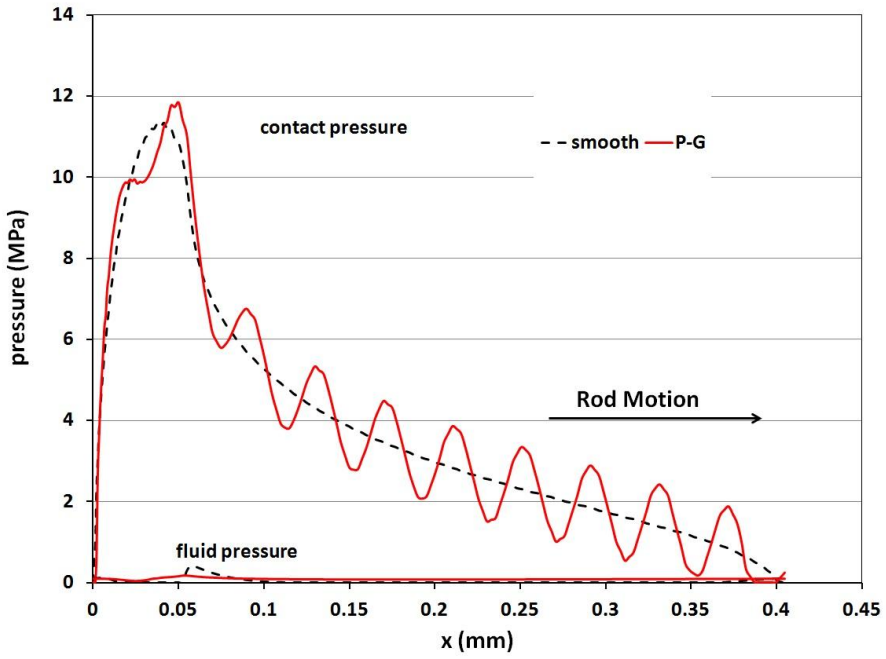

Figure 5.6a: Contact and fluid pressures of outstroke, 0.05 m/s, U-cup seal, σ=0.8μm, flooded

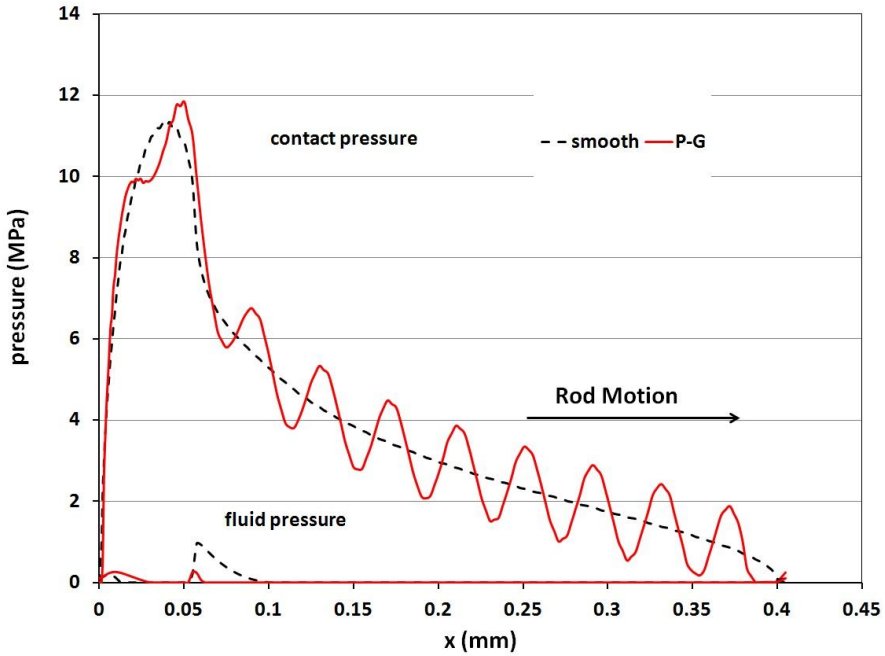

Figure 5.6b: Contact and fluid pressures of outstroke, 0.30 m/s, U-cup seal, σ=0.8μm, flooded

Figures 5.7a1, 5.7a2, 5.7b1, 5.7b2, 5.7c1 and 5.7c2 show the contact pressure and fluid pressure distributions during the instroke at rod speeds of 0.05 m/s, 0.15 m/s and 0.3 m/s. The contact pressures decrease with the increasing rod speed. As in the outstroke, the plunge-ground rod produces large oscillations in the contact pressure. At the 0.05 m/s speed, the average of the oscillating contact pressure with the plunge-ground rod is almost identical to that with the smooth rod, while the fluid pressures are also almost identical and almost linear. The oscillations in the film thickness with the plunge-ground rod produce barely discernible oscillations in the fluid pressure due to the low rod speed. At the 0.15 m/s speed, the average of the oscillating contact pressure with the plunge-ground rod still shows no significant difference compared to the smooth rod, but the fluid pressure is slightly lower than

that with the smooth rod and contains oscillations. At the 0.3 m/s speed, the average of the contact pressure with the plunge-ground rod is higher than that with the smooth rod, while the fluid pressure with the plunge-ground rod is lower than that with the smooth rod and contains significant oscillations. These contact pressure and fluid pressure results are consistent with each other and are consistent with the film thickness distributions during instroke, discussed above.

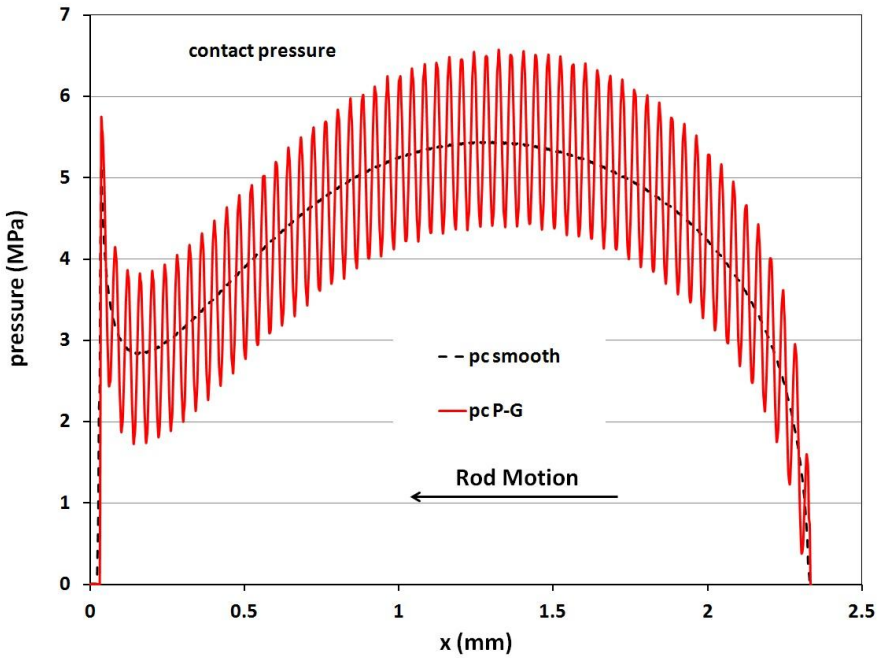

Figure 5.7a1: Contact pressures of instroke, 0.05 m/s, U-cup seal, σ=0.8μm, flooded

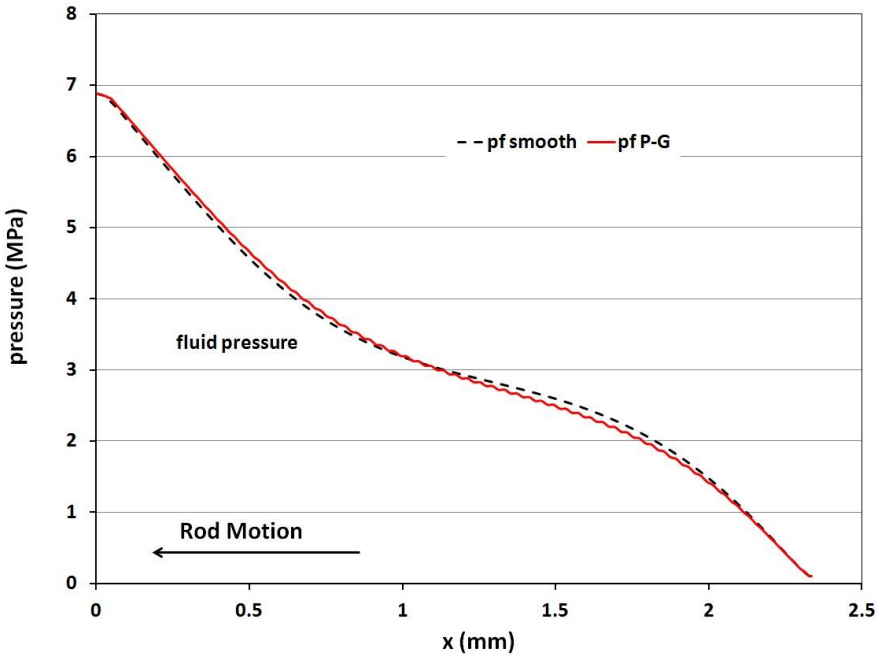

Figure 5.7a2: Fluid pressure of instroke, 0.05 m/s, U-cup seal, σ=0.8μm, flooded

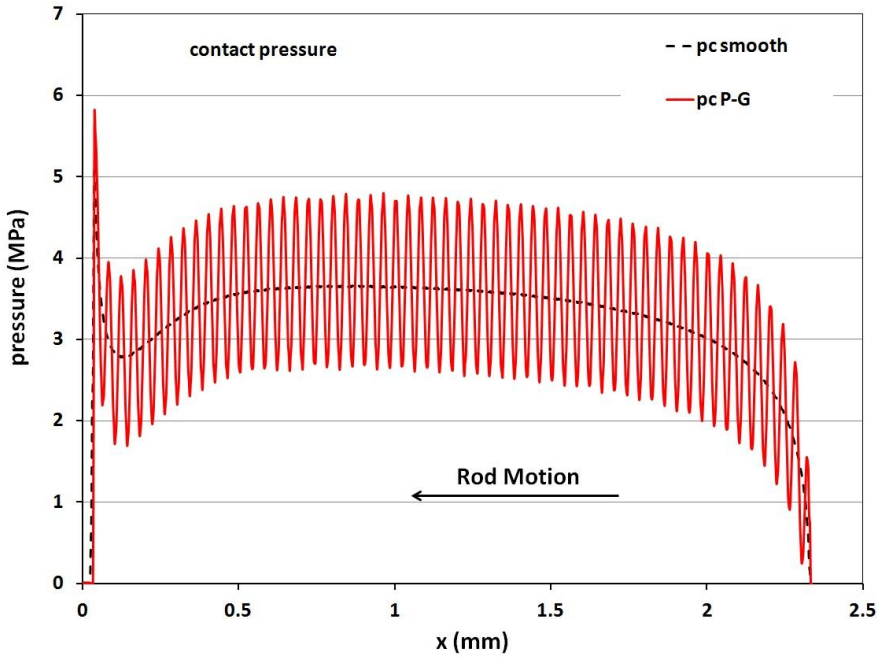

Figure 5.7b1: Contact pressures of instroke, 0.15 m/s, U-cup seal, σ=0.8μm, flooded

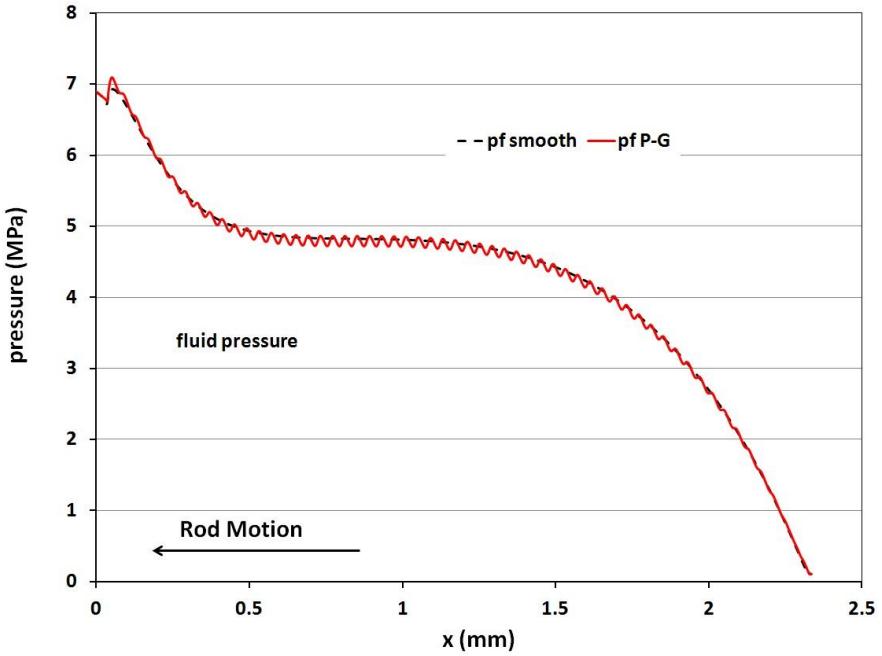

Figure 5.7b2: Fluid pressure of instroke, 0.15 m/s, U-cup seal, σ=0.8μm, flooded

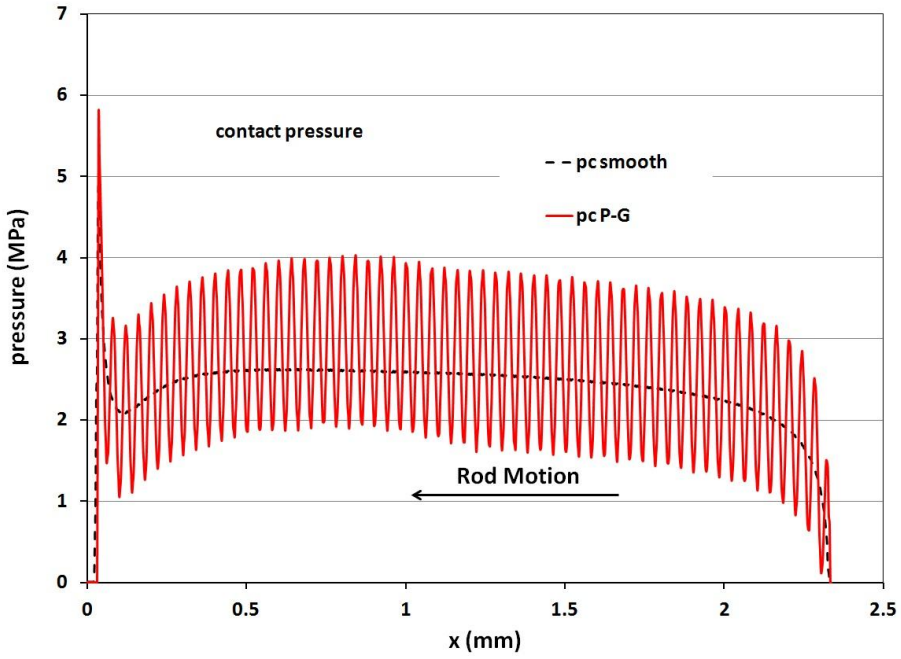

Figure 5.7c1: Contact pressures of instroke, 0.30 m/s, U-cup seal, σ=0.8μm, flooded

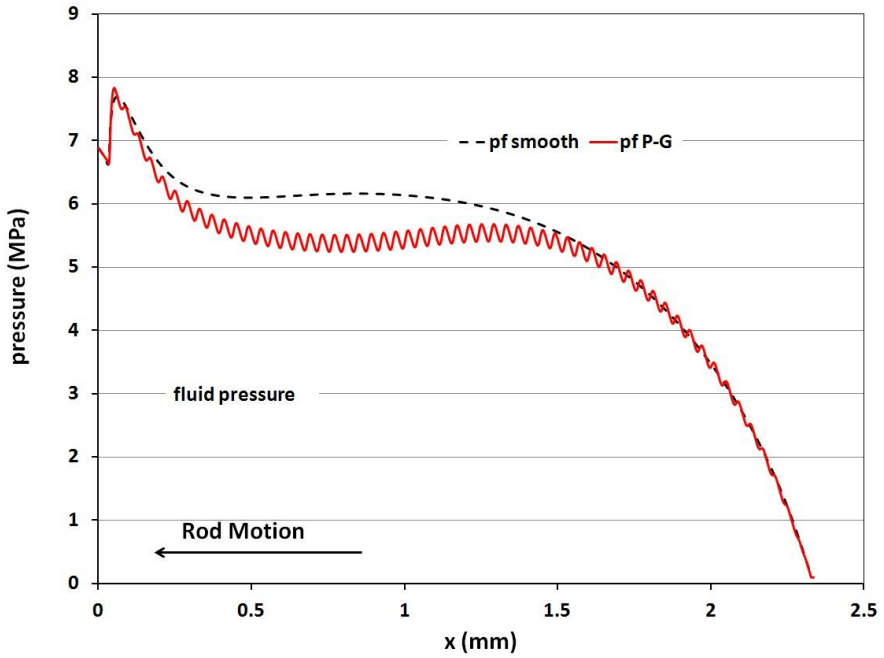

Figure 5.7c1: Fluid pressures of instroke, 0.30 m/s, U-cup seal, σ=0.8μm, flooded

Based on the above results, the fluid transport behavior with the plunge-ground rod can now be explained. During the outstroke the sealed pressure is ambient, so the fluid transport is solely produced by Couette flow for both smooth rod and plunge-ground rod. For such flow, the fluid transport depends only on the stroke length (which is fixed) and the film thickness. Since the average of the film thickness with the plunge-ground rod is almost identical to the film thickness with the smooth rod, the plunge-ground finish has no significant effect on the fluid transport during outstroke, compared to the smooth rod.

During the instroke, the film thickness increases with speed, causing the fluid transport to increase with speed. The plunge-ground rod produces a lower fluid transport than the smooth rod because of differences in film thickness. While the

average of the plunge-ground rod oscillating film thickness is almost identical to the smooth rod film thickness, the average of the plunge-ground rod oscillating film thickness cubed is larger than the cube of the smooth rod film thickness. This produces an increase in the Poiseulle flow (out of the cylinder), resulting in a decreased fluid transport with the plunge-ground rod.

The friction force results can be explained by considering the contact force and the film thickness, similar to the discussion in the previous chapter for the smooth cases. During the outstroke, the friction force is relatively independent of rod speed and surface finish because both the average contact force and average film thickness for the plunge-ground case are relatively independent of rod speed and surface finish since the film is largely cavitated. During the instroke, except at the lowest speeds, the friction force decreases with speed because the contact force decreases with speed. The friction force with the plunge-ground rod is larger than that with the smooth rod because the contact force with the plunge-ground rod is larger than that with the smooth rod. Comparing the fluid pressure distributions of the plunge-ground rod and smooth rod, it can be seen that the fluid pressures generated by the plunge-ground surface are lower than that of the smooth case at high speed; there is less fluid pressure support of the plunge-ground rod than that of the smooth rod. That is the reason why the contact force with the plunge-ground rod is larger than that with the smooth rod.

5.3.3 Leakage and Friction with Starved Boundary Conditions

The plunge-ground rod cases with starved boundary conditions are simulated and compared with the smooth rod results with starved boundary conditions, below.

The fluid transport of the outstroke and the instroke of the U-cup seal with starved boundary conditions, as a function of rod speed, are shown in Figure 5.8 for both the plunge-ground surface finish and for the smooth rod. The results for the smooth cases with starvation have been discussed in chapter 4. The outstroke transport behavior is just the same as in the flooded cases shown in the previous section, because there is no starvation during the outstroke. During the instroke under starved boundary conditions, the critical speed of the plunge-ground rod is very close to that of the smooth rod, but slightly higher. Once the rod speed exceeds the critical speed, the instroke fluid transport equals that of the outstroke, and therefore the fluid transport of the plunge-ground rod and the smooth rod are almost the same. The plunge-ground rod has no effect on the fluid transport during the instroke, as well.

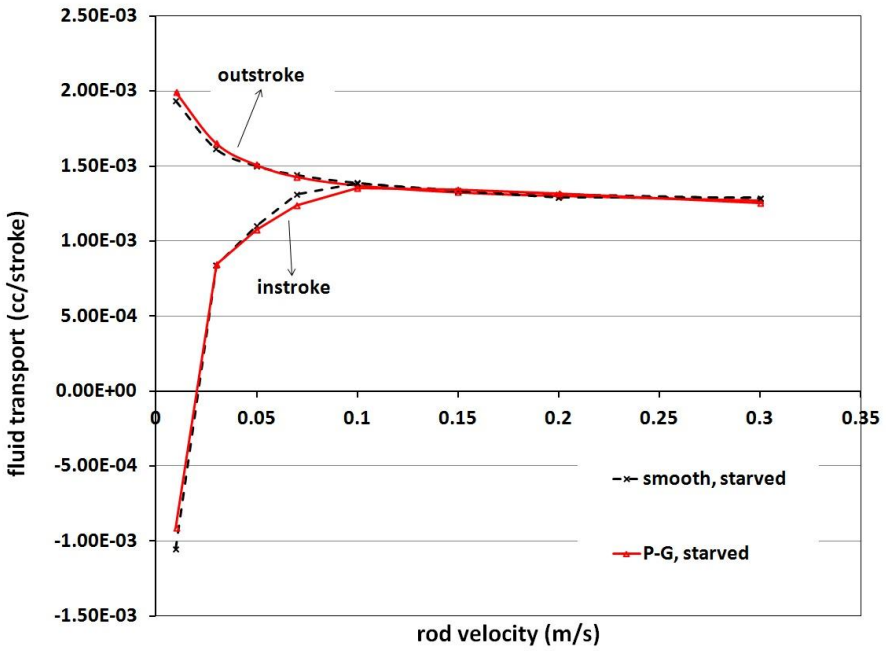

Figure 5.8: Fluid transport, U-cup seal, starved, σ=0.8μm

The friction force on the rod, as a function of rod speed, is shown in Figure 5.9. During the outstroke, the friction force behavior for both the smooth rod and plunge-ground rod are exactly the same as the flooded cases. During the instroke, the friction force behavior of the plunge-ground rod is similar to that of the smooth rod with starved boundary conditions, which has been discussed in the previous chapter. However, the plunge-ground rod decreases the friction force during the instroke when starvation occurs (the rod speed exceeds the critical speed). This is unlike the flooded boundary results where the plunge-ground rod increases the friction force during the instroke. In Papatheodorou's research [4], an additional increase in friction force is found as a result of the continual smoothing of the rod surface due to wear, which agrees with the results under the starved boundary condition in this research.

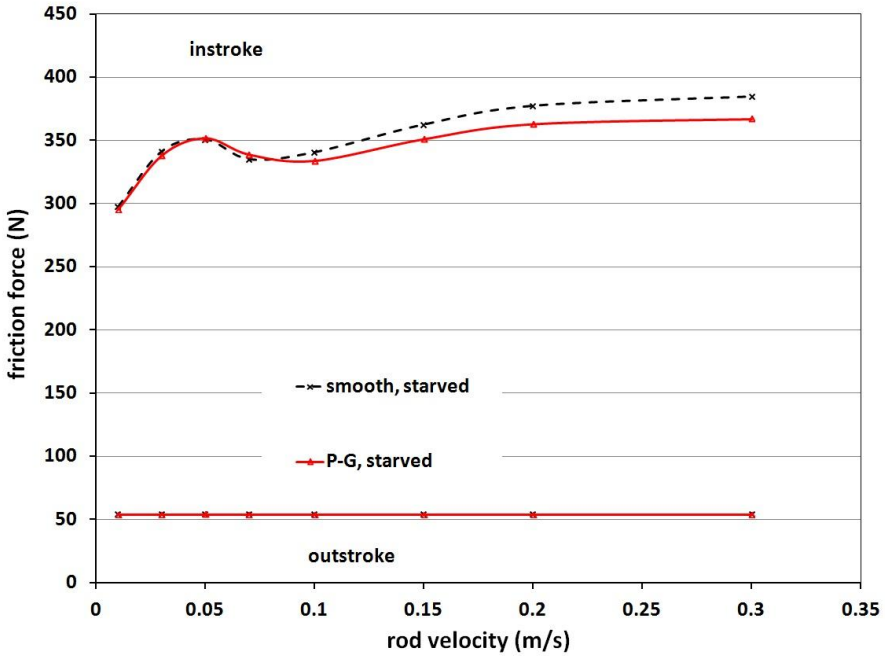

Figure 5.9: Friction force, U-cup seal, starved, σ=0.8μm

To explain the difference between the starved and flooded results, the details of the sealing zone is examined. Since the outstroke cases for both the plunge-ground rod and the smooth rod with the starved boundary are exactly the same as those with the flooded boundary, only the film thickness distribution and the fluid and contact pressure distributions during the instroke are presented and discussed.

5.3.3 Details of Sealing for Starved Boundary Conditions

The film thickness distributions during the instroke at rod speeds of 0.05 m/s, 0.15 m/s and 0.3 m/s are shown in Figures 5.10a, 5.10b and 5.10c, respectively. At the rod speed of 0.05 m/s, which is lower than the critical speed, no starvation occurs for both the plunge-ground rod and the smooth rod. Figure 5.10a is exactly the same as

Figure 5.5a, with the flooded boundary. With the starved boundary condition, the shape of the fluid film profile changes with rod speed, but the thickness does not change significantly for both the smooth rod and plunge-ground rod. With the rod speed increasing, the pressurized region (to the left of the starved boundary) decreases slightly. In addition, the pressurized region for the plunge-ground rod is longer than that for the smooth rod. At the same speed, the fluid film with the smooth rod is slightly thinner than the average film thickness of the plunge-ground cases; this is more significant at the high speed (0.30 m/s).

The comparison between the flooded cases and starved cases (Figure 5.5b vs. Figure 5.10b, and Figure 5.5c vs. Figure 5.10c) shows that for the same rod speed, the reduction in the length of the pressurized fluid film caused by starvation is less with the plunge-ground rod, than with the smooth rod. This can be explained by considering the fluid transport behaviors under flooded conditions (Figure 5.2). The degree of starvation is defined as the difference between the instroke fluid transport and the outstroke fluid transport when the rod speed is higher than the critical speed. The higher this degree of starvation is, the higher is the hypothetical net fluid carried into the cylinder under the flooded boundary condition. With the starved boundary condition, in order to match the outstroke fluid transport, the instroke fluid flow will be starved. The degree of starvation measures the required reduction in the instroke fluid transport in order for the instroke transport to equal the outstroke transport. The reduction is achieved through starvation. So the higher this degree of starvation is, the more starvation will occur during the instroke. In Figure 5.2, it can be observed that

the plunge-ground rod has a lower degree of starvation compared to that of the smooth rod. This indicates that under the starved boundary condition, the plunge-ground rod has a smaller region of starvation compared to that of the smooth rod, which is shown in the fluid film thickness distribution plots below:

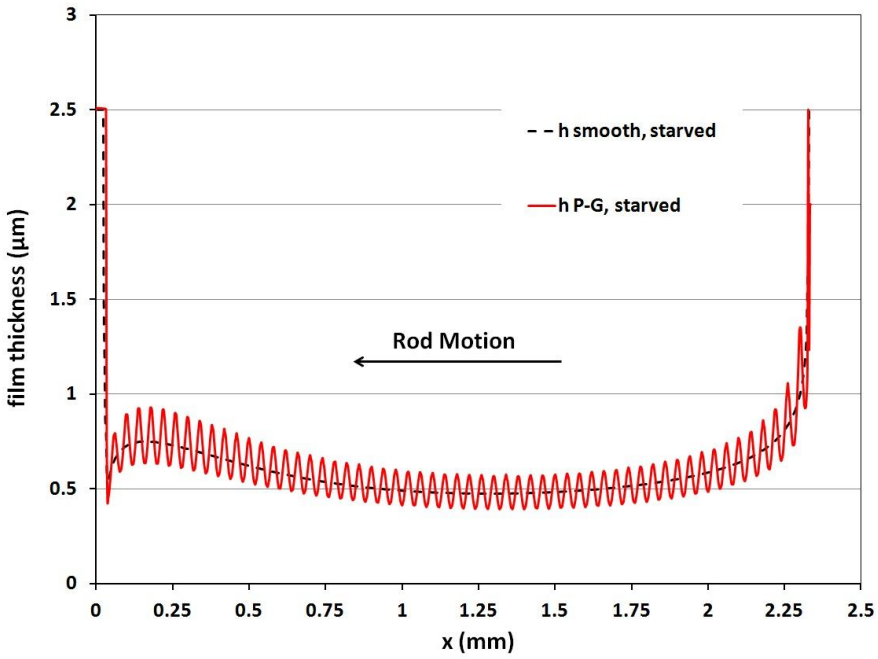

Figure 5.10a: Film thickness of instroke, 0.05 m/s, U-cup seal, σ=0.8µm, starved

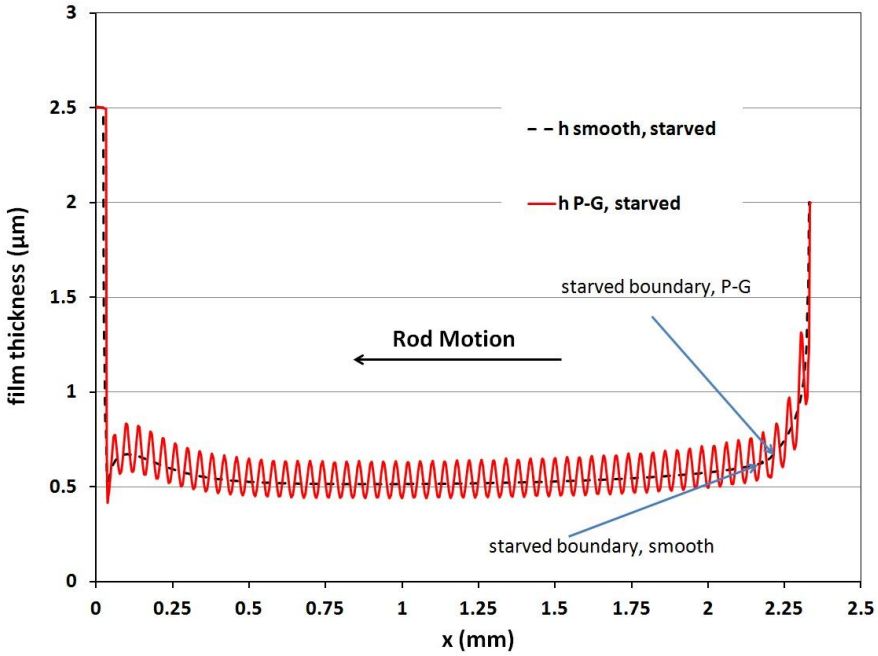

Figure 5.10b: Film thickness of instroke, 0.15 m/s, U-cup seal, σ=0.8µm, starved

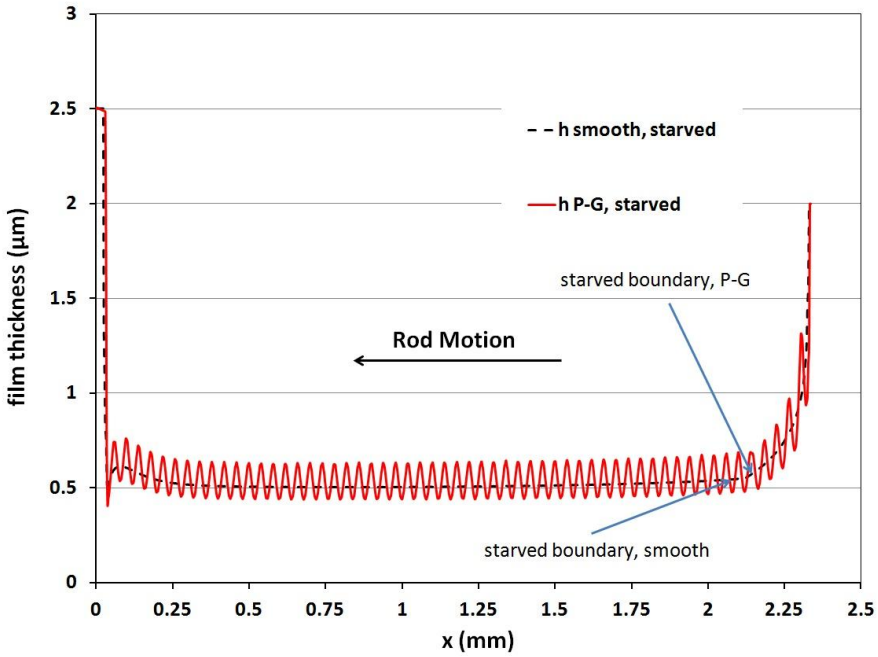

Figure 5.10c: Film thickness of instroke, 0.30 m/s, U-cup seal, σ=0.8µm, starved

Figures 5.11a1, 5.11a2, 5.11b1 and 5.11b2 show the contact pressure and fluid pressure distributions during the instroke at rod speeds of 0.15 m/s and 0.30 m/s, under the starved boundary. The pressure distributions during the instroke at the rod speed of 0.05 m/s are exactly the same as Figures 5.7a1 and 5.7a2 and are not shown here, because no starvation occurs at this rod speed. At the 0.15 m/s speed, the average of the oscillating contact pressure with the plunge-ground rod is lower than that with the smooth rod. The fluid pressure is higher than that with the smooth rod and contains oscillations. At the 0.3 m/s speed, the average of the contact pressure with the plunge-ground rod is lower than that with the smooth rod, as well, while the fluid pressure with the plunge-ground rod is higher than that with the smooth rod and contains more significant oscillations. These contact pressure and fluid pressure results are consistent with each other and are consistent with the film thickness distributions during instroke, discussed above.

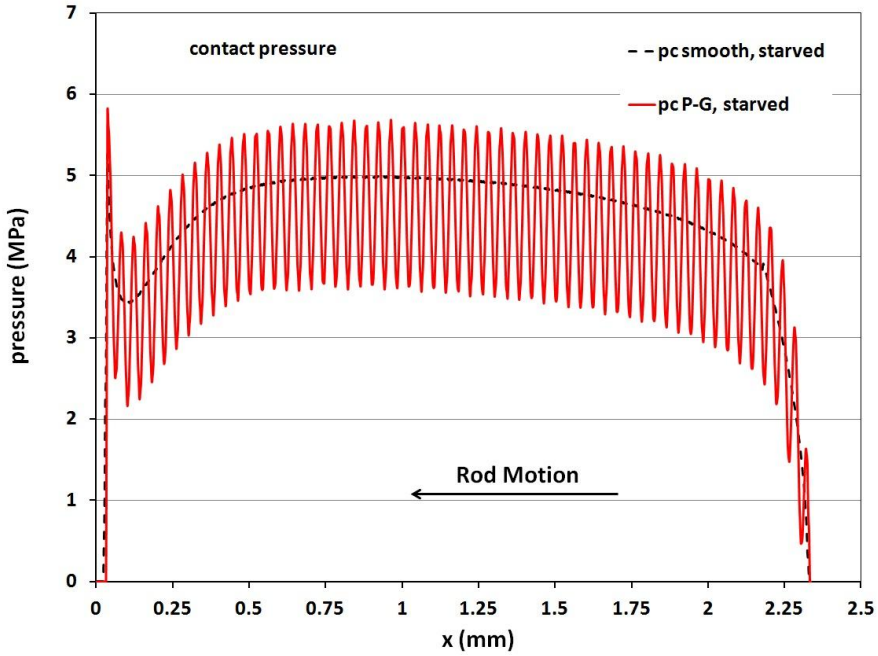

Figure 5.11a1: Contact pressures of instroke, 0.15 m/s, U-cup seal, σ=0.8μm, starved

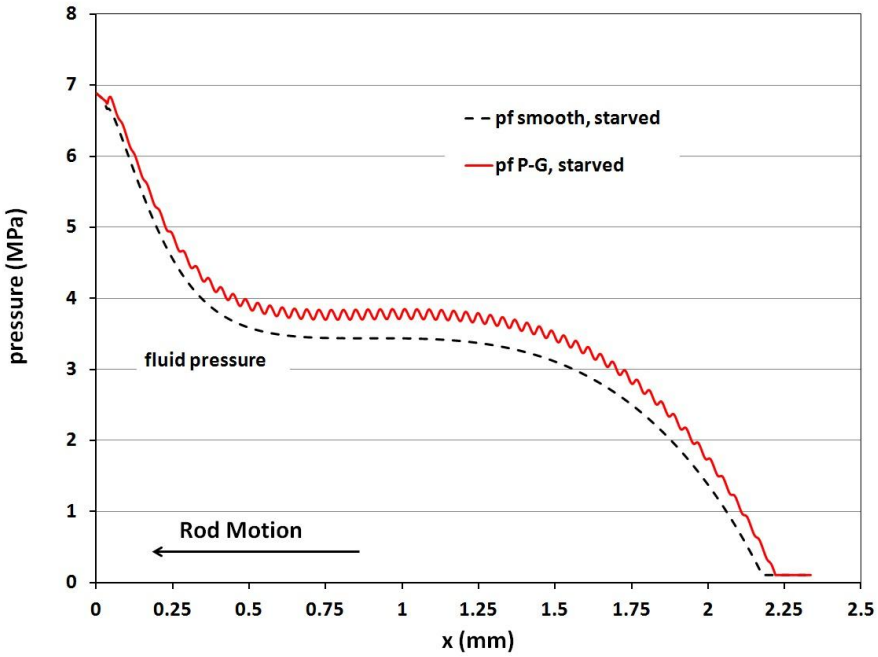

Figure 5.11a2: Fluid pressures of instroke, 0.15 m/s, U-cup seal, σ=0.8μm, starved

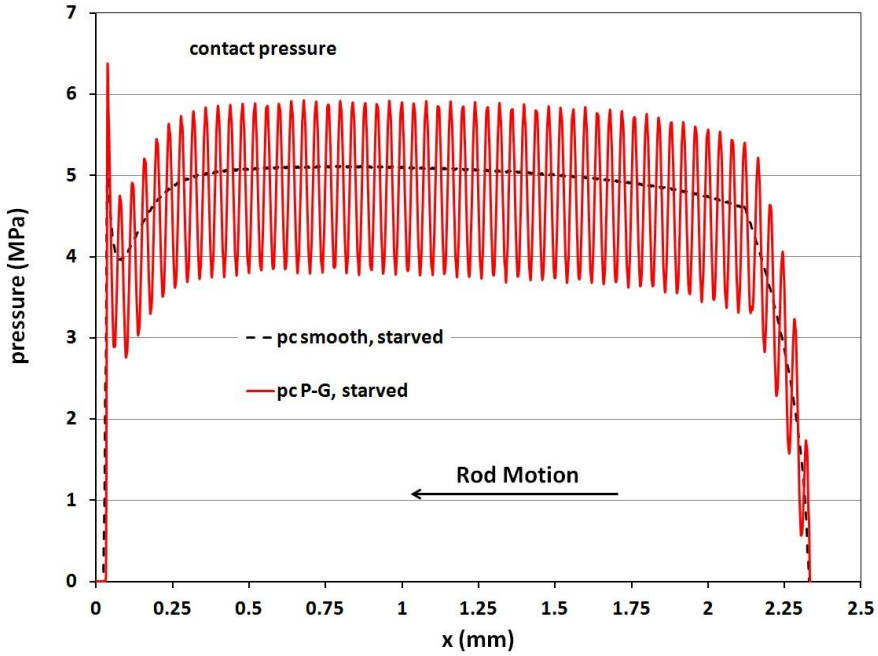

Figure 5.11b1: Contact pressures of instroke, 0.30 m/s, U-cup seal, σ=0.8μm, starved

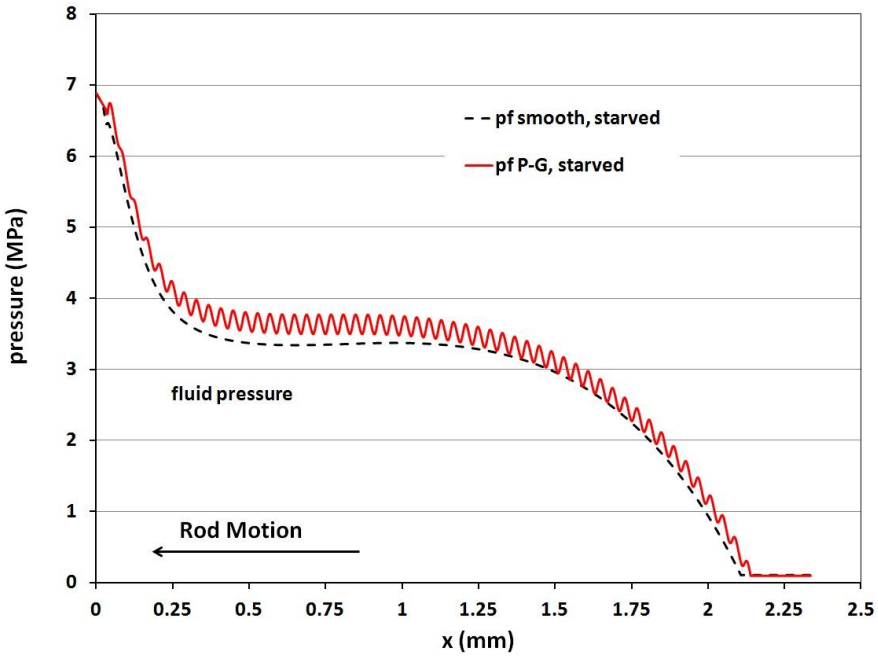

Figure 5.11b2: Fluid pressures of instroke, 0.30 m/s, U-cup seal, σ=0.8μm, starved

These results show that the effect of the plunge-ground rod surface on the contact pressure and fluid pressure under starved boundary conditions are opposite to that with flooded boundary conditions. Under starved boundary conditions, the plunge-ground rod surface decreases the contact pressure and increases fluid pressure, while under flooded boundary conditions, the plunge-ground rod surface increases the contact pressure and decreases the fluid pressure. This can be explained by the film thickness distribution. As discussed above, the starvation causes a thicker average fluid film for the plunge-ground rod, and therefore the average contact pressure for the plunge-ground rod is lower than that of the smooth rod. In addition, the length of the pressurized region is longer for the plunge-ground rod than that of the smooth rod, so that a higher average fluid pressure distribution occurs with the plunge-ground rod.

Summarizing, under the flooded boundary conditions, the plunge-ground rod generates lower fluid pressures compared to the smooth rod, especially at the high speed. This causes a higher contact force and a higher friction force at the same speed compared to the smooth rod.

Under the starved boundary conditions, the lower degree of starvation of the plunge-ground rod results in a smaller starvation area compared to the smooth rod, which means a larger fluid pressurized region for the plunge-ground rod cases. The plunge-ground rod generates larger fluid pressures which support the seal, decreasing the contact pressure, compared to the smooth rod. This causes a lower friction force at the same speed compared to the smooth rod.

5.4 Step Seal

5.4.1 Leakage and Friction

Figure 5.12 shows the fluid transport during outstroke and instroke as a function of rod speed for the plunge-ground and smooth rod finishes. Compared to the U-cup seal, the transports are much larger.

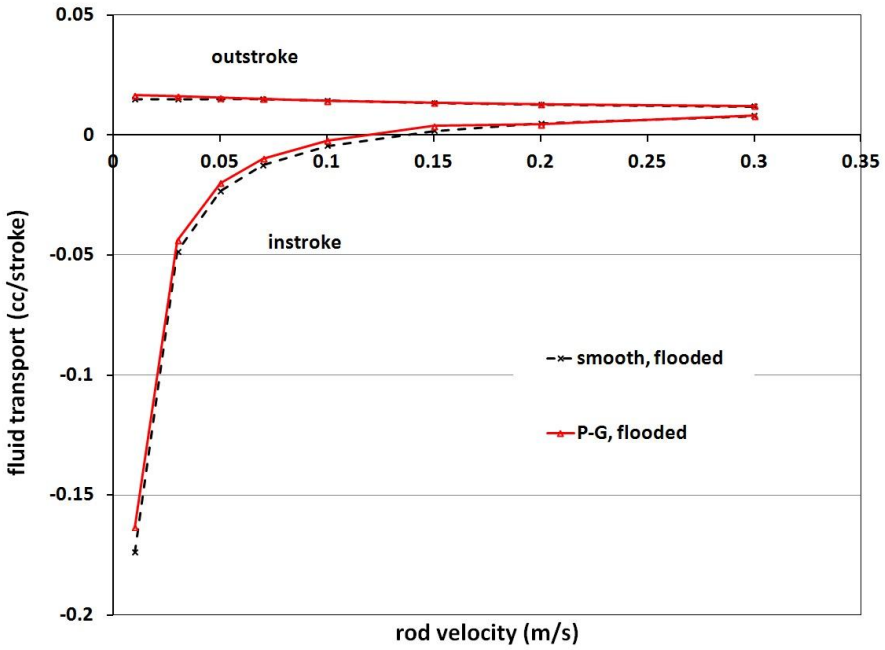

Figure 5.12: Fluid transport, step seal, σ=4.0 μm

The transport behavior for the smooth rod has been discussed in the previous chapter. Note that the critical speed where the outstroke and instroke transports are equal, occurs beyond the range covered in this research. Therefore, the step seal only

has flooded boundary cases. The curves for the plunge-ground and smooth rods generally lie on top of each other, indicating that the plunge-ground rod produces no significant effect on the fluid transport, compared with the smooth rod.

The friction force on the rod, as a function of rod speed is shown in Figure 5.13 for both smooth and plunge-ground rods. The friction force behavior of the smooth rod has been discussed in the previous chapter as well. The plunge-ground rod has no effect on the friction force compared to the smooth rod for both outstroke and instroke.

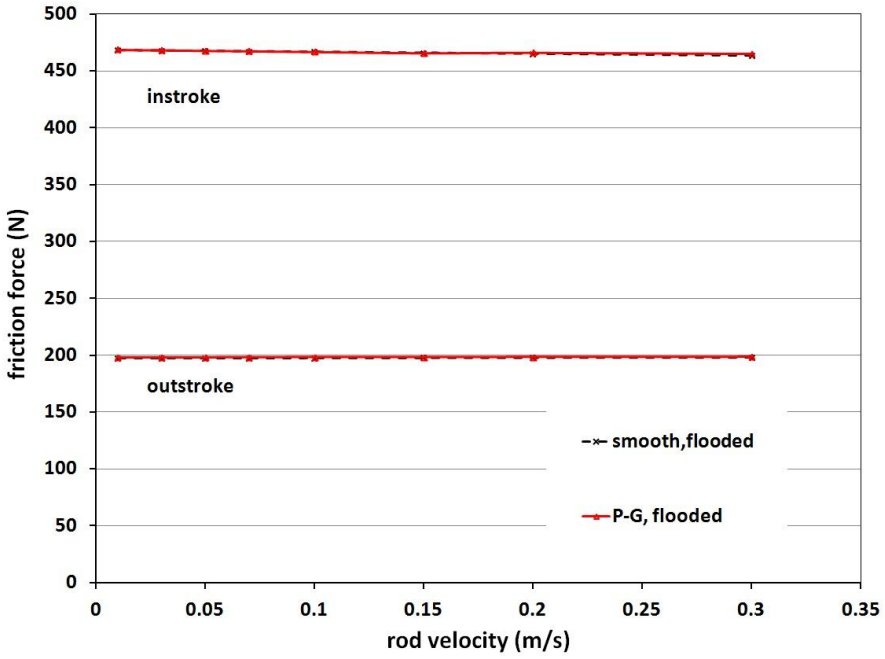

Figure 5.13: Friction force, step seal, σ=4.0 μm

5.4.2 Details of Sealing

As in the previous chapter and sections, some insight into the behavior described above can be obtained by examining the details of the sealing area.

Figure 5.14a and 5.14b show the film thickness distribution during the outstroke at a rod speed of 0.05 m/s and 0.3 m/s. These two distributions are almost identical, indicating that the film thickness is relatively independent of rod speed during the outstroke, as is the case with the U-cup seal and for the same reason. Furthermore, the average of the oscillating film thickness with the plunge-ground rod is almost identical to the film thickness with the smooth rod, also similar to the U-cup seal. It is important to note the much larger film thickness with the step seal, which has been mentioned in previous chapter where the step seal with the smooth rod is discussed. The film is almost completely supported by the asperities on the seal surface for both the smooth and plunge-ground rods, as is evidenced by the contact and fluid pressure distributions.

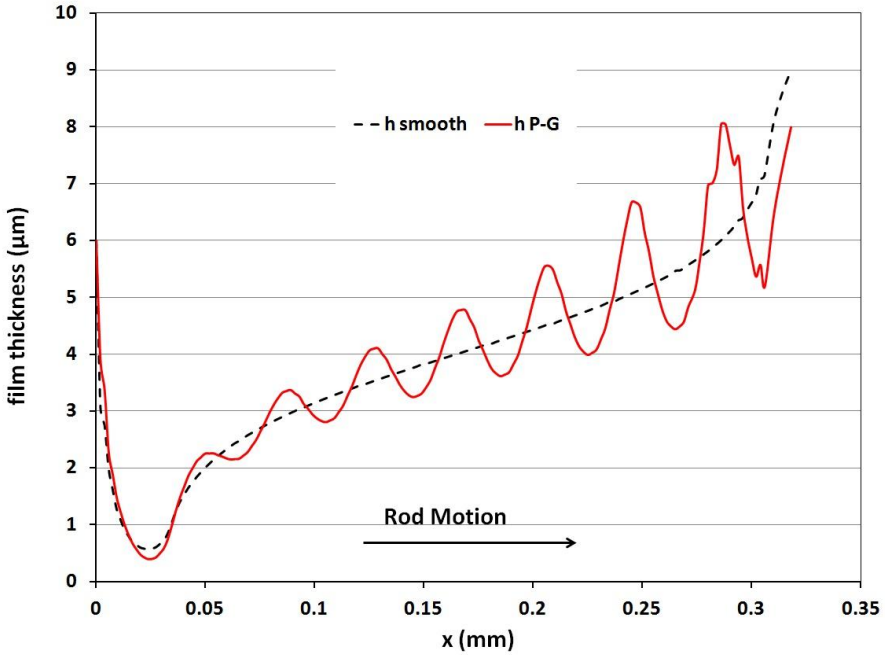

Figure 5.14a: Film thickness of outstroke, 0.05 m/s, step seal, σ=4.0 µm

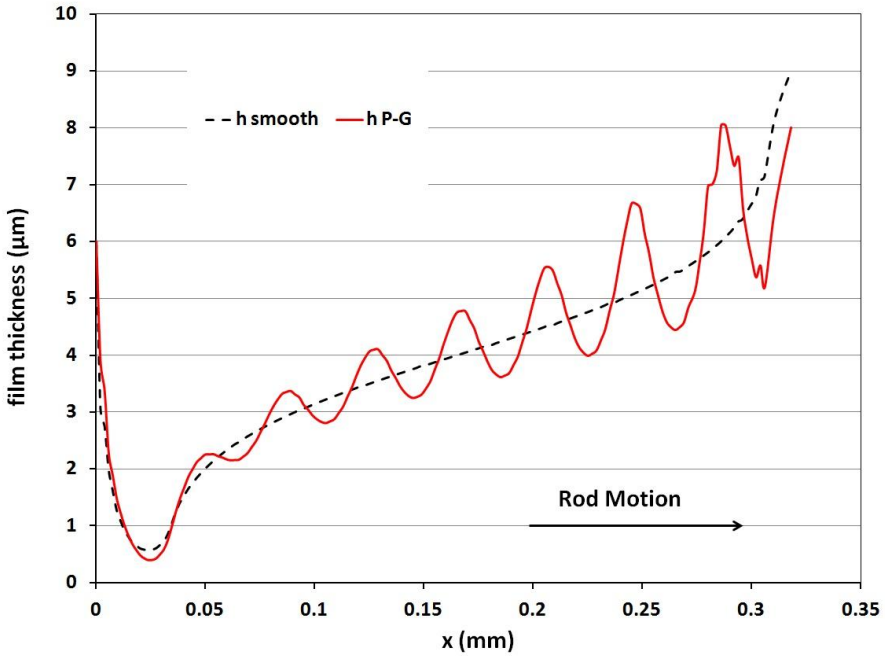

Figure 5.14b: Film thickness of outstroke, 0.30 m/s, step seal, σ=4.0 µm

The film thickness distribution during the instroke at a rod speed of 0.05 m/s and 0.3 m/s are shown in Figure 5.15a and 5.15b. These two distributions are almost identical, just like the outstroke, indicating that the film thickness is also relatively independent of rod speed during the instroke. This lack of hydrodynamic effect differs from the U-cup case and results from the much higher contact pressures, which has been discussed in the previous chapter for the smooth rod. The average of the oscillating film thickness with the plunge-ground rod is almost identical to the film thickness with the smooth rod, similar to the behavior of the U-cup seal.

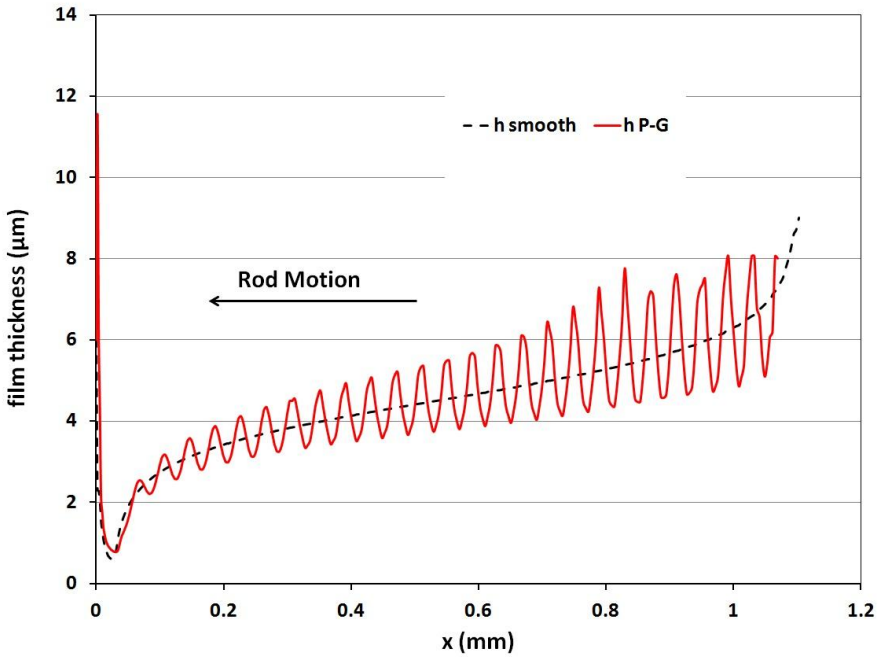

Figure 5.15a: Film thickness of instroke, 0.05 m/s, step seal, σ=4.0 μm

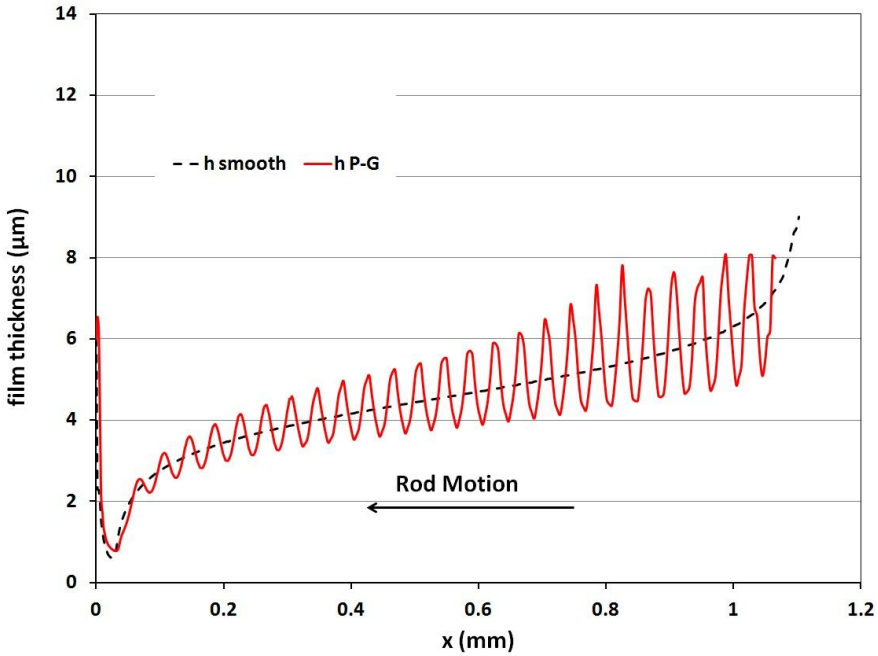

Figure 5.15b: Film thickness of instroke, 0.30 m/s, step seal, σ=4.0 μm

Figure 5.16a and 5.16b show the contact pressure and fluid pressure distributions during the outstroke at the rod speeds of 0.05 m/s and 0.3 m/s. The two distributions are almost identical, as in the case with the U-cup seal and for the same reason. The very high contact pressures, compared to the U-cup seal, are due to the much higher value of the elastic modulus of PTFE compared to polyurethane. This has been discussed earlier. As with the U-cup seal, the plunge ground rod produces large oscillations in the contact pressure. The fluid pressure distribution indicates minimal hydrodynamic action. These results are consistent with the film thickness distributions during the outstroke, discussed above, and similar to the results with the U-cup seal except for the high contact pressures.

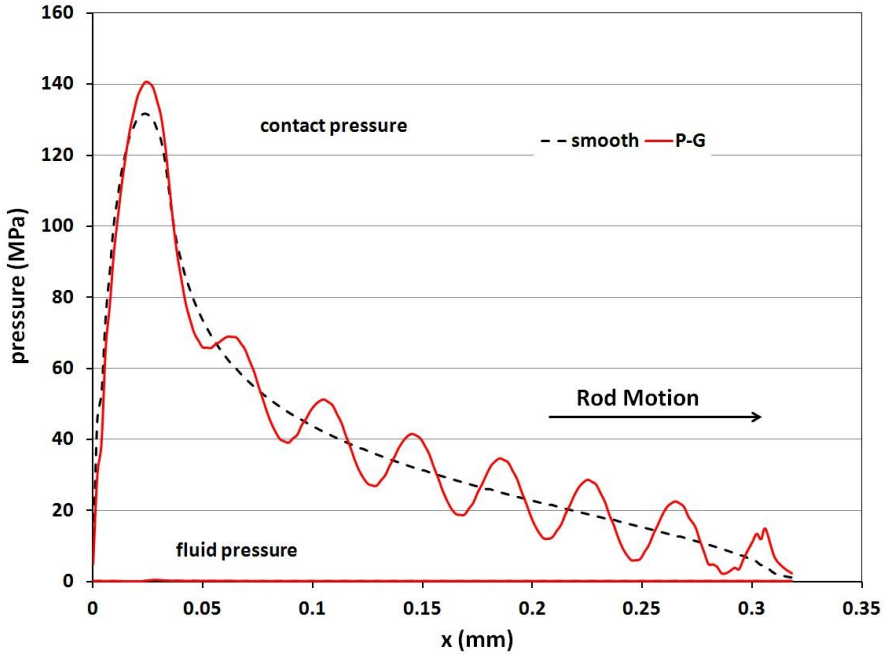

Figure 5.16a: Contact and fluid pressures of outstroke, 0.05 m/s, step seal, σ=4.0 μm

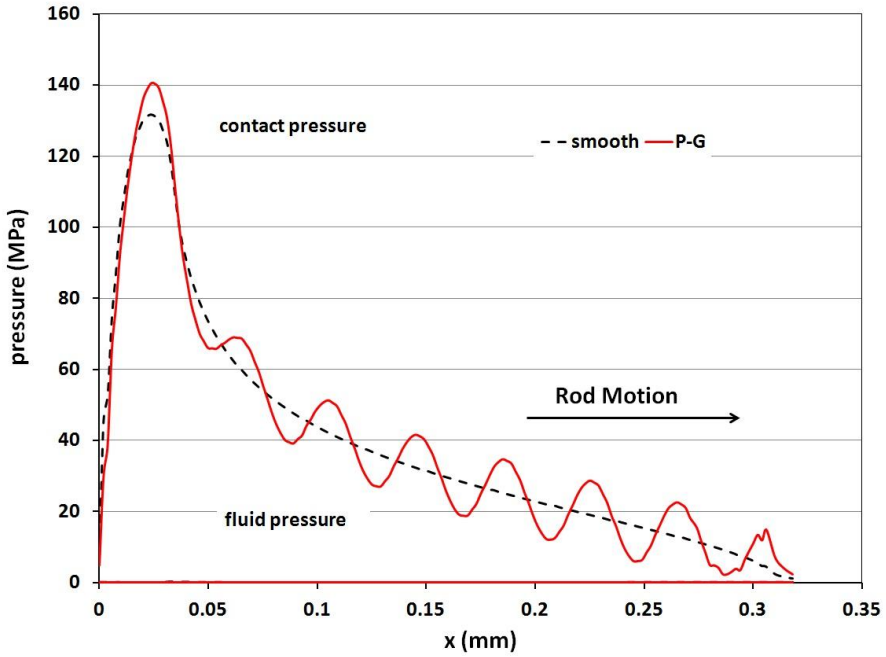

Figure 5.16b: Contact and fluid pressures of outstroke, 0.30 m/s, step seal, σ=4.0 μm

Figure 5.17a and 5.17b show the contact pressure and fluid pressure distributions during the instroke at rod speeds of 0.05 m/s and 0.3 m/s. The two distributions are almost identical, indicating that the contact and fluid pressure distributions are relatively independent of rod speed during the instroke, unlike the U-cup seal case. The smooth rod case has been discussed in the previous chapter. The very high contact pressures compared to the fluid pressures show that there are no significant hydrodynamic effects, with the film almost completely supported by the seal surface asperities. For both the 0.05 m/s and 0.3 m/s speeds, the average of the oscillating contact pressure with the plunge-ground rod is almost identical to that of the smooth rod, and the fluid pressures are also almost identical. This is in contrast to the behavior with the U-cup seal at 0.3 m/s, where the plunge-ground rod and smooth rod show differences. These contact pressure and fluid pressure results are consistent with each other and are consistent with the film thickness distributions during the instroke.

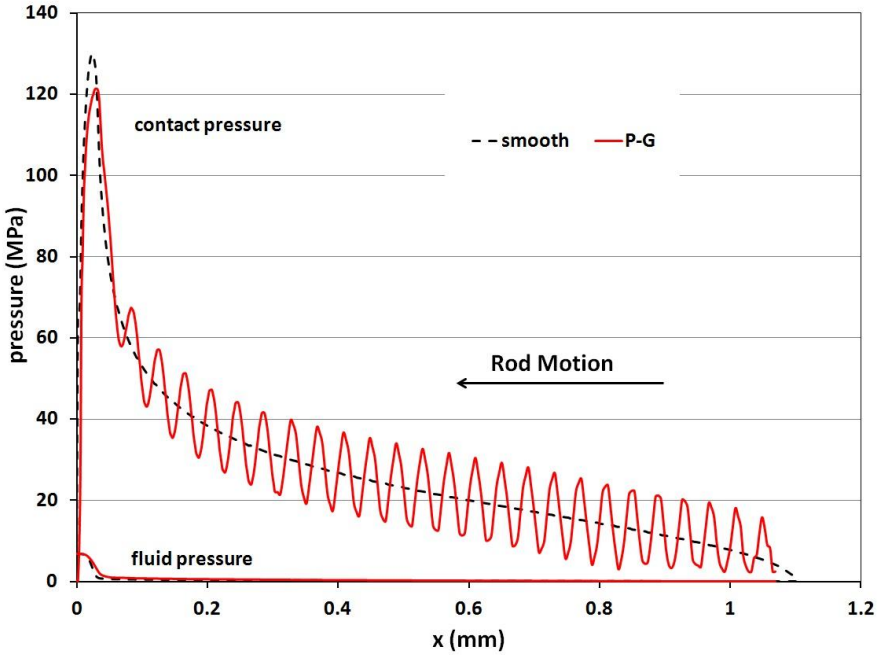

Figure 5.17a: Contact and fluid pressures of instroke, 0.05 m/s, step seal, σ=4.0 µm

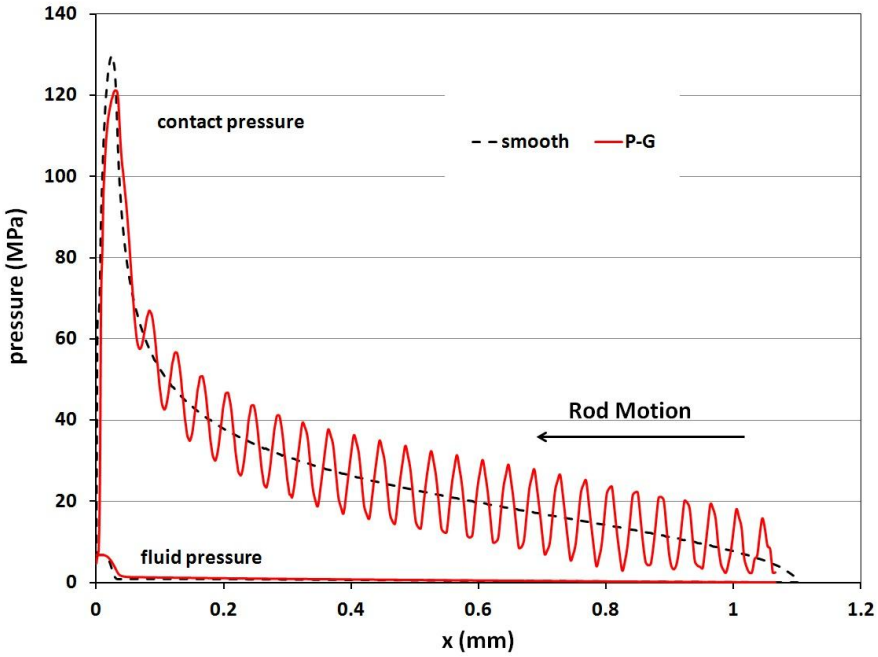

Figure 5.17b: Contact and fluid pressures of instroke, 0.30 m/s, step seal, σ=4.0 µm

The differences in the gross characteristics of the step seal compared to the U-cup seal for the smooth rod have been explained in the previous chapter. The thicker fluid films of the step seal reduce the difference in hydrodynamic pressure generation between the plunge-ground rod and the smooth rod cases, resulting in virtually the same fluid pressure distribution and the same average (in the plunge-ground rod case) film thickness and contact pressure distributions for the two types of rods. This explains why the plunge-ground rod produces no significant effects on the fluid transport and friction force compared to the smooth rod. The friction force with the step seal is larger than that with the U-cup seal due to the higher contact pressures.

5.5 Hypothetical U-cup and Step Seals

In order to further investigate the reasons for the differences in the behaviors of the U-cup and step seals, simulations of a step seal with a roughness of 0.8 μm (the same roughness as the original U-cup seal, discussed above) and of a U-cup seal with a roughness of 4.0 μm (the same roughness as the original step seal, discussed above), have been performed, under the flooded boundary conditions.

5.5.1 Leakage and Friction

Figure 5.18 shows the fluid transport vs. rod velocity for the step seal with a roughness of 0.8 μm. Unlike the 4.0 μm roughness case, this plot shows that during the instroke the plunge-ground rod produces a lower fluid transport compared to the smooth rod, just like the U-cup seal with a 0.8 μm roughness under flooded boundary conditions. The plot also shows a much lower critical speed than the 4.0 μm

roughness case, again similar to the U-cup seal with a 0.8 µm roughness under flooded boundary. However, the general shape of the outstroke transport curve is similar to that for the step seal with a 4.0 µm roughness, in that the transport levels off at the higher speeds.

The friction force vs. rod velocity for the step seal with a roughness of 0.8 µm is shown in Figure 5.19. This shows a higher friction force with the plunge-ground rod than with the smooth rod, during the instroke, similar to the U-cup seal with a 0.8 µm roughness under flooded boundary conditions. The decreasing instroke friction force with rod speed is also similar to the 0.8 µm roughness U-cup seal behavior at the higher speeds, under flooded boundary conditions.

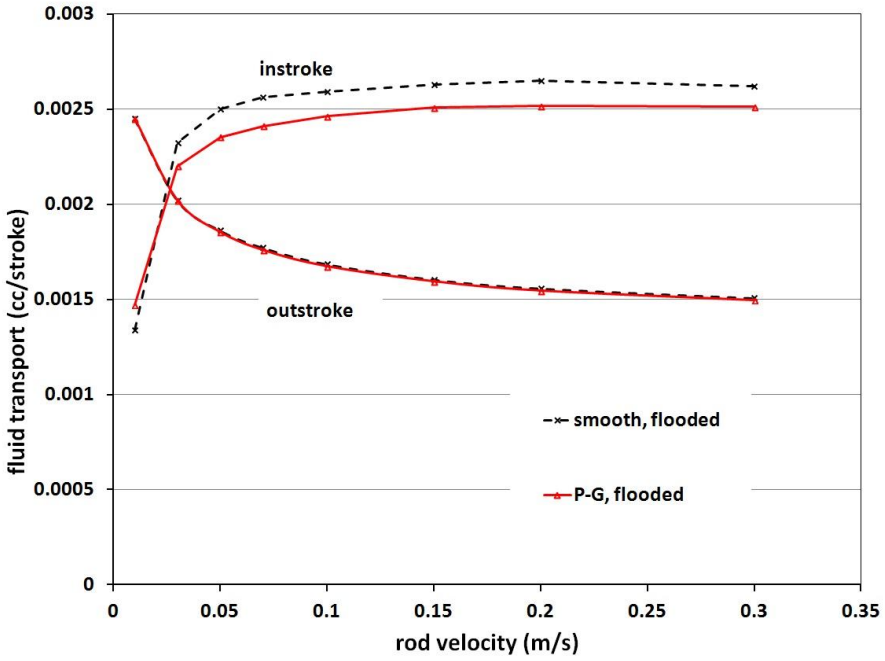

Figure 5.18: Fluid transport, step seal, σ=0.8 µm

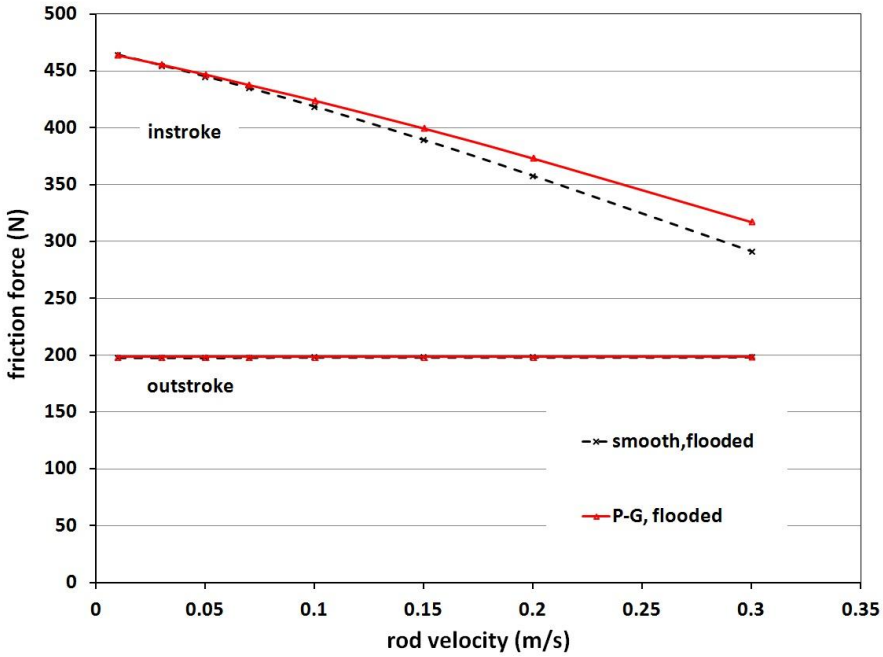

Figure 5.19: Friction force, step seal, σ=0.8 µm

Figure 5.20 shows the fluid transport vs. rod velocity for the U-cup seal with a roughness of 4.0 µm. Unlike the 0.8 µm roughness case, this plot shows that during the instroke the plunge-ground rod produces substantially the same fluid transport as the smooth rod, just like the step seal with a 4.0 µm roughness. The plot also shows a much higher critical speed than the 0.8 µm roughness case, again similar to the step seal with a 4.0 µm roughness. The general shape of the outstroke transport curve is similar to that for the step seal with a 4.0 µm roughness, in that the transport levels off at the higher speeds.

The friction force vs. rod velocity for the U-cup seal with a roughness of 4.0 µm is shown in Figure 5.21. This shows substantially the same friction force with the plunge-ground rod as with the smooth rod, during the instroke, similar to the step seal

with a 4.0 µm roughness. The instroke friction force increases slightly with rod speed, unlike the 0.8 µm roughness U-cup and somewhat closer to the behavior of the 4.0 µm roughness step seal, but there is a small hydrodynamic effect.

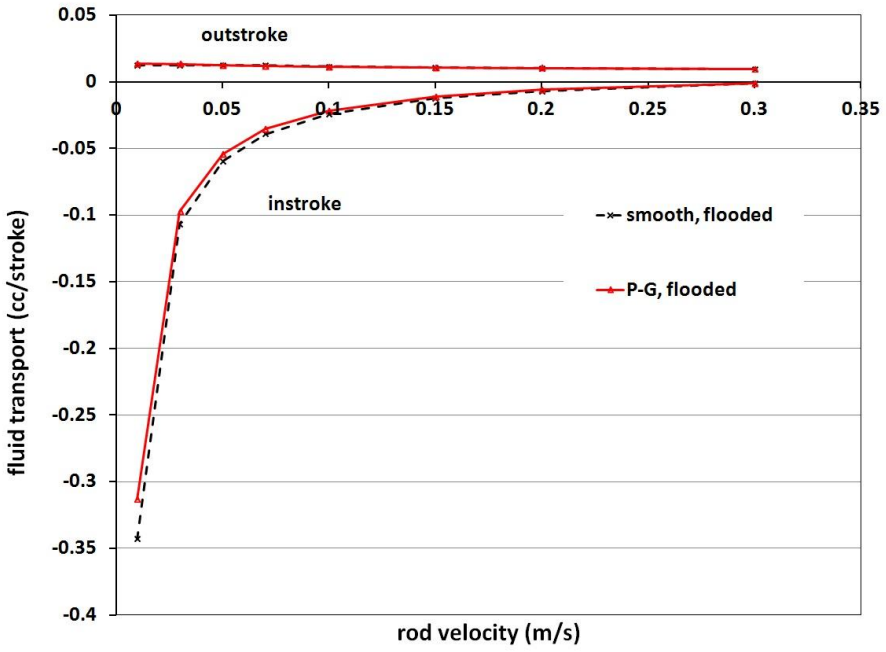

Figure 5.20: Fluid transport, U-cup seal, σ=4.0 µm

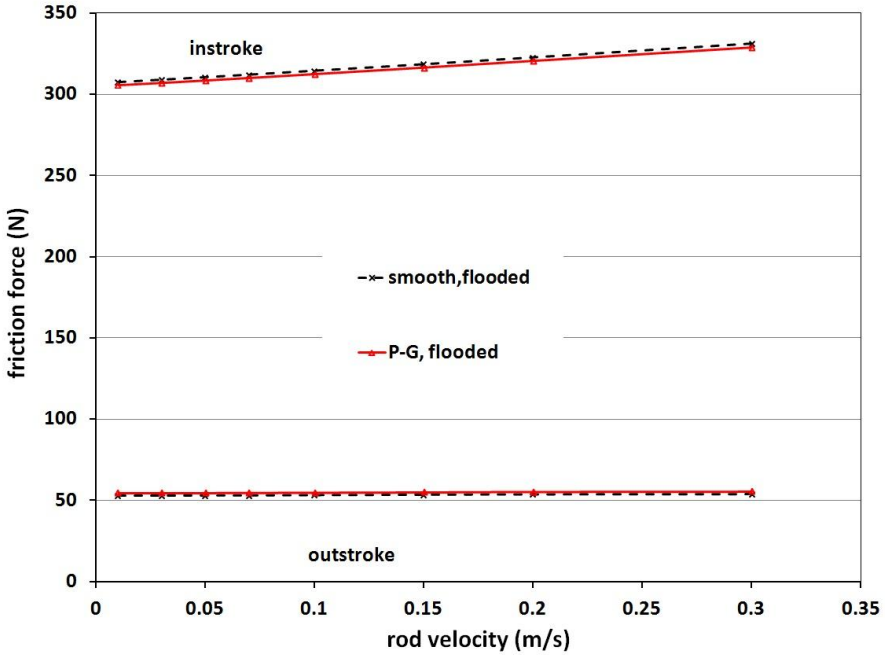

Figure 5.21: Friction force, U-cup seal, σ=4.0 μm

5.5.2 Details of Sealing

For both hypothetical U-cup and step seals, the fluid transport and friction force behaviors during the outstroke are similar to that of the original cases: the fluid transport and friction force are independent of rod speed; the plunge-ground rod has no effect on both fluid transport and friction force. Therefore, only the details of the sealing zone during the instroke are shown below.

Figure 5.22a and 5.22b shows the film thickness distributions of the hypothetical step seal (σ=0.8 μm) during the instroke at rod speeds of 0.05 m/s and 0.3 m/s. Just like the U-cup seal with a 0.8 μm roughness under flooded boundary conditions, the higher rod speeds produce thicker fluid films during the instroke, under flooded

boundary conditions. It is also seen that the average of the oscillating film thickness with the plunge-ground rod is close to the film thickness with the smooth rod.

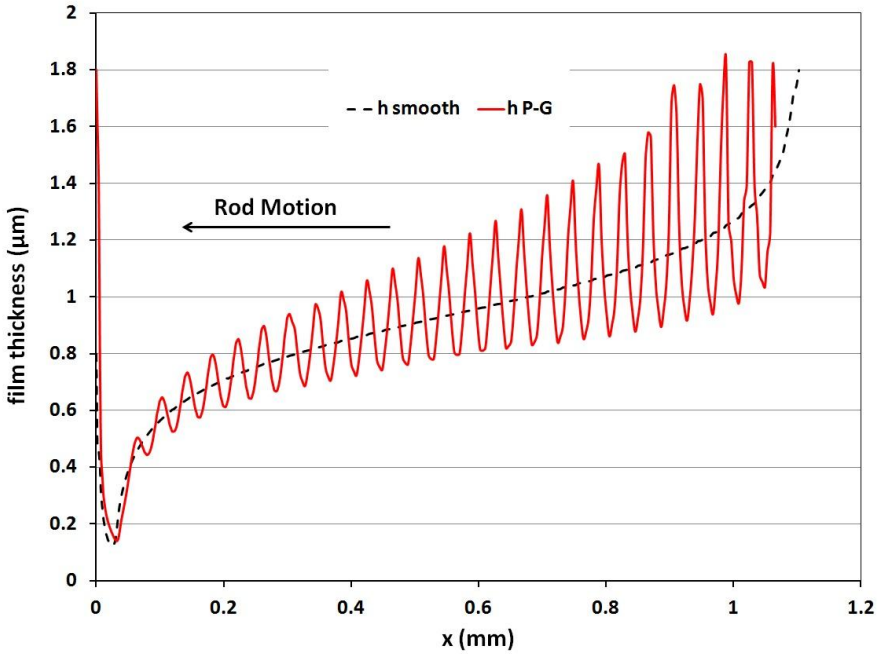

Figure 5.22a: Film thickness of instroke, 0.05 m/s, step seal, σ=0.8 μm

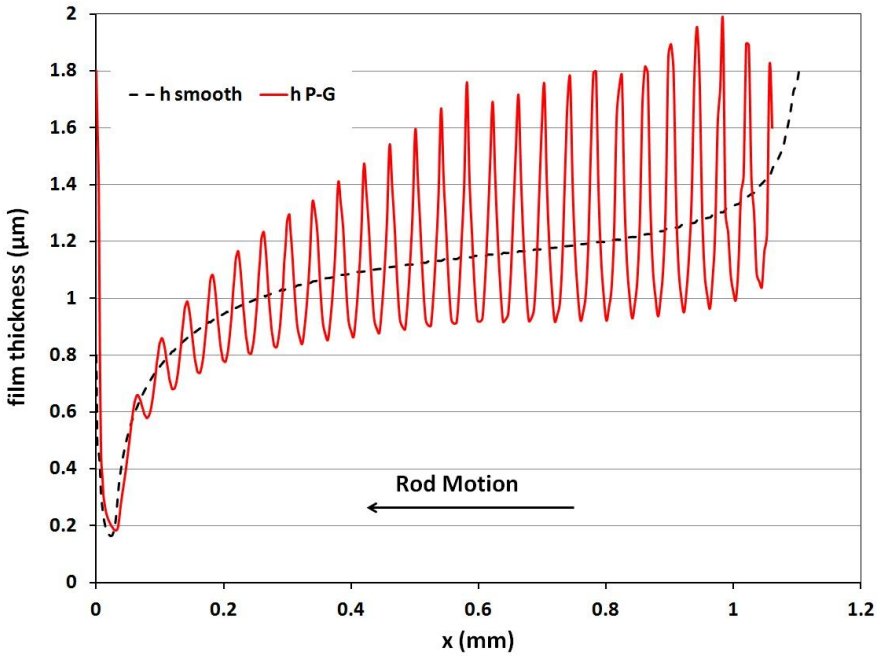

Figure 5.22b: Film thickness of instroke, 0.30 m/s, step seal, σ=0.8 μm

The contact pressure and fluid pressure distributions of the hypothetical step seal (σ=0.8 μm) during the instroke at rod speeds of 0.05 m/s and 0.3 m/s are shown in Figure 5.23a and 5.23b. Although the contact pressures are much higher than that of the U-cup seal, the contact pressures decrease while the fluid pressures increase with the increasing rod speed, which are similar to the U-cup seal with a 0.8 μm roughness. At the 0.05 m/s speed, the average of the oscillating contact pressure with the plunge-ground rod is almost identical to that with the smooth rod, while the fluid pressures are also almost identical and almost linear. At the 0.3 m/s speed, the average of the contact pressure with the plunge-ground rod is slightly higher than that with the smooth rod, while the fluid pressure with the plunge-ground rod is lower than that with the smooth rod. These contact pressure and fluid pressure results are

consistent with each other and are consistent with the film thickness distributions during instroke, discussed above.

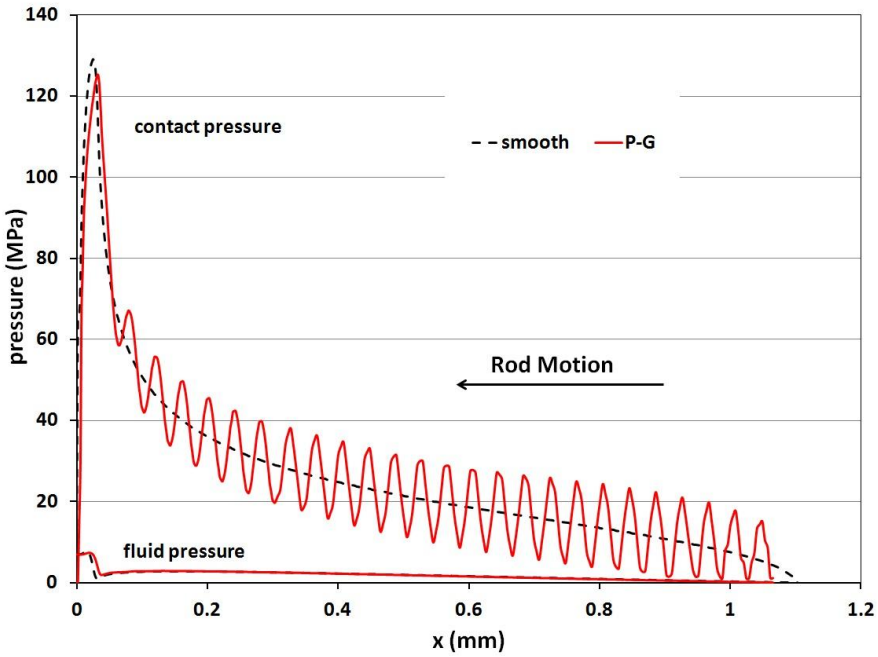

Figure 5.23a: Contact and fluid pressures of instroke, 0.05 m/s, step seal, σ=0.8 μm

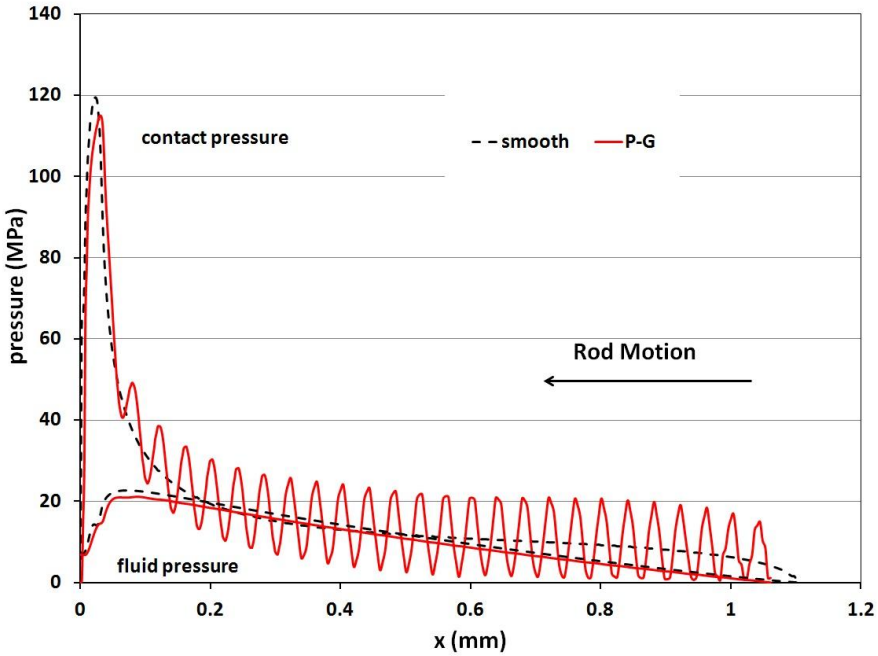

Figure 5.23b: Contact and fluid pressures of instroke, 0.30 m/s, step seal, σ=0.8 μm

Figure 5.24a and 5.24b shows the film thickness distributions of the hypothetical U-cup seal (σ=4.0 μm) during the instroke at rod speeds of 0.05 m/s and 0.3 m/s. Just like the step seal with a 4.0 μm roughness, these two distributions are almost identical, indicating that the film thickness is also relatively independent of rod speed during the instroke. The average of the oscillating film thickness with the plunge-ground rod is almost identical to the film thickness with the smooth rod.

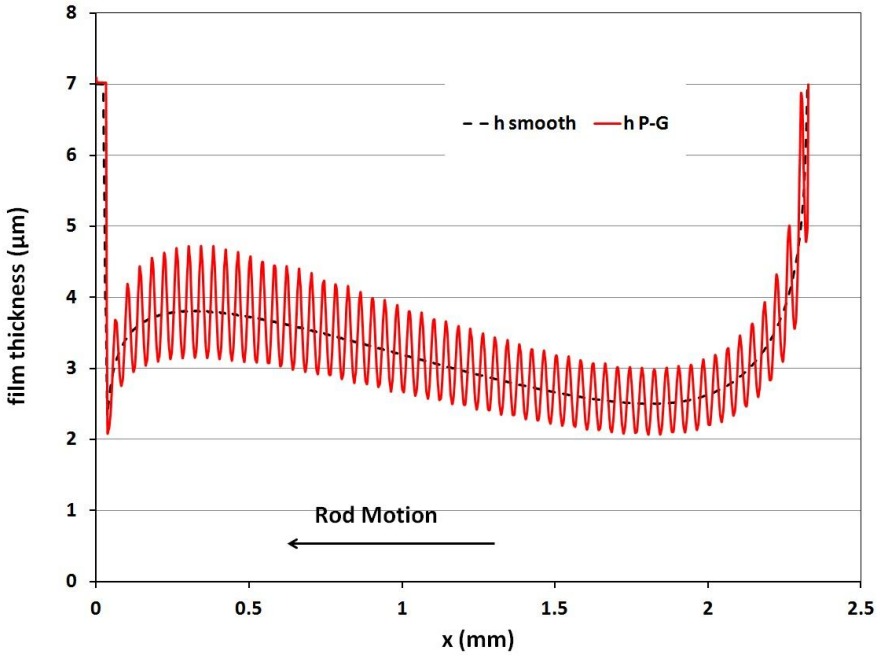

Figure 5.24a: Film thickness of instroke, 0.05 m/s, U-cup seal, σ=4.0 µm

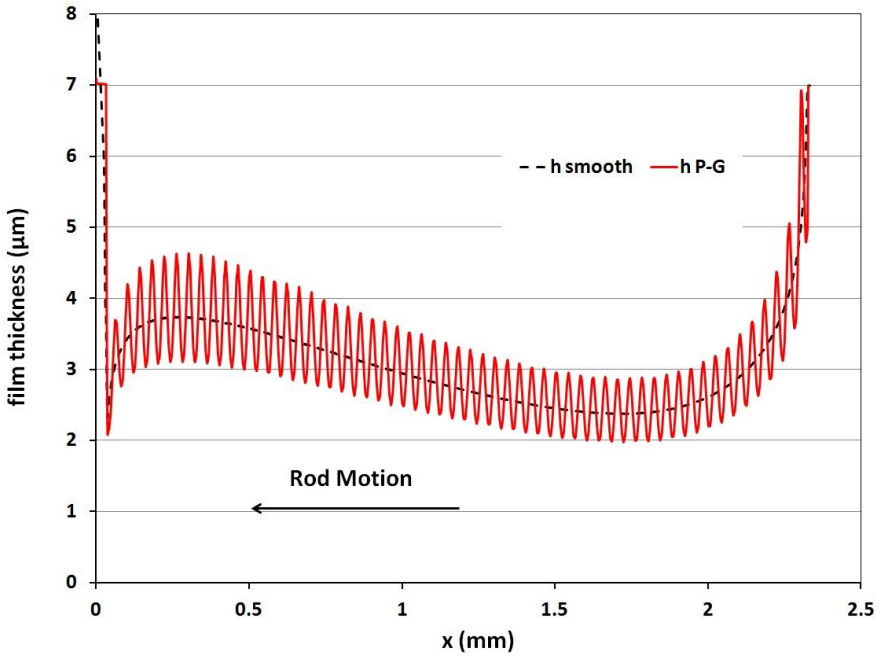

Figure 5.24b: Film thickness of instroke, 0.30 m/s, U-cup seal, σ=4.0 µm

The contact pressure and fluid pressure distributions of the hypothetical U-cup seal (σ=4.0 μm) during the instroke at rod speeds of 0.05 m/s and 0.3 m/s are shown in Figure 5.25a and 5.25b. Although the contact pressure are much smaller than that of the step seal, The two distributions are very similar, indicating that the contact and fluid pressure distributions are relatively independent of rod speed during the instroke, which are similar to the step seal with a 4.0 μm roughness. For both 0.05 m/s and 0.3 m/s speed, the average of the oscillating contact pressure with the plunge-ground rod is almost identical to that of the smooth rod. These contact pressure and fluid pressure results are consistent with each other and are consistent with the film thickness distributions during the instroke.

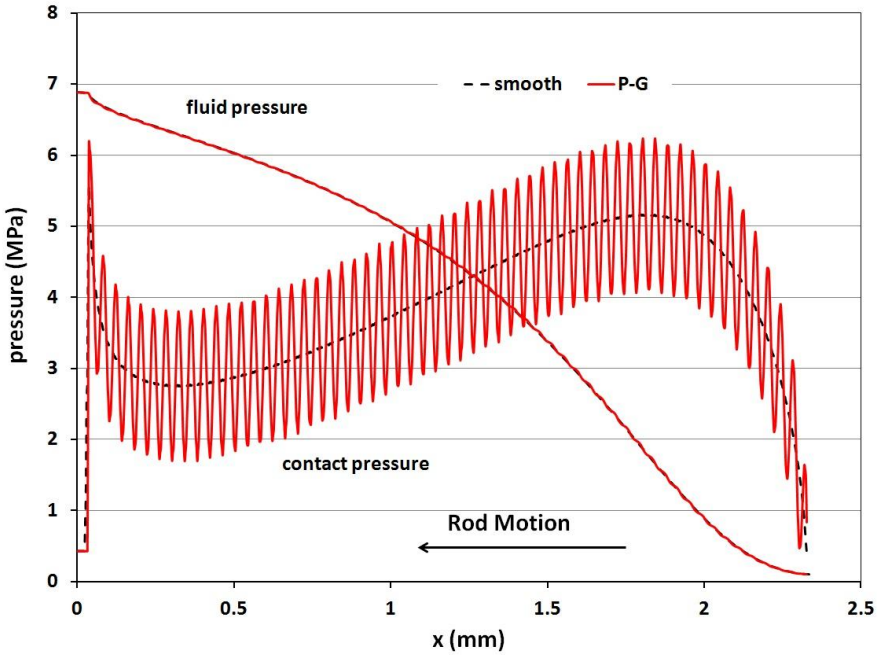

Figure 5.25a: Contact and fluid pressures of instroke, 0.05 m/s, U-cup seal, σ=4.0 μm

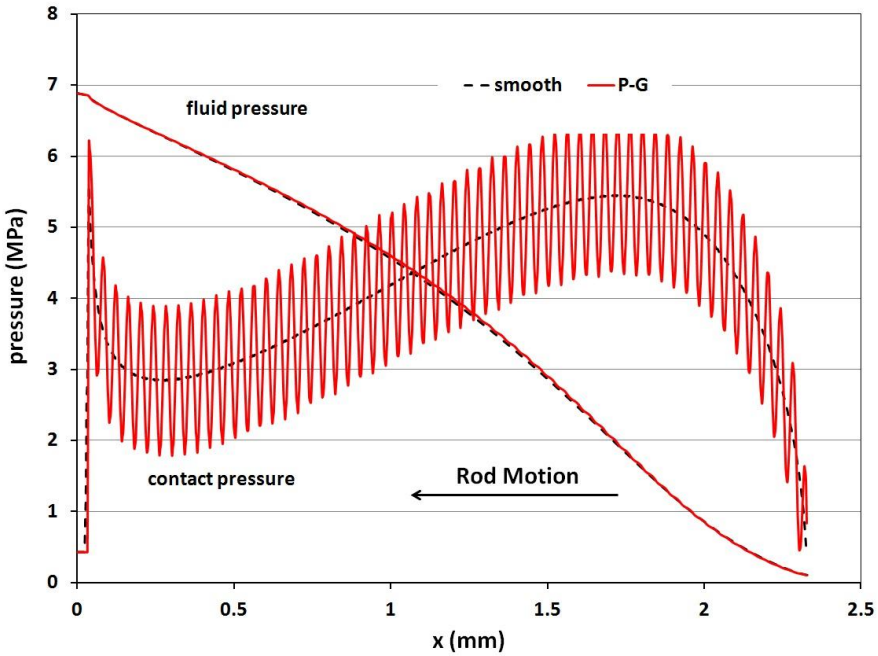

Figure 5.25b: Contact and fluid pressures of instroke, 0.30 m/s, U-cup seal, σ=4.0 μm

The comparison of the hypothetical seals and the original seals' results show that the main reason for the difference in behavior of the U-cup seal and the step seal is the difference in surface roughness of the two seals. The influence of surface roughness of the seal is the most important characteristic during the rod seal operation. It has even more effect than the geometry of the seal. It is the roughness of the seal surface that determines the overall fluid film thickness distribution. A thicker film reduces the impact of the hydrodynamic effect.

5.6 Conclusions

1. For a polyurethane U-cup seal under flooded boundary conditions, the results of this study show that a plunge-ground rod produces a lower fluid transport into the

cylinder during the instroke, compared to a smooth rod, reducing the effectiveness of the seal. The plunge-ground rod also increases the friction force on the rod. In addition, the plunge-ground rod produces large fluctuations in the contact pressure, which would be expected to increase the wear rate due to fatigue-induced wear.

2. For a polyurethane U-cup seal under starved boundary conditions, The plunge-ground rod has shorter starvation region than that of the smooth rod due to its lower degree of starvation it has under the flooded boundary conditions. The plunge-ground rod decreases the friction force on the rod compared to the smooth rod, because the lower starvation of the plunge-ground rod generates more fluid pressure to support the seal, decreasing the contact force, compared to the smooth rod case. The plunge-ground rod also produces large fluctuations in the contact pressure, which would be expected to increase the wear rate due to fatigue-induced wear.

3. For a PTFE step seal, the plunge-ground rod produces no significant effects on the fluid transport and friction force. Those effects that were observed with the U-cup seal are absent due to the larger roughness of the step seal. However, the plunge-ground rod does produce large fluctuations in the contact pressure, as with the U-cup seal, and would be expected to increase the wear rate of the step seal due to fatigue-induced wear.

4. Hypothetical studies show that the roughness of the seal surface is the most important characteristic governing the behavior of the U-cup and step seals. A

higher surface roughness produces a thicker fluid film, which decreases the influence of the hydrodynamic effect.

CHAPTER 6. ROD SEAL WITH MICRO-PATTERNED ROD USING 3D MODELS

6.1 Introduction

In this chapter, the studies on rod seals with micro-patterned rods are discussed. Two categories of surface pattern are investigated: cavities and protrusions, with 3-D models because these micro-patterns have three dimensional geometries. For cavity and protrusion patterns, both flooded and starved boundaries are discussed. Various factors that may affect seal performance such as time step, cavity depth/protrusion height, land area ratio, cavity/protrusion shape, etc., are investigated. The base parameters for the models in this chapter can be found in Table 4.1, as the U-cup seal (3-D). The surface patterns' structure and geometries are introduced in the next section.

6.2 Rod Surface Pattern

6.2.1 Geometries and Numerical Models of Surface Pattern

Studies on the friction-reduction effect of micro-patterned surfaces in various applications have been discussed in chapter 2. Based on these previous studies, several types of surface patterns are chosen for this research. Table 6.1 lists the profiles and basic geometries of these surface patterns. The area ratio is the parameter

that measures the pattern density. It is defined as the land area divided by the total sealing area: $A_r = A_{land}/A$. This area ratio is related to the contact mechanics analysis and load balance calculation, which will be discussed in the next section. Note that for the protrusion patterns, the land area is actually the flat surface of the protrusion because that is the part that contacts with the seal.

Table 6.1 Surface patterns profile and base parameters

<table>
<tr><td colspan="3">Cavities with inline round shape</td></tr>
<tr><td colspan="3"> 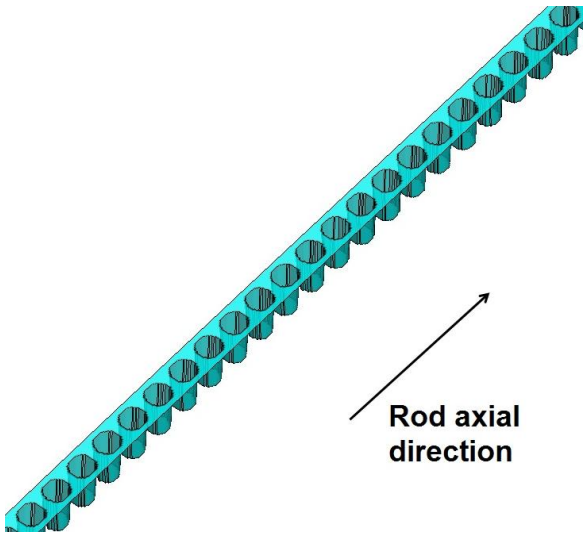
</td></tr>
<tr><td>Cavity depth:
0.5 μm - 1.5 μm</td><td>Size:
D(diameter) = 20 μm - 80 μm</td><td>Area Ratio:
0.651 - 0.912</td></tr>
</table>

Table 6.1 Surface patterns profile and base parameter (continued)

<table>
<tr><td colspan="3">Cavities with staggered round shape</td></tr>
<tr><td colspan="3"> 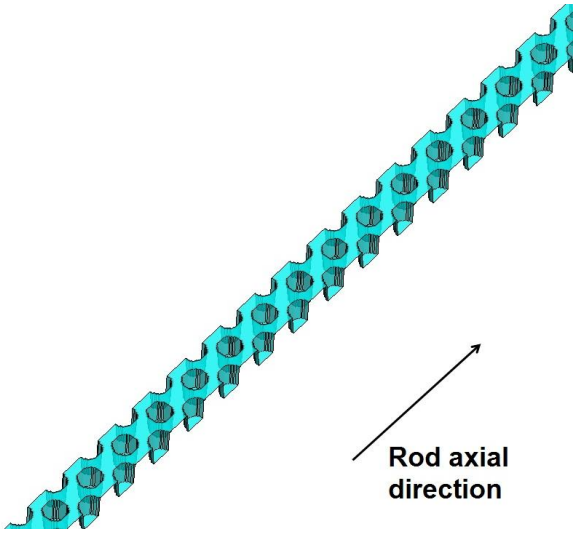
</td></tr>
<tr><td colspan="3"></td></tr>
<tr><td>Cavity depth:
0.5 µm - 1.5 µm</td><td>Size:
D(diameter) = 40 µm</td><td>Area Ratio:
0.651</td></tr>
<tr><td colspan="3">Cavities with inline equilateral triangle shape</td></tr>
<tr><td colspan="3"> 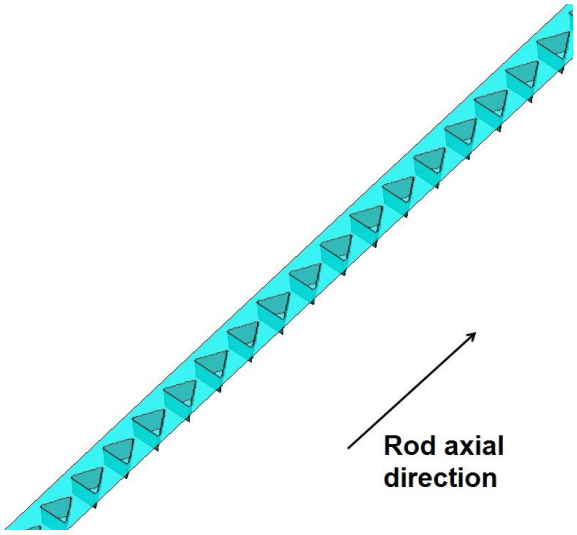
</td></tr>
<tr><td>Cavity depth:
0.5 µm - 1.5 µm</td><td>Size:
L(edge length) = 53.3 µm</td><td>Area Ratio:
0.808</td></tr>
</table>

Table 6.1 Surface patterns profile and base parameter (continued)

Protrusions with staggered round shape		
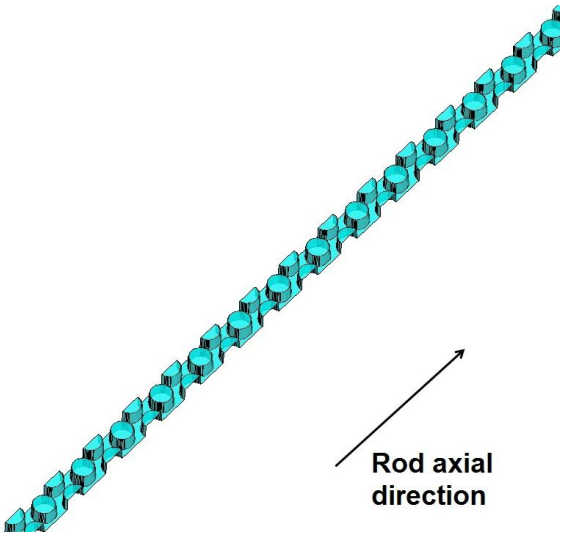		
Cavity depth: 0.5 µm - 1.5 µm	Size: D(diameter) = 40 µm	Area Ratio: 0.503 - 0.714
Protrusions with staggered square shape		
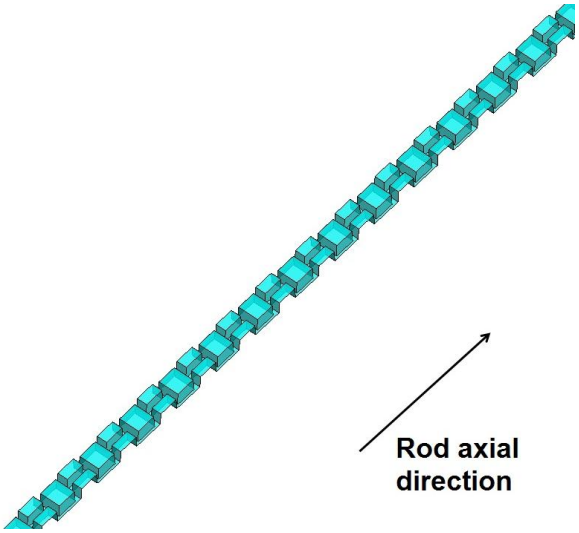		
Cavity depth: 0.5 µm	Size: L(edge length) = 40 µm	Area Ratio: 0.640

Table 6.1 Surface patterns profile and base parameter (continued)

Protrusion with opposite staggered triangle shape		
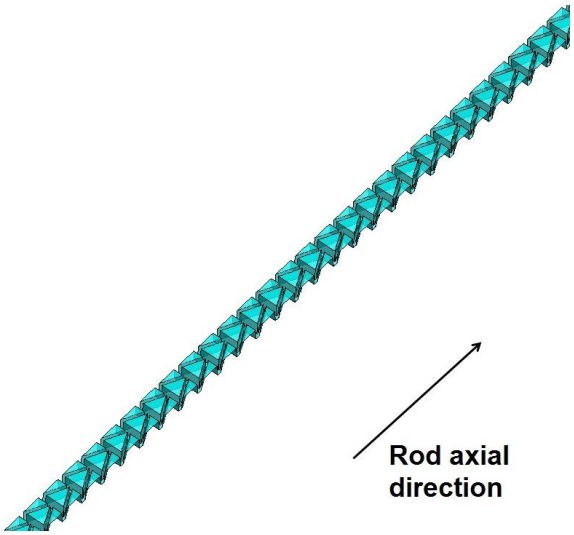		
Cavity depth: 0.5 μm	Size: L(bottom length) = 40 μm H(height) = 40 μm	Area Ratio: 0.640

6.2.2 Computational Algorithm with Rod Surface Pattern

The dynamic behavior of the seal surface is illustrated in Figure 6.1a and 6.1b. Figure 6.1a shows how the surface would look if it is perfectly elastic. The elastomer would deform into the cavities (for the protrusion cases, the elastomer would deform into the gap between protrusions). However, typical seal elastomers, like polyurethane, are viscoelastic [80, 81]. The typical relaxation time is about 0.3s [80], while the residence time of the material adjacent to each cavity is about 1.2 x 10^{-2} s to 1.0 x 10^{-4} s for rod speeds from 0.01 m/s to 0.3 m/s. Therefore, there is not

enough time for the surface material to deform into the cavities, as shown in Figure 6.1b.

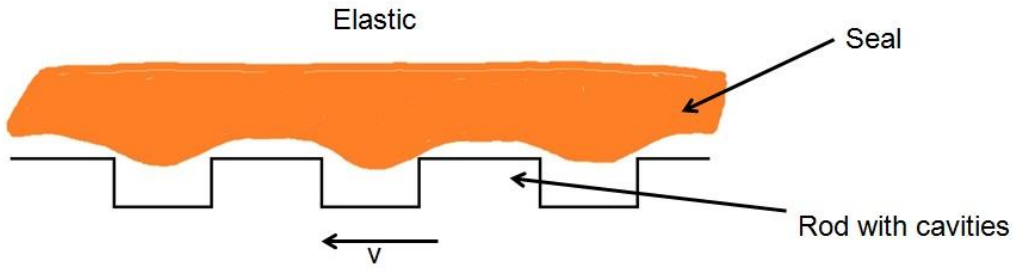

Figure 6.1a: Dynamic behavior of the seal surface with elastic material model

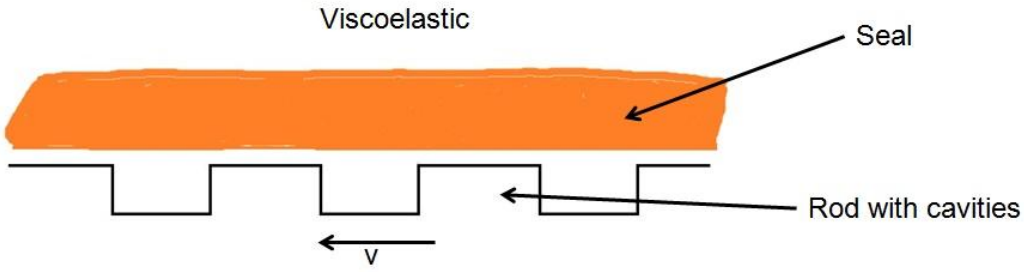

Figure 6.1b: Dynamic behavior of the seal surface with viscoelastic material model

In chapter 5, where the plunge-ground rod is modeled, the material model used is the elastic model instead of the viscoelastic model. The reason for this is that the plunge-grounded surface elevation is changing continuously (a sinusoidal wave), and there are no steep edges with cavities, which are shown in Figure 6.1a and 6.1b. It is therefore reasonable to assume that for the plunge-ground rod the seal surface behaves more like elastic material, which is shown in Figure 5.1.

Based on the considerations above, the conceptual model of the seal behavior with the patterned rod is shown in Figure 6.2. In regions adjacent to the land areas, the load per unit area L is supported by the contact pressure P_c plus the fluid pressure P_f. In regions adjacent to the cavities, the lip surface remains flat so the contact pressure is zero, and the film thickness is equal to the depth of the cavity plus the average of the film thickness around the periphery of the cavity.

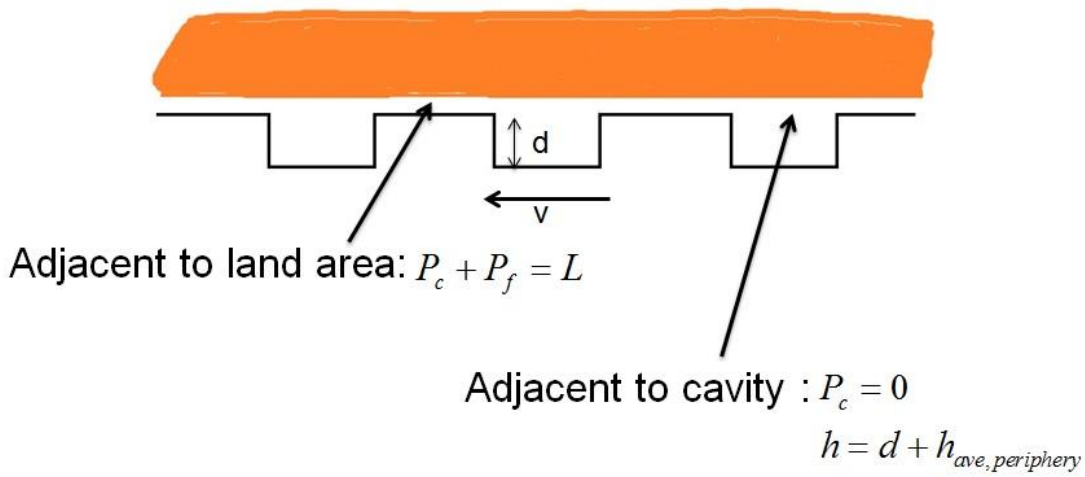

Figure 6.2: Conceptual model of the seal behavior with patterned rod

Figure 6.3a shows the positions of a 100 μm and a 200 μm thickness layer in a 2-D FEA model. This U-cup seal is mounted on a smooth rod and then on a rod with a grooved cavity pattern. The dimensions of the grooves are comparable with the triangular cavities. Figure 6.3b shows the spatial locations of these two layer boundaries after mounting and pressurization for both smooth and cavity rod cases.

From these results it is seen that the cavities on the rod will not significantly change the deformed positions of both the 100 μm and 200 μm thickness boundaries. The side boundaries between the segments also show no visible difference between the cavity case and the smooth case.

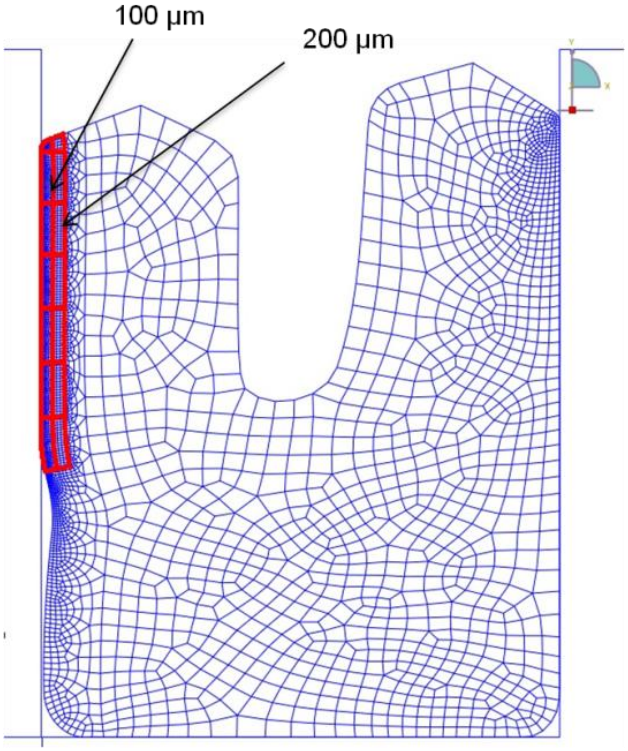

Figure 6.3a: 100 μm and 200 μm layer thicknesses

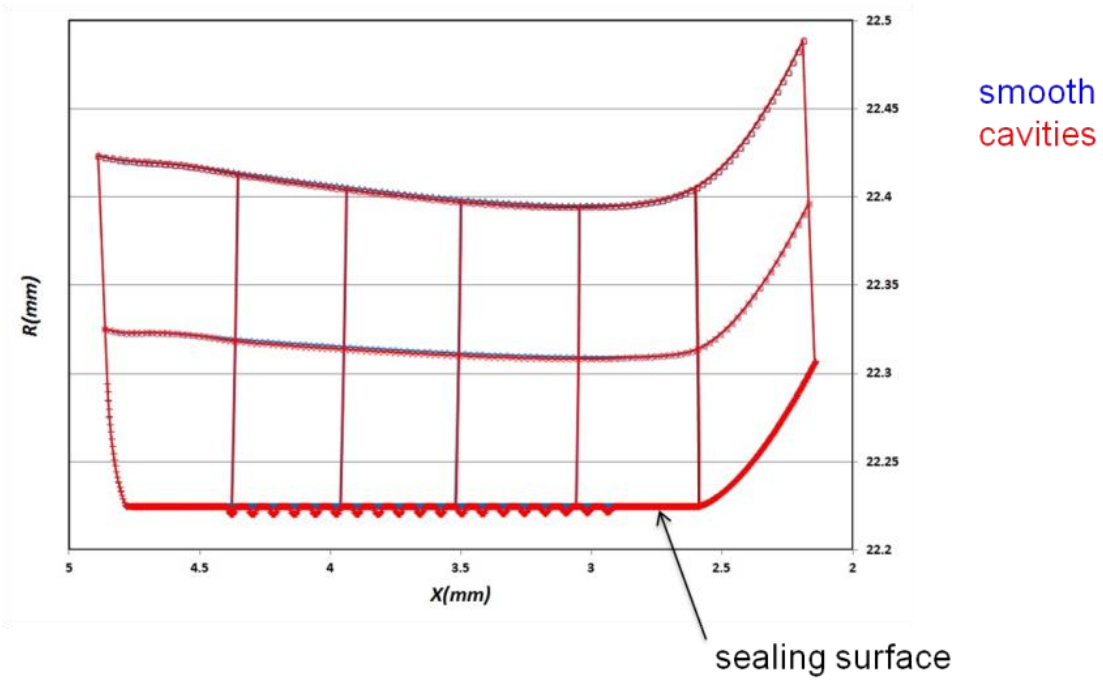

Figure 6.3b: 2-D axisymmetric analyses (instroke) smooth rod & rod containing cavities

Figure 6.4 shows the von Mises stress distributions inside the seal for the smooth rod and the patterned rod. A close up view of the patterned rod result is also shown. The stress fields outside of the 100 μm layers are virtually identical for both cases. These results show that the material outside of the 100 μm layer (and the 200 μm layer) is not affected by the micro surface pattern.

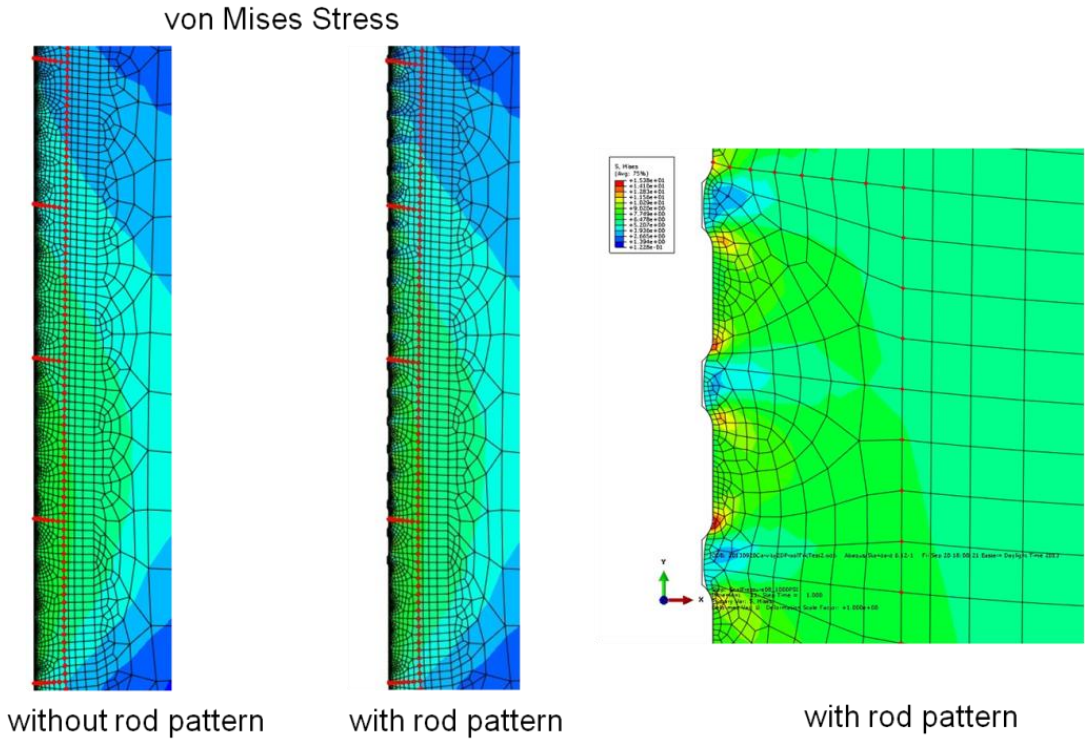

Figure 6.4: 2D stress field with & without pattern on rod

The analysis above shows that the pattern on the rod surface would not affect the force balance of the seal, therefore, the integration of the load per unit area L over the whole sealing area should equal to the integration of the static contact pressure with the smooth rod over the whole sealing area, as:

$$\int_A LdA = \int_A P_{dc,smooth}dA$$

At each location adjacent to the land area:

$$L = P_c + P_f \tag{6.1}$$

Therefore, for the load balance can be rewritten as:

$$\int_A LdA = \int_A P_c dA + \int_A P_f dA = \int_A P_{dc,smooth} dA \tag{6.2}$$

where $P_{dc,smooth}$ is the static contact pressure with a smooth rod surface.

For the patterned rod surface, $A=A_{land} + A_{cav}$, and $P_c=0$ at the cavity area. Equation 6.2 can be written as:

$$\int_{A_{land}} P_c dA + \int_{A_{land}} P_f dA + \int_{A_{cav}} P_f dA = \int_A P_{dc,smooth} dA \tag{6.3}$$

Combining equation 6.1 and 6.3:

$$\int_{A_{land}} (P_c + P_f) dA + \int_{A_{cav}} P_f dA = \int_A P_{dc,smooth} dA$$

or:

$$\int_{A_{land}} LdA = \int_A P_{dc,smooth} dA - \int_{A_{cav}} P_f dA$$

$$\frac{\int_{A_{land}} LdA}{\int_{A_{land}} P_{dc,smooth} dA} = \frac{\int_A P_{dc,smooth} dA - \int_{A_{cav}} P_f dA}{\int_{A_{land}} P_{dc,smooth} dA} \tag{6.4}$$

It is now assumed that the load per unit area L and the static contact pressure with a smooth rod $P_{dc,smooth}$ has a constant ratio for a given seal operation (rod speed and sealing boundary). This assumption is verified by comparing the load balance and torque balance with a smooth rod and a patterned rod, which will be discussed at the end of this section.

Let:

$$K = \frac{L}{P_{dc,smooth}} = constant \tag{6.5}$$

Using equation 6.5:

$$K = \frac{\int_A P_{dc,smooth} dA - \int_{A_{cav}} P_f dA}{\int_{A_{land}} P_{dc,smooth} dA} = 1 + \frac{\int_{A_{cav}} (P_{dc,smooth} - P_f) dA}{\int_{A_{land}} P_{dc,smooth} dA} \tag{6.6}$$

Note that for P_f=0:

$$K = 1 + \frac{A_{cav}}{A_{land}} = \frac{A}{A_{land}} = \frac{1}{Area\ Ratio}$$

Combining equation 6.1, 6.5 and 6.6, we have:

$$P_c = \left\{ 1 + \frac{\int_{A_{cav}} (P_{dc,smooth} - P_f) dA}{\int_{A_{land}} P_{dc,smooth} dA} \right\} P_{dc,smooth} - P_f \tag{6.7}$$

In Chapter 3, Figure 3.3 shows the scheme of the 3-D EHL computational model. With the load balance analysis discussed above, the coupling of the fluid mechanics analysis, the contact mechanics during motion, and the load balance computation can also be shown as in Figure 6.5

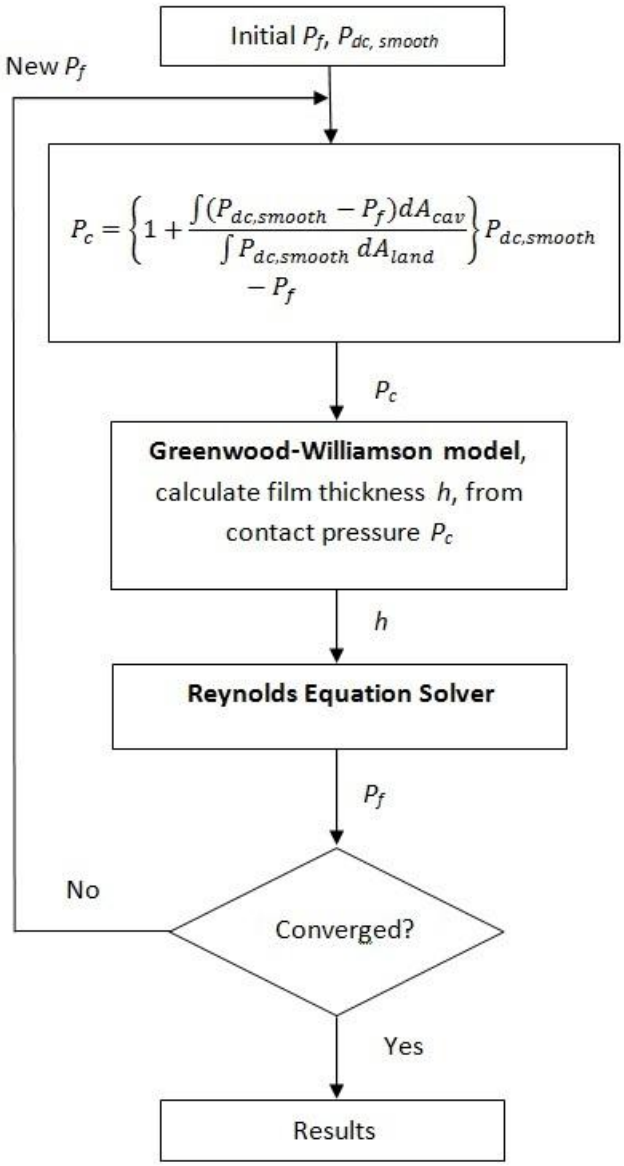

Figure 6.5: Load balance computational scheme

The justification of the assumption of equation 6.5 is as follows. Consider a thin 100 μm layer of the seal adjacent to the interface with the rod. The stresses along the internal boundary of the layer are determined by the interference mounting of the seal, and are the same for both the case of the smooth rod and the patterned rod, as shown earlier. These stresses produce a load and a torque on the layer. Treating the layer as a free body, it is seen that the load distribution along the layer surface adjacent to the rod, the external surface, must balance the load and torque produced by the stresses on the internal surface. In the case of the smooth rod, the load distribution along the external surface will be the mirror image of the load distribution along the internal surface. In the case of the patterned rod, the presence of the cavities will alter the magnitudes of the load in the land areas, but it is believed the shape of the distribution will be similar to that with a smooth rod. That distribution must generate a torque, as well as a total load, to balance that produced along the internal surface, which is the same for both the patterned rod and the smooth rod cases.

Therefore, to validate the assumption of equation 6.5, one can compare the net torque and total load produced on the external seal surface with the smooth rod and with the patterned rod. If the assumption is valid, the two torques and total loads should be equal. This comparison has been made for several cases, and the discrepancy between the two torques has been found to be less than 1%, and between the two total loads less than 0.5%, thereby validating equation 6.5. For example: for a rod with cavity pattern, the depth of the cavity is 1.50 μm, the land area ratio is 0.651. At rod speed of 0.10 m/s. The calculated non-dimensional load is 0.453, the

un-dimensional torque is 0.0051373, while the non-dimensional load for a smooth rod case at the same speed is 0.454, the non-dimensional load is 0.00051134.

6.3 Cavity Pattern with Flooded Boundary

In this section, the U-cup seal with a cavity patterned rod under flooded boundary conditions is discussed. The following parameters are changed and examined separately: the time steps, the cavity depth, the land area ratio, the shape of the cavity, the size of the cavity, and the arrangement of the cavities.

6.3.1 Effect of Time Step

Figure 6.6 shows the fluid transport during outstroke and instroke as a function of rod speed at different time steps. The surface patterns in these cases are shown in table 6.1 as the cavities with the inline round shape, with the same cavity depth of 1.50 μm and land area ratio of 0.651. As the rod is moving, the inlet of the sealing area meets the flat land area region first, and then the inlet meets the cavity.After a whole cavity goes through, the inlet region of the seal meets the flat land area region again, repeating as the surface pattern repeats. In Figure 6.6, “flat inlet” means the inlet of the sealing zone meets the beginning of the flat land area region; “cavity inlet” means the inlet of the sealing zone meets the center of the cavity; “standard” means the inlet of the sealing zone meets the flat land area in between two cavities. The latter is the case for all other parameter discussions. The curves for the different time steps generally lie on top of each other, indicating that the axial position of the rod produces no significant effect on the fluid transport.

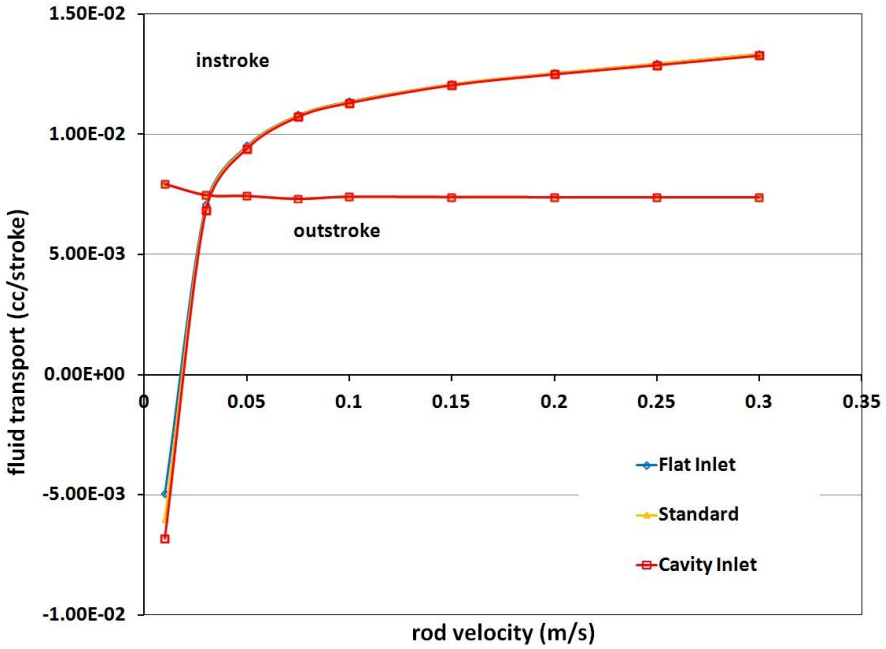

Figure 6.6: Fluid transport, U-cup seal, different time steps for cavity pattern

The friction force on the rod, as a function of rod speed is shown in Figure 6.7 for different time steps. The time step has no effect on the friction force for both outstroke and instroke. Therefore, in the following simulations, only one time step (the Standard) is calculated, instead of all the time steps that the rod goes through.

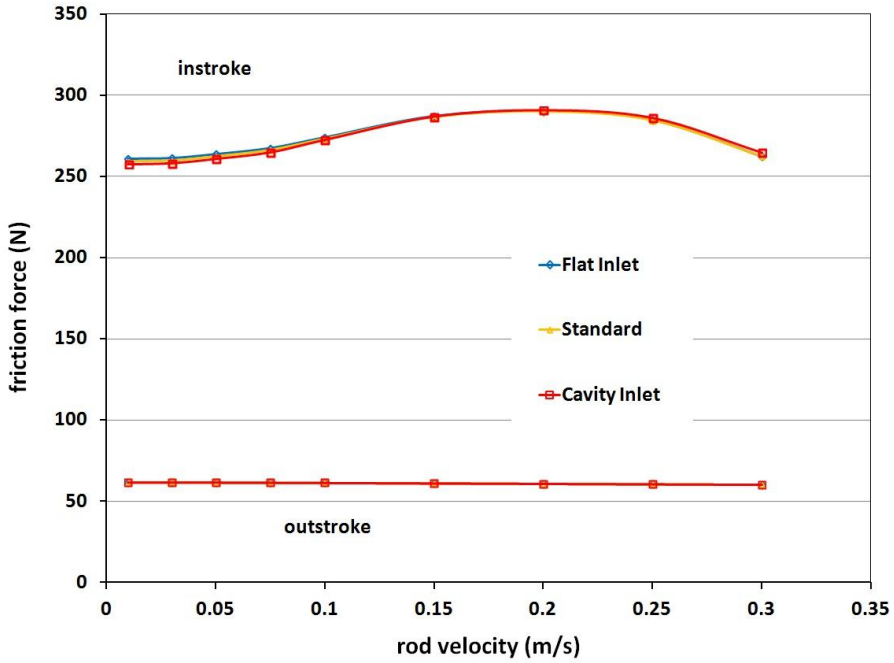

Figure 6.7: Friction force, U-cup seal, different time steps for cavity pattern

6.3.2 Effect of Cavity Depth

Figure 6.8 shows the fluid transport during outstroke and instroke as a function of rod speed for the cavity pattern rod with different cavity depths and the smooth rod, under flooded boundary conditions. The surface patterns in these cases are shown in table 6.1 as the cavities with inline round shape, with the same land area ratio of 0.651.

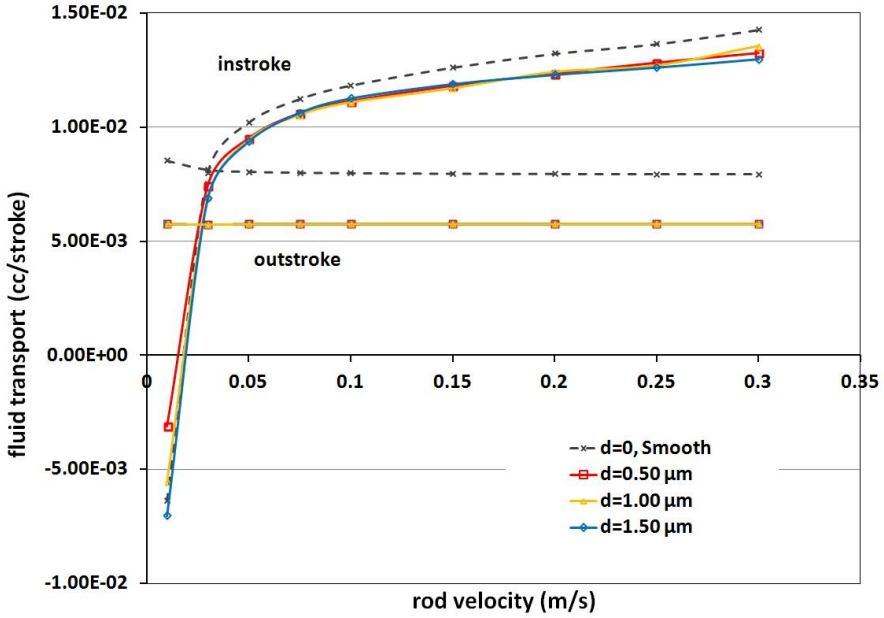

Figure 6.8: Fluid transport, U-cup seal, different cavity depths, flooded boundary conditions

The transport behavior for the smooth rod has been discussed in the previous chapter. As can be seen, the outstroke transport is relatively independent of rod speed while the instroke fluid transport increases with rod speed, for the various cavity depths, just like the smooth rod cases. The cavity cases have lower fluid transports for both outstroke and instroke, compared to the smooth rod. The curves for different cavity depths generally lie on top of each other, indicating that the variation in cavity depth produces no significant effect on the fluid transport. The difference in fluid transport between the cavity cases and smooth cases, which is mainly related to the area ratio, will be discussed in the following section. The critical speeds for all the different cavity depths and for the smooth rod are virtually the same, about 0.03 m/s. Note that above the critical speed, there is not enough fluid removed from the cylinder

during the outstroke to fully lubricate the seal during the instroke so starvation will occur. The cases for the cavity pattern under starved boundary conditions will be discussed in the following sections.

The friction force on the rod, as a function of rod speed is shown in Figure 6.9 for rods with different cavity depths and the smooth rod, under flooded boundary conditions. During the outstroke, when the sealed pressure is ambient, it is relatively low and independent of rod speed. The friction force is almost the same as that of the smooth rod but slightly lower because the cavity patterns could not change the total load balance. The cavity pattern only increases the fluid pressure slightly when the fluid flow is not cavitated. During the instroke, with a high sealed pressure, the friction force is relatively high and affected by rod speed. Depending on the rod speed and cavity depth, the textured surfaces reduce the friction below that with the smooth rod. At intermediate speeds the deepest cavities produce the greatest reduction, while at the highest speeds the shallowest cavities are the most effective. The largest reduction is about 13%. The different cavity depths produce different effects because they each affect the hydrodynamically generated pressure differently. For the case of the atmospheric sealed pressure, these results are academic, since the lubrication must be starved. But they are significant for applications with a high sealed pressure during the outstroke where flooded lubrication occurs.

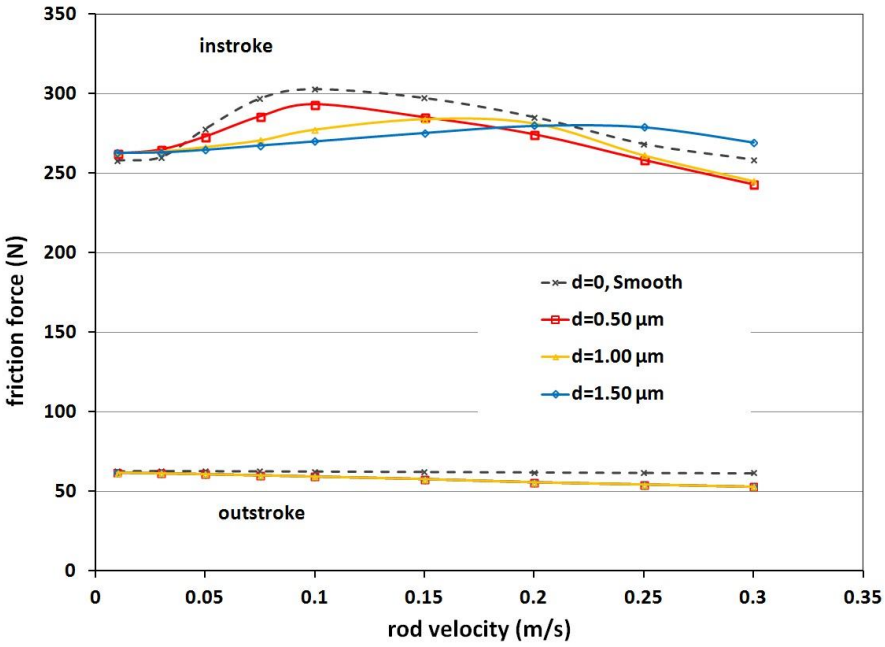

Figure 6.9: Friction force, U-cup seal, different cavity depths, flooded boundary conditions

A physical understanding of these characteristics can be obtained by examining the details of the sealing zone, namely the lubricating film thickness distribution and the fluid and contact pressure distributions.

There are several ways to visualize the film thickness distributions. Figure 6.10a shows a typical 3-D plot of the fluid film distribution with cavities during an outstroke. Figure 6.10b shows a side view of the 3-D plot, with axial and film thickness directions. The land area and the cavity area are clearly seen. In these plots, the depth of the cavities is 0.5 µm

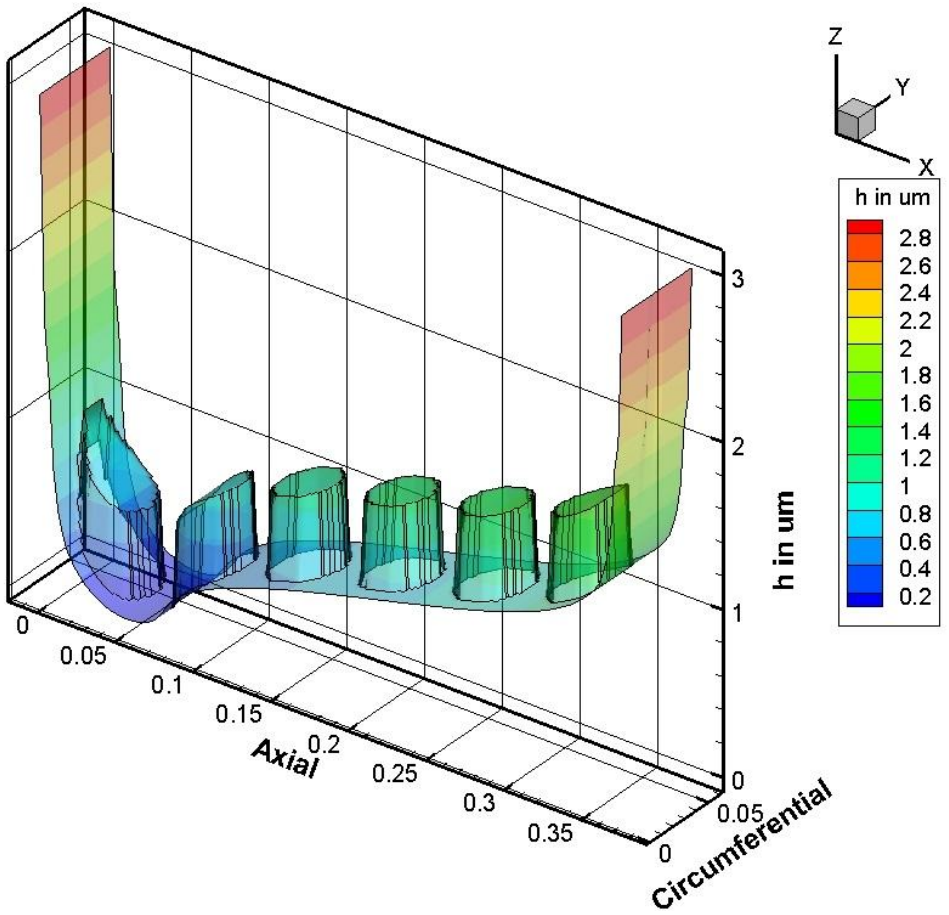

Figure 6.10a: 3-D film thickness distributions

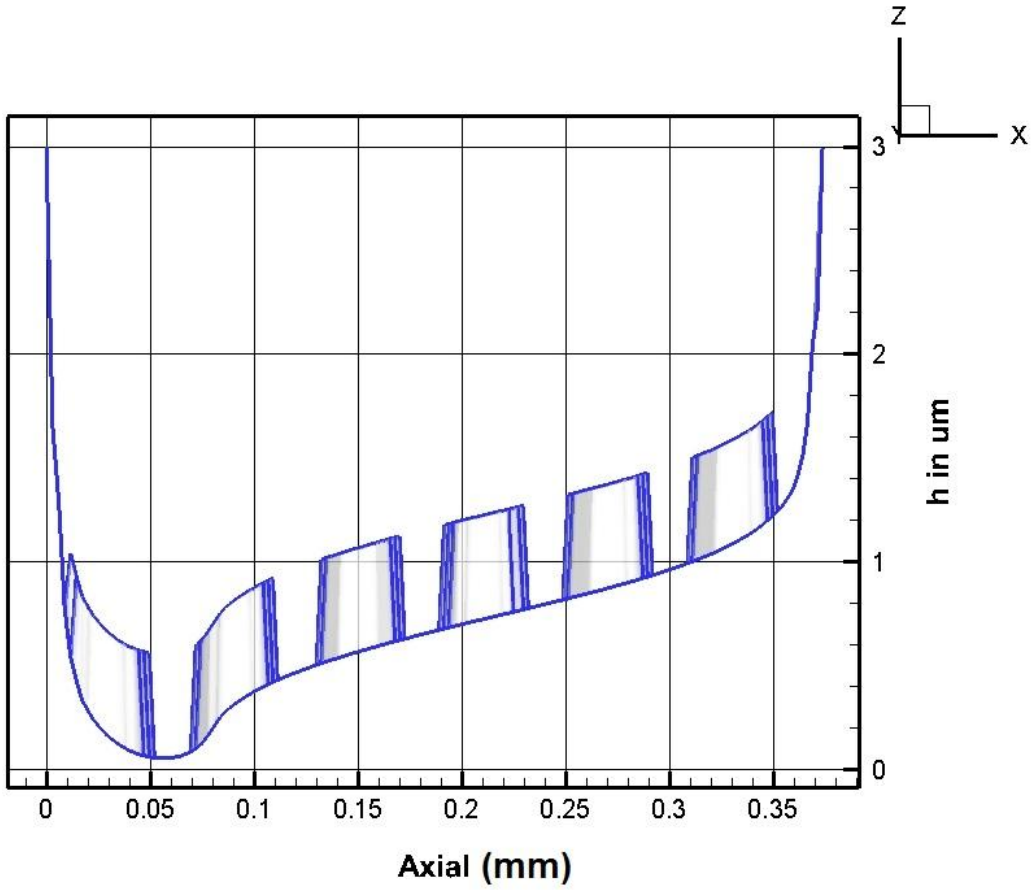

Figure 6.10b: Side view of 3-D film thickness distributions

A 2-D plot that only shows the center line of the 3-D plot is shown in Figure 6.11a. Figure 6.11b shows the 2-D plot with only the land area plotted. This last type of a plot most clearly shows the shape of the seal surface, and is the one mainly used in the presentation of the simulation results.

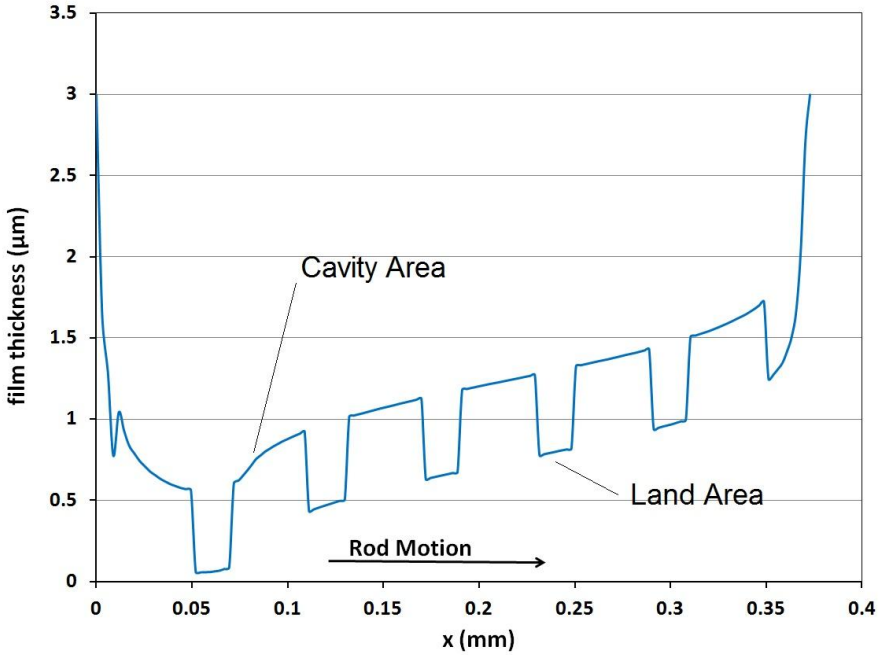

Figure 6.11a: 2-D film thickness distributions with both cavity area and land area

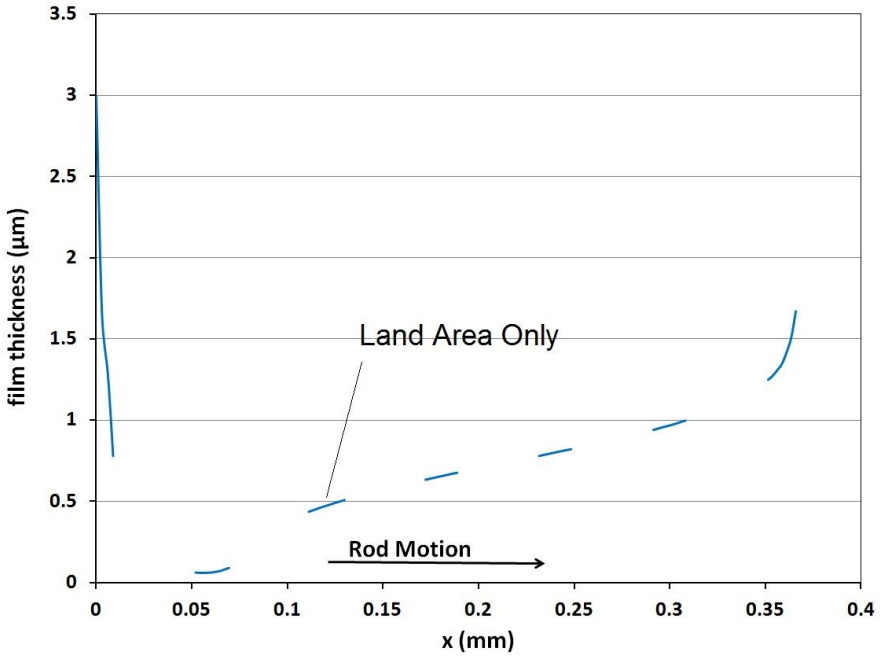

Figure 6.11b: 2-D film thickness distributions with land area only

Figure 6.12a and 6.12b show similar 3-D plots of contact pressure. The contact pressure at the cavity area is zero.

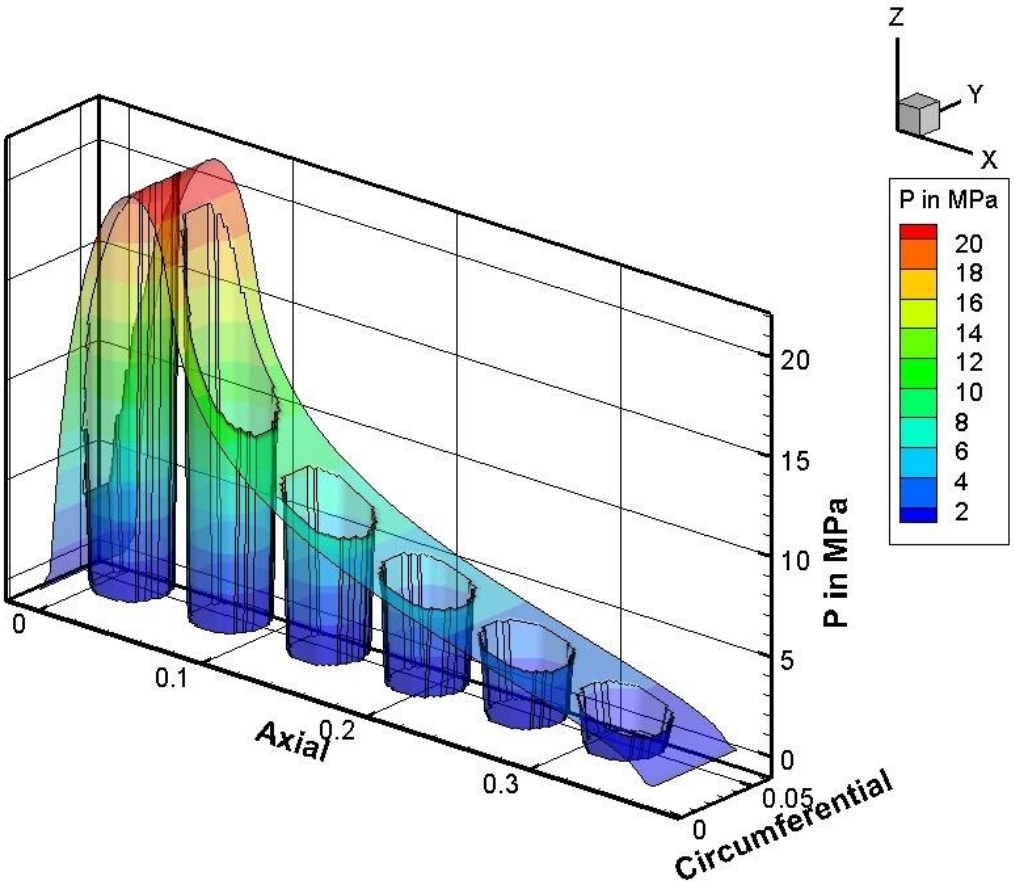

Figure 6.12a: 3-D contact pressure distributions

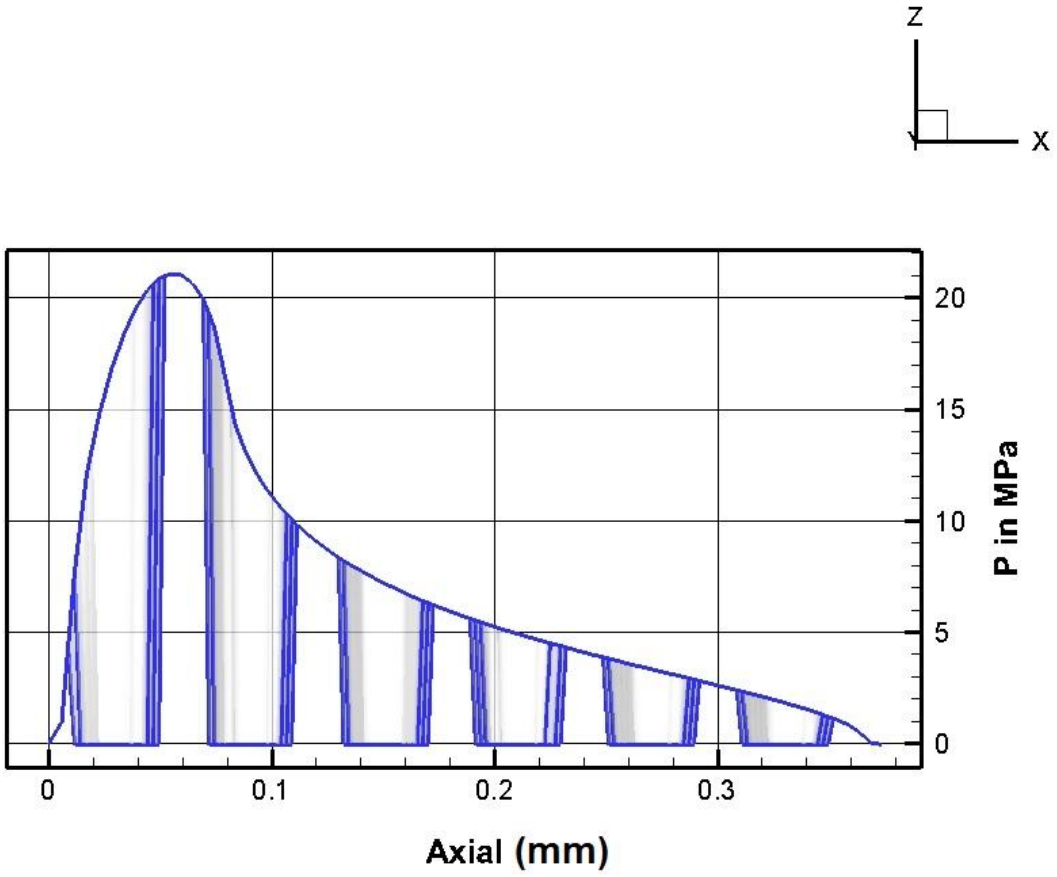

Figure 6.12b: Side view of 3-D contact pressure distributions

A similar 2-D transformation is applied to the contact pressure plots, as shown in Figure 6.13a. Since the contact pressure in the cavity area is zero, only land area values are plotted, in Figure 6.13b. Again, the latter is the type of plot mainly used in the presentation of the simulation results

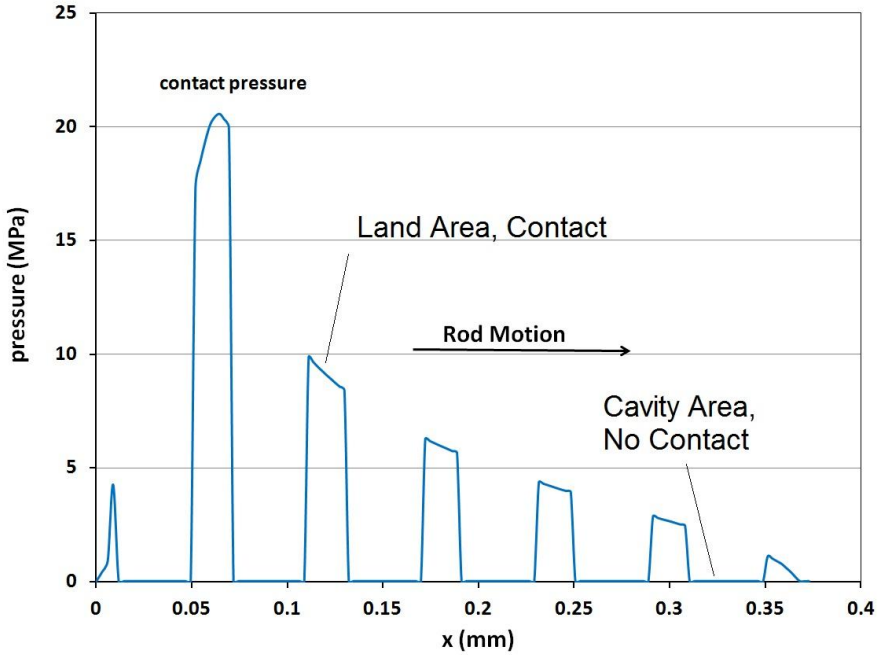

Figure 6.13a: 2-D contact pressure distributions with land and cavity areas

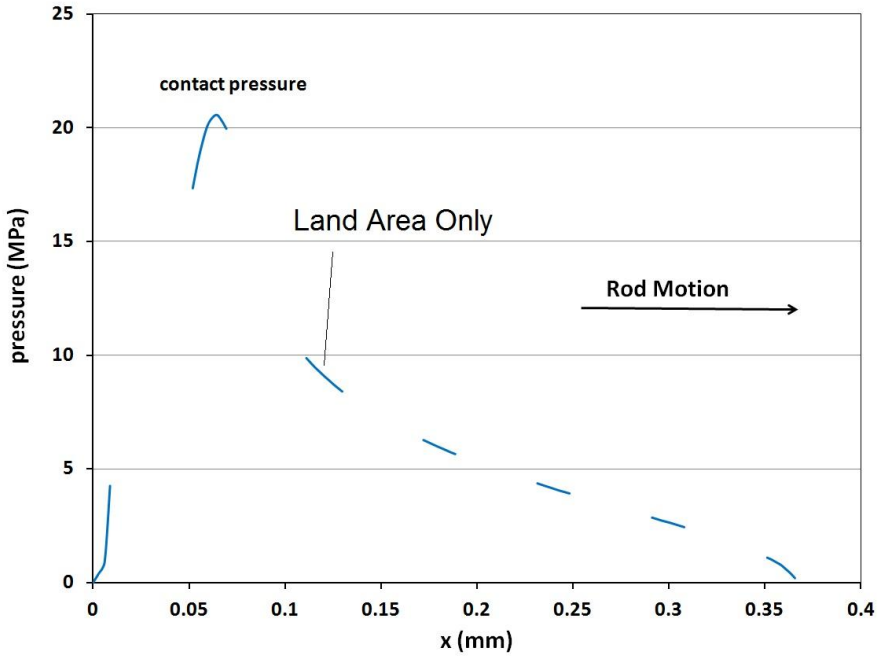

Figure 6.13b: 2-D contact pressure distributions with land area only

The fluid pressure distribution is also plotted in 2-D for the centerline. Since since the fluid pressure is changing continuously, the pressure in both the land and cavity areas is shown. The film thickness distributions during the outstroke at a rod speed of 0.03 m/s are shown in Figure 6.14. The corresponding distributions at 0.1 m/s and 0.3 m/s (not shown) are almost identical, indicating that the film thickness is relatively independent of rod speed during the outstroke. The curves for different cavity depths generally overlap, indicating that the cavity depth produces no significant effect on the fluid film during the outstroke. The film thickness in the land area with a cavity rod is thinner than that of the smooth case. The reason for this is related to the effect of land area ratio, which will be discussed in the following section.

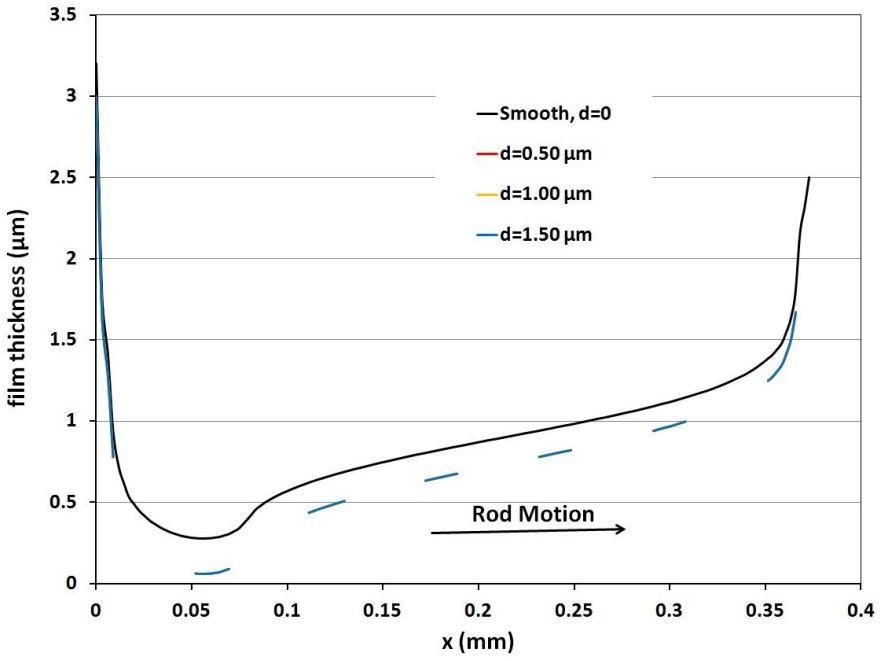

Figure 6.14: Film thickness of outstroke, 0.03 m/s, U-cup seal, different cavity depths, flooded boundary conditions

The film thickness distribution during the instroke at the rod speeds of 0.03 m/s, 0.1 m/s and 0.3 m/s are shown in Figures 6.15a, 6.15b and 6.15c, respectively. Just like during the outstroke, the cavities on the rod produce a thinner film at the land area compared to that of the smooth rod. At low speed (0.03 m/s), the curves for different cavity depths generally overlap, indicating that the cavity depth produces no significant effect on the fluid film when the instroke speed is low. At medium speed (0.1 m/s), the film thickness at the land area slightly increases with increasing cavity depth. At high speed (0.3 m/s), the film thickness distributions at the land area with 0.50 μm and 0.10 cavity depth are almost identical, while that with the 1.50 μm cavity depth is slightly thinner.

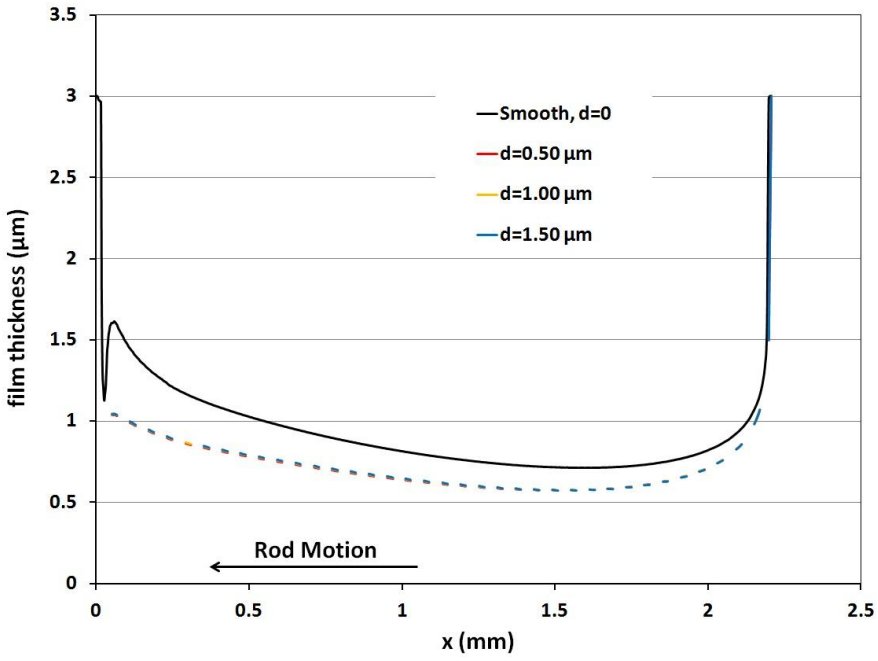

Figure 6.15a: Film thickness of instroke, 0.03 m/s, U-cup seal, different cavity depths, flooded boundary conditions

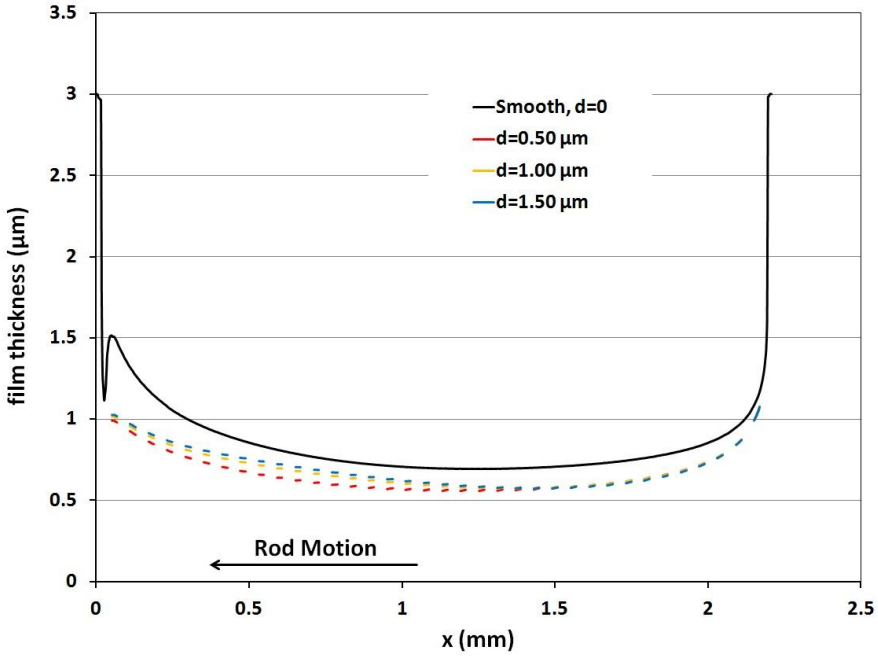

Figure 6.15b: Film thickness of instroke, 0.10 m/s, U-cup seal, different cavity depths, flooded boundary conditions

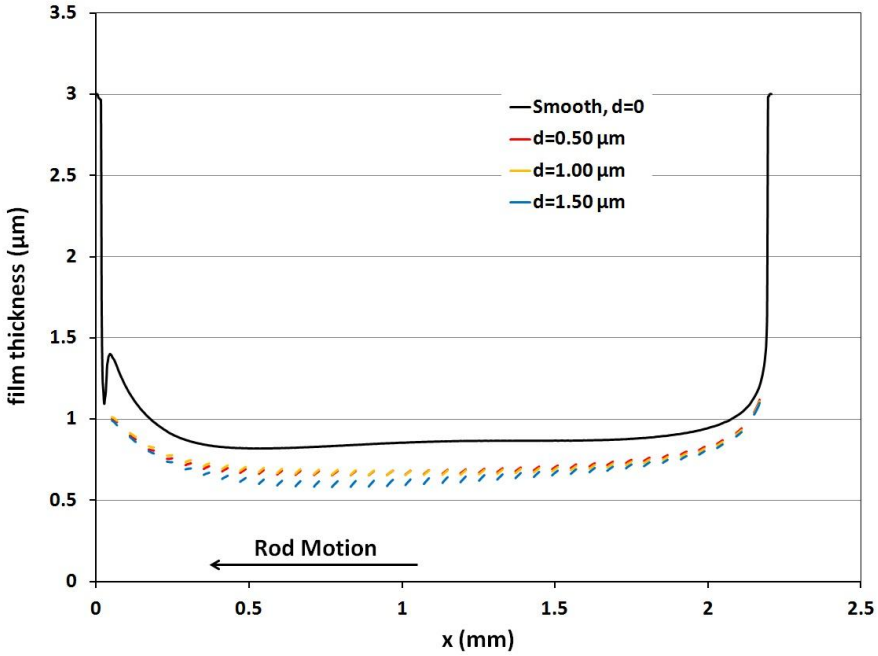

Figure 6.15c: Film thickness of instroke, 0.30 m/s, U-cup seal, different cavity depths, flooded boundary conditions

Figure 6.16 shows the contact pressure and fluid pressure distributions during the outstroke at a rod speed of 0.03 m/s. The corresponding distributions at 0.1 m/s and 0.3 m/s (not shown) are almost identical. The fact that the contact pressure distributions of the cavity rods are higher than that of the smooth rod is related to the area ratio, which will be discussed in the next section. The curves for different cavity depths generally overlap, indicating that the cavity depth produces no significant effect on the contact pressure during the outstroke. The contact pressure in the land area is determined by both the area ratio and the fluid pressure, as shown in equation 6.7. During the outstroke, the fluid pressure is not elevated above ambient and is not affected by the cavity depth and the area ratios are the same for different cavity depth cases. Thus, the contact pressure is not affected by the cavity depth during the outstroke. This result is consistent with the film thickness distributions during the outstroke.

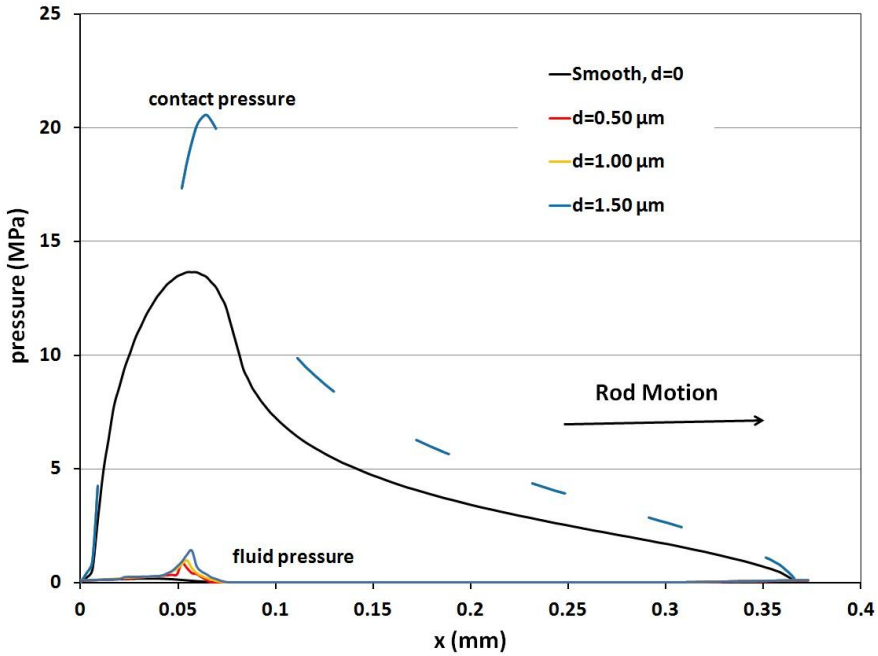

Figure 6.16: Contact and fluid pressure of outstroke, 0.03 m/s, U-cup seal, different cavity depths, flooded boundary conditions

The contact pressure and fluid pressure distributions during the instroke are shown in Figures 6.17a1, 6.17a2, 6.17b1, 6.17b2, 6.17c1, and 6.17c2 at rod speeds of 0.03 m/s, 0.1 m/s and 0.3 m/s. The contact pressures for the cavity cases are always higher than that of the smooth rod, just like in the outstroke cases. At 0.03 m/s, the contact pressure and fluid pressure distributions for various cavity depths are almost identical, indicating that the cavity depth has no significant effect on contact and fluid pressure at low speed. At 0.10 m/s, the contact pressure decreases while the fluid pressure increases with increasing cavity depth. At 0.30 m/s, the contact and fluid pressures with 0.50 µm and 0.10 µm cavity depths are almost identical, while the contact pressure with a 1.50 µm cavity depth is higher and the fluid pressure is lower.

In addition, with increasing rod speed, the oscillations of the contact and fluid pressure caused by the cavity patterns become more significant.

These contact pressure and fluid pressure results are consistent with each other and are consistent with the film thickness distributions during the instroke.

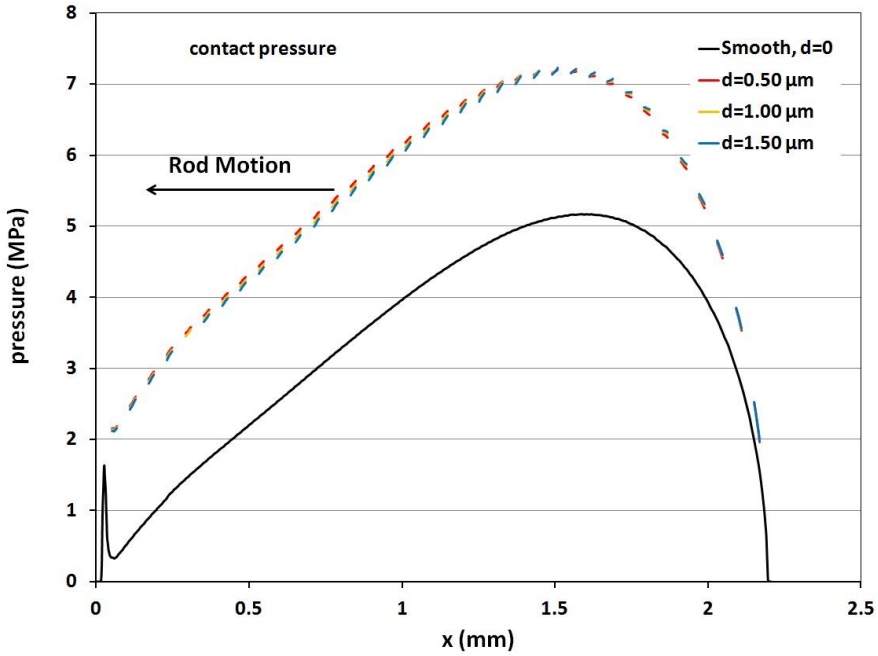

Figure 6.17a1: Contact pressure of instroke, 0.03 m/s, U-cup seal, different cavity depths, flooded boundary conditions

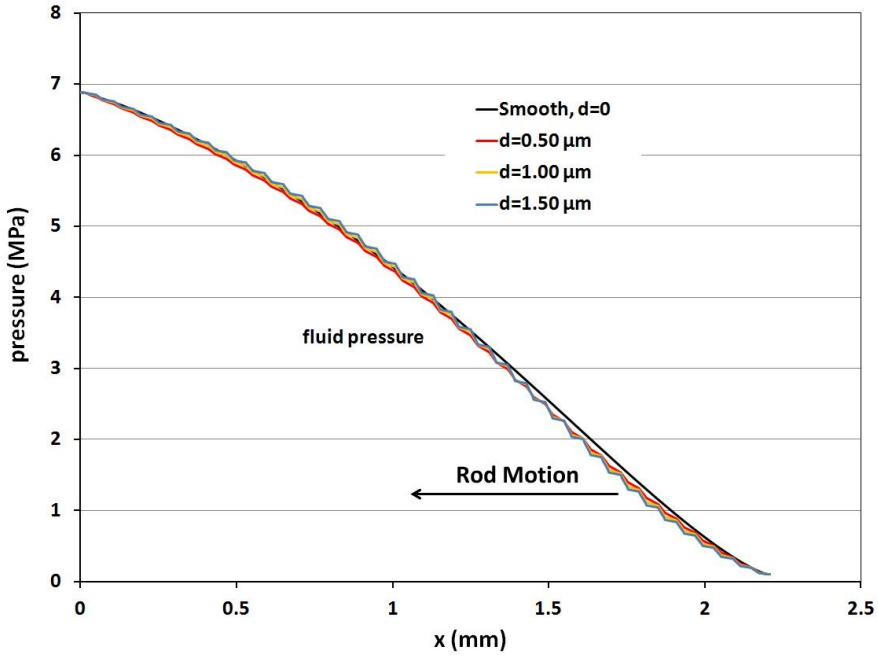

Figure 6.17a2: Fluid pressure of instroke, 0.03 m/s, U-cup seal, different cavity depths, flooded boundary conditions

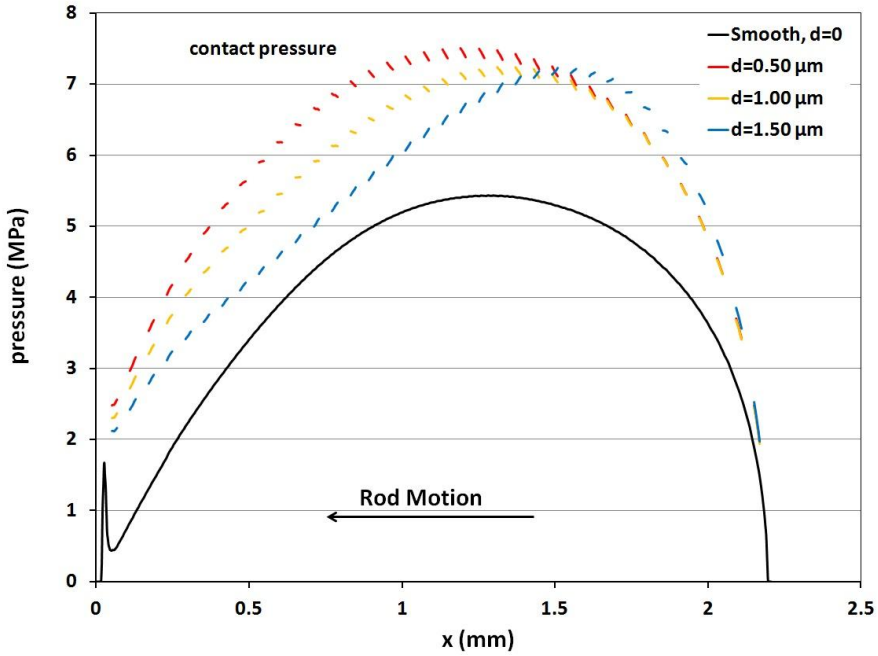

Figure 6.17b1: Contact pressure of instroke, 0.10 m/s, U-cup seal, different cavity depths, flooded boundary conditions

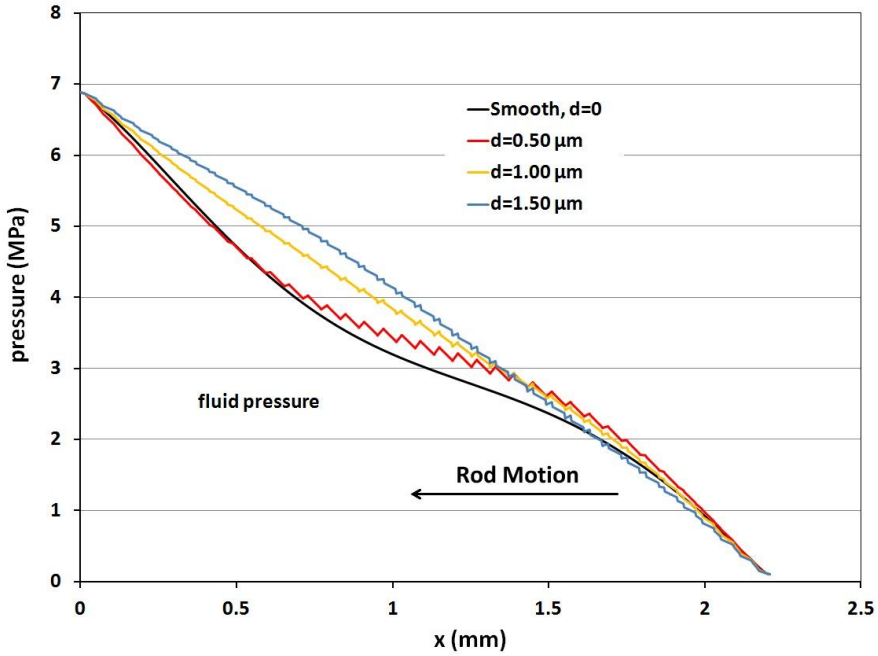

Figure 6.17b2: Fluid pressure of instroke, 0.10 m/s, U-cup seal, different cavity depths, flooded boundary conditions

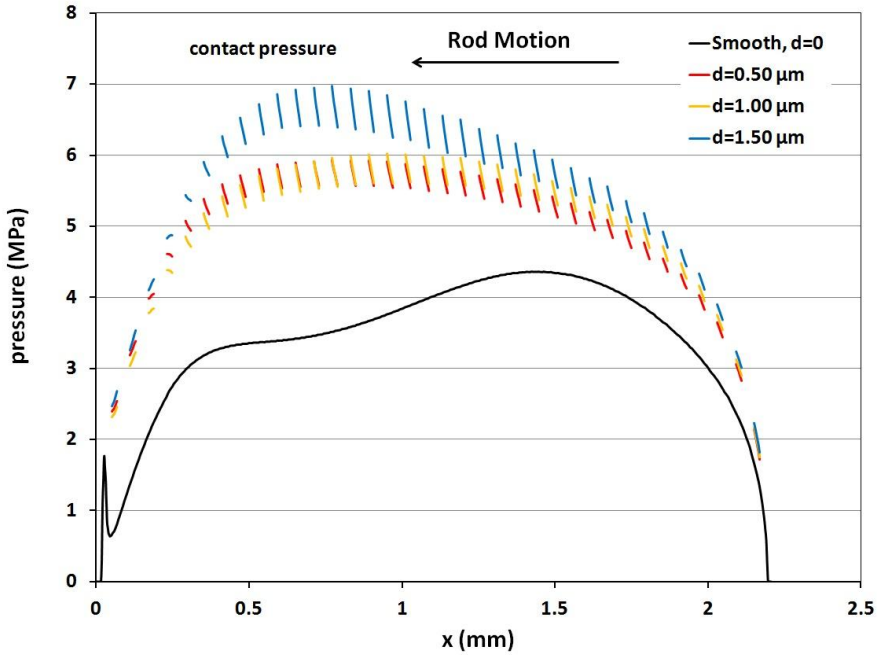

Figure 6.17c1: Contact pressure of instroke, 0.30 m/s, U-cup seal, different cavity depths, flooded boundary conditions

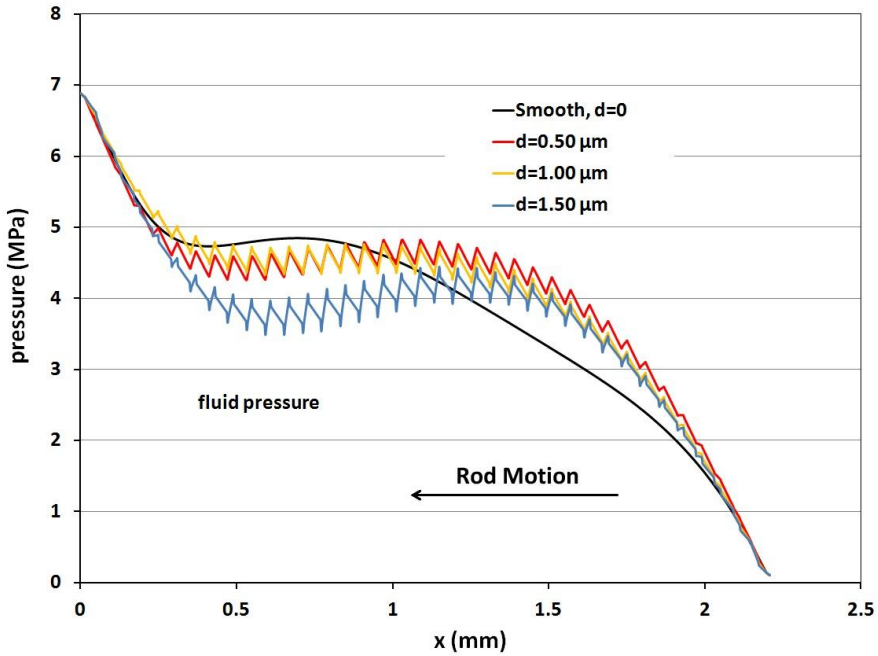

Figure 6.17c2: Fluid pressure of instroke, 0.30 m/s, U-cup seal, different cavity depths, flooded boundary conditions

It is now possible to explain the effect of cavity depth on the behavior of the seal. During the outstroke, the seal pressure is ambient, and the fluid pressure is zero in most of the sealing zone due to the cavitation. The cavity depth has no effect on fluid pressure. The contact pressures for various cavity depths are identical because of the same land area ratio (see next section 6.3.3), and are relatively independent of rod speed. Therefore, the film thickness distributions on the land area are the same for different cavity depths. The fluid transport is determined by the film thickness on the land area since the cavities are unconnected, and deeper cavities have no effect on fluid transport when fluid cavitation has already occurred. The friction force is generally determined by contact pressure and fluid pressure. Thus, the cavity depth has no effect on both fluid transport and friction force behavior during the outstroke.

The fluid pressure is increased slightly for the cavity cases compared to the smooth rod case, before the fluid film started to cavitate. This increased fluid pressure reduces the contact pressure, and friction force slightly for the cavity cases.

During the instroke, the fluid transports are determined by both the fluid film distribution and the fluid pressure (Couette and Poiseuille flow). The effects of cavity depth on fluid film and fluid pressure counter each other, resulting in almost identical fluid transport behavior between various cavity depths during the instroke. At low speed, the cavities have no significant effect on fluid pressure. Since the seal surface is supported by the fluid and contact pressures acting together, the contact pressures are almost identical for different cavity depths. Thus, at low speed, the cavity depth has no significant effect on friction force. At intermediate speed, a deeper cavity generates higher dynamic fluid pressure distribution, causing a lower contact pressure distribution. That is the reason for the maximum friction force reduction occurring with the highest cavity depth. At high speed, the fluid pressure generated by the lower and medium cavity depth patterns are almost identical, and are higher than that generated by the high cavity depth pattern. That causes a higher contact pressure and higher friction force for the 1.50 μm cavity depth cases, compared to the lower cavity depth results.

6.3.3 Effect of Land Area Ratio

Figure 6.18 shows the fluid transport during outstroke and instroke as a function of rod speed for the cavity patterned rod with different land area ratios and for the

smooth rod, under flooded boundary conditions. The surface patterns in these cases are shown in table 6.1 as the cavities with inline round shape, with cavity depth of 1.5 μm. The corresponding distributions with cavity depths of 0.5 μm, and 1.0 μm (not shown) are almost identical, which is consistent with the previous section's results: the cavity depth has no significant effect on fluid transport during both instroke and outstroke. During the outstroke, the fluid transport decreases with decreasing area ratio. During the instroke, the area ratio effect is small.

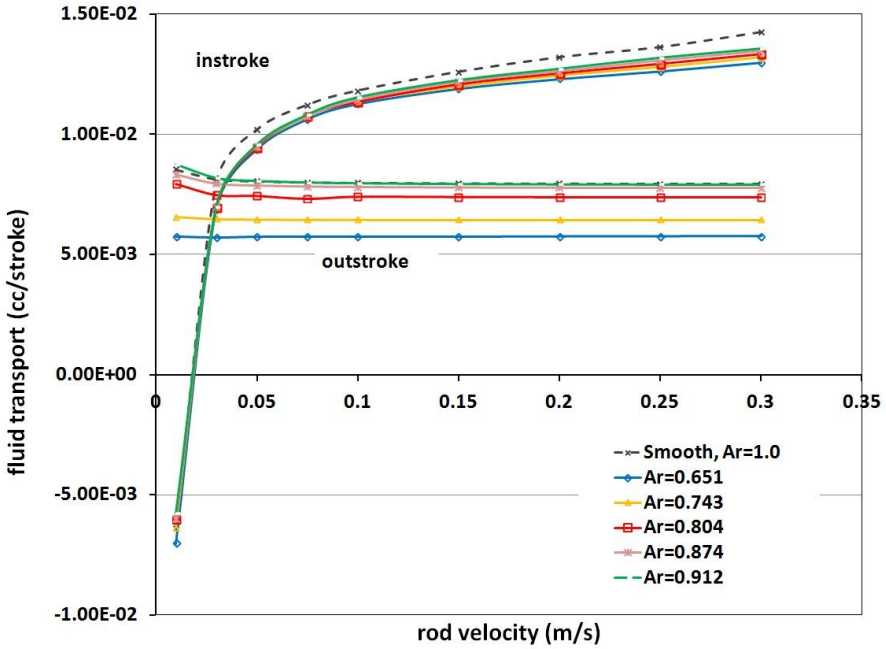

Figure 6.18: Fluid transport, U-cup seal, d=1.50 μm, different land area ratios, flooded boundary conditions

The friction force on the rod, as a function of rod speed is shown in Figures 6.19a, 6.19b, and 6.19c for rods with different land area ratios and the smooth rod, under

flooded boundary conditions. The cavity depths are 0.5 μm, 1.0 μm, and 1.5 μm. During the outstroke, the area ratio has no significant effect on the friction force. During the instroke, the area ratio's effect on friction force is related to cavity depth. With a lower cavity depth (d=0.50 μm), the friction force is relatively the same for the various area ratios at low and medium rod speed; At high rod speed, the friction force decreases with decreasing area ratio. For the intermediate cavity depth (d=1.00 μm), the friction force is almost identical for the various area ratios at low rod speed, At medium and high rod speed, the friction force decreases with decreasing area ratio. The friction force with these cavity depth patterns could be higher than that of the smooth case for some high area ratios, at high rod speed. For a higher cavity depth (d=1.50 μm), the friction force values are very close to each other at the low rod speed. At the medium rod speed, the friction force decreases with decreasing area ratio, and the maximum friction reduction occurs when the rod speed is around 0.1m/s and the area ratio is 0.651 (the smallest), with the 1.50 μm depth of cavities. The largest reduction is about 13%. At high rod speed, the friction forces are similar for various area ratios again, and are higher than that of the smooth rod case.

To explain the fluid transport and friction behavior with the effect of area ratio, it is necessary to examine the details of the sealing zone.

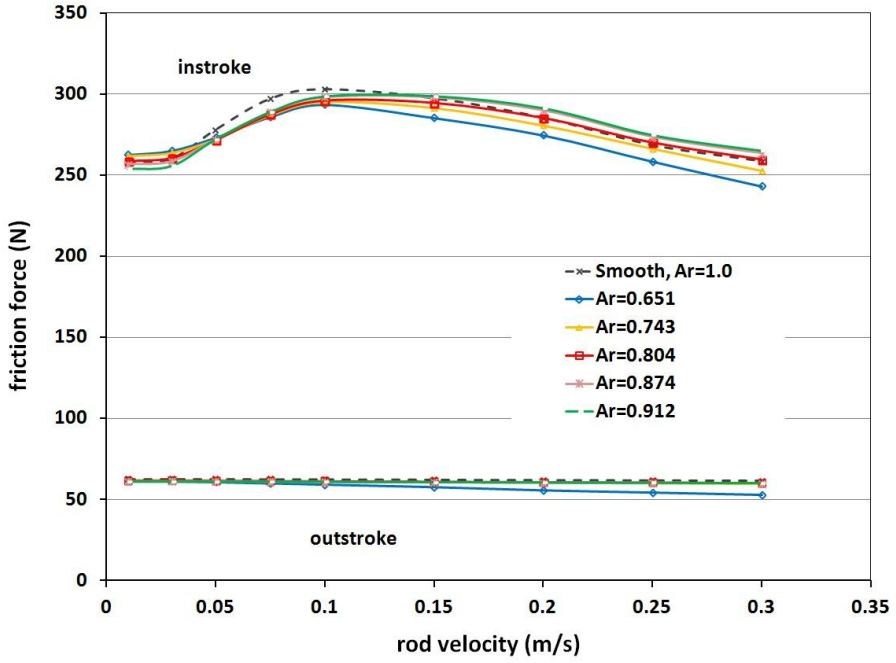

Figure 6.19a: Fluid transport, U-cup seal, d=0.50 µm, different land area ratios, flooded boundary conditions

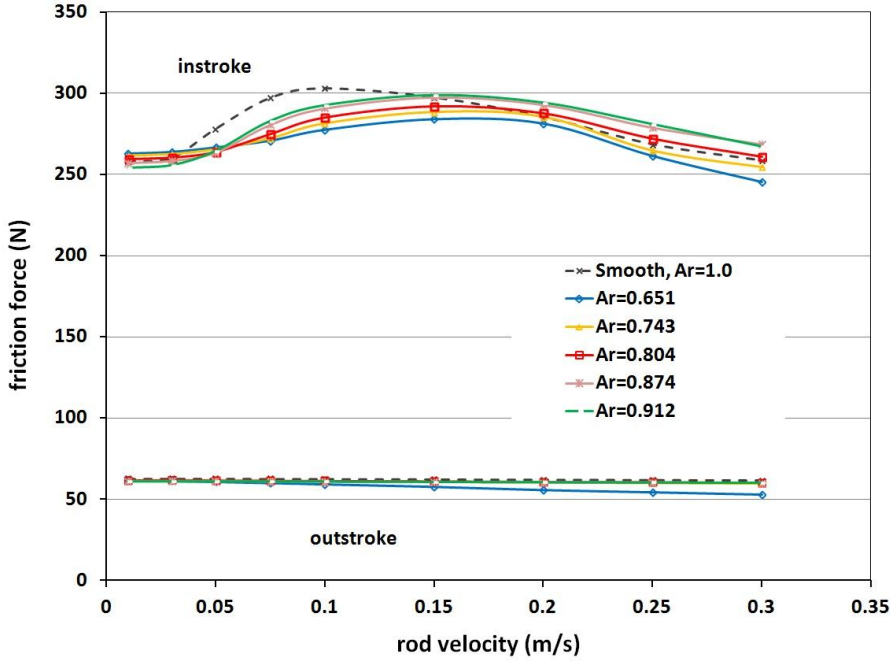

Figure 6.19b: Friction force, U-cup seal, d=1.00 µm, different land area ratios, flooded boundary conditions

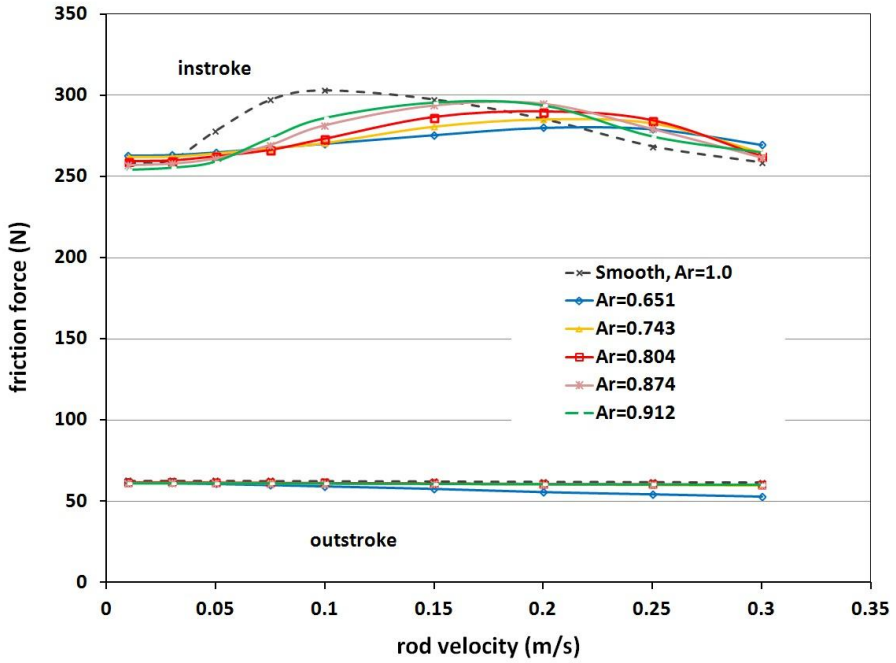

Figure 6.19c: Friction force, U-cup seal, d=1.50 μm, different land area ratios, flooded boundary conditions

Figure 6.20 shows the film thickness distributions during the outstroke at the rod speed of 0.03 m/s, with the cavity depth of 0.50 μm. The corresponding distributions at 0.10 m/s and 0.30 m/s, with the cavity depth of 1.00 μm and 1.50 μm (not shown) are almost identical. These are consistent with the results in the previous section, showing that the cavity depth has no effect on the fluid film at the same area ratio. The film thickness decreases with the decreasing area ratio. Since there is no hydrodynamic effect during the outstroke, the effect of area ratio on the fluid film is only related to the contact pressure, which will be discussed later.

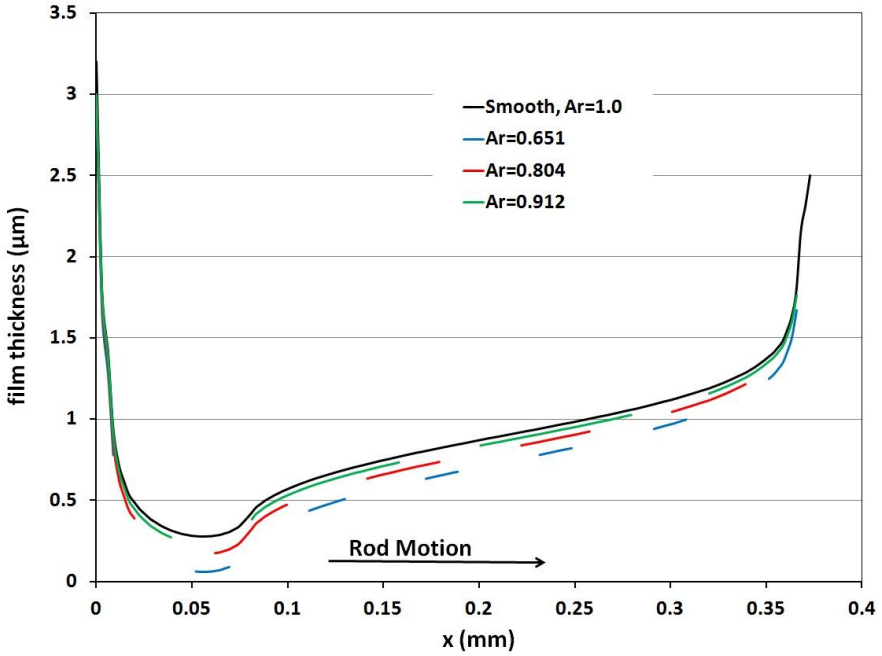

Figure 6.20: Film thickness of outstroke, 0.03 m/s, U-cup seal, d=0.50 µm, different land area ratios

The film thickness distribution during the instroke at rod speeds of 0.03 m/s, 0.10 m/s and 0.30 m/s with a cavity depth of 0.50µm are shown in Figure 6.21a, 6.21b, and 6.21c. The corresponding distribution with the cavity depths of 1.00µm and 1.50µm are very similar and are not shown. These are consistent with the results of the cavity depth effect in the previous section: the cavity depth has only a slight effect on the fluid film, during the instroke. These Figures show that the film thickness distribution decreases with the decreasing of the area ratio. The reason for the area ratio effect on the fluid film will be explained when the contact pressure distributions are discussed.

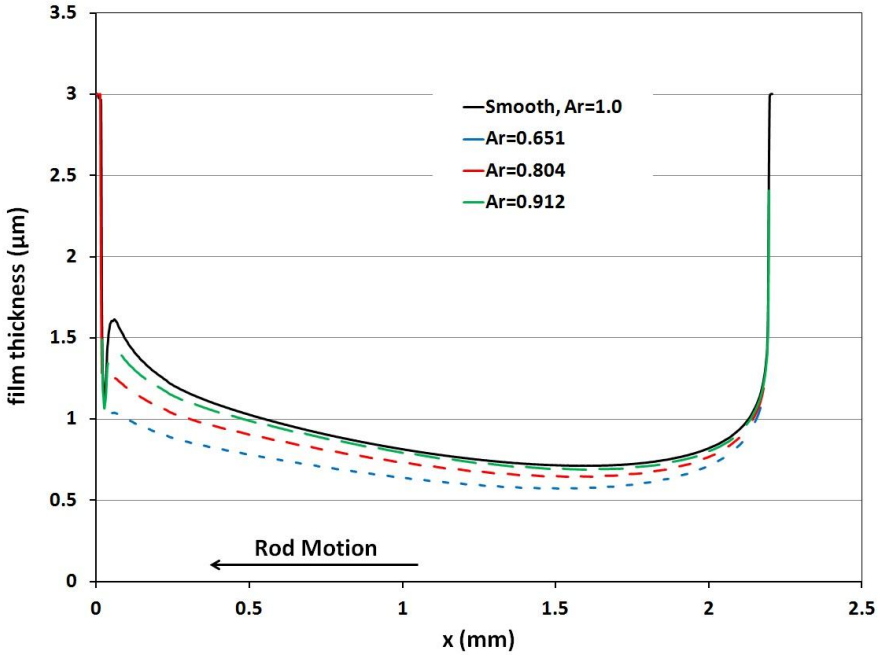

Figure 6.21a: Film thickness of instroke, 0.03 m/s, U-cup seal, d=0.50 µm, different land area ratios, flooded boundary conditions

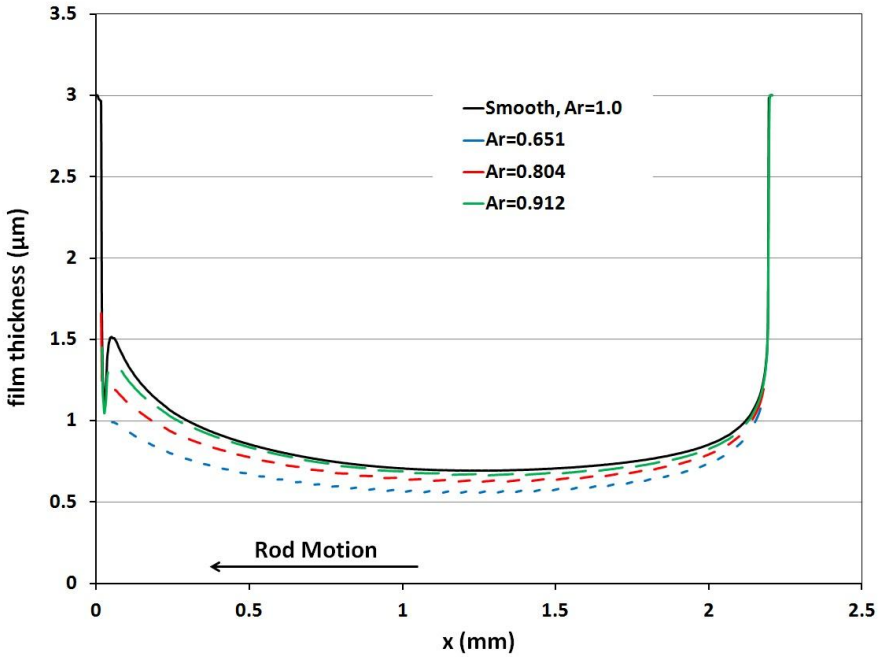

Figure 6.21b: Film thickness of instroke, 0.10 m/s, U-cup seal, d=0.50 µm, different land area ratios, flooded boundary conditions

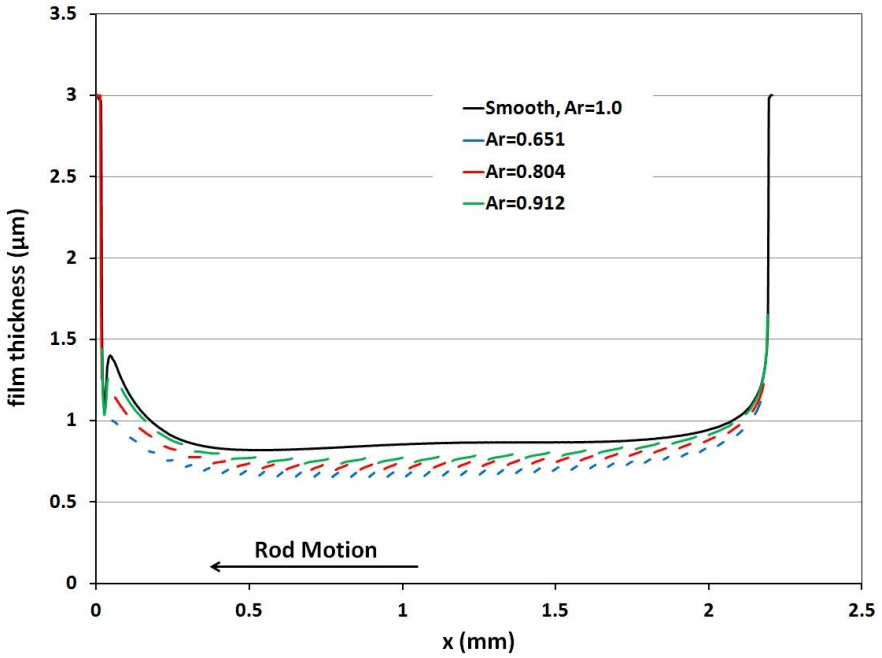

Figure 6.21c: Film thickness of instroke, 0.30 m/s, U-cup seal, d=0.50 μm, different land area ratios, flooded boundary conditions

Figure 6.22 shows the contact pressure and fluid pressure distributions during the outstroke at a rod speed of 0.03 m/s, with a cavity depth of 0.50 μm. The corresponding distributions at 0.10 m/s and 0.30 m/s, with the cavity depths of 1.00 μm and 1.50 μm (not shown) are almost identical. This is consistent with the results in the previous section that the cavity depth has no effect on contact pressure, at the same area ratio. During the outstroke, since the sealed pressure is ambient, fluid cavitation occurs in most of the sealing area. The fluid pressure is zero for most of the region.

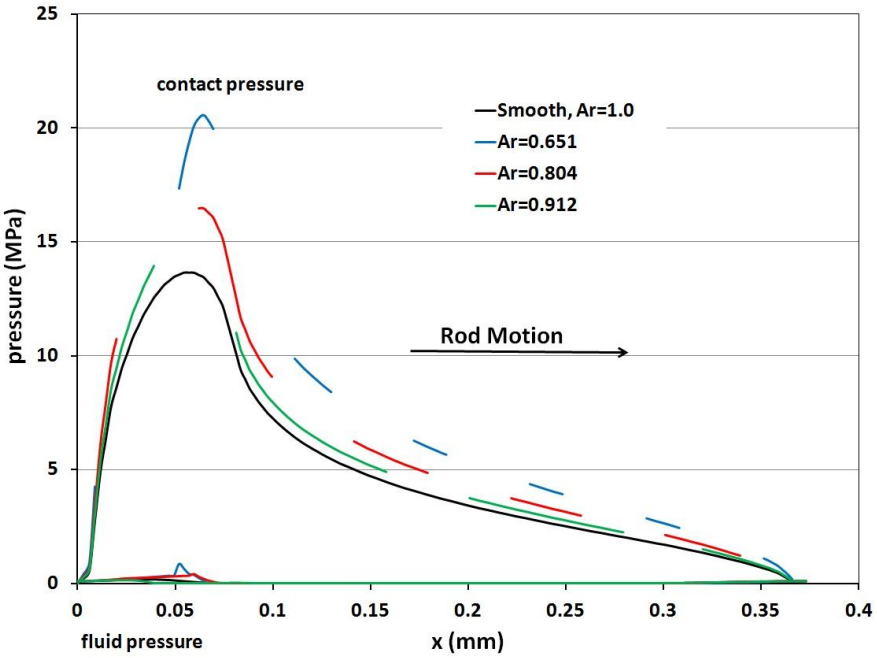

Figure 6.22: Contact and fluid pressure of outstroke, 0.03 m/s, U-cup seal, d=0.50 μm, different land area ratios

From equation 6.7, when P_f=0:

$$P_c = \left\{1 + \frac{\int_{A_{cav}} P_{dc,smooth} dA}{\int_{A_{land}} P_{dc,smooth} dA}\right\} P_{dc,smooth} = \frac{1}{Area\ Ratio} P_{dc,smooth}$$

Therefore, at the land area, the contact pressure should increase with decreasing area ratio, which is shown in Figure 6.22. With the Greenwood-Williamson model, a higher contact pressure causes a thinner contact film. These results are consistent with the film thickness distributions during the outstroke.

The contact and fluid pressure distributions during the instroke are shown in three groups, for different cavity depths. In the first group, Figures 6.23a1, 6.23a2, 6.23b1, 6.23b2, 6.23c1, and 6.23c2 show the contact and fluid pressure distributions

at rod speeds of 0.03 m/s, 0.1 m/s and 0.3 m/s, with the cavity depth of 0.50 μm. The contact pressure at the land area increases with decreasing area ratio at the different speeds. At low and medium rod speeds (0.03 m/s and 0.10 m/s), the area ratios have very little effect on the fluid pressure distributions. At the high rod speed, the lower area ratio case generates higher fluid pressures, while the higher land ratio cases show very small differences in fluid pressure.

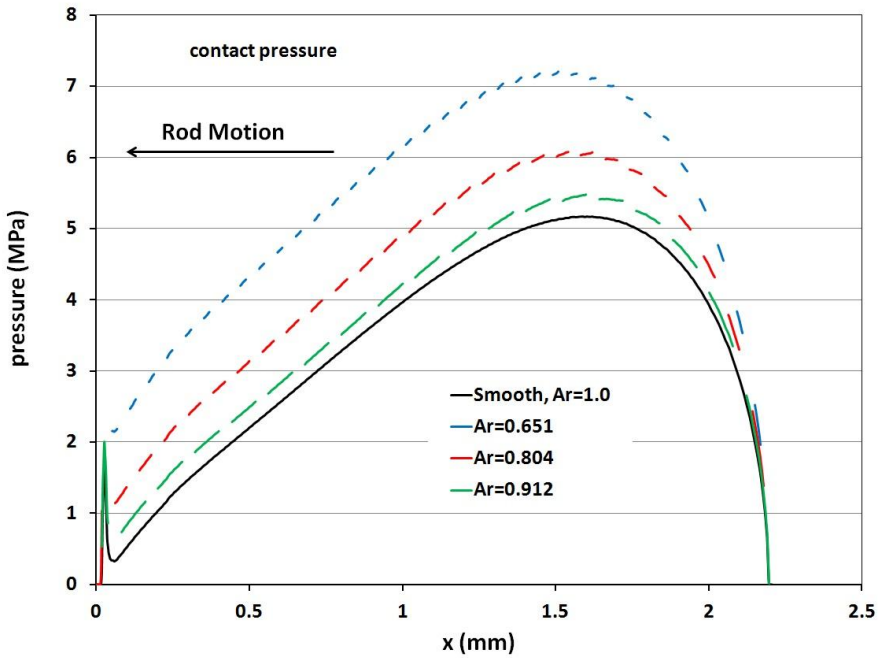

Figure 6.23a1: Contact pressure of instroke, 0.03 m/s, U-cup seal, d=0.50 μm, different land area ratios, flooded boundary conditions

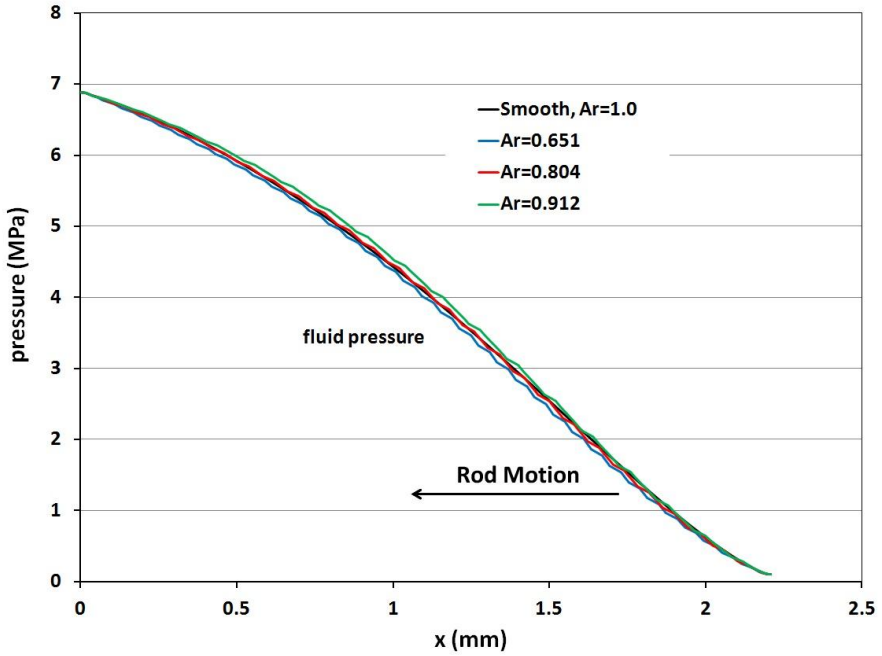

Figure 6.23a2: Fluid pressure of instroke, 0.03 m/s, U-cup seal, d=0.50 μm, different land area ratios, flooded boundary conditions

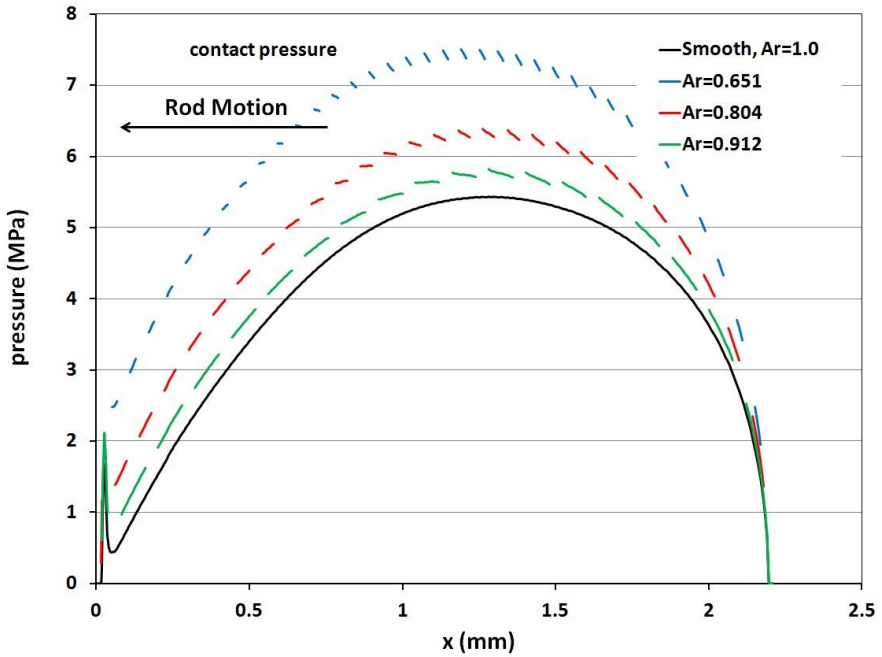

Figure 6.23b1: Contact pressure of instroke, 0.10 m/s, U-cup seal, d=0.50 μm, different land area ratios, flooded boundary conditions

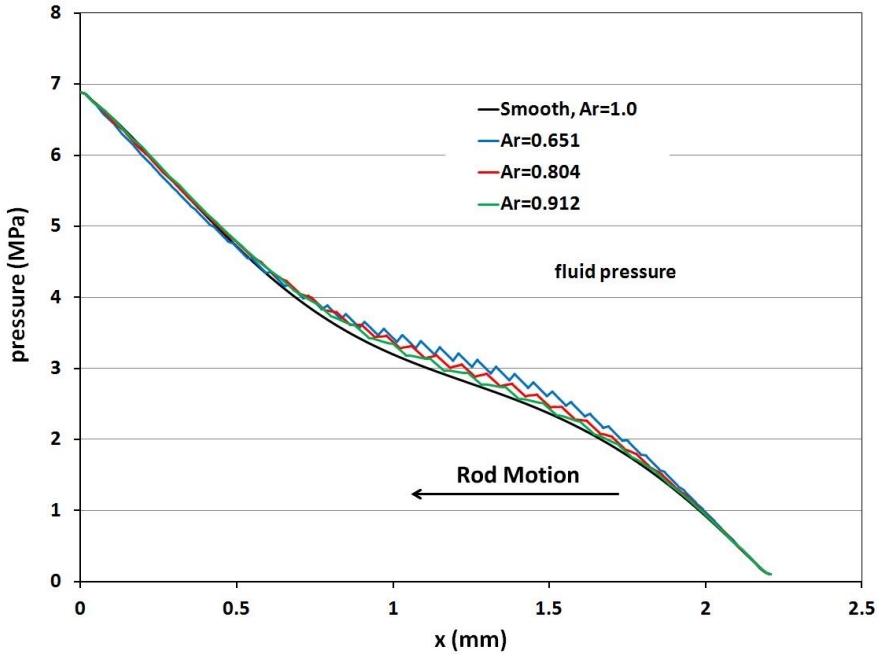

Figure 6.23b2: Fluid pressure of instroke, 0.10 m/s, U-cup seal, d=0.50 µm, different land area ratios, flooded boundary conditions

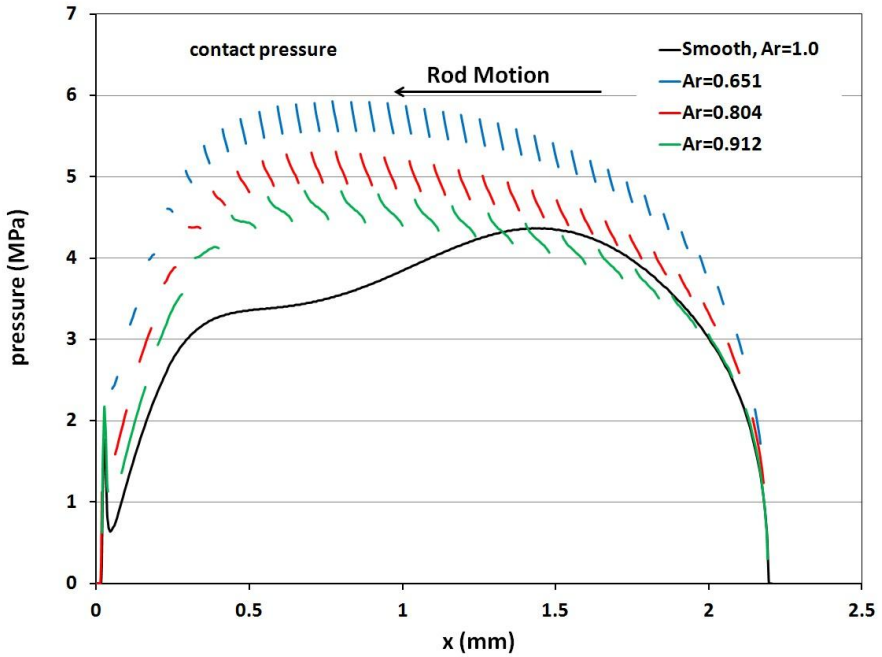

Figure 6.23c1: Contact pressure of instroke, 0.30 m/s, U-cup seal, d=0.50 µm, different land area ratios, flooded boundary conditions

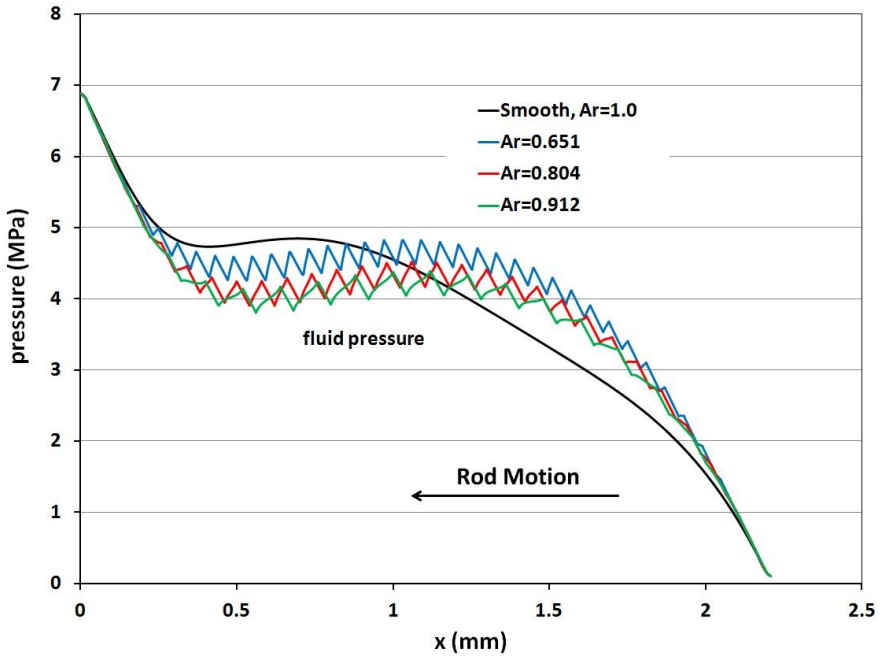

Figure 6.23c2: Fluid pressure of instroke, 0.30 m/s, U-cup seal, d=0.50 μm, different land area ratios, flooded boundary conditions

Still consider equation 6.7. During the instroke, the fluid pressure is not zero, The contact pressure distribution is determined by both fluid pressure and land area ratio:

$$P_c = \left\{1 + \frac{\int_{A_{cav}} P_{dc,smooth} dA}{\int_{A_{land}} P_{dc,smooth} dA} - \frac{\int_{A_{cav}} P_f dA}{\int_{A_{land}} P_{dc,smooth} dA}\right\} P_{dc,smooth} - P_f$$
$$= \left\{\frac{1}{Area\ Ratio} - \frac{\int_{A_{cav}} P_f dA}{\int_{A_{land}} P_{dc,smooth} dA}\right\} P_{dc,smooth} - P_f \quad (6.8)$$

At low and medium rod speeds, the fluid pressures are almost identical for different area ratios. The lower area ratio will have a higher contact pressure. This is consistent with the film thickness distribution results.

Notice that a higher contact pressure at the land area does not necessarily indicate a higher friction, because of the difference in total land area. While the total load is the same for the different cases, and the total load is the sum of the contact pressure and fluid pressure, the contact pressure can be estimated from the fluid pressure distributions. For the cavity depth of the 0.50μm cases, the fluid pressure distributions at low and intermediate rod speeds are almost identical for the various area ratios, while at high speed the fluid pressure increases, but not significantly, with the decreasing area ratio. This indicates that the total contact pressure and friction force, at low and medium rod velocities, are almost the same for different land area ratios. At the high rod speed, the contact pressure and friction force decrease with decreasing area ratio. This is consistent with the friction force results shown earlier.

In the second group, Figures 6.24a1, 6.24a2, 6.24b1, 6.24b2, 6.24c1, and 6.24c2 show the contact and fluid pressure distributions at rod speeds of 0.03 m/s, 0.1 m/s and 0.3 m/s, with the cavity depth of 1.00 μm. These distributions are very similar to that of the 0.50μm cavity depth. The explanation is similar to that discussed above. Note that at the medium rod speed (0.10 m/s) for the 1.00μm cavity depth, the difference between the fluid pressures are more significant than those at the 0.50μm depth. The fluid pressure increases with decreasing area ratio. That is the reason for the effect of the area ratio on the friction force at the medium speed for this cavity depth, as shown in Figure 6.19b.

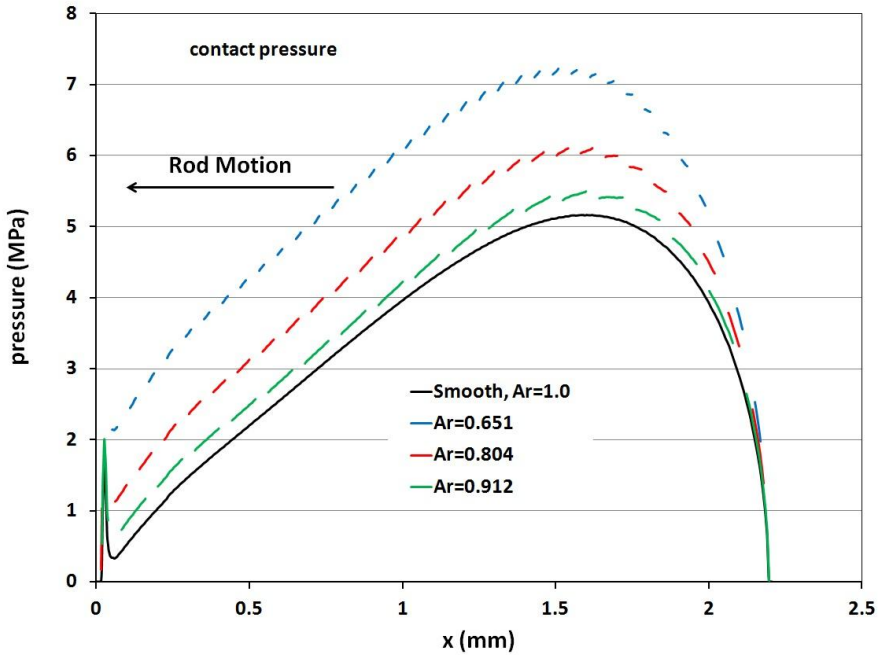

Figure 6.24a1: Contact pressure of instroke, 0.03 m/s, U-cup seal, d=1.00 µm, different land area ratios, flooded boundary conditions

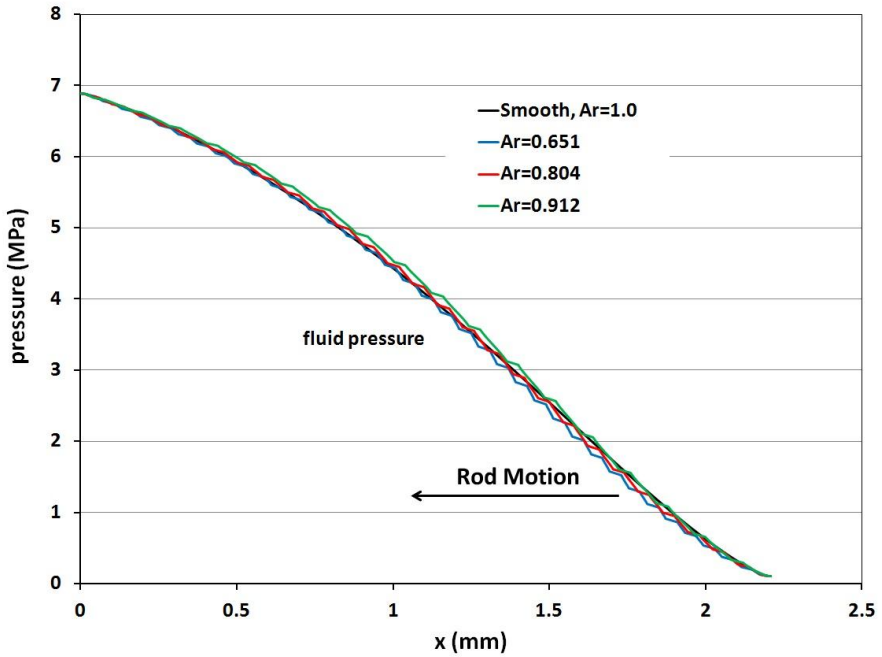

Figure 6.24a2: Fluid pressure of instroke, 0.03 m/s, U-cup seal, d=1.00 µm, different land area ratios, flooded boundary conditions

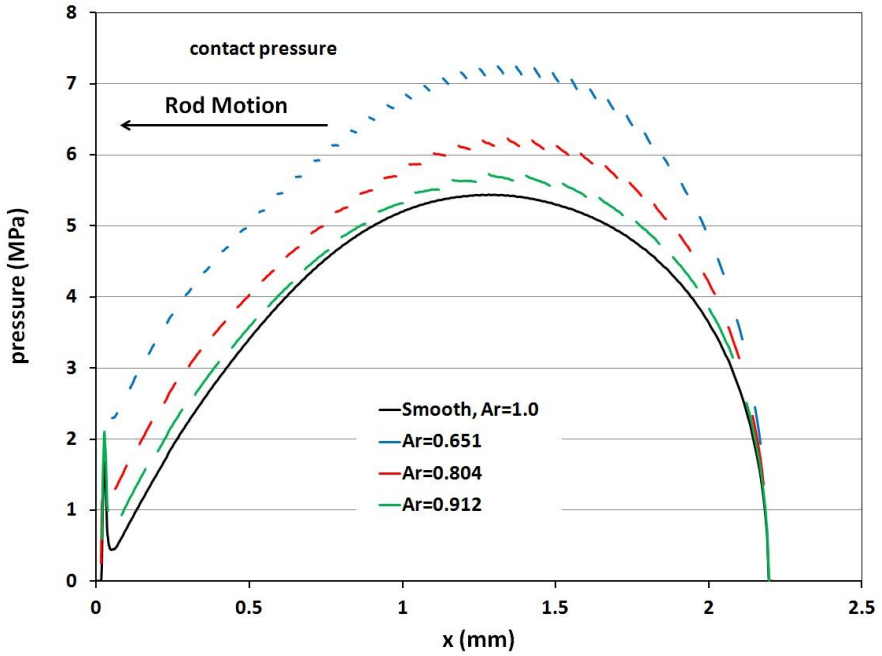

Figure 6.24b1: Contact pressure of instroke, 0.10 m/s, U-cup seal, d=1.00 µm, different land area ratios, flooded boundary conditions

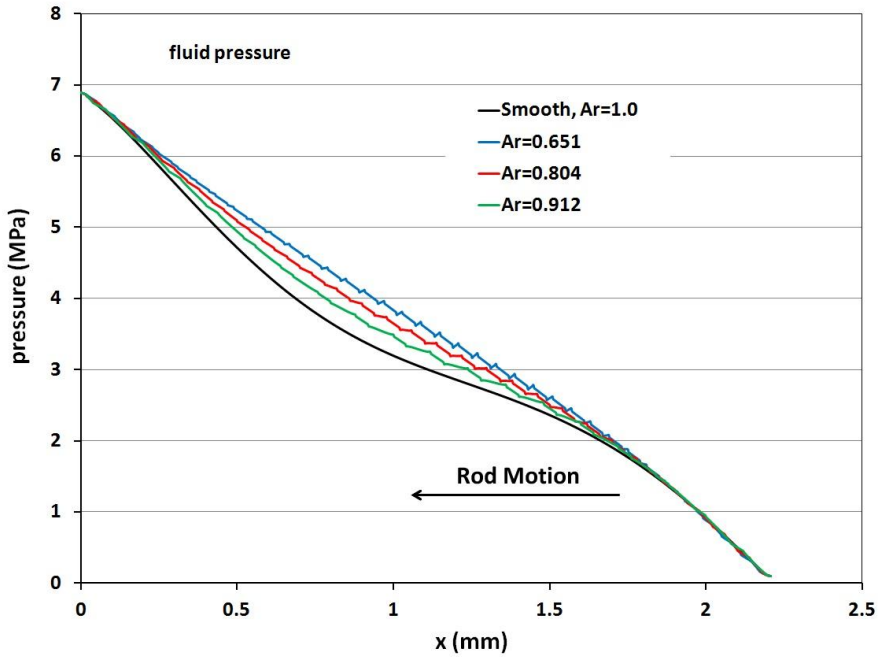

Figure 6.24b2: Fluid pressure of instroke, 0.10 m/s, U-cup seal, d=1.00 µm, different land area ratios, flooded boundary conditions

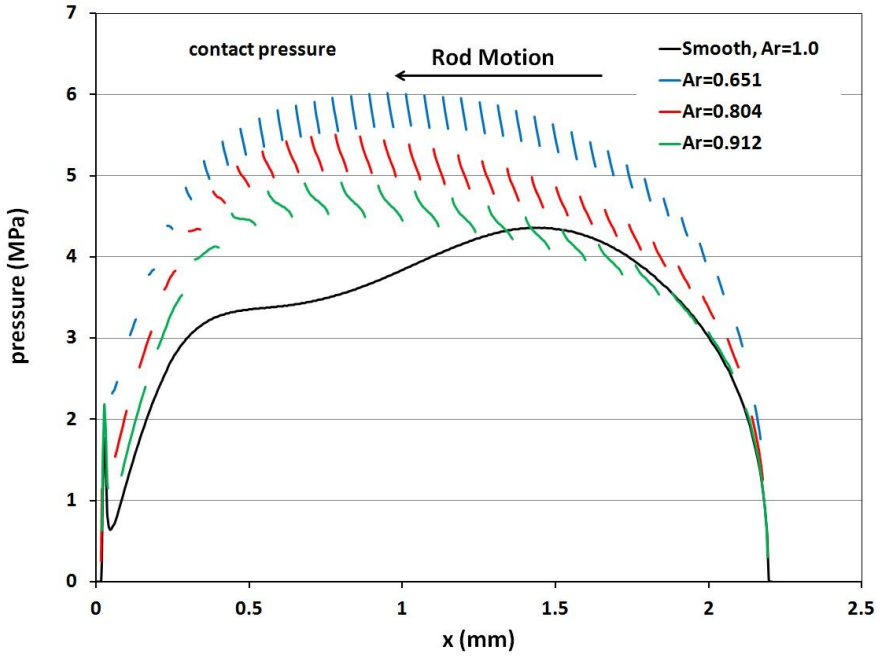

Figure 6.24c1: Contact pressure of instroke, 0.30 m/s, U-cup seal, d=1.00 µm, different land area ratios, flooded boundary conditions

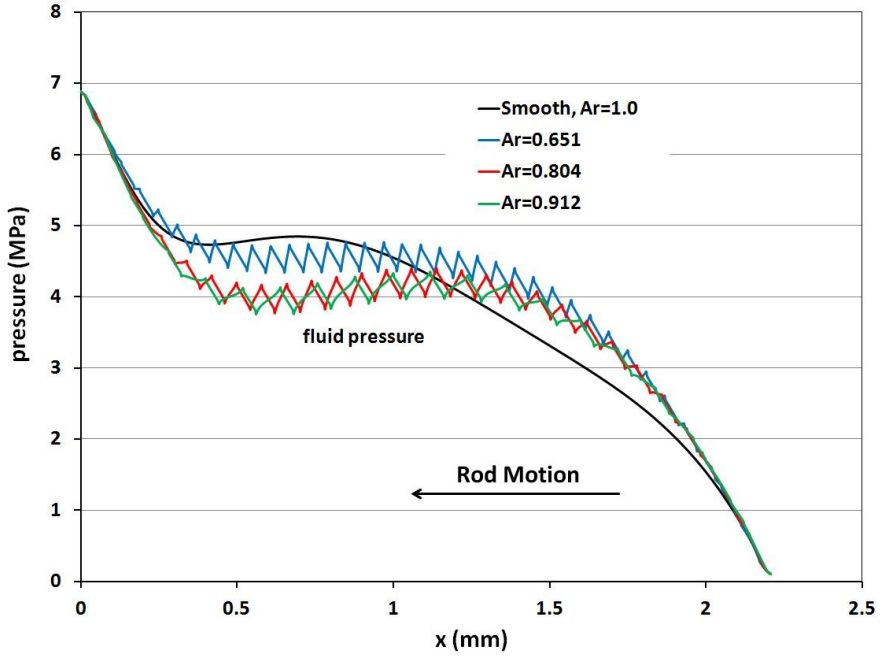

Figure 6.24c2: Fluid pressure of instroke, 0.30 m/s, U-cup seal, d=1.00 µm, different land area ratios, flooded boundary conditions

In the third group, Figures 6.25a1, 6.25a2, 6.25b1, 6.25b2, 6.25c1, and 6.25c2 show the contact and fluid pressure distributions at rod speeds of 0.03 m/s, 0.1 m/s and 0.3 m/s, with the cavity depth of 1.50 μm. At low and medium rod speed, the contact pressure and fluid pressure distributions are very similar to that with the cavity depth of 1.00μm, with the same explanations. Note that the fluid pressure distribution of Ar=0.651, at the rod speed of 0.10 m/s with the cavity depth of 1.50μm has the largest increase compared to the smooth cases, that causes the largest friction reduction (Figure 6.19c). At the high rod speed with the cavity depth of 1.50 μm, the fluid pressure is slightly lower than that of the smooth case, and the variation of fluid pressure with area ratio is insignificant. These results are consistent with the friction results, shown in Figure 6.19c.

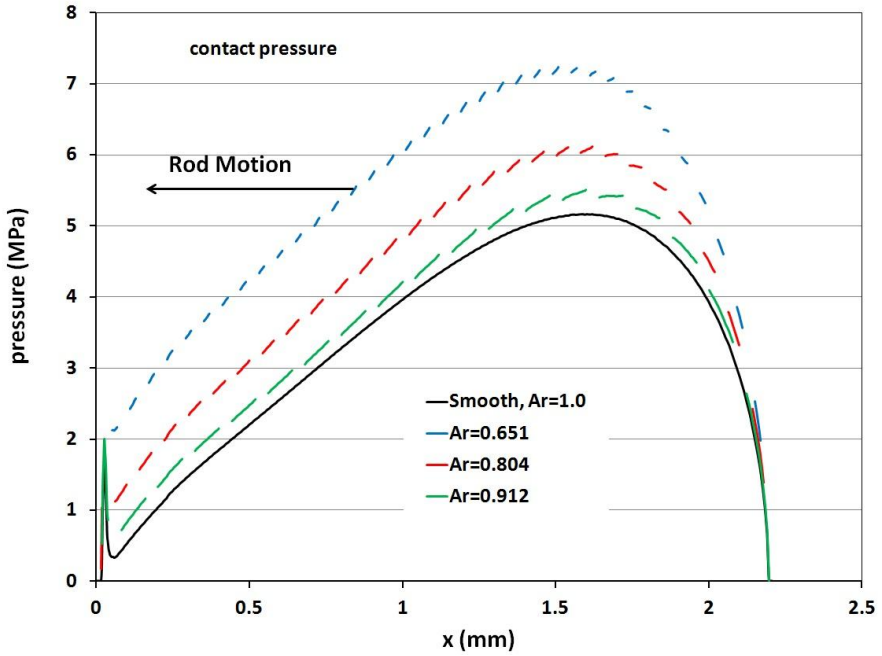

Figure 6.25a1: Contact pressure of instroke, 0.03 m/s, U-cup seal, d=1.50 µm, different land area ratios, flooded boundary conditions

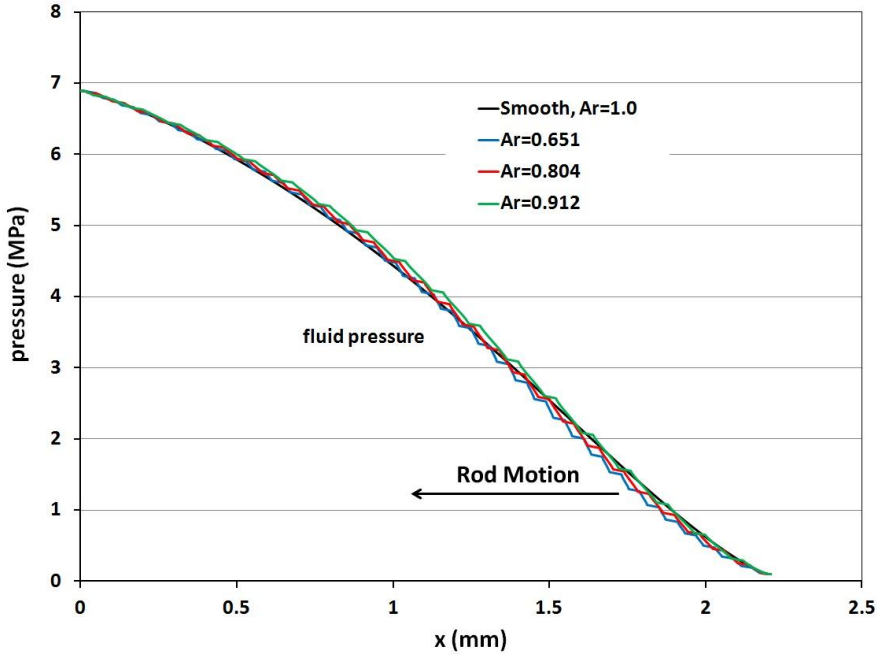

Figure 6.25a2: Fluid pressure of instroke, 0.03 m/s, U-cup seal, d=1.50 µm, different land area ratios, flooded boundary conditions

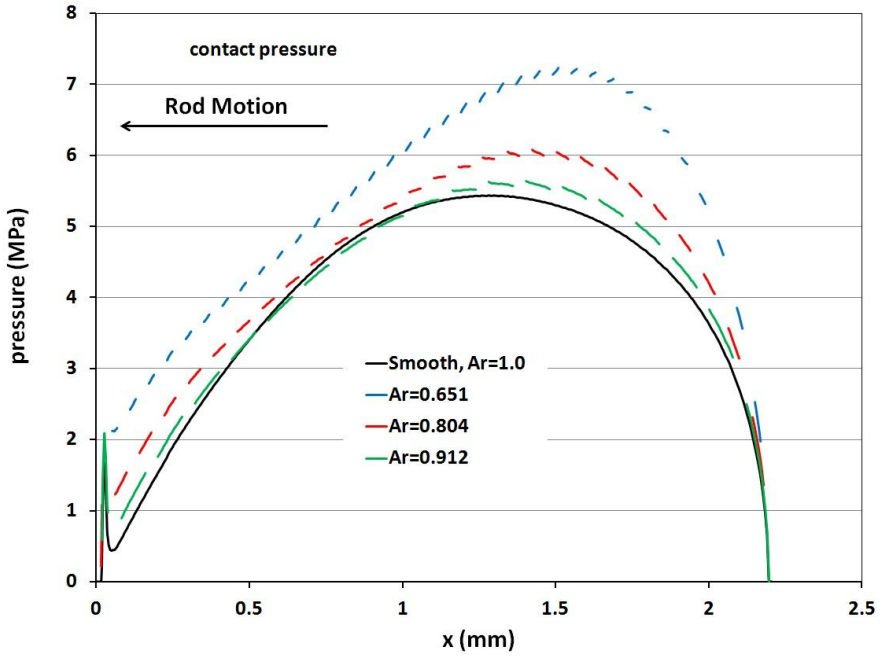

Figure 6.25b1: Contact pressure of instroke, 0.10 m/s, U-cup seal, d=1.50 µm, different land area ratios, flooded boundary conditions

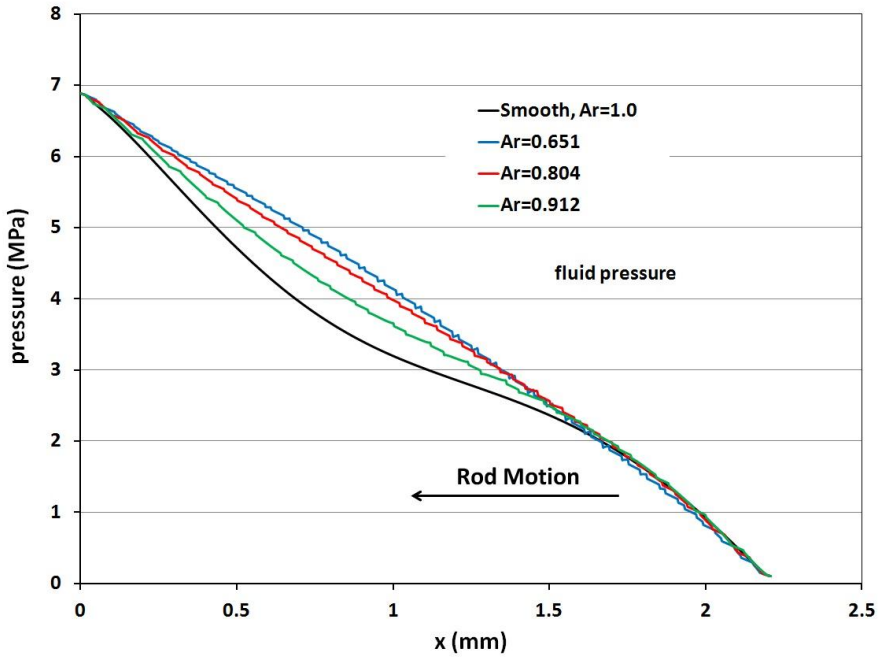

Figure 6.25b2: Fluid pressure of instroke, 0.10 m/s, U-cup seal, d=1.50 µm, different land area ratios, flooded boundary conditions

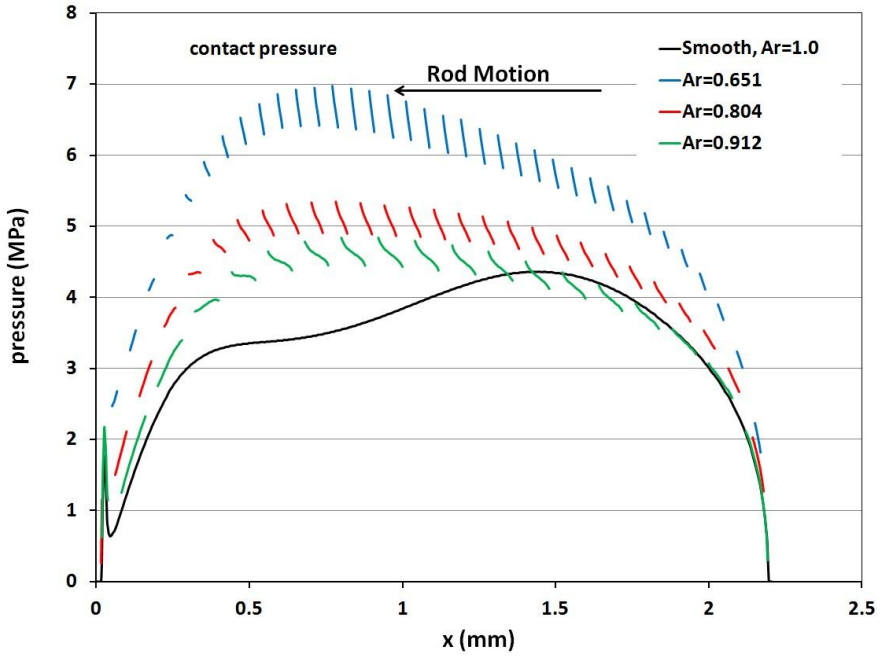

Figure 6.25c1: Contact pressure of instroke, 0.30 m/s, U-cup seal, d=1.50 µm, different land area ratios, flooded boundary conditions

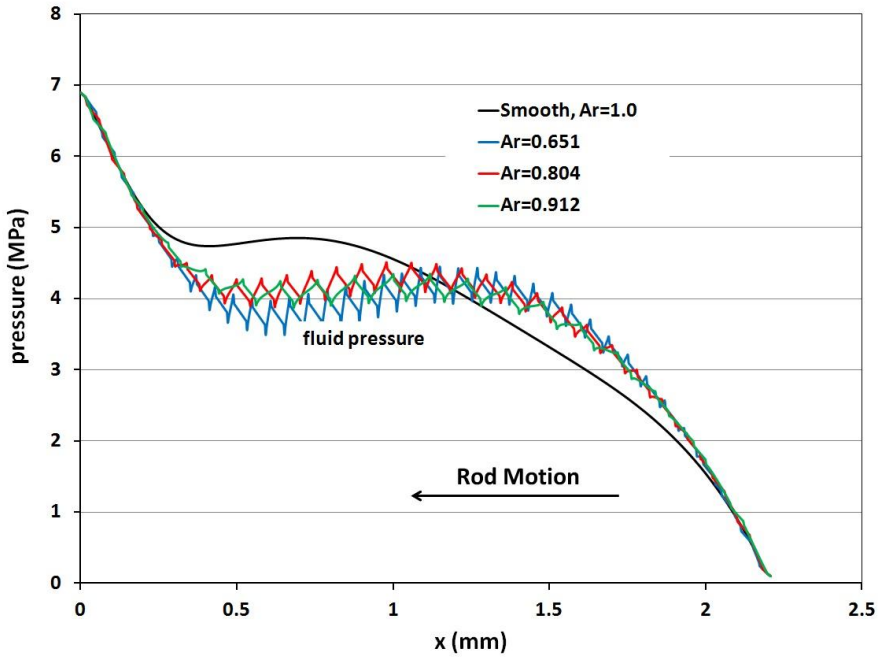

Figure 6.25c2: Fluid pressure of instroke, 0.30 m/s, U-cup seal, d=1.50 µm, different land area ratios, flooded boundary conditions

The effect of area ratio can now be summarized. During the outstroke, the fluid transport decreases with decreasing area ratio, while the area ratio has no significant effect on friction force. The area ratio changed the land area film thickness by changing the contact pressure per land area. The different land area film thickness determines the outstroke fluid transport. The area ratio could not change the total contact force due the load balance. It also could not affect the dynamic pressure due to the large cavitation occurring during the outstroke. Those are the reason that area ratio has no significant effect on friction force. During the instroke, the area ratio does not have significant effect on the fluid transport because the area ratio affects both the fluid film and fluid pressure in opposite ways. These two factors have counter effects on the fluid transport and the net result is no difference between the various area ratio cases. The area ratio has effects on the friction force, which depend on the cavity depths, and are mainly determined by the fluid pressure generated. The largest friction reduction of 13% occurs at the rod speed of 0.1 m/s, with an area ratio of 0.651 and the cavity depth of 1.50μm in this research.

6.3.4 Effect of Cavity Shape

Figure 6.26 shows the fluid transport during the outstroke and instroke as a function of rod speed with different cavity depths, for different cavity shapes. The surface patterns in these cases are shown in table 6.1 as the cavities with inline round shape and cavities with inline equilateral triangle shape (round and triangle in the plots). The land area ratio for these cases is 0.651. The curves for the different

shapes generally lie on top of each other, indicating that the shape of the cavities produces no significant effect on the fluid transport.

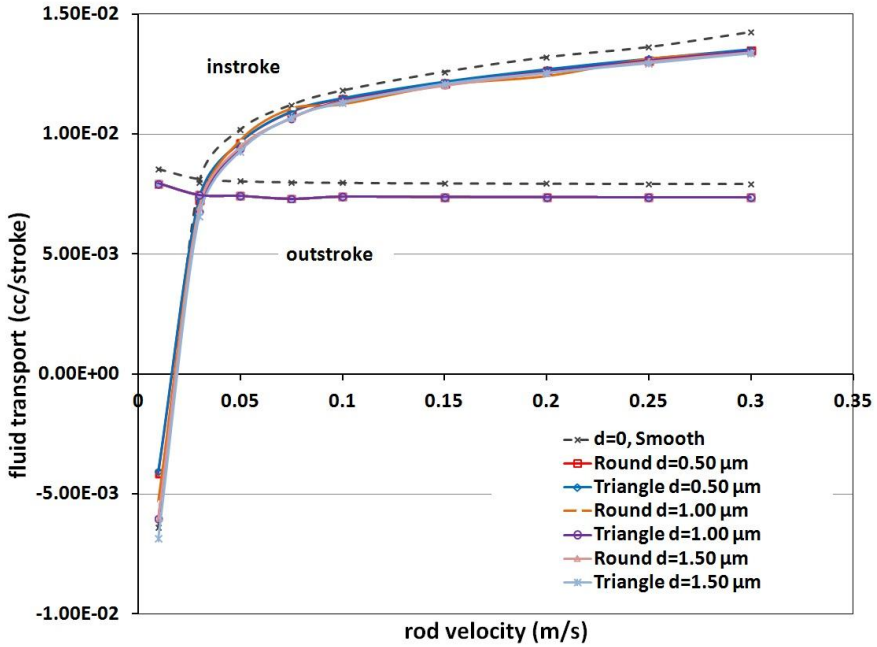

Figure 6.26: Fluid transport, U-cup seal, different cavity shapes, flooded boundary conditions

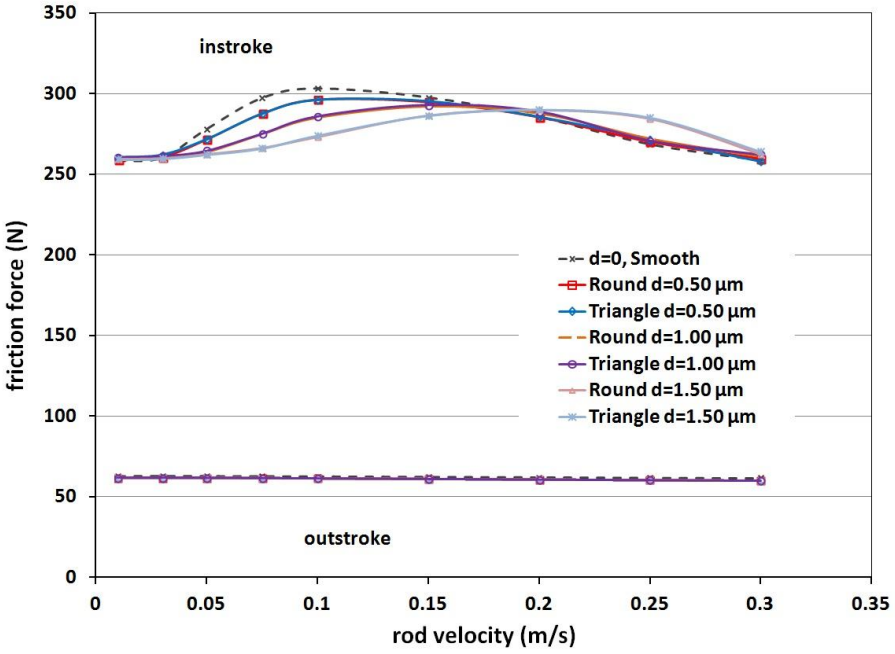

Figure 6.27: Friction force, U-cup seal, different cavity shapes, flooded boundary conditions

The friction force on the rod as a function of rod speed is shown in Figure 6.27 for the different cavity shapse, with various cavity depths. For the same cavity depth, the cavity shapes has no effect on the friction force for both outstroke and instroke.

6.3.5 Effect of Cavity Size

Figure 6.28 shows the fluid transport during the outstroke and instroke as a function of rod speed with different cavity sizes (radius of the round shape), with the cavity depth of 1.50µm and the land area ratio of 0.651. The surface patterns in these cases are shown in table 6.1 as the cavities with inline round shape. During the

outstroke, the fluid transport increases slightly with the increasing radius. The size of the cavity affects the shape of the inlet during the outstroke. Since most of the outstroke sealing area is cavitated, the fluid transport is mainly determined by the shape of the inlet fluid film, thus affecting the fluid transport slightly. During the instroke, the curves for the different radii generally lie on top of each other, indicating that the shape of the cavities produces no significant effect on the fluid transport during the instroke.

The friction force on the rod, as a function of rod speed is shown in Figure 6.29 for different cavity sizes. The cavity radius has no effect on the friction force for both outstroke and instroke. Notice that R=20μm is the size in most of the previous cases in this study if it is not specified.

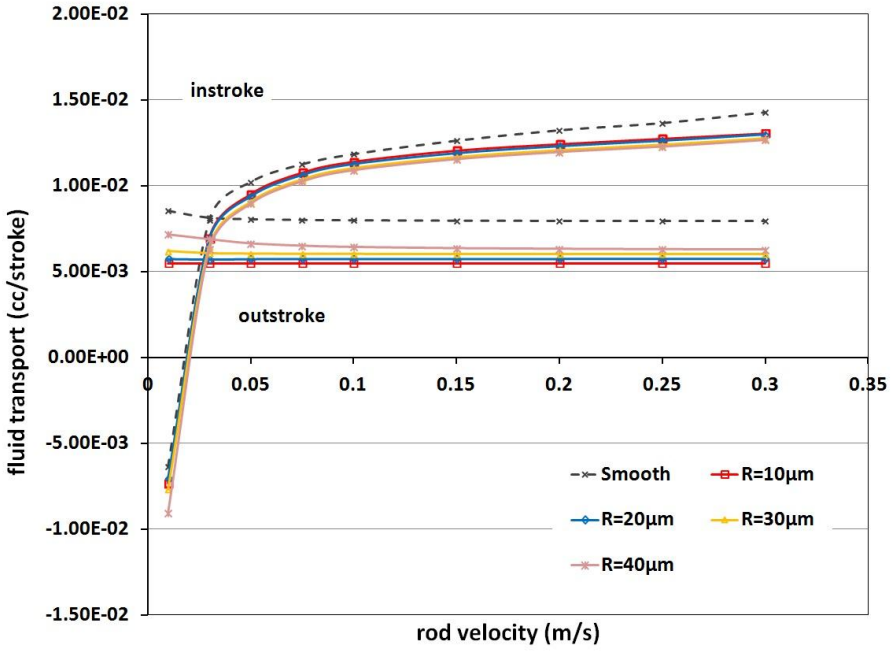

Figure 6.28: Fluid transport, U-cup seal, different cavity radii, flooded boundary conditions

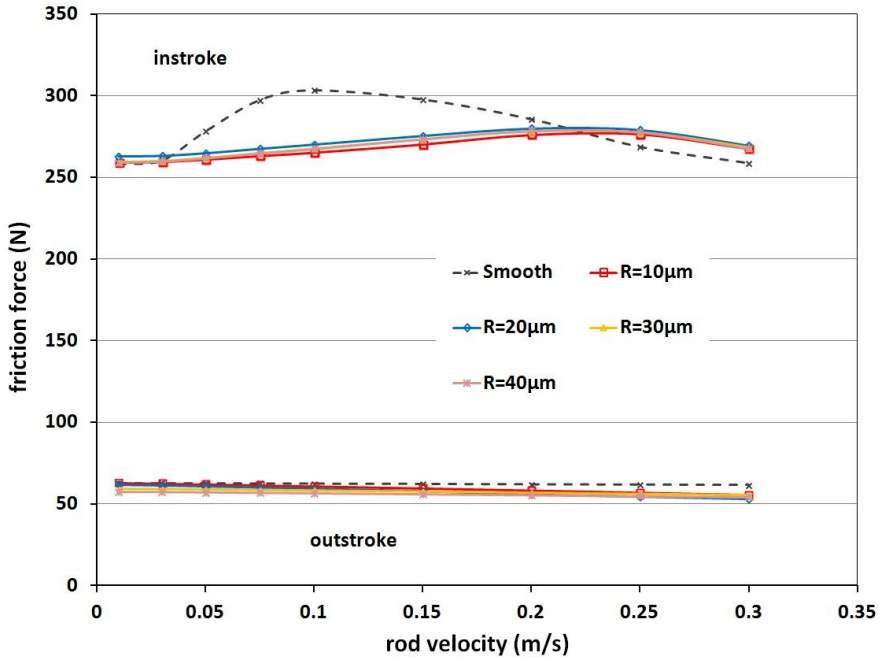

Figure 6.29: Friction force, U-cup seal, different cavity radii, flooded boundary conditions

6.3.6 Effect of Pattern Arrangement

Figure 6.30 shows the fluid transport during the outstroke and instroke as a function of rod speed with different cavity arrangements. The surface patterns in these cases are shown in table 6.1 as the cavities with inline round shape and cavities with staggered round shape, (inline round and staggered round in the plots). The land area ratio for these cases is 0.651, and the cavity depth is 1.50µm. The curves for the different arrangements generally lie on top of each other, indicating that the arrangement of cavities produces no significant effect on the fluid transport.

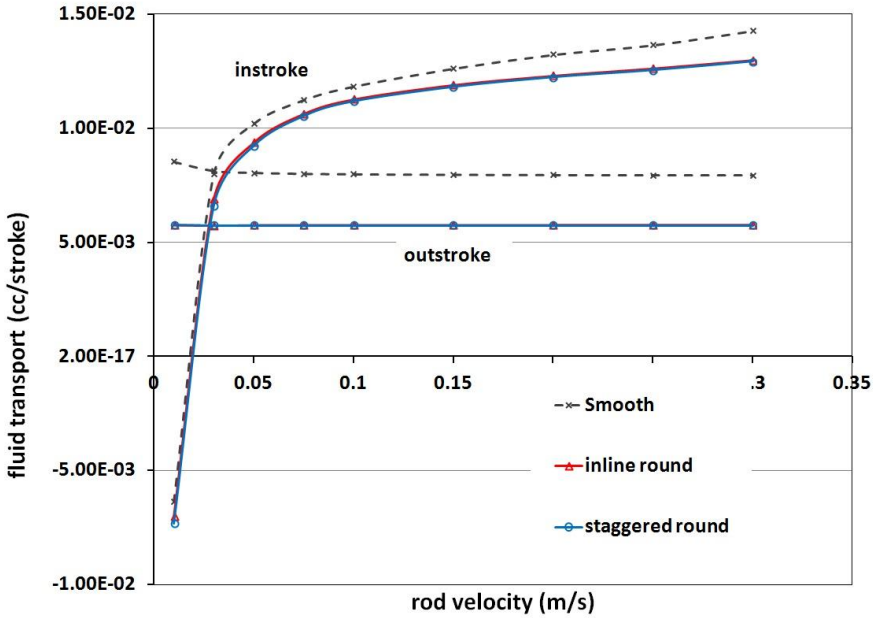

Figure 6.30: Fluid transport, U-cup seal, different cavity arrangements, flooded boundary conditions

The friction force on the rod, as a function of rod speed is shown in Figure 6.31 for different cavity arrangements. The cavity arrangement has no effect on the friction force for both outstroke and instroke.

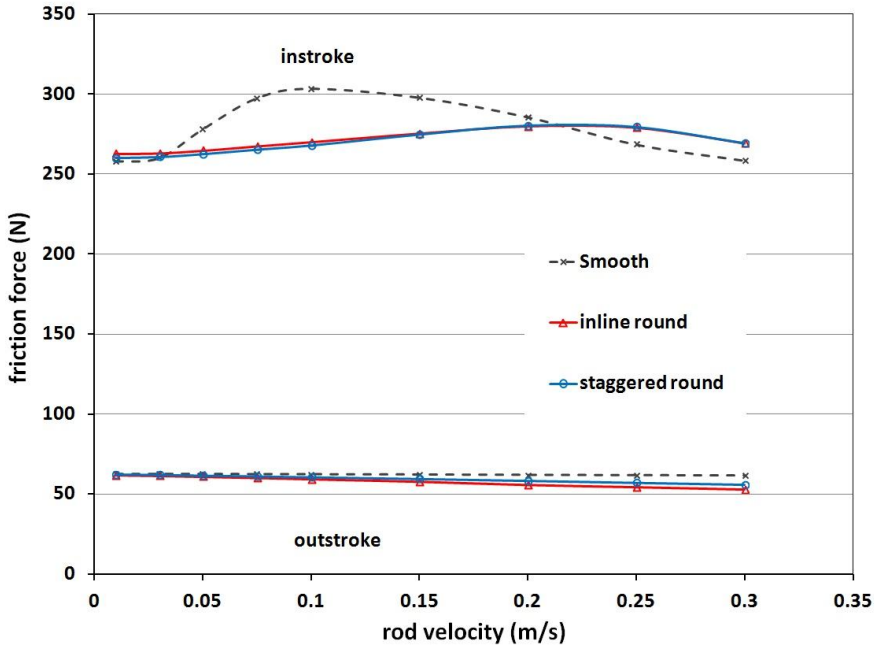

Figure 6.31: Friction force, U-cup seal, different cavity arrangements, flooded boundary conditions

6.3.7 Summary

For the U-cup seal with a cavity patterned rod under flooded boundary conditions, the time steps, the shape of the cavity, the size of the cavity, and the arrangement of the cavities have no significant effect on fluid transport or friction force. The cavity depth and the land area ratio can affect the fluid transport and friction force behavior. Under flooded boundary conditions, the cavity pattern can reduce the friction force on the rod, depending on rod speed, cavity depth and area ratio, with a maximum friction reduction of 13% in this research.

6.4 Cavity Pattern with Starved Boundary

The rods with cavity patterns and with starved boundary conditions are simulated and compared with the smooth rod results with starved boundary conditions, below. Since only cavity depth and land area ratio are expected to have significant effects on seal performance, only these two parameters are discussed.

6.4.1 Effect of Cavity Depth with Starved Boundary

Figure 6.32 shows the fluid transport during outstroke and instroke as a function of rod speed for the cavity patterned rod with different cavity depths and the smooth rod, under starved boundary conditions. The surface patterns in these cases are shown in table 6.1 as the cavities with inline round shape, with a land area ratio of 0.651. The results for the smooth cases with starvation have been discussed in chapter 4. The outstroke transport behavior is just the same as in the flooded cases shown in the previous section, because there is no starvation during the outstroke. The critical speed of the cavity patterned rod is close to that of the smooth rod, but slightly higher. At 0.03 m/s rod speed, starvation occurs for the cavity cases, but not for the smooth cases. From Figure 6.8, the results with flooded boundary conditions, it is seen that the degrees of starvation (difference between the fluid transport during instroke and outstroke under flooded conditions, see section 5.3.3) for the cavity cases are larger than that of the smooth case, due to the higher fluid transport reduction effect of the cavity patterns (the effect of area ratio) on outstroke than that on instroke.

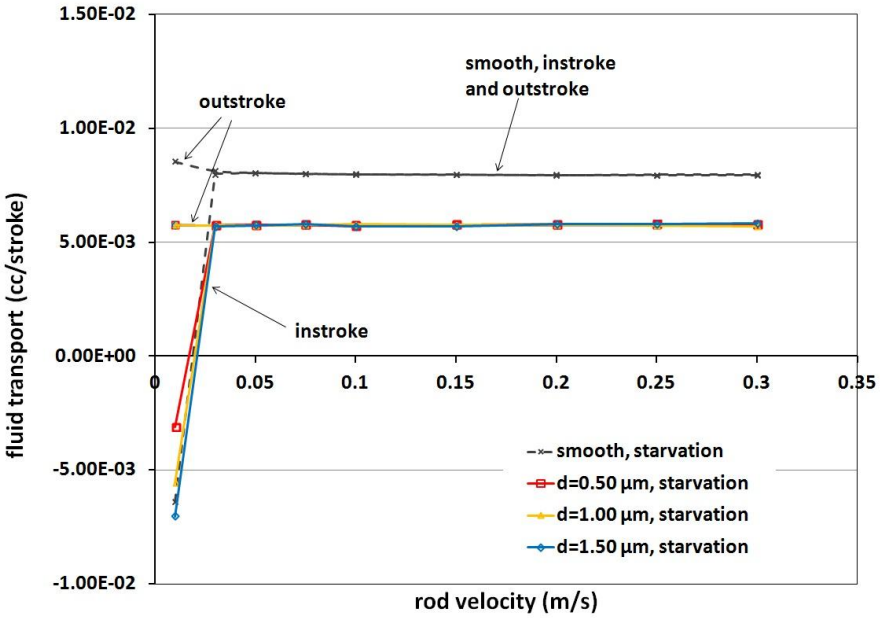

Figure 6.32: Fluid transport, U-cup seal, different cavity depths, starved boundary conditions

The friction force on the rod, as a function of rod speed, under starved boundary conditions, is shown in Figure 6.33. During the outstroke, the friction force behavior for both the smooth rod and plunge-ground rod are exactly the same as the flooded cases. During the instroke, the friction force behaviors of the cavity cases are similar to that of the smooth rod with starved boundary conditions. These friction forces results are much higher than under flooded boundary conditions, this difference between starved and flooded boundary conditions has been explained in chapter 4. The friction forces of the cavity cases are higher than that of the smooth rod. At the same speed, the friction force increases slightly with decreasing cavity depth. At the high rod speed, the differences between the various cavity depths are not significant. From the friction force plots, it also can be seen that at the 0.03 m/s rod speed,

starvation occurs for the cavity cases, but not for the smooth cases, which is consistent with the fluid transport results.

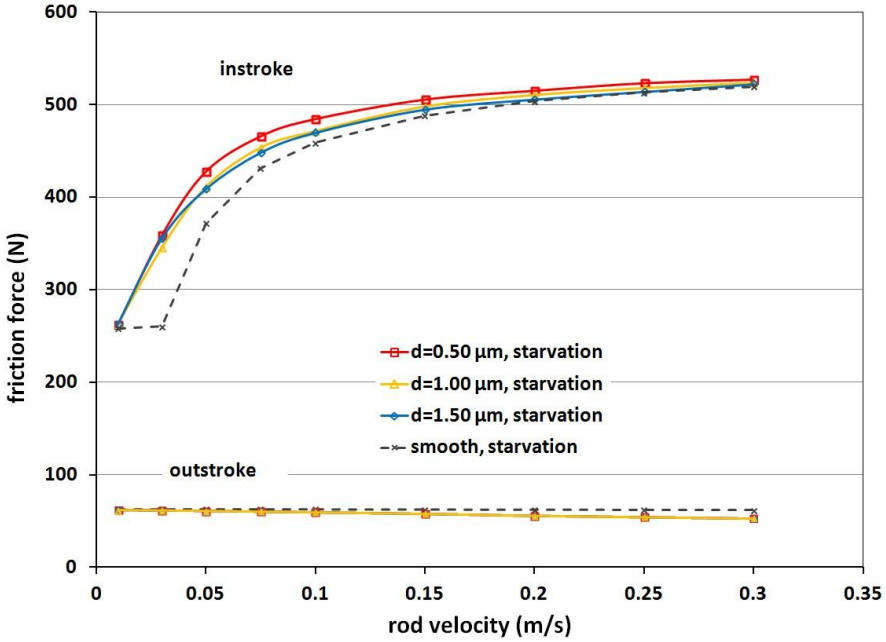

Figure 6.33: Friction force, U-cup seal, different cavity depths, starved boundary conditions

To explain the fluid transport and friction force behavior with the starved boundary, the details of the sealing zone are examined.

The film thickness distributions during the instroke at rod speeds of 0.03 m/s, 0.1 m/s, and 0.3 m/s are shown in Figures 6.34a, 6.34b, and 6.34c, respectively. At the rod speed of 0.03 m/s, which is lower than the critical speed of the smooth case, but higher than the critical speed of the cavity cases, starvation only occurs for the cavity cases. The starvation area of the 0.50 µm depth is longer than the other two. From Figure 6.8

it can be seen that the degree of starvation for the 0.50 μm depth case is larger than the other two cases. At the rod speed of 0.10 m/s, both cavity and smooth cases show significant starvation. The cavity cases have longer starvation zones than that of the smooth case. Also, the starvation area grows longer with decreasing cavity depth. Although the degrees of starvation have no significant difference at this speed in Figure 6.8, the fluid pressure distribution, which will be discussed below, also affects the starvation behavior. Still, the degrees of starvation for the cavity cases are larger than that of the smooth case, causing the longer starvation area for the cavity cases. At the rod speed of 0.30 m/s, the starvation area dominates the sealing zone for both cavity cases and the smooth case. The lengths of the starvation area (or pressurized zone) are almost identical for the various cavity depth cases.

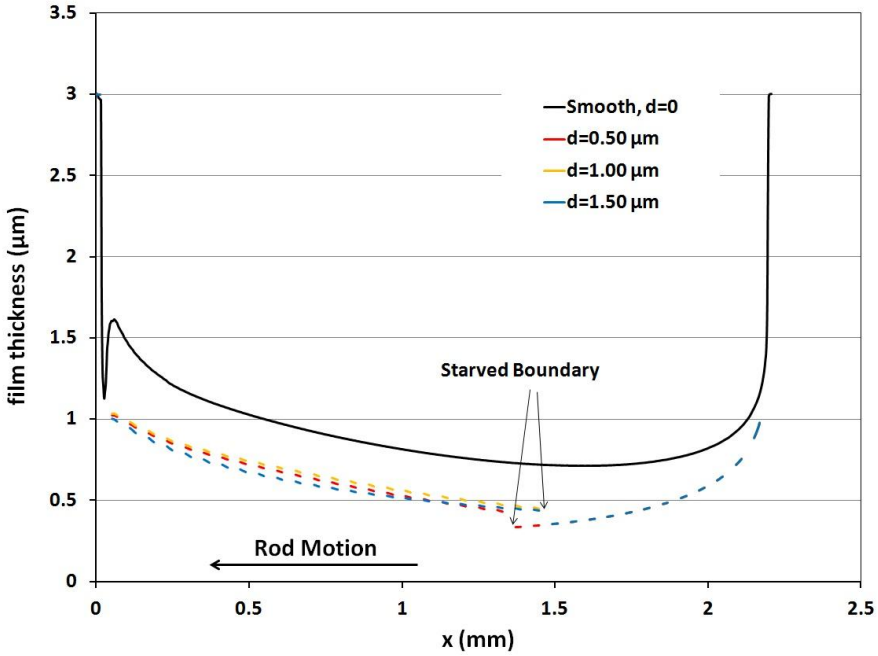

Figure 6.34a: Film thickness of instroke, 0.03 m/s, U-cup seal, different cavity depths, starved boundary conditions

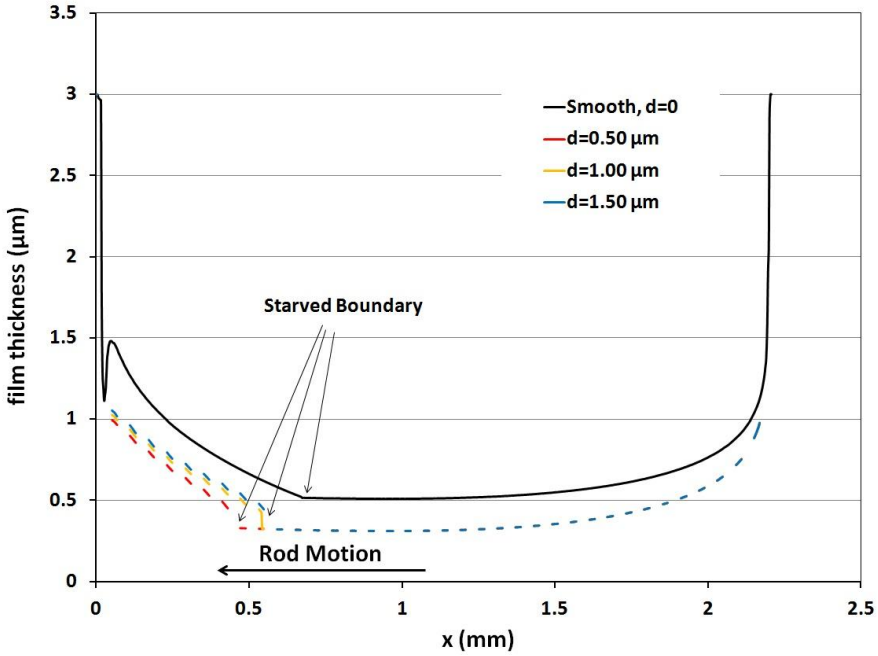

Figure 6.34b: Film thickness of instroke, 0.10 m/s, U-cup seal, different cavity depths, starved boundary conditions

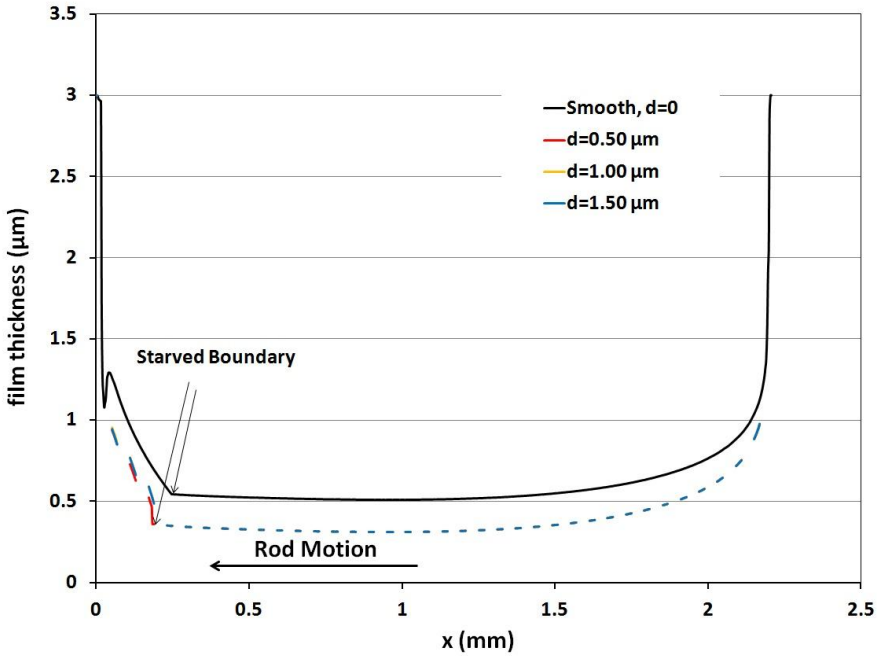

Figure 6.34c: Film thickness of instroke, 0.30 m/s, U-cup seal, different cavity depths, starved boundary conditions

Figures 6.35a1, 6.35a2, 6.35b1, 6.35b2, 6.35c1, and 6.35c2 show the contact pressure and fluid pressure distributions during the instroke at rod speeds of 0.03 m/s, 0.10 m/s, and 0.30 m/s under the starved boundary conditions. At the 0.03 m/s speed, the contact pressure of the 0.50 μm depth case is higher than the other two because of the longer starvation area. The fluid pressure of the 0.50 μm depth case is lower than the other two for the same reason. There is no starvation at this speed for the smooth case. Therefore the fluid pressure of the smooth case is significantly larger than that of the cavity cases. At the 0.10 m/s speed, starvation occurs for both the smooth rod and the cavity rod. The starvation area increases with decreasing cavity depth at this speed. The fluid pressure decreases, while the contact pressure increases with decreasing cavity depth. At the 0.30 m/s speed, there are no significant differences

between the three cavity cases for both contact pressure and fluid pressure. For the fluid pressure distribution, the differences between the smooth rod and cavity rods are also very small.

All these contact and fluid pressure results are consistent with each other, and are consistent with the fluid film results.

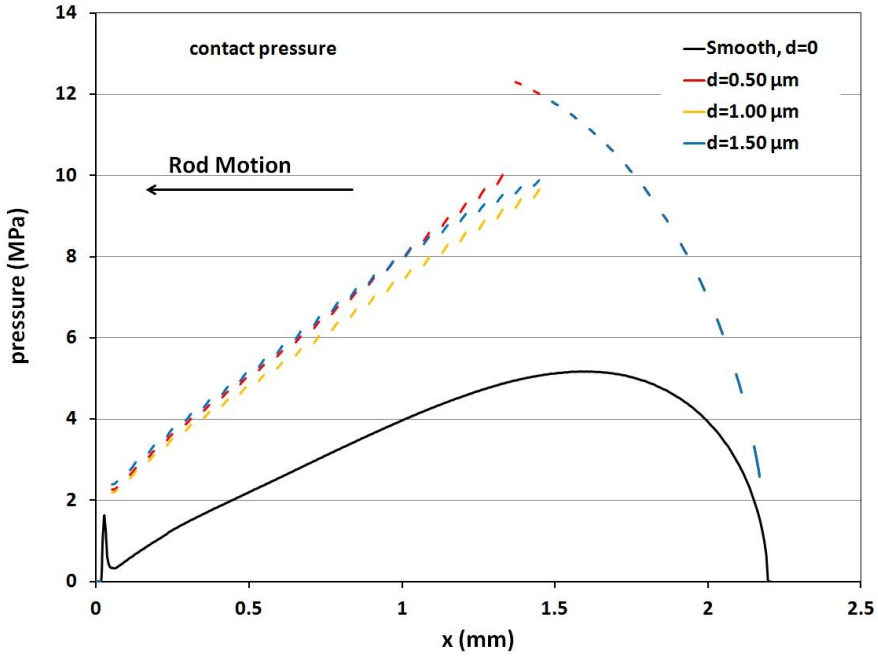

Figure 6.35a1: Contact pressure of instroke, 0.03 m/s, U-cup seal, different cavity depths, starved boundary conditions

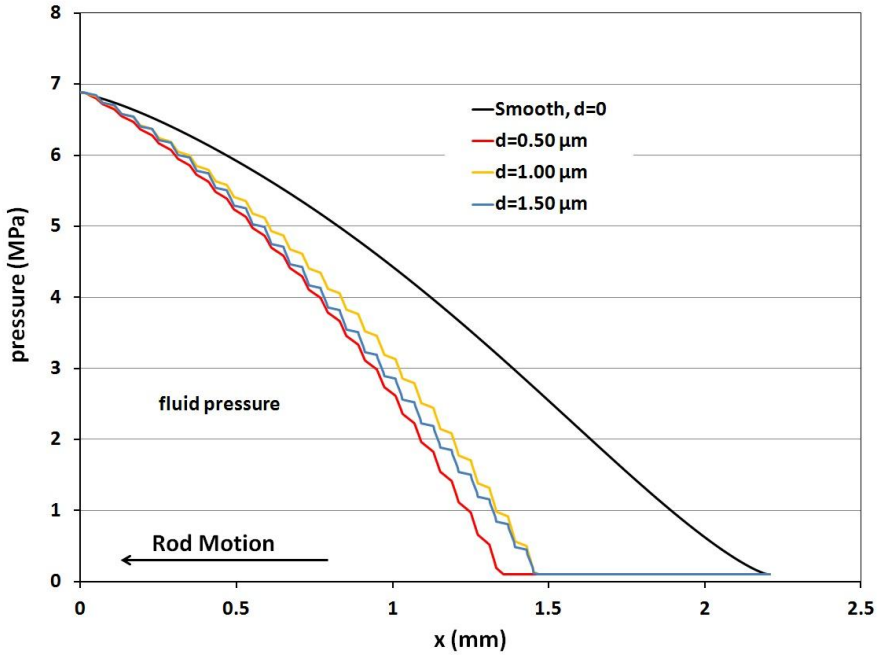

Figure 6.35a2: Fluid pressure of instroke, 0.03 m/s, U-cup seal, different cavity depths, starved boundary conditions

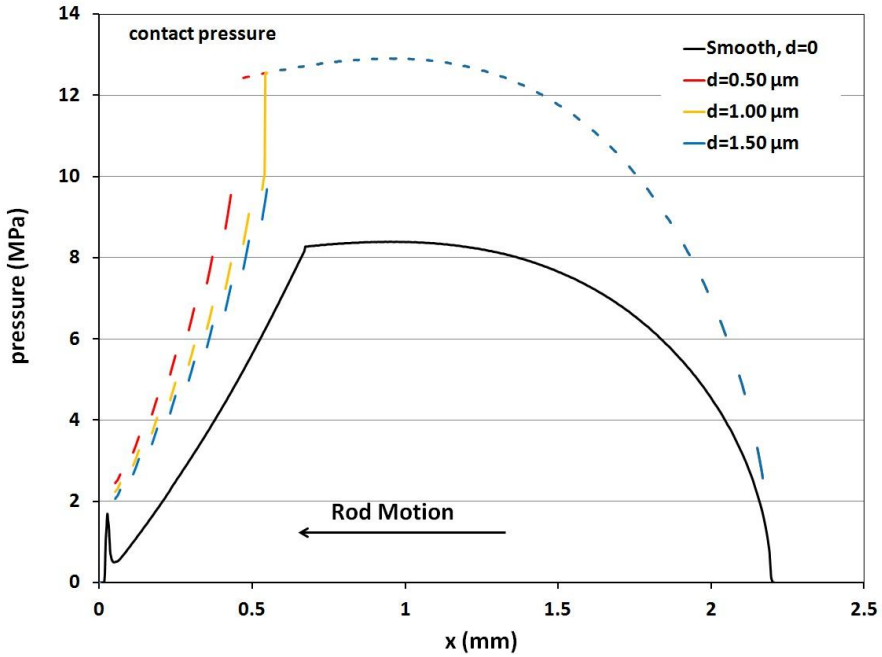

Figure 6.35b1: Contact pressure of instroke, 0.10 m/s, U-cup seal, different cavity depths, starved boundary conditions

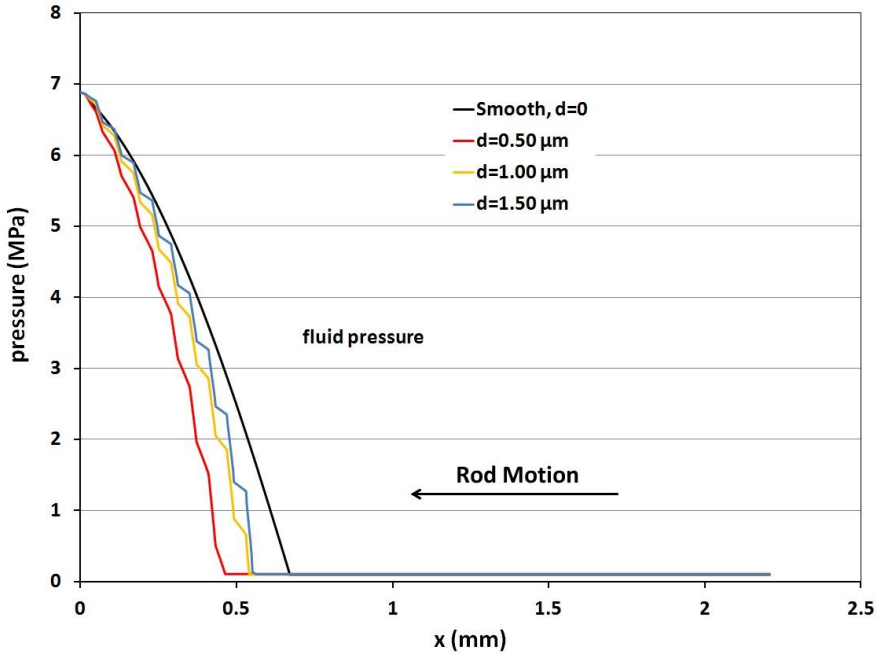

Figure 6.35b2: Fluid pressure of instroke, 0.10 m/s, U-cup seal, different cavity depths, starved boundary conditions

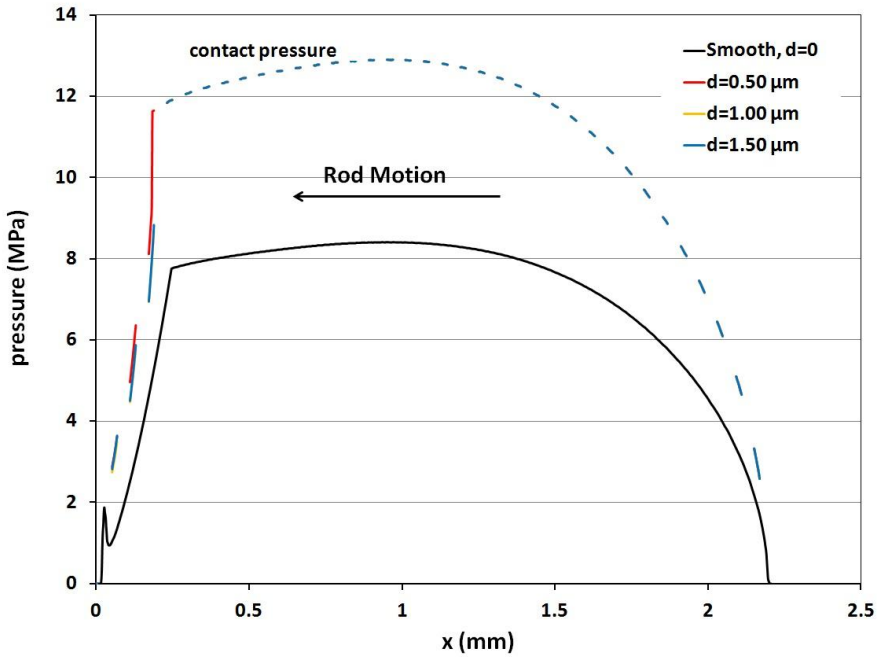

Figure 6.35c1: Contact pressure of instroke, 0.30 m/s, U-cup seal, different cavity depths, starved boundary conditions

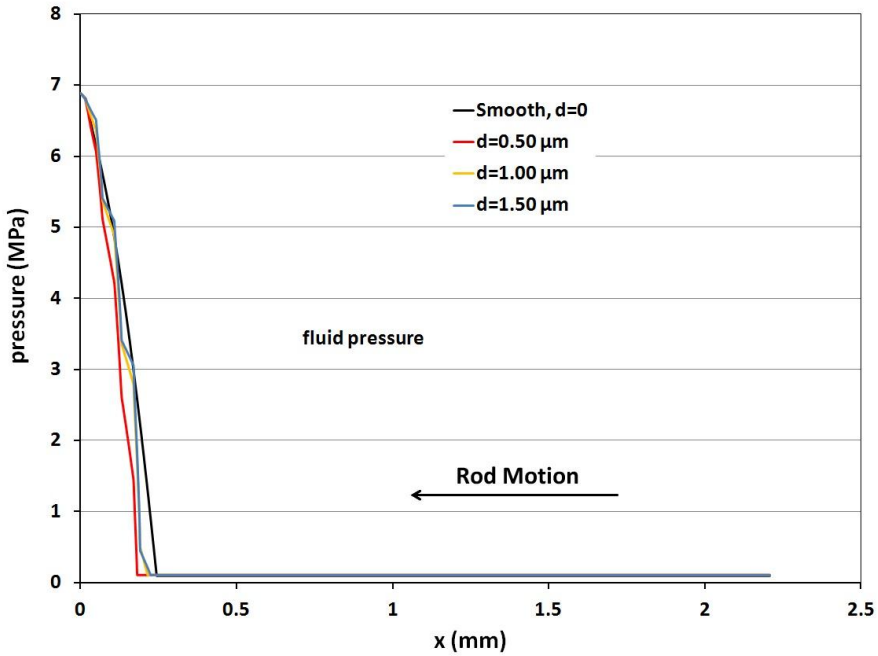

Figure 6.35c2: Fluid pressure of instroke, 0.30 m/s, U-cup seal, different cavity depths, starved boundary conditions

Summarizing, from the flooded boundary results, the cavity rod has a larger degree of starvation than that of the smooth rod. With the starved boundary conditions, the cavity rod creates a larger starvation region than that of the smooth rod, causing less fluid pressure generation and higher contact pressures between the rod and the seal. The friction forces with the cavity rods are higher than that of the smooth rod because of the higher contact pressures. The overall effects of cavity depth are not significant on both fluid transport and friction force under the starved boundary conditions, especially at higher rod speeds during the instroke. The main reason is that in the starvation area, which dominates at high rod speed, the cavity depth has no effect with the starved fluid, just like the similar situation in the cavitation area during the outstroke.

6.4.2 Effect of Land Area Ratio with Starved Boundary Conditions

The results in the previous section show that the cavity depth has little effect on seal behavior with the starved boundary conditions. In this section, only results with 1.50 μm depth are presented and discussed.

Figure 6.36 shows the fluid transport during outstroke and instroke as a function of rod speed for the cavity patterned rod with different land area ratios and for the smooth rod, under starved boundary conditions. The surface patterns in these cases are shown in table 6.1 as the cavities with inline round shape, with a cavity depth of 1.50 μm. The outstroke transport behavior is just the same as in the flooded cases shown in the previous section, because there is no starvation during the outstroke.

During the instroke under starved boundary conditions, the critical speed of the cavity patterned rod is close to that of the smooth rod. At 0.03 m/s rod speed, starvation occurs only for the cavity cases with area ratios of 0.651 and 0.743, but not for the area ratios of 0.804 and 0.912, and the smooth cases. From Figure 6.18, the results with flooded boundary conditions, the degree of starvation for the cavity cases increases with decreasing area ratio, due to the higher fluid transport reduction effect of the cavity patterns (the effect of area ratio) on outstroke than that on instroke, which increases with decreasing area ratio.

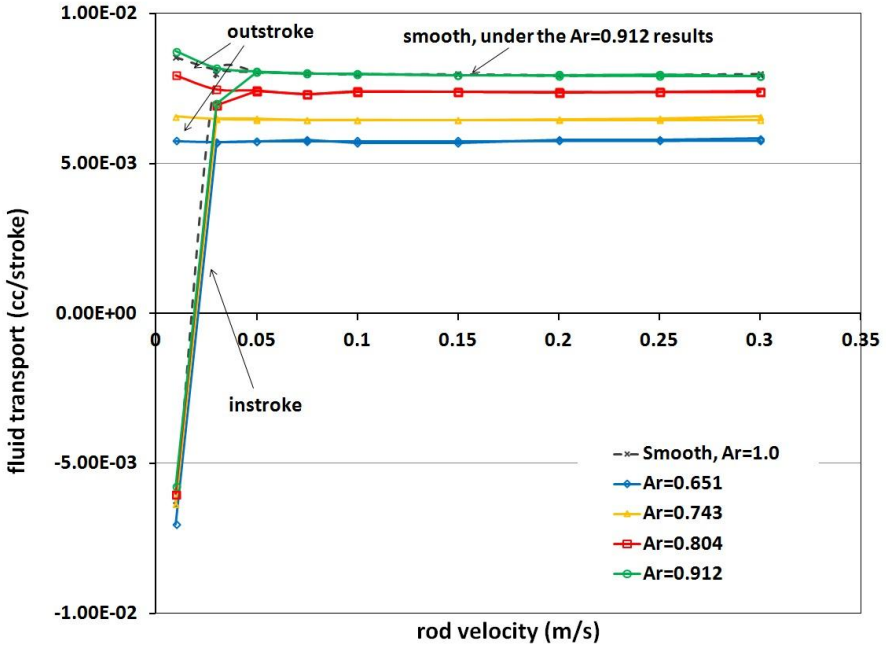

Figure 6.36: Fluid transport, U-cup seal, d=1.50 μm, different land area ratios, starved boundary conditions

The friction force on the rod, as a function of rod speed, is shown in Figure 6.37 for rods with different land area ratios and the smooth rod, under starved boundary conditions. During the outstroke, the friction force behavior for both the smooth rod and plunge-ground rod are exactly the same as the flooded cases. During the instroke, the friction force behaviors of the cavity cases are similar to that of the smooth rod with starved boundary conditions, but are generally higher.

Beyond the critical speed (around 0.03 m/s for all cases), the friction force increases slightly with decreasing area ratio at the same speed. At high rod speeds, the differences between different cases are not significant. From the friction force plots it also can be seen that at the 0.03 m/s rod speed, starvation occurs for the area

ratio of 0.651 and 0.743 cases, but not for the other cases, which is consistent with the fluid transport results.

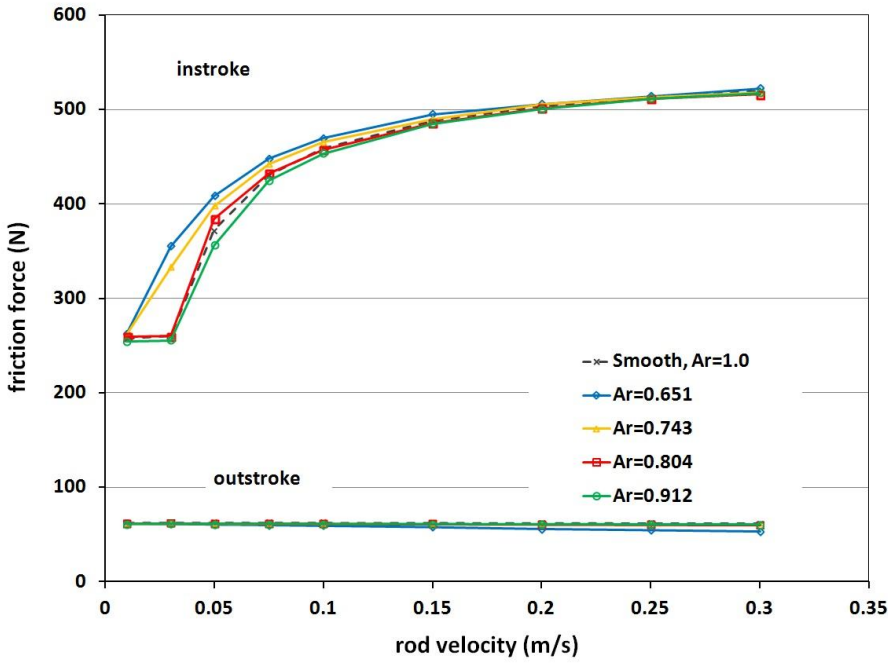

Figure 6.37: Friction force, U-cup seal, d=1.50 μm, different land area ratios, starved boundary conditions

To explain the results with the starved boundary for the effect of area ratio, the details of the sealing zone are examined. Since the results with the area ratios of 0.651 and 0.743 are very close, the details of the 0.743 area ratio will not be shown.

The film thickness distributions during the instroke at rod speeds of 0.03 m/s, 0.1 m/s, and 0.3 m/s are shown in Figures 6.38a, 6.38b, and 6.38c, respectively. It can be seen that at all speeds, the area ratio affects the fluid film thickness with the starved boundary conditions just like with the flooded boundary. The film thickness on the

land area decreases with decreasing area ratio. At the rod speed of 0.03 m/s, which is lower than the critical speed of the smooth case and area ratios of 0.804 and 0.912 cases, but higher than the critical speed of the 0.651 area ratio case, , starvation only occur for the Ar=0.651 case. At the rod speed of 0.10 m/s, all cases have significant starvation. The starvation area increases with decreasing area ratio, because of the increasing degree of starvation. At the rod speed of 0.30 m/s, the starvation area dominates the sealing area for both cavity cases and smooth cases. The lengths of the starvation area (or pressurized zone) are almost identical for the various area ratios

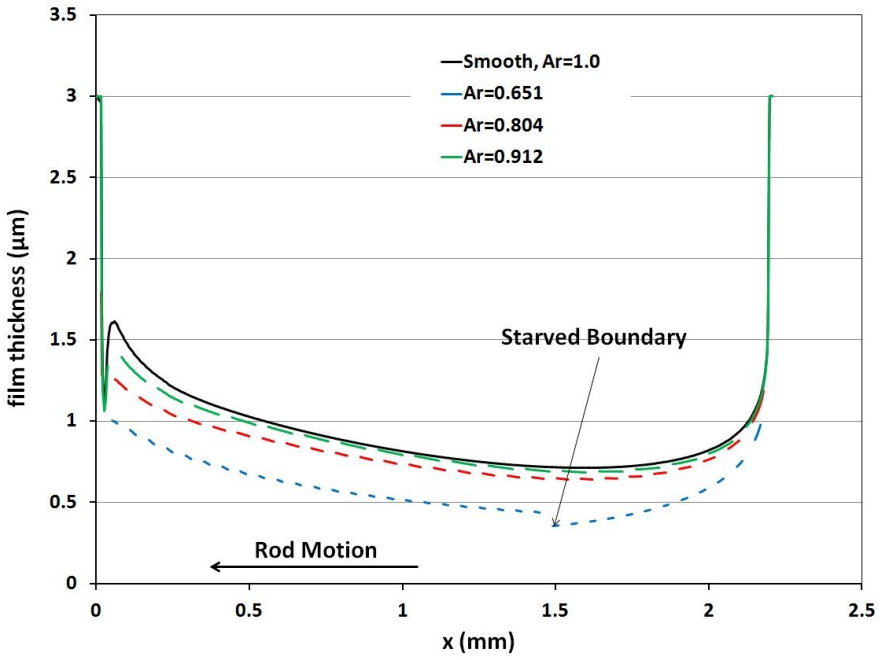

Figure 6.38a: Film thickness of instroke, 0.03 m/s, U-cup seal, different land area ratios, starved boundary conditions

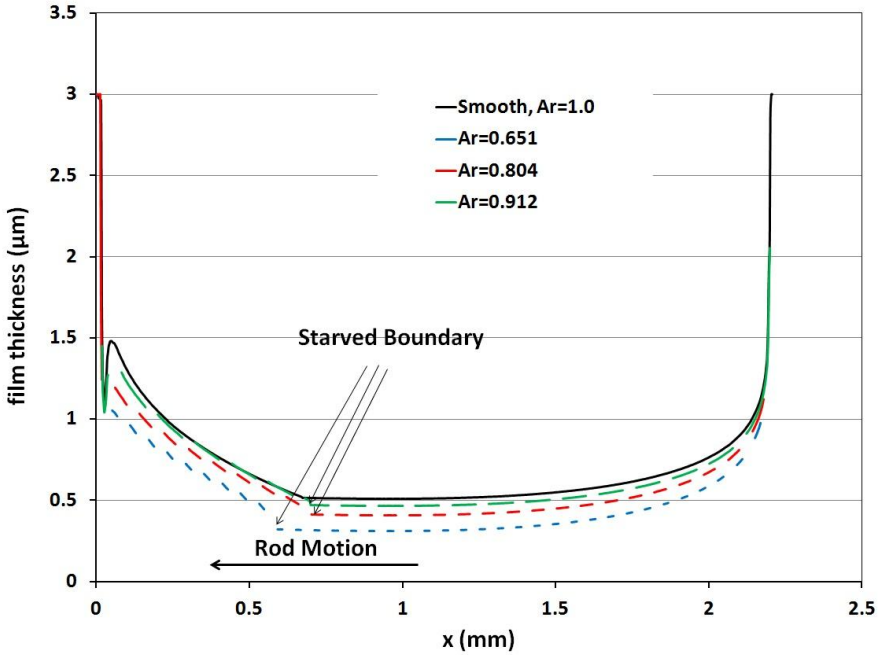

Figure 6.38b: Film thickness of instroke, 0.10 m/s, U-cup seal, different land area ratios, starved boundary conditions

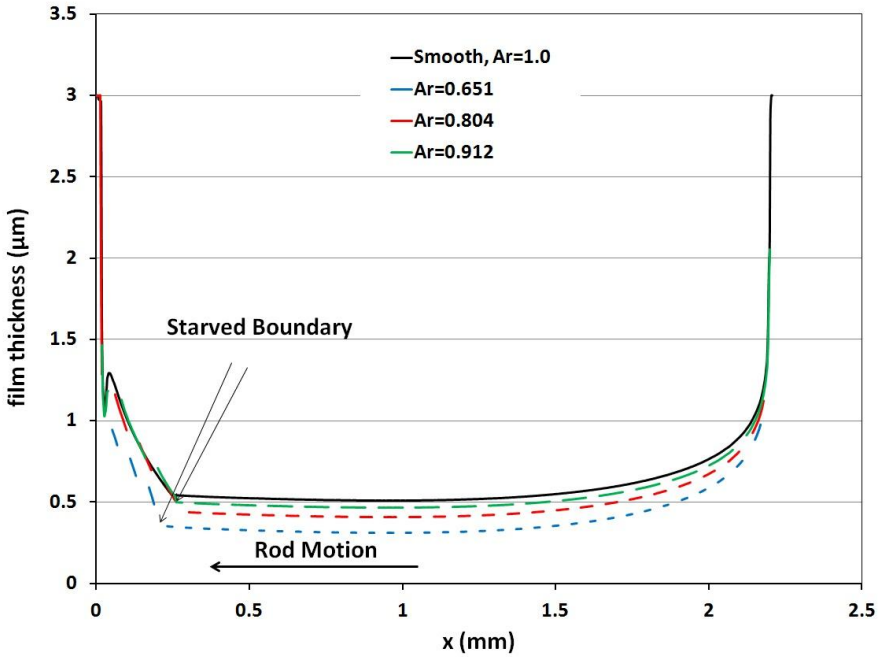

Figure 6.38c: Film thickness of instroke, 0.30 m/s, U-cup seal, different land area ratios, starved boundary conditions

Figure 6.39a1, 6.39a2, 6.39b1, 6.39b2, 6.39c1, and 6.39c2 show the contact pressure and fluid pressure distributions during the instroke at rod speeds of 0.03 m/s, 0.10 m/s, and 0.30 m/s under the starved boundary conditions.

At the 0.03 m/s speed, the contact pressure increases with decreasing area ratio, which is similar to the results with the flooded boundary conditions, and for the same reason. From the contact and fluid pressure, it also can be seen that only the area ratio of 0.651 has starvation at this speed. For the same reason as for the flooded boundary conditions, the over-all contact force cannot be estimated by the contact pressure on the land area alone, because of the different total land areas for the various area ratios. Comparing the fluid pressure is a way to analyze the integrated contact pressure and friction force through the load balance. At this low speed, the fluid pressures of the 0.651 area ratio case are significantly less than those of the other cavity cases and the smooth rod case, while the other cavity cases and the smooth case have almost identical fluid pressure distributions. The total contact force of the 0.651 area ratio case should be higher than the rest, and that of the smooth rod. The same is therefore true of the friction force. This is consistent with the results in Figure 6.37. At the 0.10 m/s rod speed, starvation occurs for all cases. The starvation area increases with decreasing area ratio at this speed, but not significantly for the 0.912 and 0.804 area ratio cases. The fluid pressure of the 0.651 area ratio case is smaller than the rest, but the differences between 0.651 area ratio case and other cases are smaller than at 0.03 m/s rod speed. is is also consistent with the friction force results. At the 0.30 m/s speed, the lengths of starvation area are

very close for the various cases including that of the smooth rod. For the fluid pressure distribution, the differencse between smooth rod and cavity rods are also very small.

All these contact and fluid pressure results are consistent with each other, and are consistent with the fluid film results.

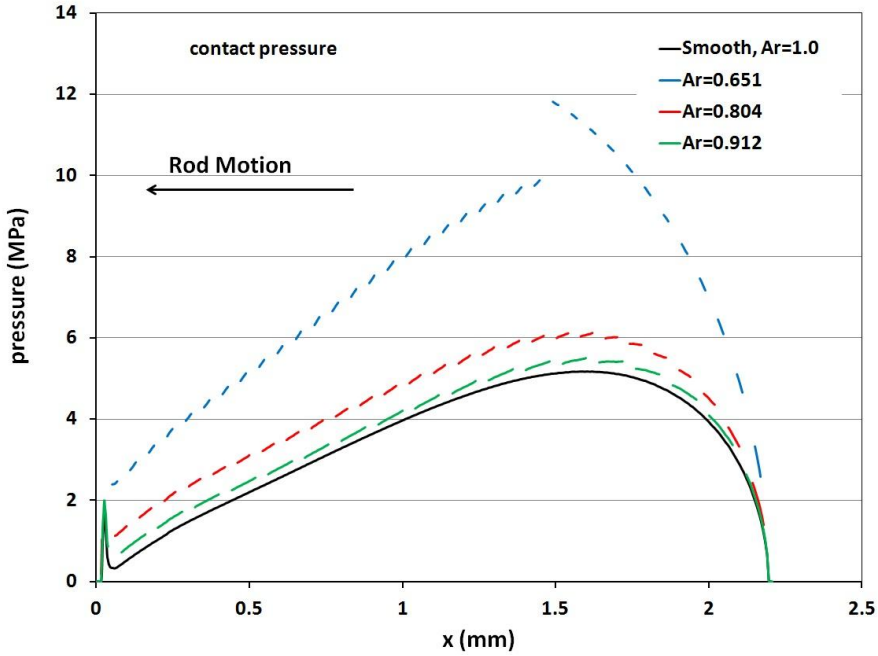

Figure 6.39a1: Contact pressure of instroke, 0.03 m/s, U-cup seal, different land area ratios, starved boundary conditions

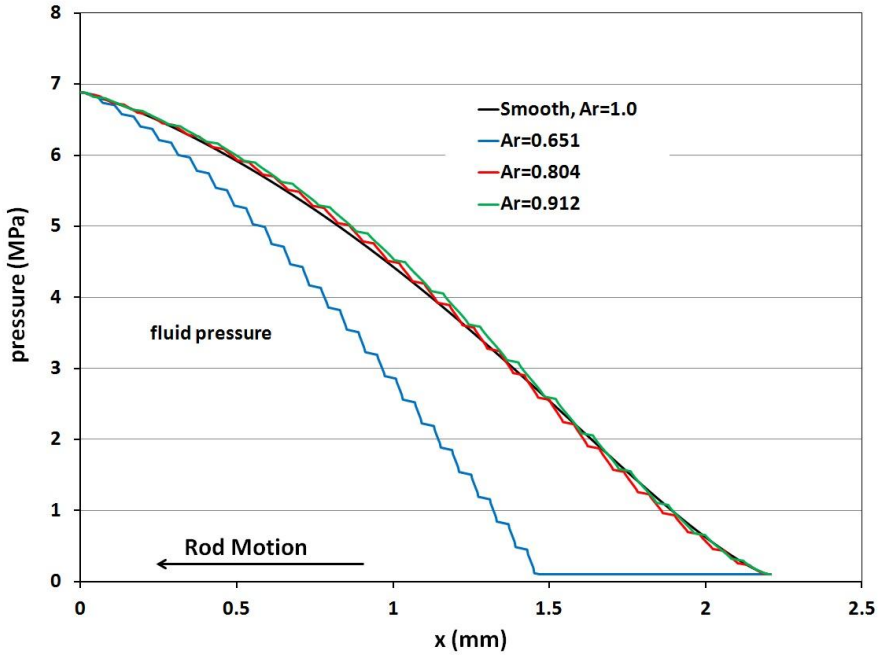

Figure 6.39a2: Fluid pressure of instroke, 0.03 m/s, U-cup seal, different land area ratios, starved boundary conditions

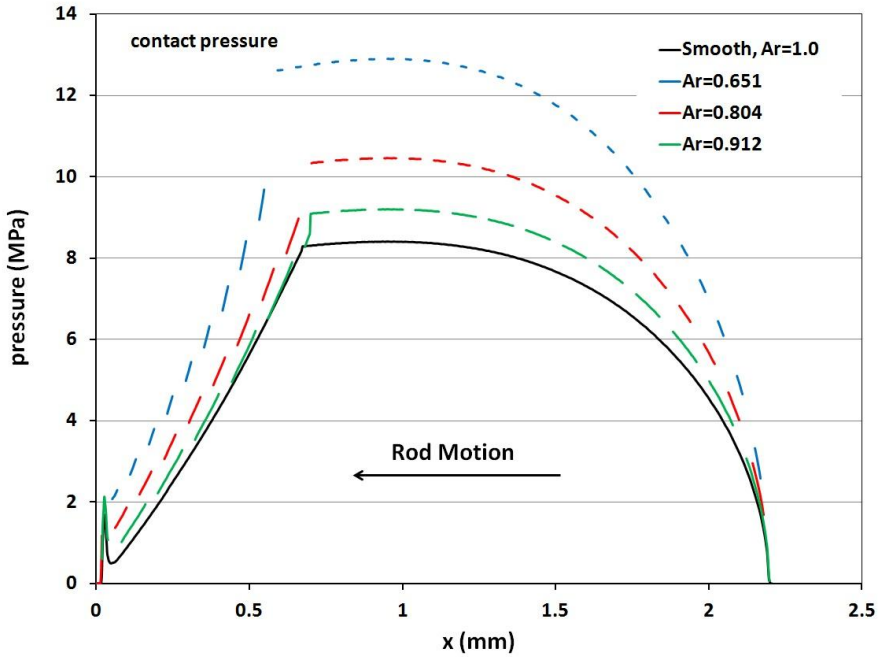

Figure 6.39b1: Contact pressure of instroke, 0.10 m/s, U-cup seal, different land area ratios, starved boundary conditions

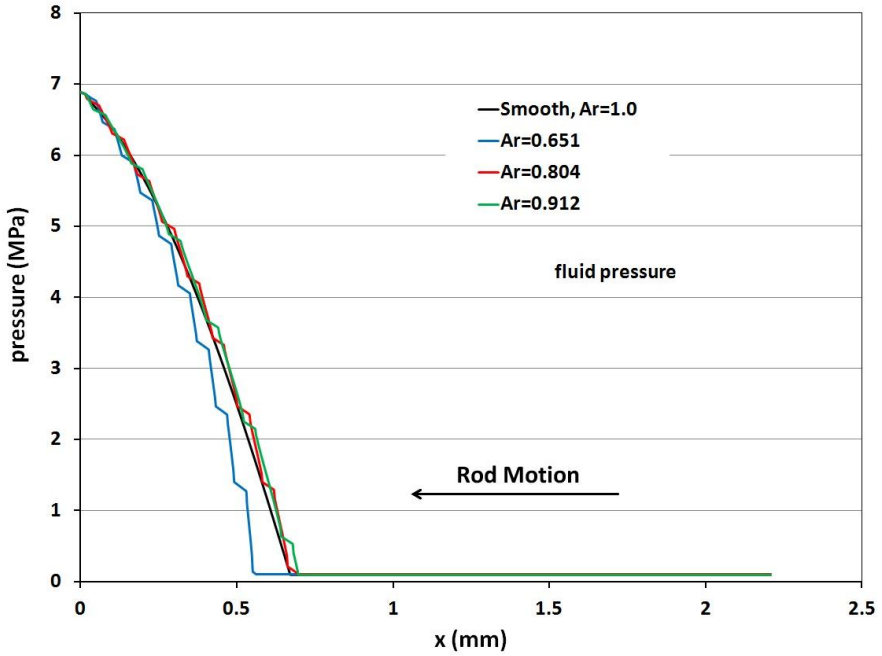

Figure 6.39b2: Fluid pressure of instroke, 0.10 m/s, U-cup seal, different land area ratios, starved boundary conditions

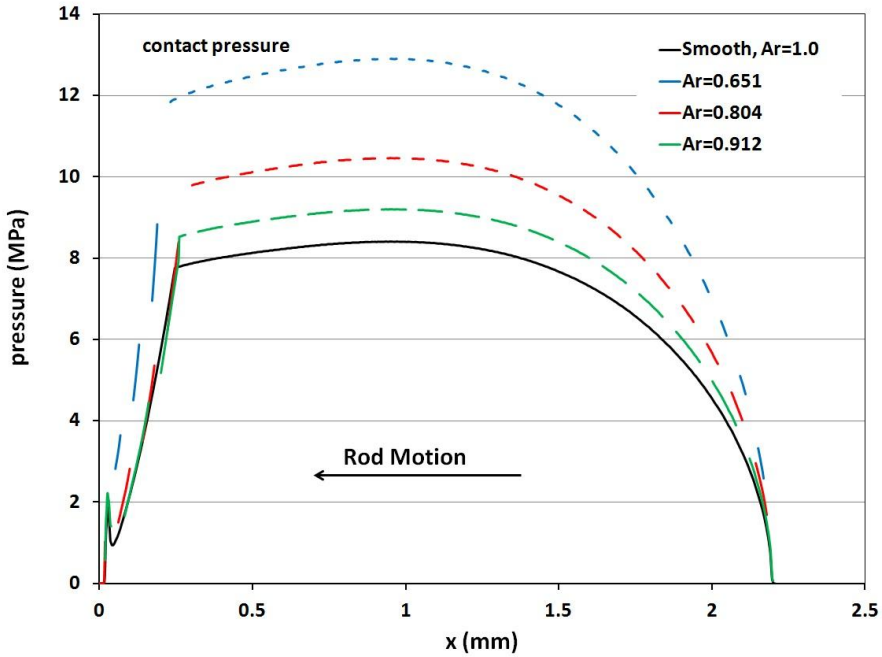

Figure 6.39c1: Contact pressure of instroke, 0.30 m/s, U-cup seal, different land area ratios, starved boundary conditions

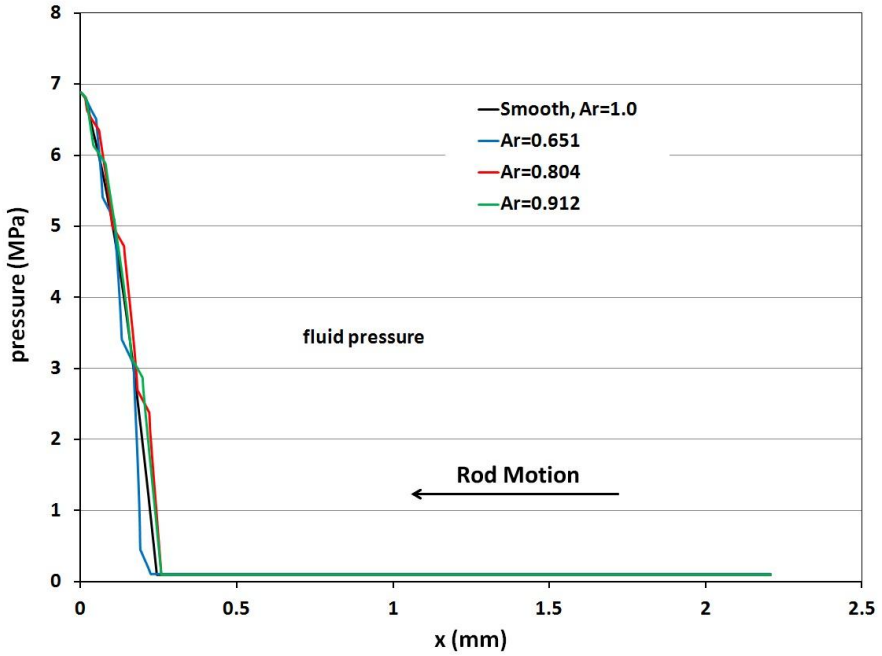

Figure 6.39c2: Fluid pressure of instroke, 0.30 m/s, U-cup seal, different land area ratios for cavity pattern, starved boundary conditions

In summary, with the starved boundary conditions, the area ratio only has an effect on the friction force at low rod speed. The decreasing area ratio increases the friction force. At same speed, the starvation area increases with the decreasing area ratio. This effect is not significant at medium and high speed. The main reason is that in the starvation area, which dominates at high rod speed, the different area ratios do not affect the starved fluid.

6.4.3 Conclusions

Under the starved boundary conditions, the cavity patterns no longer have a friction reduction effect compared to the smooth rod case. Instead, the cavity

patterns increase the friction due to the larger starvation area compared to the smooth rod. The overall effects of cavity depth are not significant on both fluid transport and friction force under the starved boundary conditions, especially at higher rod speeds during the instroke. The area ratio only has an effect on the friction force at low rod speed. The decreasing area ratio increases the friction force. This effect is not significant at medium and high speed.

6.5 Protrusion Pattern with Flooded Boundary

In this section, the U-cup seal with protrusion patterned rods under flooded boundary conditions are discussed. The following parameters are changed and examined separately: the time steps, the protrusion height, the land area ratio, and the shape of the protrusion. Note that for the protrusion patterns, the seal contacts the rod on the protrusion surface, so the "land area" here is the protrusion area, instead of the virgin rod surface in the cavity cases.

6.5.1 Effect of Time Steps

Similar to that of the cavity pattern, Figure 6.40 shows the fluid transport during outstroke and instroke as a function of rod speed at different time steps. The surface patterns in these cases are shown in table 6.1 as the protrusions with staggered round shape. The concept of the time step has been discussed in a previous section and is not repeated here. The curves for the different time steps for the protrusions pattern generally lie on top of each other, indicating that axial position of the rod produces no significant effect on the fluid transport.

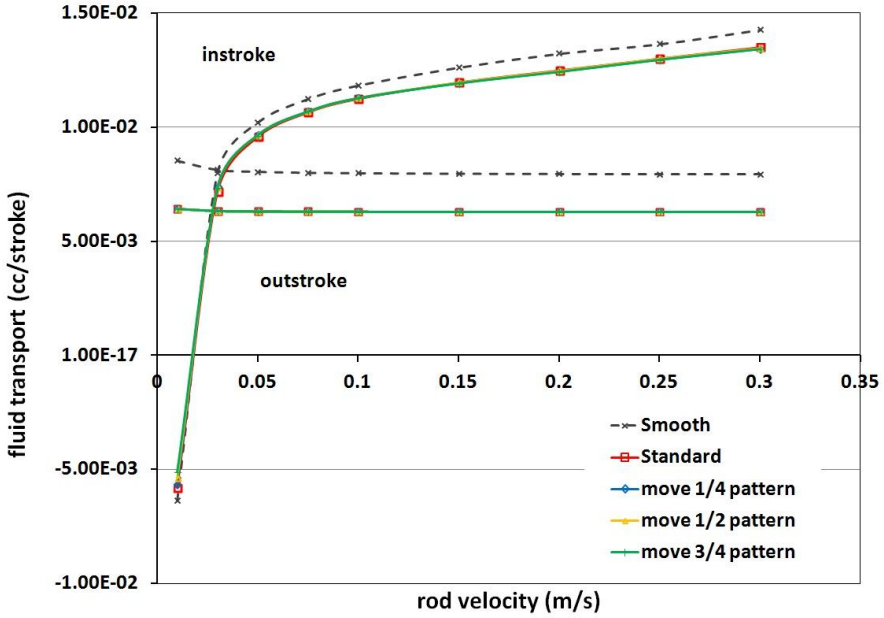

Figure 6.40: Fluid transport, U-cup seal, different time steps for protrusion pattern

The friction force on the rod, as a function of rod speed is shown in Figure 6.41 for different time steps. The time steps have no effect on the friction force for both outstroke and instroke. Therefore, in the following simulations, only one time step (the Standard) is calculated, instead of all the time steps that the rod goes through.

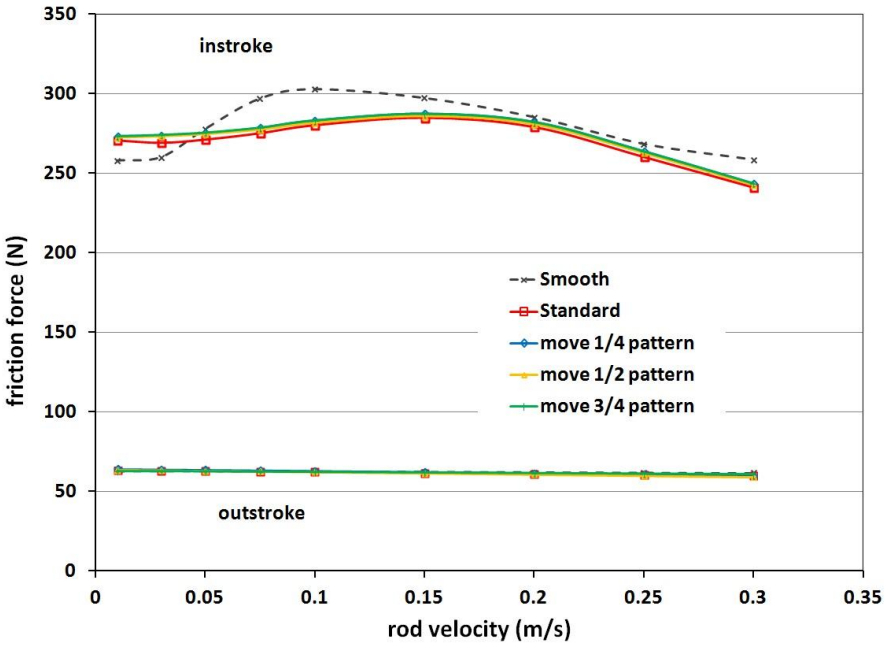

Figure 6.41: Friction force, U-cup seal, different time steps for protrusion pattern

6.5.2 Effect of Protrusion Height

Figure 6.42 shows the fluid transport during outstroke and instroke as a function of rod speed for the protrusion pattern rod with different protrusion heights and for the smooth rod, under the flooded boundary conditions. The surface patterns in these cases are shown in table 6.1 as the protrusions with staggered round shape, with the same land area ratio of 0.649.

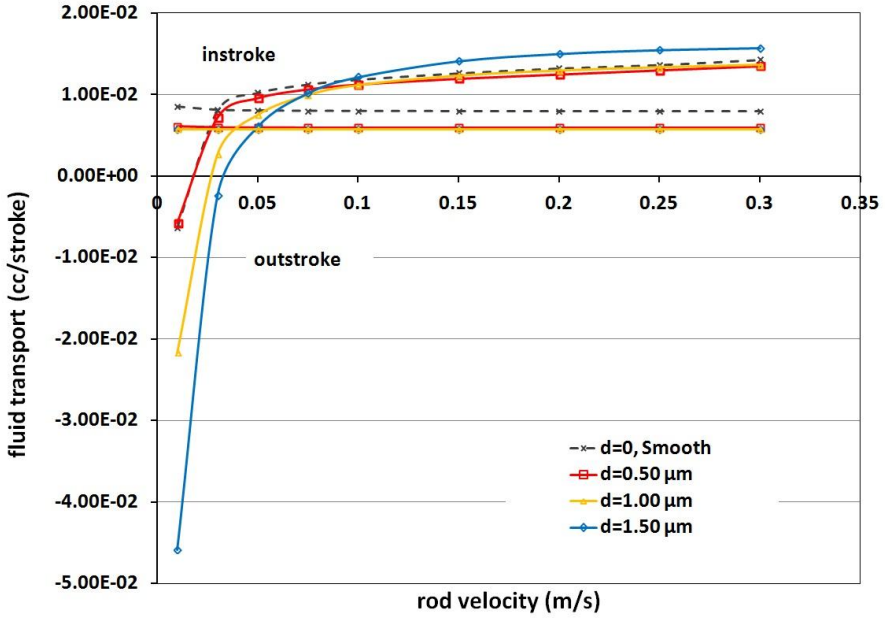

Figure 6.42: Fluid transport, U-cup seal, different protrusion heights, flooded boundary conditions

The outstroke transports for the protrusion cases are relatively independent of rod speed, just like the smooth case and the cavity cases. The protrusion height has no significant effect on fluid transport during the outstroke, also like the cavity cases with the cavity depth effect. However, the protrusion height has influence on the instroke fluid transport, which is unlike the cavity depth. The increasing protrusion height increases the critical speed. An examination of the fluid film distributions can explain this effect on fluid transport, which will be discussed later.

The friction force on the rod as a function of rod speed is shown in Figure 6.43 for rods with different protrusion heights and for the smooth rod, under flooded boundary conditions. Comparing Figures 6.43 and 6.9, which shows the effect of cavity depth, it

can be seen that these two Figures are very similar, indicating that the protrusion height has a similar effect on friction force as that of the cavity depth, with a similar explanation.

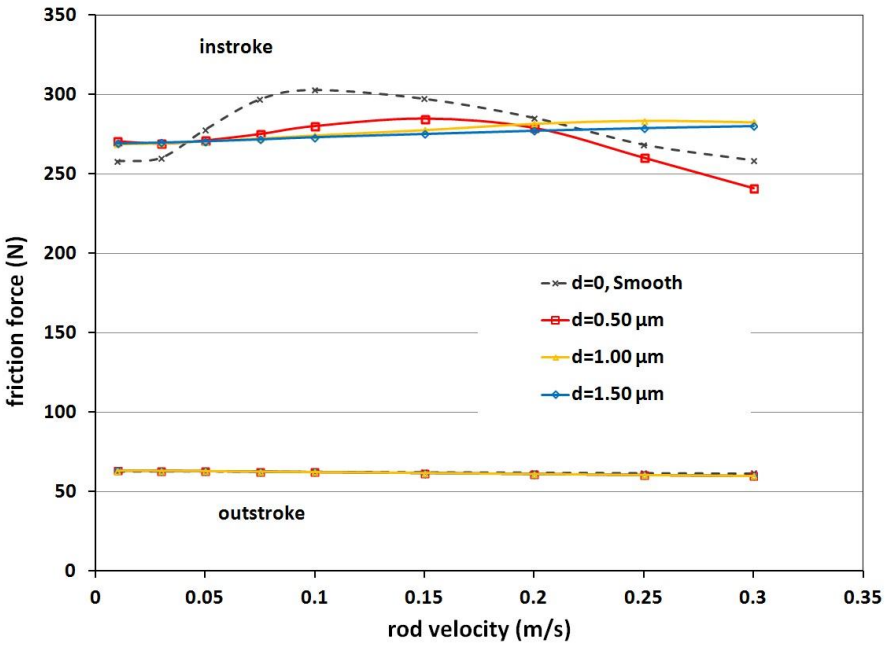

Figure 6.43: Friction force, U-cup seal, different protrusion heights, flooded boundary conditions

The main difference between the cavity and protrusion patterns is as follows. For the cavity patterns, the cavity areas, which have a thicker fluid film than the land areas, are not connected. For the protrusion cases, the protrusions also are not connected, but the voids between the protrusions are connected. These voids act like "cavities" as the protrusion area plays the role of land area. Thus, the thicker fluid films of the voids connect as a fluid channel. During the outstroke, since the fluid is

cavitated, the protrusion height has little effect since the main flow channel, the land area fluid film, is controlled by the area ratio. During the instroke with a flooded boundary, higher protrusion heights cause thicker films. As discussed earlier, the instroke fluid transport combines the Couette flow and Poiseuille flow. When the speed is low and the Poiseuille flow dominates, an increasing film thickness causes the Poiseuille flow increase quicker than that of the Couette flow (as equation 3.8 shows). The results is the thicker fluid film allows more fluid to be pushed out of the hydraulic cylinder than is dragged in, meaning there is more leakage. The critical speeds with the thicker fluid films are higher. At higher speeds when the Couette flow dominates, the film thickness increase causes the total instroke fluid transport to increase. This explains the effect of protrusion height on fluid transport. Figure 6.44 shows film thickness distributions with both protrusion and void areas ("un-patterned area" in Figure) during the instroke at a rod speed of 0.03 m/s. The average film thickness lies between the protrusion and void areas.

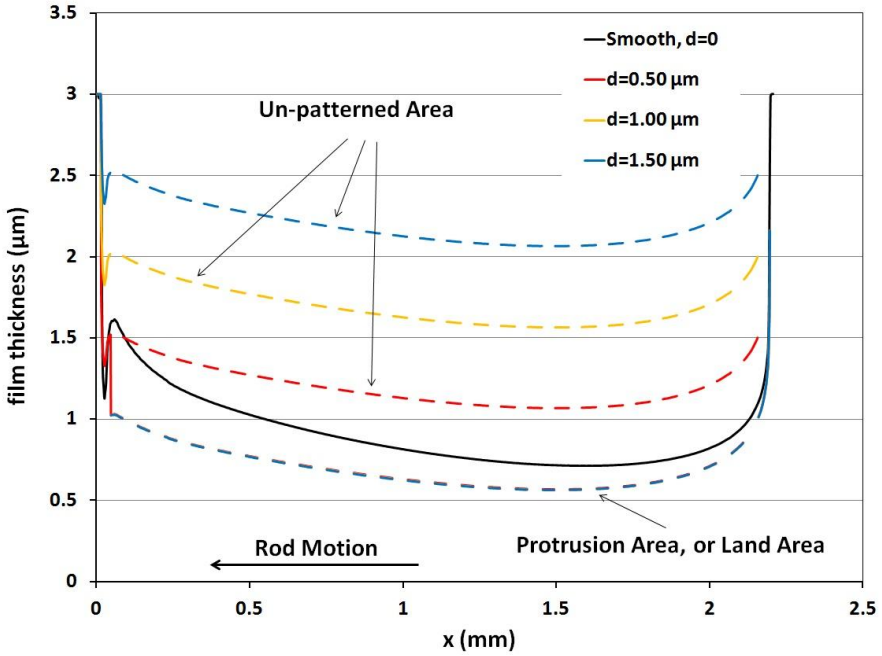

Figure 6.44: Film thickness of instroke, 0.03 m/s, U-cup seal, different protrusion heights, flooded boundary conditions

6.5.3 Effect of Land Area Ratio

Figure 6.45 shows the fluid transport during outstroke and instroke as a function of rod speed for the protrusion pattern rod with different land area ratios and the smooth rod, under the flooded boundary conditions. The surface patterns in these cases are shown in table 6.1 as the protrusions with staggered round shape, with the same protrusion height of 0.50µm. The higher protrusion heights will cause the critical speed to increase, and are not presented in this research. The friction force on the rod as a function of rod speed is shown in Figure 6.46. Comparing Figures 6.45 and 6.46 with Figures 6.18 and 6.19a, the effects of area ratio for the protrusion

patterns are almost the same as that for the cavity patterns, with the same explanation, which is not repeated here.

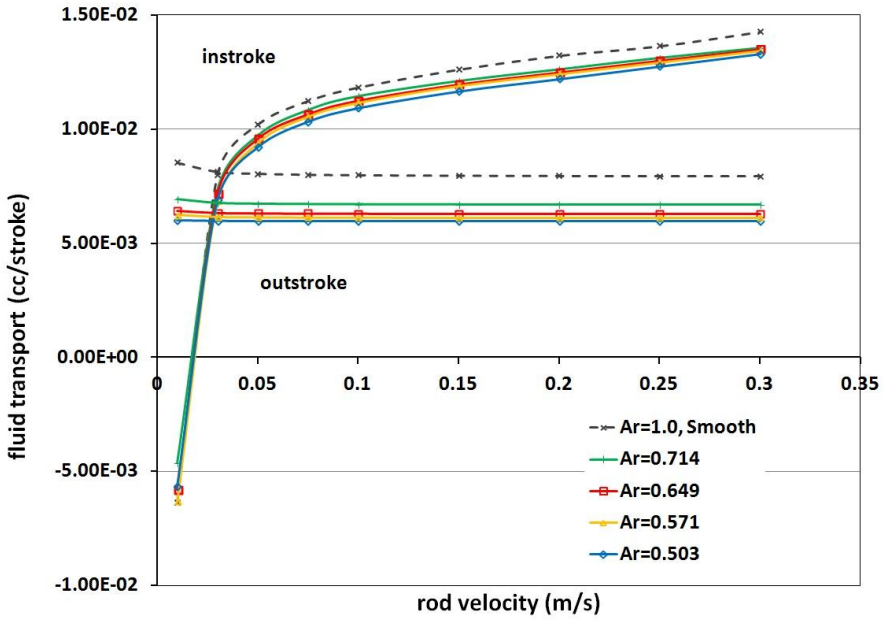

Figure 6.45: Fluid transport, U-cup seal, d=0.50 μm, different land area ratios, protrusions pattern, flooded boundary conditions

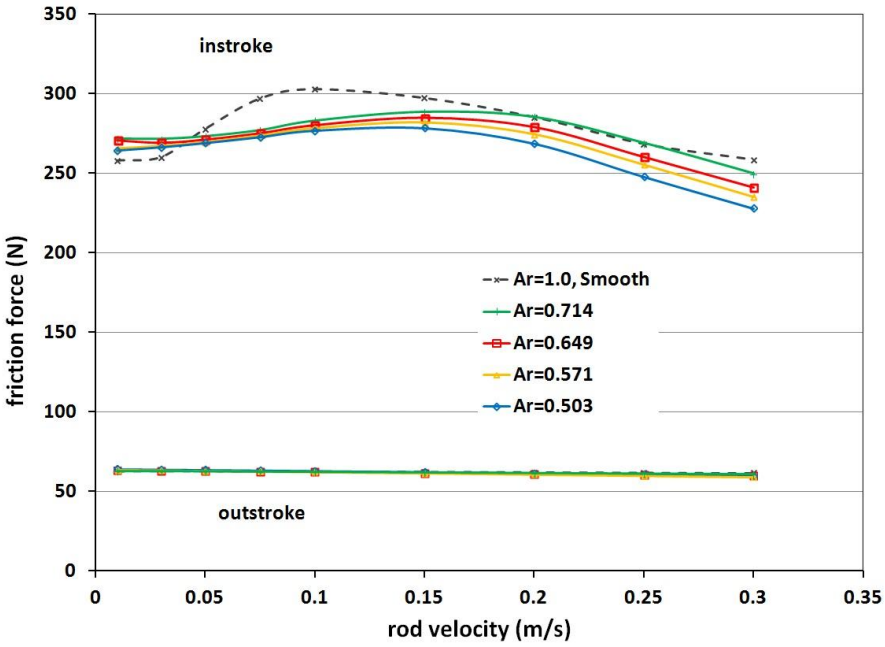

Figure 6.46: Fluid transport, U-cup seal, d=0.50 μm, different land area ratios, flooded boundary conditions

6.5.4 Effect of Protrusion Shape

Figure 6.47 shows the fluid transport during the outstroke and instroke as a function of rod speed with different protrusion shapes. The surface patterns in these cases are shown in table 6.1 as the protrusions with staggered round shape, protrusions with staggered square shape, and protrusions with opposite staggered triangle shape, (round, square, and triangle in the plots). The land area ratio for the round shape is 0.649, and for the square and triangle shapes are 0.640. The protrusion heights for all three shapes are 0.5μm. Besides the effect of area ratio, the shape of protrusions produces no significant effect on the fluid transport.

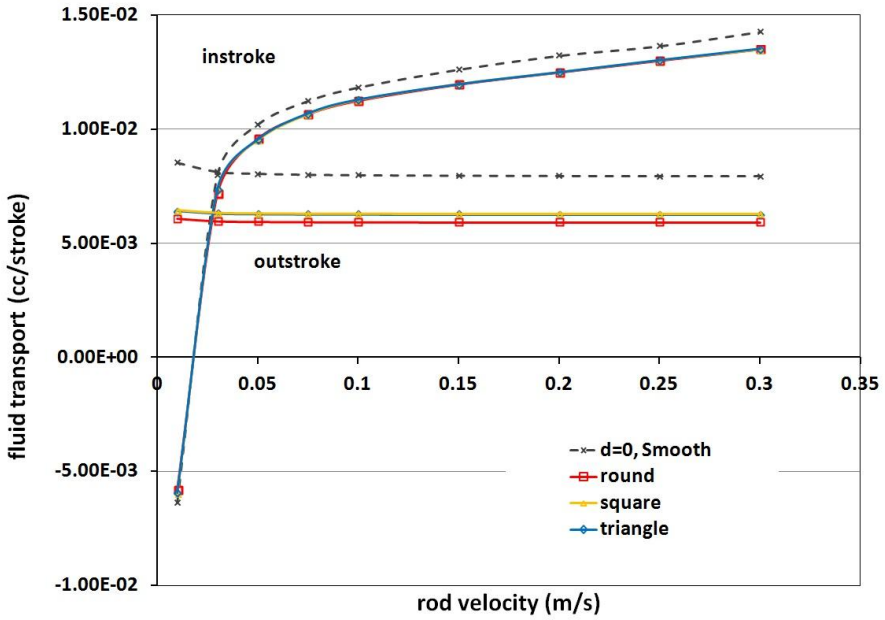

Figure 6.47: Fluid transport, U-cup seal, different protrusion shapes, flooded boundary conditions

The friction force on the rod, as a function of rod speed is shown in Figure 6.48 for different protrusion shapes. The protrusion shape has no significant effect on the friction force for both outstroke and instroke.

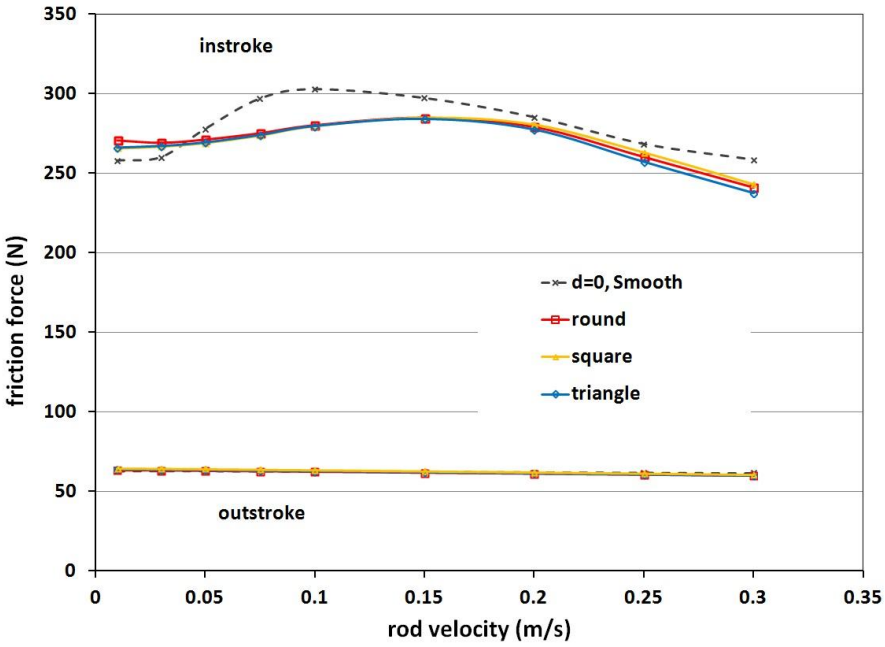

Figure 6.48: Friction force, U-cup seal, different protrusion shape, flooded boundary conditions

6.5.5 Summary

For the U-cup seal with protrusion patterned rod under flooded boundary conditions, the time steps and the shape of the protrusions have no significant effect on fluid transport or friction force, just like the cavity pattern. The protrusion heights and the land area ratio have similar effect as that of the cavity depth and the area ratio for cavities. The height of the protrusion pattern may affect the fluid transport during the instroke, changing the critical speed, by changing the average film thickness.

6.6 Protrusion Pattern with Starved Boundary Conditions

Since the protrusion pattern has a very similar behavior as that of the cavity pattern, only the effects of the area ratio for the protrusion patterns under starved boundary conditions are shown.

Figure 6.49 shows the fluid transport during outstroke and instroke as a function of rod speed for the protrusion patterned rod with different land area ratios and for the smooth rod, under starved boundary conditions. The surface patterns in these cases are shown in table 6.1 as the protrusions with staggered round shape, with a protrusion height of 0.50 μm. The friction force on the rod, as a function of rod speed is shown in Figure 6.50 for different area ratios under starved boundary conditions.

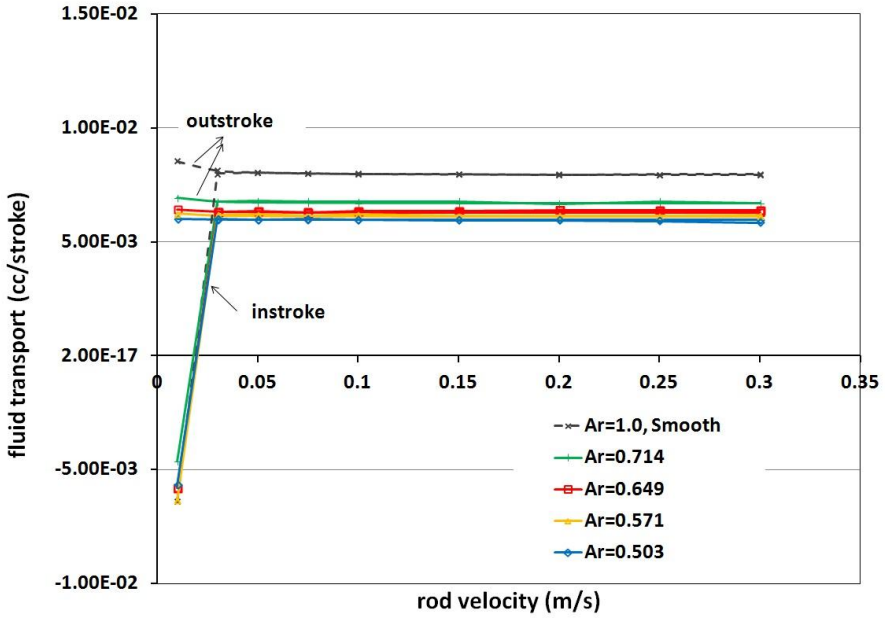

Figure 6.49: Fluid transport, U-cup seal, different area ratios for protrusion pattern, starved boundary conditions

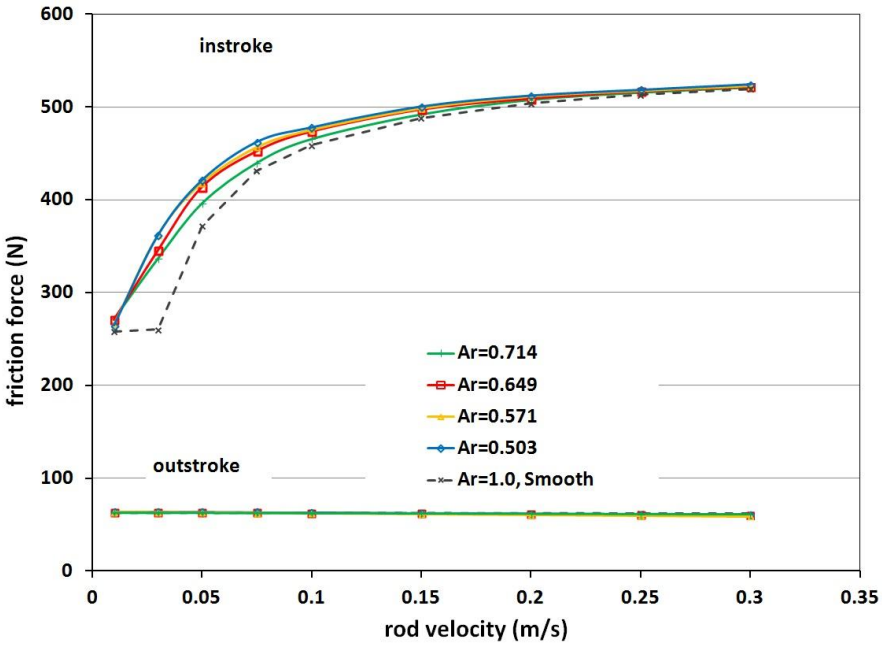

Figure 6.50: Friction force, U-cup seal, different area ratio for protrusion pattern, starved boundary conditions

Figures 6.49 and 6.36, and Figures 6.50 and 6.37 are very similar, respectively, indicating that the effect of the area ratio of the protrusion cases under the starved boundary conditions are the same as that of the cavity cases, with the same explaination, which has been discussed in previous chapters.

6.7 Conclusions

This chapter discussed the patterned rod surfaces' effects on seal performance. Two categories of surface pattern are investigated: cavities and protrusions, both under flooded and starved boundary conditions.

1. Both cavity and protrusion patterns have effects on the fluid transport and friction force, compare to the smooth rod. The effects under flooded boundary conditions are generally larger than that under starved boundary conditions.

2. Under flooded boundary conditions, the cavity patterns can reduce the friction force while keeping the critical speed almost constant compared to the smooth rod.

3. Under starved boundary conditions, the cavity patterns increase the friction force compared to the smooth rod, by increasing the starvation area.

4. For the cavity patterns, the movement of the rod into various axial positions (time step changing), the shape of the cavity, the size of the cavity, and the arrangement of the cavities have no significant effect on both fluid transport and friction force.

5. The cavity depth and the land area ratio can affect the fluid transport and friction force behavior. The effects of both are larger under flooded boundary conditions than under starved boundary conditions.

6. The protrusion patterns have very similar effects as the cavity patterns. One difference is that the height of the protrusion pattern affects the fluid transport during the instroke and changes the critical speed, by changing the average film thickness.

CHAPTER 7. CONCLUSIONS

The numerical models for analyzing reciprocating hydraulic rod seals with various rod surfaces are developed in this research. These models consist of coupled fluid mechanics, contact mechanics and deformation analyses. Previous research only considered the surface roughness of the seal, assuming a perfectly smooth rod. Furthermore, there have been no previous simulations of the rod seal that consider starved lubrication boundary conditions. In the present work, a plunge-ground rod surface is considered, and then various micro-patterns on the rod surfaces are taken into account. For the smooth rod and the various rod surfaces, both flooded and starved lubrication boundary conditions are applied.

The studies on the U-cup and step seals with a smooth rod show that for both the U-cup and step seals, the fluid transport during outstroke is relatively independent of rod speed because almost the entire lubricating film is cavitated and hydrodynamic effects are minimal. The film thickness distributions are almost identical at all speeds. The fluid transport during the instroke increases with increasing rod speed. There is a critical speed above which the instroke fluid transport exceeds that of the outstroke. Below this critical speed the seal leaks, above this critical speed, fluid starvation occurs. For the U-cup seal, this critical speed is between 0.03 m/s and 0.075 m/s; for the step seal, the critical speed is beyond the speed range studied.

The studies on the U-cup and step seals with a smooth rod also show that The friction force during the outstroke is almost independent of rod speed. The reason is similar to that for the fluid transport phenomenon. The friction force behavior during the instroke is not the same for the U-cup seal and step seal. For the U-cup seal with a flooded boundary, the friction force increases to a peak value at low speed and then decreases with increasing rod speed. That is because the fluid pressure decreases at low speed and then increases at high speed while the contact pressure does the opposite. For the U-cup seal with a starved boundary, the friction force increases with increasing rod speed because the starvation zone grows longer with increasing speed, the pressurized region decreases and so does the fluid pressure while the contact pressure increases. The contact pressure of the starved case is much larger than that of the flooded case, at the same rod speed, resulting in a much larger friction force. For the step seal with a flooded boundary (starvation does not occur for the step seal in this research), the friction force is almost independent of rod speed, since the hydrodynamic effect on the fluid pressure is insignificant compared to the contact pressures.

Studies on the seal surface characteristic parameters α and β have been performed for the smooth rod cases. With an increasing α (the measure of asperity radius), the film thickness of the U-cup seal decreases, causing a smaller fluid transport during both instroke and outstroke. The critical speed decreases with the increasing α value. The profiles of friction versus rod speed curves have similar shapes for various α values, but quantitatively different. The friction force with a

starved boundary is much larger than that of the flooded case, for the same rod speed. With an increasing β (the measure of asperity density) the film thickness of the U-cup seal increases, causing a larger fluid transport during both instroke and outstroke. The critical speed increases with the increasing β value. The profiles of friction versus rod speed curves have similar shape for various β values, but quantitatively different. The friction force with a starved boundary is much larger than that of the flooded case, for the same rod speed.

The studies on U-cup and step seals with a plunge-ground rod show that for a polyurethane U-cup seal under flooded boundary conditions, a plunge-ground rod produces a lower fluid transport into the cylinder during the instroke compared to a smooth rod, reducing the effectiveness of the seal. The plunge-ground rod also increases the friction force on the rod. In addition, the plunge-ground rod produces large fluctuations in the contact pressure, which would be expected to increase the wear rate due to fatigue-induced wear. For the U-cup seal under starved boundary conditions, the plunge-ground rod has a shorter starvation region than that of the smooth rod due to the smaller degree of starvation. The plunge-ground rod decreases the friction force on the rod compared to the smooth rod, because the lower degree of starvation generates more fluid pressure to support the seal, decreasing the contact force, compared to the smooth rod case. The plunge-ground rod also produces large fluctuations in the contact pressure, which would be expected to increase the wear rate due to fatigue-induced wear. For a PTFE step seal, the plunge-ground rod produces no significant effects on the fluid transport and friction

force. Those effects that were observed with the U-cup seal are absent due to the larger roughness of the step seal and resulting larger film thickness. However, the plunge-ground rod does produce large fluctuations in the contact pressure, as with the U-cup seal, and would be expected to increase the wear rate of the step seal due to fatigue-induced wear.

Hypothetical studies on both the U-cup and step seals with a plunge-ground rod show that the roughness of the seal surface is the most important characteristic governing the behavior of those seals. A higher surface roughness produces a thicker fluid film, which decreases the influence of the hydrodynamic effect.

The studies on the micro-patterned rod surfaces' effects on seal performance consider two categories of surface pattern: cavities and protrusions, both under flooded and starved boundary conditions. The results show that both cavity and protrusion patterns have effects on the fluid transport and friction force, compared to the smooth rod. The effects under flooded boundary conditions are generally larger than those under starved boundary conditions. Under flooded boundary conditions, the cavity patterns can reduce the friction force while keeping the critical speed almost constant compared to the smooth rod. Under the starved boundary conditions, the cavity patterns increase the friction force compared to the smooth rod, by increasing the starvation area.

The studies show that for cavity patterns, the movement of the rod into various axial positions (time step changing), the shape of the cavity, the size of the cavity,

and the arrangement of the cavities have no significant effect on both fluid transport and friction force, while the cavity depth and the land area ratio can affect the fluid transport and friction force behavior. The protrusion patterns have very similar effects as the cavity patterns. One difference is that the height of the protrusion pattern affects the fluid transport during the instroke and changes the critical speed, by changing the average film thickness.

In summary, the numerical models developed in this research provide an effective tool for analyzing the hydraulic rod seals performance, taking rod surface patterns, and starved boundary conditions into account. The results of this research show that the rod surface pattern may have significant, though small, effects on both fluid transport (leakage) and friction force behavior of the seal. The effects of the rod surface pattern should not be neglected in the design and optimization of seals.

There are some general suggestion for seal designers based on this research:

1. The critical speed of a rod seal should be as low as possible

2. To reduce the starvation, the seal design should match instroke and outstroke transports as close as possible.

3. Considering the friction reduction in the present range of studies and the cost of manufacturing the micro-patterned rod, the micro-texture technique is not economical at this stage.

Appendix A：Fluid Mechanics Solution Algorithm

The finite volume scheme developed in this research uses a grid point cluster shown in Figure A.1. P is the central grid point, E and W are east and west grid points, along the *x*, or axial direction; N and S are north and south grid points, along the *y*, or radial direction. The rod moves in the *x* direction; for the instroke, $U<0$ and for the outstroke $U>0$. The boundary of the control volume is shown by the dotted line, going through points *e*, *w*, *n* and *s*, which are midway between the node pairs EP, WP, NP and SP.

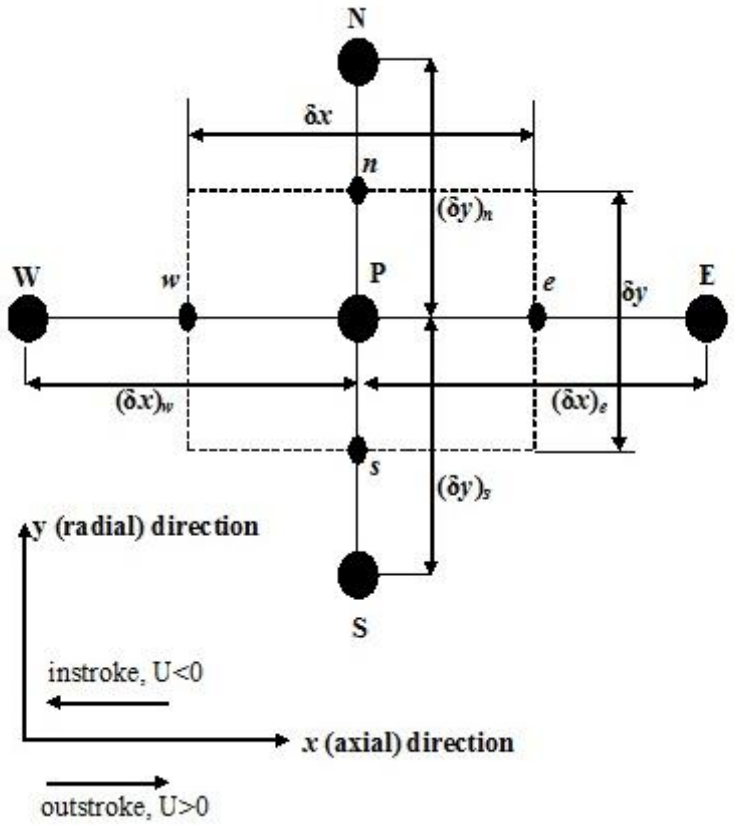

Figure A.1: Finite volume discretization scheme implemented

Referring to Figure A.1:

$$(\delta x)_e = x_E - x_P;\ (\delta x)_w = x_P - x_W;\ \delta x = \frac{(\delta x)_e + (\delta x)_w}{2}$$

$$(\delta y)_n = y_N - y_P;\ (\delta y)_s = y_P - y_S;\ \delta y = \frac{(\delta y)_n + (\delta y)_s}{2}$$

Defining $K = \phi_{xx} H^3 e^{-\hat{\alpha} F \Phi} = \phi_{yy} H^3 e^{-\hat{\alpha} F \Phi}$; ($\phi_{xx} = \phi_{yy}$ in this research)

Eq.(3.9) becomes:

$$\frac{\partial}{\partial \hat{x}}\left(K\frac{\partial}{\partial \hat{x}}(F\Phi)\right)+\Lambda\frac{\partial}{\partial \hat{y}}\left(K\frac{\partial}{\partial \hat{y}}(F\Phi)\right)$$
$$=6\zeta\frac{\partial}{\partial \hat{x}}(\{1+(1-F)\Phi\}\{H_T+\phi_{s.c.x}\})$$
$$+12\varepsilon\frac{\partial}{\partial \hat{t}}(\{1+(1-F)\Phi\}H_T) \quad \text{(A.1)}$$

Integrating Eq.(A.1) over the control volume along x direction, from x_w to x_e yields,

$$\int_{x_w}^{x_e}\frac{\partial}{\partial \hat{x}}\left(K\frac{\partial}{\partial \hat{x}}(F\Phi)\right)d\hat{x}+\int_{x_w}^{x_e}\Lambda\frac{\partial}{\partial \hat{y}}\left(K\frac{\partial}{\partial \hat{y}}(F\Phi)\right)d\hat{x}$$
$$-6\zeta\int_{x_w}^{x_e}\frac{\partial}{\partial \hat{x}}(\{1+(1-F)\Phi\}\{H_T+\phi_{s.c.x}\})\,d\hat{x} \quad \text{(A.2)}$$
$$-12\varepsilon\int_{x_w}^{x_e}\frac{\partial}{\partial \hat{t}}(\{1+(1-F)\Phi\}H_T)d\hat{x}=0$$

Applying the finite volume method to Eq.(A.2):

$$\left[K\frac{\partial}{\partial \hat{x}}(F\Phi)\right]_e-\left[K\frac{\partial}{\partial \hat{x}}(F\Phi)\right]_w \quad \text{Term1}$$

$$+\Lambda\frac{\partial}{\partial \hat{y}}\left(K\frac{\partial}{\partial \hat{y}}(F\Phi)\right)\delta x \quad \text{Term2}$$

$$-6\zeta\langle[\{1+(1-F)\Phi\}\{H_T+\phi_{s.c.x}\}]_e - [\{1+(1-F)\Phi\}\{H_T+\phi_{s.c.x}\}]_w\rangle \quad \text{Term3} \quad \text{(A.3)}$$

$$-12\varepsilon\frac{\partial}{\partial \hat{t}}(\{1+(1-F)\Phi\}H_T)\,\delta x \quad \text{Term4}$$

$$=0$$

Similarly, integrating Eq.(A.3) over the control volume along y direction, from y_s to y_n yields:

$$\int_{y_s}^{y_n}\left\{\left[K\frac{\partial}{\partial \hat{x}}(F\Phi)\right]_e-\left[K\frac{\partial}{\partial \hat{x}}(F\Phi)\right]_w\right\}d\hat{y} \quad \text{Term1} \quad \text{(A.4)}$$

$$+\Lambda \int_{y_s}^{y_n} \left[\frac{\partial}{\partial \hat{y}} \left(K \frac{\partial}{\partial \hat{y}} (F\Phi) \right) \delta x \right] d\hat{y} \qquad \text{Term2}$$

$$-6\zeta \int_{y_s}^{y_n} \langle [\{1 + (1-F)\Phi\}\{H_T + \phi_{s.c.x}\}]_e - [\{1 + (1-F)\Phi\}\{H_T + \phi_{s.c.x}\}]_w \rangle \, d\hat{y} \qquad \text{Term3}$$

$$-12\varepsilon \int_{y_s}^{y_n} \left[\frac{\partial}{\partial \hat{t}} (\{1 + (1-F)\Phi\} H_T) \, \delta x \right] d\hat{y} \qquad \text{Term4}$$

$$= 0$$

Eq.(A.4) yields:

$$\left\{ \left[K \frac{\partial}{\partial \hat{x}} (F\Phi) \right]_e - \left[K \frac{\partial}{\partial \hat{x}} (F\Phi) \right]_w \right\} \delta y \qquad \text{Term1}$$

$$+\Lambda \left\{ \left[K \frac{\partial}{\partial \hat{y}} (F\Phi) \right]_n - \left[K \frac{\partial}{\partial \hat{y}} (F\Phi) \right]_n \right\} \delta x \qquad \text{Term2}$$

$$-6\zeta \langle [\{1 + (1-F)\Phi\}\{H_T + \phi_{s.c.x}\}]_e - [\{1 + (1-F)\Phi\}\{H_T + \phi_{s.c.x}\}]_w \rangle \delta y \qquad \text{Term3} \qquad \text{(A.5)}$$

$$-12\varepsilon \left[\frac{\partial}{\partial \hat{t}} (\{1 + (1-F)\Phi\} H_T) \right] \delta x \delta y \qquad \text{Term4}$$

$$= 0$$

Approximating the derivatives in Term1 and Term2 with finite differences gives:

$$\left\{ \left[K \frac{\partial}{\partial \hat{x}} (F\Phi) \right]_e - \left[K \frac{\partial}{\partial \hat{x}} (F\Phi) \right]_w \right\} \delta y = \left\{ K_e \frac{F_E \Phi_E - F_P \Phi_P}{\delta \hat{x}_e} - K_w \frac{F_P \Phi_P - F_W \Phi_W}{\delta \hat{x}_w} \right\} \delta y \qquad \text{(A.6)}$$

$$= Term1$$

$$\Lambda\left\{\left[K\frac{\partial}{\partial\hat{y}}(F\Phi)\right]_n-\left[K\frac{\partial}{\partial\hat{y}}(F\Phi)\right]_n\right\}\delta x$$
$$=\Lambda\left\{K_n\frac{F_N\Phi_N-F_P\Phi_P}{\delta\hat{x}_n}-K_s\frac{F_P\Phi_P-F_S\Phi_S}{\delta\hat{x}_s}\right\}\delta x$$
$$=Term2$$

where K_e, K_w, K_n and K_s can be written in terms of harmonic means as:

$$K_e=\frac{2K_EK_P}{(K_E+K_P)}\,,K_w=\frac{2K_WK_P}{(K_W+K_P)}\,,K_n=\frac{2K_NK_P}{(K_N+K_P)}\,,K_s=\frac{2K_SK_P}{(K_S+K_P)}$$

An upwind scheme is applied to Term3 in Eq.(A.5) where the scheme is dependent on the direction of flow [119]:

For $U > 0$, the outstroke cases, in the upwind scheme, the unsolved parameters (F and Φ) on edge "e" yields to that on point P while the parameters on edge "w" yields to that on point W. Term 3. becomes:

$$-6\zeta[\{1+(1-F_P)\Phi_{\mathrm{P}}\}(H_T+\phi_{s.c.x})_e - \{1+(1-F_W)\Phi_{\mathrm{W}}\}\{H_T+\phi_{s.c.x}\}_w]\delta y=Term3 \quad \text{(A.7a)}$$

For $U < 0$, the instroke cases, in the upwind scheme, the parameters on edge "e" yields to that on point E while the parameters on edge "w" yields to that on point P. Term 3. becomes:

$$-6\zeta[\{1+(1-F_E)\Phi_{\mathrm{E}}\}(H_T+\phi_{s.c.x})_e - \{1+(1-F_P)\Phi_{\mathrm{P}}\}\{H_T+\phi_{s.c.x}\}_w]\delta y=Term3 \quad \text{(A.7b)}$$

where

$$(H_T+\phi_{s.c.x})_e=[(H_T+\phi_{s.c.x})_E+(H_T+\phi_{s.c.x})_P]/2$$

$$\text{and } (H_T + \phi_{s.c.x})_w = [(H_T + \phi_{s.c.x})_W + (H_T + \phi_{s.c.x})_P]/2$$

The squeeze film term, or Term4 in Eq.(A.5) can be expressed as:

$$\begin{aligned} -12\varepsilon \frac{\delta x \delta y}{\Delta t} \langle [\{1 + (1 - F_P)\Phi_{\mathrm{P}}\}(H_T)_P\ ]^{now} \\ - [\{1 + (1 - F_P)\Phi_{\mathrm{P}}\}(H_T)_P\ ]^{last} \rangle = Term4 \end{aligned} \tag{A.8}$$

where terms with a superscript of "*now*" means the parameters at the calculated time step while a superscript of "*last*" indicates the parameters at the previous time step.

Rearranging Eq.(A.5):

$$\begin{aligned} &(Term1)^{now} + (Term2)^{now} + (Term3)^{now} \\ &\quad - 12\varepsilon \frac{\delta x \delta y}{\Delta t} \{(1 - F_P)(H_T)_P \Phi_{\mathrm{P}}\}^{now} \\ &\quad - 12\varepsilon \frac{\delta x \delta y}{\Delta t} \langle [(H_T)_P\ ]^{now} - [\{1 + (1 - F_P)\Phi_{\mathrm{P}}\}(H_T)_P\ ]^{last} \rangle \\ &\quad = 0 \end{aligned} \tag{A.9}$$

For the outstroke (with a positive rod velocity) $U>0$:

$$\begin{aligned} &\frac{\delta y K_e}{\delta \hat{x}_e} F_P \Phi_{\mathrm{P}} + \frac{\delta y K_{ew}}{\delta \hat{x}_w} F_P \Phi_{\mathrm{P}} + \Lambda \frac{\delta x K_n}{\delta \hat{y}_n} F_P \Phi_{\mathrm{P}} + \Lambda \frac{\delta x K_s}{\delta \hat{y}_s} F_P \Phi_{\mathrm{P}} \\ &\quad + 6\zeta \delta y (H_T + \phi_{s.c.x})_e (1 - F_P) \Phi_{\mathrm{P}} \\ &\quad + 12\varepsilon \frac{\delta x \delta y}{\Delta t} (1 - F_P)(H_T)_P \Phi_{\mathrm{P}} \\ &\quad = \frac{\delta y K_e}{\delta \hat{x}_e} F_E \Phi_{\mathrm{E}} \\ &+ \frac{\delta y K_w}{\delta \hat{x}_w} F_W \Phi_{\mathrm{W}} + 6\zeta \delta y (H_T + \phi_{s.c.x})_w (1 - F_W) \Phi_{\mathrm{W}} \\ &\quad + \Lambda \frac{\delta x K_n}{\delta \hat{y}_n} F_N \Phi_{\mathrm{N}} \end{aligned} \tag{A.10}$$

$$+\Lambda\frac{\delta x K_s}{\delta\hat{y}_s}F_S\Phi_{\mathrm{S}}$$

$$-6\zeta\delta y[(H_T+\phi_{s.c.x})_e-(H_T+\phi_{s.c.x})_w]$$

$$-12\varepsilon\frac{\delta x\delta y}{\Delta t}\langle(H_T)_P-\left[\left\{1+\left(1-{F_P}^{last}\right)\Phi_{\mathrm{P}}{}^{\mathrm{last}}\right\}{(H_T)_P}^{last}\right]\rangle$$

For the instroke (with a negative rod velocity) U<0:

$$\frac{\delta y K_e}{\delta\hat{x}_e}F_P\Phi_{\mathrm{P}}+\frac{\delta y K_{ew}}{\delta\hat{x}_w}F_P\Phi_{\mathrm{P}}+\Lambda\frac{\delta x K_n}{\delta\hat{y}_n}F_P\Phi_{\mathrm{P}}+\Lambda\frac{\delta x K_s}{\delta\hat{y}_s}F_P\Phi_{\mathrm{P}}$$

$$-6\zeta\delta y(H_T+\phi_{s.c.x})_w(1-F_P)\Phi_{\mathrm{P}}$$

$$+12\varepsilon\frac{\delta x\delta y}{\Delta t}(1-F_P)(H_T)_P\Phi_{\mathrm{P}}$$

$$=\frac{\delta y K_e}{\delta\hat{x}_e}F_E\Phi_{\mathrm{E}}-6\zeta\delta y(H_T+\phi_{s.c.x})_e(1-F_E)\Phi_{\mathrm{E}}$$

$$+\frac{\delta y K_w}{\delta\hat{x}_w}F_W\Phi_{\mathrm{W}}$$

$$+\Lambda\frac{\delta x K_n}{\delta\hat{y}_n}F_N\Phi_{\mathrm{N}}$$

$$+\Lambda\frac{\delta x K_s}{\delta\hat{y}_s}F_S\Phi_{\mathrm{S}}$$

$$-6\zeta\delta y[(H_T+\phi_{s.c.x})_e-(H_T+\phi_{s.c.x})_w]$$

$$-12\varepsilon\frac{\delta x\delta y}{\Delta t}\langle(H_T)_P-\left[\left\{1+\left(1-{F_P}^{last}\right)\Phi_{\mathrm{P}}{}^{\mathrm{last}}\right\}{(H_T)_P}^{last}\right]\rangle$$

(A.11)

Eq.(A.10) and Eq.(A.11) can be written in the form of a system of algebraic equations:

$$A_P\Phi_{\mathrm{P}}=A_E\Phi_{\mathrm{E}}+A_W\Phi_{\mathrm{W}}+\mathrm{b_{EW}}$$

$$A_P\Phi_{\mathrm{P}}=A_N\Phi_{\mathrm{N}}+A_S\Phi_{\mathrm{S}}+\mathrm{b_{NS}}$$

(A.12)

So, for the outstroke:

$$A_P = \frac{\delta y K_e}{\delta \hat{x}_e} F_P + \frac{\delta y K_{ew}}{\delta \hat{x}_w} F_P + \Lambda \frac{\delta x K_n}{\delta \hat{y}_n} F_P + \Lambda \frac{\delta x K_s}{\delta \hat{y}_s} F_P$$
$$+ 6\zeta \delta y (H_T + \phi_{s.c.x})_e (1 - F_P) + 12\varepsilon \frac{\delta x \delta y}{\Delta t} (1 - F_P)(H_T)_P$$

$$A_E = \frac{\delta y K_e}{\delta \hat{x}_e} F_E$$

$$A_W = \frac{\delta y K_w}{\delta \hat{x}_w} F_W + 6\zeta \delta y (H_T + \phi_{s.c.x})_w (1 - F_W)$$

$$\mathrm{b_{EW}} = \Lambda \frac{\delta x K_n}{\delta \hat{y}_n} F_N \Phi_\mathrm{N} + \Lambda \frac{\delta x K_s}{\delta \hat{y}_s} F_S \Phi_\mathrm{S}$$
$$- 6\zeta \delta y [(H_T + \phi_{s.c.x})_e - (H_T + \phi_{s.c.x})_w]$$
$$- 12\varepsilon \frac{\delta x \delta y}{\Delta t} \langle (H_T)_P - \left[\{1 + \left(1 - {F_P}^{last}\right) {\Phi_\mathrm{P}}^{\mathrm{last}}\} {(H_T)_P}^{last}\right] \rangle \quad \text{(A.13)}$$

and,

$$A_N = \Lambda \frac{\delta x K_n}{\delta \hat{y}_n} F_N$$

$$A_S = \Lambda \frac{\delta x K_s}{\delta \hat{y}_s} F_S$$

$$\mathrm{b_{NS}} = \frac{\delta y K_e}{\delta \hat{x}_e} F_E \Phi_\mathrm{E} + \frac{\delta y K_w}{\delta \hat{x}_w} F_W \Phi_\mathrm{W} + 6\zeta \delta y (H_T + \phi_{s.c.x})_w (1 - F_W) \Phi_\mathrm{W}$$
$$- 6\zeta \delta y [(H_T + \phi_{s.c.x})_e - (H_T + \phi_{s.c.x})_w]$$
$$- 12\varepsilon \frac{\delta x \delta y}{\Delta t} \langle (H_T)_P - \left[\{1 + \left(1 - {F_P}^{last}\right) {\Phi_\mathrm{P}}^{\mathrm{last}}\} {(H_T)_P}^{last}\right] \rangle$$

For the instroke:

$$A_P = \frac{\delta y K_e}{\delta \hat{x}_e} F_P + \frac{\delta y K_{ew}}{\delta \hat{x}_w} F_P + \Lambda \frac{\delta x K_n}{\delta \hat{y}_n} F_P + \Lambda \frac{\delta x K_s}{\delta \hat{y}_s} F_P$$
$$- 6\zeta \delta y (H_T + \phi_{s.c.x})_w (1 - F_P) + 12\varepsilon \frac{\delta x \delta y}{\Delta t} (1 - F_P)(H_T)_P$$
$$A_E = \frac{\delta y K_e}{\delta \hat{x}_e} F_E - 6\zeta \delta y (H_T + \phi_{s.c.x})_e (1 - F_E) \quad \text{(A.14)}$$

$$A_W = \frac{\delta y K_w}{\delta \hat{x}_w} F_W$$

$$\mathrm{b_{EW}} = \Lambda \frac{\delta x K_n}{\delta \hat{y}_n} F_N \Phi_{\mathrm{N}} + \Lambda \frac{\delta x K_s}{\delta \hat{y}_s} F_S \Phi_{\mathrm{S}}$$
$$- 6\zeta \delta y [(H_T + \phi_{s.c.x})_e - (H_T + \phi_{s.c.x})_w]$$
$$- 12\varepsilon \frac{\delta x \delta y}{\Delta t} \langle (H_T)_P - [\{1 + (1 - F_P{}^{last}) \Phi_{\mathrm{P}}{}^{\mathrm{last}}\} (H_T)_P{}^{last}] \rangle$$

and,

$$A_N = \Lambda \frac{\delta x K_n}{\delta \hat{y}_n} F_N$$

$$A_S = \Lambda \frac{\delta x K_s}{\delta \hat{y}_s} F_S$$

$$\mathrm{b_{NS}} = \frac{\delta y K_e}{\delta \hat{x}_e} F_E \Phi_{\mathrm{E}} - 6\zeta \delta y (H_T + \phi_{s.c.x})_e (1 - F_E) \Phi_{\mathrm{E}} + \frac{\delta y K_w}{\delta \hat{x}_w} F_W \Phi_{\mathrm{W}}$$
$$- 6\zeta \delta y [(H_T + \phi_{s.c.x})_e - (H_T + \phi_{s.c.x})_w]$$
$$- 12\varepsilon \frac{\delta x \delta y}{\Delta t} \langle (H_T)_P - [\{1 + (1 - F_P{}^{last}) \Phi_{\mathrm{P}}{}^{\mathrm{last}}\} (H_T)_P{}^{last}] \rangle$$

To use the TDMA, it is necessary to convert the above equations to index notation:

$$A_{i,j} \Phi_{\mathrm{i,j}} = B_{i,j} \Phi_{\mathrm{i+1,j}} + C_{i,j} \Phi_{\mathrm{i-1,j}} + D_{i,j}$$
$$A_{i,j} \Phi_{\mathrm{i,j}} = E_{i,j} \Phi_{\mathrm{i,j+1}} + F_{i,j} \Phi_{\mathrm{i,j-1}} + G_{i,j} \qquad \text{(A.15)}$$

For the outstroke:

$$A_{i,j} = \left\{ \frac{\Delta y}{\Delta x} \left[\frac{2K_{i+1,j} K_{i,j}}{(K_{i+1,j} + K_{i,j})} + \frac{2K_{i-1,j} K_{i,j}}{(K_{i-1,j} + K_{i,j})} \right] \right.$$
$$\left. + \Lambda \frac{\Delta x}{\Delta y} \left[\frac{2K_{i,j+1} K_{i,j}}{(K_{i,j+1} + K_{i,j})} + \frac{2K_{i,j-1} K_{i,j}}{(K_{i,j-1} + K_{i,j})} \right] \right\} F_{i,j}$$
$$+ 6\zeta \Delta y \frac{[(H_T + \phi_{s.c.x})_{i+1,j} + (H_T + \phi_{s.c.x})_{i,j}]}{2} (1 - F_{i,j}) \qquad \text{(A.16)}$$
$$+ 12\varepsilon \frac{\Delta x \Delta y}{\Delta t} (H_T)_{i,j} (1 - F_{i,j})$$

$$B_{i,j} = \frac{\Delta y}{\Delta x}\frac{2K_{i+1,j}K_{i,j}}{\left(K_{i+1,j}+K_{i,j}\right)}F_{i+1,j}$$

$$C_{i,j} = \frac{\Delta y}{\Delta x}\frac{2K_{i-1,j}K_{i,j}}{\left(K_{i-1,j}+K_{i,j}\right)}F_{i-1,j} + 6\zeta\Delta y\frac{\left[(H_T+\phi_{s.c.x})_{i-1,j}+(H_T+\phi_{s.c.x})_{i,j}\right]}{2}(1-F_{i-1,j})$$

$$D_{i,j} = \Lambda\frac{\Delta x}{\Delta y}\left[\frac{2K_{i,j+1}K_{i,j}}{\left(K_{i,j+1}+K_{i,j}\right)}F_{i,j+1}\Phi_{i,j+1}+\frac{2K_{i,j-1}K_{i,j}}{\left(K_{i,j-1}+K_{i,j}\right)}F_{i,j-1}\Phi_{i,j-1}\right] - 6\zeta\Delta y\left[\frac{(H_T+\phi_{s.c.x})_{i+1,j}+(H_T+\phi_{s.c.x})_{i,j}}{2} - \frac{(H_T+\phi_{s.c.x})_{i-1,j}+(H_T+\phi_{s.c.x})_{i,j}}{2}\right] - 12\varepsilon\frac{\Delta x\Delta y}{\Delta t}\langle(H_T)_{i,j} - \left[\left\{1+\left(1-F_{i,j}{}^{last}\right)\Phi_{\mathrm{i,j}}{}^{\mathrm{last}}\right\}(H_T)_{i,j}{}^{last}\right]\rangle$$

and,

$$E_{i,j} = \Lambda\frac{\Delta x}{\Delta y}\frac{2K_{i,j+1}K_{i,j}}{\left(K_{i,j+1}+K_{i,j}\right)}F_{i,j+1}$$

$$F_{i,j} = \Lambda\frac{\Delta x}{\Delta y}\frac{2K_{i,j-1}K_{i,j}}{\left(K_{i,j-1}+K_{i,j}\right)}F_{i,j-1}$$

$$G_{i,j} = \frac{\Delta y}{\Delta x}\left[\frac{2K_{i+1,j}K_{i,j}}{\left(K_{i+1,j}+K_{i,j}\right)}F_{i+1,j}\Phi_{i+1,j} + \frac{2K_{i-1,j}K_{i,j}}{\left(K_{i-1,j}+K_{i,j}\right)}F_{i-1,j}\Phi_{i-1,j}\right]$$
$$+ 6\zeta\Delta y\frac{\left[(H_T+\phi_{s.c.x})_{i-1,j} + (H_T+\phi_{s.c.x})_{i,j}\right]}{2}(1$$
$$- F_{i-1,j})\Phi_{i-1,j}$$
$$- 6\zeta\Delta y\left[\frac{(H_T+\phi_{s.c.x})_{i+1,j} + (H_T+\phi_{s.c.x})_{i,j}}{2}\right.$$
$$\left.- \frac{(H_T+\phi_{s.c.x})_{i-1,j} + (H_T+\phi_{s.c.x})_{i,j}}{2}\right]$$
$$- 12\varepsilon\frac{\Delta x\Delta y}{\Delta t}\langle(H_T)_{i,j}$$
$$- \left[\left\{1+\left(1-F_{i,j}{}^{last}\right)\Phi_{\mathrm{i,j}}{}^{\mathrm{last}}\right\}(H_T)_{i,j}{}^{last}\right]\rangle$$

For the instroke:

$$A_{i,j} = \left\{\frac{\Delta y}{\Delta x}\left[\frac{2K_{i+1,j}K_{i,j}}{\left(K_{i+1,j}+K_{i,j}\right)} + \frac{2K_{i-1,j}K_{i,j}}{\left(K_{i-1,j}+K_{i,j}\right)}\right]\right.$$
$$\left. + \Lambda\frac{\Delta x}{\Delta y}\left[\frac{2K_{i,j+1}K_{i,j}}{\left(K_{i,j+1}+K_{i,j}\right)} + \frac{2K_{i,j-1}K_{i,j}}{\left(K_{i,j-1}+K_{i,j}\right)}\right]\right\}F_{i,j}$$
$$- 6\zeta\Delta y\frac{\left[(H_T+\phi_{s.c.x})_{i-1,j} + (H_T+\phi_{s.c.x})_{i,j}\right]}{2}\left(1-F_{i,j}\right)$$
$$+ 12\varepsilon\frac{\Delta x\Delta y}{\Delta t}(H_T)_{i,j}\left(1-F_{i,j}\right) \qquad \text{(A.17)}$$

$$B_{i,j} = \frac{\Delta y}{\Delta x}\frac{2K_{i+1,j}K_{i,j}}{\left(K_{i+1,j}+K_{i,j}\right)}F_{i+1,j}$$
$$- 6\zeta\Delta y\frac{\left[(H_T+\phi_{s.c.x})_{i+1,j} + (H_T+\phi_{s.c.x})_{i,j}\right]}{2}(1-F_{i+1,j})$$

$$C_{i,j} = \frac{\Delta y}{\Delta x}\frac{2K_{i-1,j}K_{i,j}}{\left(K_{i-1,j}+K_{i,j}\right)}F_{i-1,j}$$

$$D_{i,j} = \Lambda \frac{\Delta x}{\Delta y}\left[\frac{2K_{i,j+1}K_{i,j}}{\left(K_{i,j+1}+K_{i,j}\right)}F_{i,j+1}\Phi_{i,j+1} + \frac{2K_{i,j-1}K_{i,j}}{\left(K_{i,j-1}+K_{i,j}\right)}F_{i,j-1}\Phi_{i,j-1}\right]$$

$$- 6\zeta\Delta y\left[\frac{(H_T+\phi_{s.c.x})_{i+1,j} + (H_T+\phi_{s.c.x})_{i,j}}{2}\right.$$

$$\left. - \frac{(H_T+\phi_{s.c.x})_{i-1,j} + (H_T+\phi_{s.c.x})_{i,j}}{2}\right]$$

$$- 12\varepsilon\frac{\Delta x\Delta y}{\Delta t}\langle(H_T)_{i,j}$$

$$- \left[\left\{1+\left(1-F_{i,j}{}^{last}\right)\Phi_{\mathrm{i,j}}{}^{\mathrm{last}}\right\}(H_T)_{i,j}{}^{last}\right]\rangle$$

and,

$$E_{i,j} = \Lambda\frac{\Delta x}{\Delta y}\frac{2K_{i,j+1}K_{i,j}}{\left(K_{i,j+1}+K_{i,j}\right)}F_{i,j+1}$$

$$F_{i,j} = \Lambda\frac{\Delta x}{\Delta y}\frac{2K_{i,j-1}K_{i,j}}{\left(K_{i,j-1}+K_{i,j}\right)}F_{i,j-1}$$

$$G_{i,j} = \frac{\Delta y}{\Delta x}\left[\frac{2K_{i+1,j}K_{i,j}}{\left(K_{i+1,j}+K_{i,j}\right)}F_{i+1,j}\Phi_{i+1,j} + \frac{2K_{i-1,j}K_{i,j}}{\left(K_{i-1,j}+K_{i,j}\right)}F_{i-1,j}\Phi_{i-1,j}\right]$$

$$- 6\zeta\Delta y\frac{\left[(H_T+\phi_{s.c.x})_{i+1,j} + (H_T+\phi_{s.c.x})_{i,j}\right]}{2}(1$$

$$- F_{i+1,j})\Phi_{i+1,j}$$

$$- 6\zeta\Delta y\left[\frac{(H_T+\phi_{s.c.x})_{i+1,j} + (H_T+\phi_{s.c.x})_{i,j}}{2}\right.$$

$$\left. - \frac{(H_T+\phi_{s.c.x})_{i-1,j} + (H_T+\phi_{s.c.x})_{i,j}}{2}\right]$$

$$- 12\varepsilon\frac{\Delta x\Delta y}{\Delta t}\langle(H_T)_{i,j}$$

$$- \left[\left\{1+\left(1-F_{i,j}{}^{last}\right)\Phi_{\mathrm{i,j}}{}^{\mathrm{last}}\right\}(H_T)_{i,j}{}^{last}\right]\rangle$$

It is straightforward to derive the one-dimensional form of Eq.(A.16) and Eq.(A.17).

For the one-dimensional (axisymmetrical) case:

$$A_i \Phi_{\mathrm{i}} = B_i \Phi_{\mathrm{i+1}} + C_{i,j} \Phi_{\mathrm{i-1}} + D_i \tag{A.18}$$

For the outstroke:

$$\begin{aligned}
A_i = & \left\{ \frac{1}{\Delta x} \left[\frac{2K_{i+1}K_i}{(K_{i+1}+K_i)} + \frac{2K_{i-1}K_i}{(K_{i-1}+K_i)} \right] \right\} F_i \\
& + 6\zeta \frac{[(H_T + \phi_{s.c.x})_{i+1} + (H_T + \phi_{s.c.x})_i]}{2} (1 - F_i) \\
& + 12\varepsilon \frac{\Delta x}{\Delta t} (H_T)_i (1 - F_i) \\
B_i = & \frac{1}{\Delta x} \frac{2K_{i+1}K_i}{(K_{i+1}+K_i)} F_{i+1} \\
C_i = & \frac{1}{\Delta x} \frac{2K_{i-1}K_i}{(K_{i-1}+K_i)} F_{i-1} \\
& + 6\zeta \frac{\left[(H_T + \phi_{s.c.x})_{i-1,j} + (H_T + \phi_{s.c.x})_{i,j}\right]}{2} (1 - F_{i-1}) \\
D_i = & -6\zeta \left[\frac{(H_T + \phi_{s.c.x})_{i+1} + (H_T + \phi_{s.c.x})_i}{2} \right. \\
& \left. - \frac{(H_T + \phi_{s.c.x})_{i-1} + (H_T + \phi_{s.c.x})_i}{2} \right] \\
& - 12\varepsilon \frac{\Delta x}{\Delta t} \langle (H_T)_i - \left[\left\{ 1 + \left(1 - F_i^{\,last}\right) \Phi_{\mathrm{i}}^{\,\mathrm{last}} \right\} (H_T)_i^{\,last} \right] \rangle
\end{aligned} \tag{A.19}$$

For the instroke:

$$\begin{aligned}
A_i = & \left\{ \frac{1}{\Delta x} \left[\frac{2K_{i+1}K_i}{(K_{i+1}+K_i)} + \frac{2K_{i-1}K_i}{(K_{i-1}+K_i)} \right] \right\} F_i \\
& - 6\zeta \frac{[(H_T + \phi_{s.c.x})_{i-1} + (H_T + \phi_{s.c.x})_i]}{2} (1 - F_i) \\
& + 12\varepsilon \frac{\Delta x}{\Delta t} (H_T)_i (1 - F_i) \\
B_i = & \frac{1}{\Delta x} \frac{2K_{i+1}K_i}{(K_{i+1}+K_i)} F_{i+1} \\
& - 6\zeta \frac{[(H_T + \phi_{s.c.x})_{i+1} + (H_T + \phi_{s.c.x})_i]}{2} (1 - F_{i+1}) \\
C_i = & \frac{1}{\Delta x} \frac{2K_{i-1}K_i}{(K_{i-1}+K_i)} F_{i-1}
\end{aligned} \tag{A.20}$$

$$D_i = -6\zeta \left[\frac{(H_T + \phi_{s.c.x})_{i+1} + (H_T + \phi_{s.c.x})_i}{2} \right.$$
$$\left. - \frac{(H_T + \phi_{s.c.x})_{i-1} + (H_T + \phi_{s.c.x})_i}{2} \right]$$
$$- 12\varepsilon \frac{\Delta x}{\Delta t} \langle (H_T)_i - \left[\left\{ 1 + \left(1 - F_i^{last} \right) \Phi_{\mathrm{i}}^{\mathrm{last}} \right\} (H_T)_i^{last} \right] \rangle$$

REFERENCES

[1] K. Stelson, P. Li, *et al*., *CCEFP 7th annual report* vol. 1: Center for Compact and Efficient Fluid Power, 2013.

[2] M. J. W. Schouten, R. P. B. J. Dollevoet, and B. M. de Laat, "Design of optimized seals for leak-free hydraulic cylinders. research on the total sealing concept of reciprocating seals running against ceramic and chromium plated rods for hydraulic cylinders," in *15th International Conference on Fluid Sealing*, Masstricht, The Netherlands, 1997, pp. 111-131.

[3] B. S. Nau, "An historical review of studies of polymeric seals in reciprocating hydraulic systems," *Journal of Engineering Tribology*, vol. 213 pp. 215-226, 1999.

[4] T. Papatheodorou, "Influence of hard chrome plated rod surface treatments on sealing behavior of hydraulic rod seals," *Sealing Technology*, vol. 2005-4 pp. 5-10, Apr 2005.

[5] P. C. Hadinata and L. S. Stephens, "Soft elastohydrodynamic analysis of radial lip seals with deterministic microasperities on the shaft," *Journal of Tribology-Transactions of the Asme*, vol. 129 (4), pp. 851-859, Oct 2007.

[6] V. Kanakasabai, K. H. Warren, and L. S. Stephens, "Surface analysis of the elastomer in lip seals run against shafts manufactured with micro-cavity patterns," *Proceedings of the Institution of Mechanical Engineers Part J-Journal of Engineering Tribology*, vol. 224 (J8), pp. 723-736, 2010.

[7] W. Li, L. S. Stephens, and J. F. Wenk, "Experimental benchmarking of the numerical model of a radial lip seal with a surface textured shaft," *Tribology Transactions*, vol. 56 (1), pp. 75-87, Jan 2013.

[8] G. K. Nikas, "Eighty years of research on hydraulic reciprocating seals: review of tribological studies and related topics since the 1930s," *Proceedings of the Institution of Mechanical Engineers Part J-Journal of Engineering Tribology*, vol. 224 (J1), pp. 1-23, 2010.

[9] C. M. White and D. F. Denny, "The sealing mechanism of flexible packings," *Scientific and Technical Memorandum No. 3/47, UK Ministry of Supply,* 1947.

[10] H. K. Müller, "Leakage and friction of flexible packings at reciprocating motion with special consideration of hydrodynamic film formation," *Proceedings of the 2nd International Conference on Fluid Sealing,* pp. 13-28(BHRA), 1964.

[11] G. J. Field and B. S. Nau, "An experimental study of reciprocating rubber seals," in *Proceedings of the IMechE Symposium on Elastohydrodynamic Lubrication,*, Leeds, UK, 1972.

[12] F. Hirano and M. Kaneta, "Theoretical investigation of friction and sealing characteristics of flexible seals for reciprocating motion," *Proceedings of the 5th International Conference on Fluid Sealing,* 1971.

[13] G. J. Field, "The elastohydrodynamic lubrication of rectangular section rubber seals under conditions of reciprocating motion," PhD Thesis, City University London, England, 1973.

[14] G. J. Field and B. S. Nau, "Film thickness and friction measurements during reciprocation of a rectangular section rubber seal ring," in *6th BHRA International Conference on Fluid Sealing*, Munich, Germany, 1973, pp. 45-56.

[15] S. Iwanami and N. Tikamori, "Oil leakage from an O-ring packing," *Proceedings of the 1st International Conference on Fluid Sealing,* 1961.

[16] M. Kaneta, "Sealing characteristics of double reciprocating seals," *Journal of Japan Society of Lubrication Engineers,* vol. 30 (3), pp. 194-200, 1985.

[17] H. Kambayashi and H. Ishiwata, "A study of oil seals for reciprocating motion," *Proceedings of the 2nd International Conference on Fluid Sealing,* pp. 29-40(BHRA), 1964.

[18] A. F. C. Kanters, "On the calculation of leakage and friction of reciprocating elastomeric seals," PhD Thesis, Eindhoven University of Technology, the Netherlands, 1990.

[19] M. Visscher and A. F. C. Kanters, "Literature review and discussion on measurements of leakage, lubricant film thickness and friction of reciprocating elastomeric seals," *STLE Lubrication Engineering,* vol. 46 (12), pp. 785-791, 1990.

[20] M. Visscher, "The measurement of the film thickness and roughness deformation of lubricated elastomers," PhD Thesis, Eindhoven University of Technology, the Netherlands, 1992.

[21] J. M. Lawrie and J. P. O'Donoghue, "The mechanism of lubrication in a reciprocating seal," *Proceedings of the 2nd International Conference on Fluid Sealing,* pp. 69-80(BHRA), 1964.

[22] Gawrys and Kollek, "The effect of operation conditions on the design of seals for reciprocating motion," *Proceedings of the 10th International Conference on Fluid Sealing,* pp. 285-294(BHRA), 1984.

[23] L. E. Cheyney, W. J. Mueller, and R. E. Duval, "Frictional characteristics of O-rings with a typical hydraulic fluid," *ASME Transaction,* vol. 72 (4), pp. 291-297, 1950.

[24] P. G. Molari, "Stresses in O-ring gaskets," *Proceedings of the 6th International Conference on Fluid Sealing,* pp. 15-31(BHRA), 1973.

[25] R. M. Austin, R. K. Flitney, and B. S. Nau, "Contact stress, friction and the lubricant film of hydraulic cylinder seals," *Proceedings of the 8th International Conference on Fluid Sealing,* pp. 11-20(BHRA), 1978.

[26] Y. Kawahara and Y. Ohtake, "Oil film formation of oil seals for reciprocating motion," *Proceedings of the 9th International Conference on Fluid Sealing,* pp. 73-85(BHRA), 1981.

[27] A. Strozzi, "Static stresses in an unpressurized, rounded, rectangular, elastomeric seal," *ASLE Transactions,* vol. 29 (4), pp. 558-564, 1986.

[28] H. Lindgren, "Pressure distribution in scraper ring contacts," *Wear,* vol. 115 (1-2), pp. 31-40, 1987.

[29] H. Blok and H. J. Koens, "The breathing film between a flexible seal and a reciprocating rod," *Proceedings of the Institution of Mechanical Engineers,* vol. 180 (2), pp. 221-223, 1965.

[30] A. D. Roberts and D. Tabor, "Fluid film lubrication of rubber - an interferometric study," *Wear,* vol. 11 (2), pp. 163-166, 1968.

[31] Y. Kanzaki, Y. Kawahara, and M. Kaneta, "Optical interferometric observations of oil film behaviour in reciprocating rubber seals," *Transaction of Japanese Society of Mechanical Engieers,* vol. 62 (600), pp. 3229-3236, 1996.

[32] Y. Kanzaki, Y. Kawahara, and M. Kaneta, "Oil film behaviour and friction characteristics in reciprocating rubber seals. Part 1 : single contact," *Proceedings of the 15th International Conference on Fluid Sealing*, pp. 79-95(BHRA), 1997.

[33] M. Kaneta, H. Todoroki, H. Nishikawa, and Y. Kanzaki, "Tribology of flexible seals for reciprocating motion," *Journal of Tribology-Transactions of the Asme*, vol. 122 pp. 787-795, 2000.

[34] A. S. Rana, "A tribological study of elastomeric reciprocating seals for hydraulic actuators," PhD Thesis, Imperical College London, England, 2005.

[35] K. B. Schrader, "zur klaerung des abdichtvor-ganges gummielastischer abdichtungen axial verschieb-barer hydrostatischer bauteile," PhD Thesis, Dresden University of Technology, German, 1978.

[36] A. S. Rana, R. S. Sayles, G. K. Nikas, and I. Jalisi, "An experimental technique for investigating the sealing principles of reciprocating elastomeric seals for use in linear hydraulic actuator assemblies," *Proceedings of the 2nd World Tribology Congress, Vienna, Austria*, 2001.

[37] A. S. Rana and R. S. Sayles, "An experimental study on the friction behaviour of aircraft hydraulic actuator elastomeric reciprocating seals," *Proceedings of the 31st Leeds-Lyon Symposium on Tribology, 2004*, 2004.

[38] G. Poll, A. Gabelli, P. G. Binnington, and J. Qu, "Dynamic Mapping of Rotary Lip Seal Lubricant Films by Fluorescent Image Processing," in *Fluid Sealing*. vol. 8, B. S. Nau, Ed., ed: Springer Netherlands, 1992, pp. 55-77.

[39] A. Gabelli and G. Poll, "Formation of Lubricant Film in Rotary Sealing Contacts: Part I—Lubricant Film Modeling," *Journal of Tribology*, vol. 114 (2), pp. 280-287, 1992.

[40] G. Poll and A. Gabelli, "Formation of Lubricant Film in Rotary Sealing Contacts: Part II—A New Measuring Principle for Lubricant Film Thickness," *Journal of Tribology*, vol. 114 (2), pp. 290-296, 1992.

[41] K. Ottink and G. Poll, "Analysis of the lubricant film thickness on rod seals by application of the fluorescence method," *Proceedings of the 21st International Conference on Fluid Sealing*, pp. 179-190(BHRA), 2011.

[42] P. Chadwick, "Thermo-mechanics of rubber like materials," *Philosophical Transactions of The Royal Society*, vol. 276 (1260), pp. 371-403, 1974.

[43] C. Price and F. P. Wolf, "Thermodynamics of rubber elasticity (and discussion)," *Proceedings of The Royal Society A.,* vol. 351 (1666), pp. 331-350, 1976.

[44] P. Chadwick and C. F. M. Creasy, "Modified entropic elasticity of rubber like materials," *Journal of the Mechanics and Physics of Solids,* vol. 32 (5), pp. 337-357, 1984.

[45] R. W. Ogden, "Large deformation isotropic elasticity - on the correlation of theory and experiment for incompressible rubberlike solids," *Proceedings of The Royal Society A.,* vol. 326 (1567), pp. 565-584, 1972.

[46] R. W. Ogden, "Elastic deformations of rubberlike solids," *Mechanics of Solids: The Rodney Hill 60th anniversary volume. (A 83-25302 10-39),* pp. 499-537, 1982.

[47] R. W. Ogden, *Non-linear elastic deformations*. New York, USA: Dover Publications, 1997.

[48] L. R. G. Treloar, H. G. Hopkins, R. S. Rivlin, and J. M. Ball, "The mechanics of rubber elasticity," *Proceedings of The Royal Society A.,* vol. 351 (1666), pp. 301-330, 1976.

[49] M. Mooney, "A theory of large elastic deformation," *Journal of Applied Physics,* vol. 11 (9), pp. 582-592, 1940.

[50] R. S. Rivlin, "Large elastic deformations of isotropic materials. IV. Further developments of the general theory," *Philosophical Transactions of The Royal Society,* vol. 241 (835), pp. 379-397, 1948.

[51] R. S. Lakes, *Viscoelastic solids*: CRC Press LLC, 1999.

[52] A. F. C. Kanters and M. Visscher, "Lubrication of reciprocating seals: experiments on the influence of surface roughness on friction and leakage," in *15th Leeds-Lyon Symposium on Tribology,* Leeds, UK, 1988, pp. 69-77.

[53] R. Gohar, *Elastohydrodynamics*, 2nd ed. London, UK: imperical College Press, 2001.

[54] G. K. Nikas and R. S. Sayles, "Study of leakage and friction of flexible seals for steady motion via a numerical approximation method," *Tribology International,* vol. 39 (9), pp. 921-936, 2006.

[55] J. A. Greenwood and J. B. Williams, "Contact of nominally flat surfaces," *Proceedings of the Royal Society of London Series a-Mathematical and Physical Sciences,* vol. 295 (1442), pp. 300-319, 1966.

[56] G. J. Field and B. S. Nau, "A theoretical study of the elastohydrodynamic lubrication of reciprocating rubber seals," *ASLE Transactions,* vol. 18 (1), pp. 48-54, 1975.

[57] L. E. C. Ruskell, "A rapidly converging theoretical solution to the elastohydrodynamic problem for rectangular rubber seals," *Journal of Mechanical Engineering Science,* vol. 22 pp. 9-16, 1980.

[58] Y. Yang and W. F. Hughes, "An elastohydrodynamic analysis of preloaded sliding seals," *ASLE Transactions,* vol. 27 pp. 197-202, 1983.

[59] E. Prati and A. Strozzi, "A study on the elastohydrodynamic problem in rectangular, elastomeric seals," *ASME Journal of Tribology,* vol. 106 (4), pp. 505-512, 1984.

[60] G. K. Nikas, "Elastohydrodynamics and mechanics of rectangular elastomeric seals for reciprocating piston rods," *Journal of Tribology-Transactions of the Asme,* vol. 125 (1), pp. 60-69, Jan 2003.

[61] G. K. Nikas, "Transient elastohydrodynamic lubrication of rectangular elastomeric seals for linear hydraulic actuators," *Proceedings of the Institution of Mechanical Engineers Part J-Journal of Engineering Tribology,* vol. 217 (J6), pp. 461-473, 2003.

[62] G. K. Nikas, "Theoretical study of solid back-up rings for elastomeric seals in hydraulic actuators," *Tribology International,* vol. 37 (9), pp. 689-699, Sep 2004.

[63] G. K. Nikas and R. S. Sayles, "Nonlinear elasticity of rectangular elastomeric seals and its effect on elastohydrodynamic numerical analysis," *Tribology International,* vol. 37 (8), pp. 651-660, Aug 2004.

[64] G. K. Nikas and R. S. Sayles, "Nonlinear elasticity of rectangular elastomeric seals and its effect on elastohydrodynamic numerical analysis," *Sealing Technology,* vol. 2005 (3), pp. 6-11, 2005.

[65] G. K. Nikas and R. S. Sayles, "Computational model of tandem rectangular elastomeric seals for reciprocating motion," *Tribology International,* vol. 39 (7), pp. 622-634, Jul 2006.

[66] S. T. Tzeng and E. Saibel, "Surface roughness effect on slider bearing lubrication," *ASLE Transactions,* vol. 10 (3), pp. 334-338, 1967.

[67] N. Patir and H. S. Cheng, "Average flow model for determining effects of 3-dimensional roughness on partial hydrodynamic lubrication," *Journal of Lubrication Technology-Transactions of the Asme,* vol. 100 (1), pp. 12-17, 1978.

[68] N. Patir and H. S. Cheng, "Application of average flow model to lubrication between rough silding surfaces," *Journal of Lubrication Technology-Transactions of the Asme,* vol. 101 (2), pp. 220-230, 1979.

[69] H. G. Elrod, "A general theory for laminar lubrication with Reynolds roughness," *Journal of Lubrication Technology-Transactions of the Asme,* vol. 101 (1), pp. 8-14, 1979.

[70] J. H. Tripp, "Surface roughness effects in hydrodynamic lubrication: the flow factor method," *Journal of Lubrication Technology-Transactions of the Asme,* vol. 105 (3), pp. 458-465, 1983.

[71] H. G. Elrod, "A cavitation algorithm," *Journal of Lubrication Technology-Transactions of the Asme,* vol. 103 (3), pp. 350-354, 1981.

[72] P. Payvar and R. F. Salant, "A Computational method for cavitation in a wavy mechanical seal," *Journal of Tribology-Transactions of the Asme,* vol. 114 (1), pp. 199-204, Jan 1992.

[73] S. R. Harp and R. F. Salant, "An average flow model of rough surface lubrication with inter-asperity cavitation," *Journal of Tribology-Transactions of the Asme,* vol. 123 (1), pp. 134-143, Jan 2001.

[74] S. R. Harp and R. F. Salant, "Inter-asperity cavitation and global cavitation in seals: An average flow analysis," *Tribology International,* vol. 35 (2), pp. 113-121, Feb 2002.

[75] G. K. Nikas, "Analytical study of the extrusion of rectangular elastomeric seals for linear hydraulic actuators," *Proceedings of the Institution of Mechanical Engineers Part J-Journal of Engineering Tribology,* vol. 217 (J5), pp. 365-373, 2003.

[76] B. Yang and R. F. Salant, "A numerical model of a reciprocating rod seal with a secondary lip," *Tribology Transactions,* vol. 51 (2), pp. 119-127, 2008.

[77] B. Yang and R. F. Salant, "Soft EHL simulations of U-cup and step hydraulic rod seals," *Journal of Tribology-Transactions of the Asme,* vol. 131 (2), Apr 2009.

[78] A. Thatte and R. F. Salant, "Transient EHL analysis of an elastomeric hydraulic seal," *Tribology International,* vol. 42 (10), pp. 1424-1432, Oct 2009.

[79] A. Thatte and R. F. Salant, "Elastohydrodynamic analysis of an elastomeric hydraulic rod seal during fully transient operation," *Journal of Tribology-Transactions of the Asme,* vol. 131 (3), Jul 2009.

[80] A. Thatte and R. F. Salant, "Visco-elastohydrodynamic model of a hydraulic rod seal during transient operation," *Journal of Tribology-Transactions of the Asme,* vol. 132 (4), Oct 2010.

[81] A. Thatte and R. F. Salant, "Effects of multi-scale viscoelasticity of polymers on high-pressure, high-frequency sealing dynamics," *Tribology International,* vol. 52 pp. 75-86, Aug 2012.

[82] T. Schmidt, M. André, and G. Poll, "A transient 2D-finite-element approach for the simulation of mixed lubrication effects of reciprocating hydraulic rod seals," *Tribology International,* vol. 43 (10), pp. 1775-1785, 2010.

[83] X. H. Jia, S. Jung, W. Haas, and R. F. Salant, "Numerical simulation and experimental study of shaft pumping by laser structured shafts with rotary lip seals," *Tribology International,* vol. 44 (5), pp. 651-659, May 2011.

[84] X. H. Jia, S. Jung, W. Haas, and R. F. Salant, "Numerical simulation and experimental study of shaft pumping by plunge ground shafts with rotary lip seals," *Tribology International,* vol. 48 pp. 155-161, Apr 2012.

[85] A. Blatter, M. Maillat, S. M. Pimenov, G. A. Shafeev, A. V. Simakin, and E. N. Loubnin, "Lubricated sliding performance of laser-patterned sapphire," *Wear,* vol. 232 (2), pp. 226-230, 1999.

[86] A. Ronen, I. Etsion, and Y. Kligerman, "Friction-reducing surface-texturing in reciprocating automotive components," *Tribology Transactions,* vol. 44 (3), pp. 359-366, 2001/01/01 2001.

[87] X. Wang, K. Kato, K. Adachi, and K. Aizawa, "The effect of laser texturing of SiC surface on the critical load for the transition of water lubrication mode from hydrodynamic to mixed," *Tribology International,* vol. 34 (10), pp. 703-711, 2001.

[88] M. Wakuda, Y. Yamauchi, S. Kanzaki, and Y. Yasuda, "Effect of surface texturing on friction reduction between ceramic and steel materials under lubricated sliding contact," *Wear,* vol. 254 (3–4), pp. 356-363, 2// 2003.

[89] P. Andersson, J. Koskinen, S. Varjus, Y. Gerbig, H. Haefke, S. Georgiou, *et al.*, "Microlubrication effect by laser-textured steel surfaces," *Wear,* vol. 262 (3–4), pp. 369-379, 2/4/ 2007.

[90] M. Scaraggi, "Textured surface hydrodynamic lubrication: Discussion," *Tribology Letters,* vol. 48 (3), pp. 375-391, 2012.

[91] M. Scaraggi, F. P. Mezzapes, G. Carbone, and A. Ancona, "Friction properties of lubricatied laster-micro texured surfaces: An experimental study from boundary to hydrodynamic lubrication," *Tribology Letters,* vol. 49 (1), pp. 117-125, 2013.

[92] M. Scaraggi, F. P. Mezzapes, G. Carbone, D. Sorgente, and P. M. Lugara, "Minimize friction of lubricated laser-microtextured-surfaces by tuning microholes depth," *Tribology International,* vol. 75 pp. 123-127, 2014.

[93] Y. Kligerman, I. Etsion, and A. Shinkarenko, "Improving tribological performance of piston rings by partial surface texturing," *Journal of Tribology,* vol. 127 (3), pp. 632-638, 2005.

[94] G. Ryk, Y. Kligerman, and I. Etsion, "Experimental Investigation of Laser Surface Texturing for Reciprocating Automotive Components," *Tribology Transactions,* vol. 45 (4), pp. 444-449, 2002.

[95] G. Ryk and I. Etsion, "Testing piston rings with partial laser surface texturing for friction reduction," *Wear,* vol. 261 (7–8), pp. 792-796, 10/20/ 2006.

[96] I. Etsion, Y. Kligerman, and G. Halperin, "Analytical and experimental investigation of laser-textured mechanical seal faces," *Tribology Transactions,* vol. 42 (3), pp. 511-516, 1999/01/01 1999.

[97] I. Etsion and G. Halperin, "A laser surface textured hydrostatic mechanical seal," *Tribology Transactions,* vol. 45 (3), pp. 430-434, 2002/01/01 2002.

[98] A. Shinkarenko, Y. Kligerman, and I. Etsion, "The effect of elastomer surface texturing in soft elasto-hydrodynamic lubrication," *Tribology Letters,* vol. 36 (2), pp. 95-103, Nov 2009.

[99] A. Shinkarenko, Y. Kligerman, and I. Etsion, "The effect of surface texturing in soft elasto-hydrodynamic lubrication," *Tribology International,* vol. 42 (2), pp. 284-292, Feb 2009.

[100] A. Shinkarenko, Y. Kligerman, and I. Etsion, "The validity of linear elasticity in analyzing surface texturing effect for elastohydrodynamic lubrication," *Journal of Tribology-Transactions of the Asme,* vol. 131 (2), Apr 2009.

[101] Y. Kligerman and A. Shinkarenko, "The effect of tapered edges on lubrication regimes in surface-textured elastomer seals," *Tribology International,* vol. 44 (12), pp. 2059-2066, Nov 2011.

[102] I. Etsion, "State of the art in laser surface texturing," *Journal of Tribology-Transactions of the Asme,* vol. 127 (1), pp. 248-253, Jan 2005.

[103] Y. P. Chiu, "An analysis and prediction of lubricant film starvation in rolling contact systems," *ASLE Transactions,* vol. 17 (1), pp. 22-35, 1974/01/01 1974.

[104] R. J. Boness, "The effect of oil supply on cage and roller motion in a lubricated roller bearing," *Journal of Tribology,* vol. 92 (1), pp. 39-51, 1970.

[105] D. E. Brewe, B. J. Hamrock, and C. M. Taylor, "effect of geometry on hydrodynamic film thickness," *Journal of Tribology,* vol. 101 (2), pp. 231-237, 1979.

[106] D. E. Brewe and B. J. Hamrock, "Analysis of starvation effects on hydrodynamic lubrication in nonconforming contacts," *Journal of Tribology,* vol. 104 (3), pp. 410-417, 1982.

[107] L. van der Tempel, H. Moes, and R. Bosma, "Starvation in dynamically loaded flexible short journal bearings," *Journal of Tribology,* vol. 107 (4), pp. 516-521, 1985.

[108] B. Vincent, P. Maspeyrot, and J. Frěne, "Starvation and cavitation effects in finite grooved journal bearing," in *Tribology Series*. vol. Volume 30, C. M. T. T. H. C. C. D. Dowson and G. Dalmaz, Eds., ed: Elsevier, 1995, pp. 455-464.

[109] D. Vijayaraghavan and J. T. G. Keith, "Analysis of a finite grooved misaligned journal bearing considering cavitation and starvation effects," *Journal of Tribology,* vol. 112 (1), pp. 60-67, 1990.

[110] D. Vijayaraghavan, T. G. Keith, and D. E. Brewe, "Effect of lubricant supply starvation on the thermohydrodynamic performance of a journal bearing," *Tribology Transactions,* vol. 39 (3), pp. 645-653, 1996/01/01 1996.

[111] L. D. Wedeven, D. Evans, and A. Cameron, "Optical analysis of ball bearing starvation," *Journal of Tribology,* vol. 93 (3), pp. 349-361, 1971.

[112] C. R. Gentle and M. Pasdari, "Computer simulation of starvation in thrust-loaded ball-bearings," *Wear,* vol. 92 (1), pp. 125-134, 12/1/ 1983.

[113] D. N. Olaru and M. D. Gafitanu, "Starvation in ball bearings," *Wear,* vol. 170 (2), pp. 219-234, 12/1/ 1993.

[114] G. Popovici, "Effects of lubricant starvation on performance of elasto-hydrodynamically lubricated contacts," PhD Thesis, University of Twente, the Netherlands, 2005.

[115] B. J. Hamrock and D. Dowson, "Elastohydrodynamic lubrication of elliptical contacts for materials of low elastic modulus I—fully flooded conjunction," *Journal of Tribology,* vol. 100 (2), pp. 236-245, 1978.

[116] B. J. Hamrock and D. Dowson, "Elastohydrodynamic lubrication of elliptical contacts for materials of low elastic modulus: II—starved conjunction," *Journal of Tribology,* vol. 101 (1), pp. 92-98, 1979.

[117] O. Reynolds, "On the theory of lubrication and its application to Mr. Beauchamp Tower's experiments, including and experimental determination of the viscosity of olive oil," *Philosophical Transactions of The Royal Society London,* vol. 177 pp. 157-234, 1886.

[118] B. J. Hamrock, S. R. Schmid, and B. O. Jacobson, *Fundamentals of Fluid Film Lubrication,* 2nd ed. New York: Marcel Dekker Inc., 2004.

[119] S. V. Patankar, *Numerical heat transfer and fluid flow*. Washington: Hemisphere Pub. Corp., 1980.

[120] B. Yang, "Elastohydrodynamic model of reciprocating hydraulic rod seals," PhD Thesis, Georgia Institute of Technology, Atlanta, GA, 2010.

[121] A. Thatte, "Multi-scale multi-physics model and hybrid computational framework for predicting dynamics of hydraulic rod seals," PhD Thesis, Georgia Institute of Technology, Atlanta, GA, 2010.

[122] D. W. Peaceman and H. H. Rachford Jr, "The numerical solution of parabolic and elliptic differential equations," *Journal of the Society for Industrial and Applied Mathematics*, vol. 3 (1), pp. 28-41, 1955.

[123] J. L. Streator, "A model of mixed lubrication with capillary effects," in *28th Leeds-Lyon Symposium on Tribology*, Vienna, Austria, 2001, pp. 121-128.